

Quasar absorption-line measurements of the cosmological variability of fundamental constants

Adrian Lucas Malec

Presented in fulfillment of the requirements
of the degree of Doctor of Philosophy

2016



Faculty of Science, Engineering and Technology
Swinburne University of Technology

Abstract

Investigating the possibility that the fundamental physical constants of nature actually vary offers a potential route for the discovery of new fundamental physics. Spectra of quasar (QSO) absorption systems are a source of observational constraints on this variation over cosmological scales. In this thesis, the variation of the fine structure constant, α , is constrained using the many-multiplet (MM) method applied to a highly sensitive subset of transitions – those of Zn and Cr II – in the spectra of 9 rare “metal-strong” QSO absorbers, observed with Keck/HIRES and VLT/UVES spectrographs. The use of this subset of lines reduces the effect of the long-range wavelength distortions detected in previous works, while allowing the competitive weighted-mean constraint of $\Delta\alpha/\alpha = (0.04 \pm 1.69_{\text{stat}} \pm 1.15_{\text{sys}}) \times 10^{-6}$ to be obtained, comparable in sensitivity to previous large-sample studies. The systematic error is a quadrature addition of the effects from long and short-range wavelength distortions in the spectra, the former being small compared to previous studies, thereby confirming the efficacy of the Zn/Cr II approach. This result is consistent with no temporal variation in α for the range of absorption redshifts in this sample ($z_{\text{abs}} = 1.072\text{--}2.308$). The low angular separations amongst the sample prevented a meaningful constraint on the spatial variation of α . To constrain the proton-to-electron mass ratio μ , 86 H₂ and 7 HD transitions were simultaneously fitted in the Keck/HIRES spectrum of J2123–0050 at $z_{\text{abs}} = 2.059$ to obtain the constraint $\Delta\mu/\mu = (+5.6 \pm 5.5_{\text{stat}} \pm 2.9_{\text{sys}}) \times 10^{-6}$. A wide suite of consistency tests were performed, including a detailed search for systematic errors. The systematic error is a quadrature addition of three main effects: long and short-range wavelength calibration errors and effects from re-dispersion of the spectra. The result is consistent with no temporal variation in μ , for the given precision. The complex fit was facilitated by, and demonstrated the benefits of, the “comprehensive” fitting approach, in contrast to the “line-by-line” approach applied in previous studies.

I dedicate this thesis to my parents
Teresa and Stan Malec
And
To the memory of my grandmother
Helena Gruzka

Acknowledgements

This thesis would not have been possible without the tremendous academic creativity and insight of my supervisor Michael Murphy. I give you my sincere thanks for your support, patience and guidance through the many years. Your feedback significantly improved the quality of this thesis.

I give my heartfelt thanks to my co-supervisor Chris Blake. I don't think I could have gotten this far without your understanding, support and initiative.

Thank you to Bob Carswell for the titanic effort in maintaining VPFIT and continually adding new features. A long list of thanks to Jason X. Prochaska for all your work on data reduction, not limited to writing HIRES REDUX, tracking down bugs and explanations of the reduction process. I thank all of my publication co-authors for their contributions, especially Ruth Buning and Wim Ubachs. I thank the Swinburne Time Allocation Committee for Keck, ESO Observing Programmes Committee and Directorate and the Australian Gemini Office for recognising the value of this work. My appreciation and thanks to my thesis examiners, Alberto Fernández-Soto and Graça Rocha for reviewing my thesis and improving it through your valuable feedback.

Thank you to everyone I met at the Centre for Astrophysics and Supercomputing, especially Jonathan Whitmore, Glenn Kacprzak, Paul Coster, Virginia Killborn, Jarrod Hurley, Sarah Maddison, Evelyn Caris, Carlos Conteras and Tyler Evans. A special thanks to Chris Fluke for seeing me through my undergraduate studies all the way through to the end of my PhD. I thank everyone at Swinburne Research for your continued work in supporting the Centre, with a special thanks to Pamela Green. I thank the past and present Centre directors Matthew Bailes, Warrick Couch and Karl Glazebrook for their leadership in making the Centre a world-class institution for astronomy. I am grateful to Margaret Mazzolini for developing an undergraduate degree that prepared me for research, and to Birgit Loch for giving me the opportunity to teach mathematics at Swinburne. I would also like to express my gratitude to Peter Binks for his encouragement, support and mentorship outside the academic world.

My warmest thanks to Kristy for your love and support during a difficult and busy time. I thank my loving family – Mum, Dad and my sister Judy. Mum,

thank you for your gentle encouragement and support through all of the years of my education. Dad, thank you for sparking my interest in science at an early age and for translating an entire book on space so that I could read it. When I found the book again, I realised I had been reading about and looking at an illustration of one of the (yet to be completed) Keck telescopes at the age of 8. I could not have predicted or dreamed that many years later I would be standing inside its impressive structure and that I'd be leading it across the sky, collecting light with the hope of learning something new about the Universe.

Some of the data presented herein were obtained at the W.M. Keck Observatory, which is operated as a scientific partnership among the California Institute of Technology, the University of California and the National Aeronautics and Space Administration. The Observatory was made possible by the generous financial support of the W.M. Keck Foundation.

The author of this thesis wishes to recognise and acknowledge the very significant cultural role and reverence that the summit of Mauna Kea has always had within the indigenous Hawaiian community. We are most fortunate to have the opportunity to conduct observations from this mountain.

Based on observations made with ESO Telescopes at the La Silla Paranal Observatory under programme ID 084.A-0136.

This research has made use of the SIMBAD database, operated at CDS, Strasbourg, France.

Declaration

The work presented in this thesis has been carried out in the Centre for Astrophysics & Supercomputing at Swinburne University of Technology between March 2008 and September 2015. This thesis contains no material that has been accepted for the award of any other degree or diploma. To the best of my knowledge, this thesis contains no material previously published or written by another author, except where due reference is made in the text of the thesis. All work presented is primarily that of the author.

Chapter 4 and a portion of Chapter 1 have been published as ‘*Keck telescope constraint on cosmological variation of the proton-to-electron mass ratio*’ Malec, A. L., Buning, R., Murphy, M. T., Milutinovic, N., Ellison, S. L., Prochaska, J. X., Kaper, L., Tumlinson, J., Carswell, R. F., and Ubachs, W.: 2010, *MNRAS* **403**, 1541. Alterations have been made to this work in order to maintain consistency of style.

Contents of Chapters 2 and 3 have *not* appeared in a refereed journal, but are expected to be submitted for publication in the near future.

Where the contributions to the work in this thesis are not my own, this is acknowledged in the Foreword section of each chapter, if applicable.

Adrian Lucas Malec
Melbourne, Australia
16 September 2015

Contents

Abstract	i
List of Figures	xi
List of Tables	xv
1 Introduction	1
1.1 Fundamental physical constants	2
1.2 Varying fundamental constants	5
1.3 QSO constraints on α variation	8
1.4 QSO constraints on μ variation	14
1.5 Searches for systematic effects	19
1.6 Thesis outline	21
2 Zn II and Cr II absorption observations and data reduction	23
2.1 Foreword	23
2.2 Introduction	24
2.3 Observational and laboratory data	28
2.4 Data reduction	44
3 Constraints on $\Delta\alpha/\alpha$ using Zn II and Cr II transitions	53
3.1 Introduction	54
3.2 Analysis	54
3.3 Results	91
3.4 Systematic error analysis	93
3.5 Discussion	100
4 Robust $\Delta\mu/\mu$ constraint from molecular absorption spectra	105
4.1 Foreword	106
4.2 Introduction	106
4.3 Data	107
4.4 Analysis and results	116
4.5 Internal consistency and systematic errors	138

4.6	Discussion	151
5	Conclusions	157
5.1	Summary	157
5.2	Future work	160
6	References	163
A	Fiducial models of blending Mg I absorption	173
B	Catalogue of H₂ laboratory parameters	195

List of Figures

2.1	Metal-line shifts with varying α	27
3.1	Data and model fit for the J0058+0051 HIRES spectrum Zn II and Cr II transitions, centred at $z_{\text{abs}} = 1.072$	64
3.2	Data and model fit for the J0058+0051 UVES spectrum Zn II and Cr II transitions, centred at $z_{\text{abs}} = 1.072$	65
3.3	Data and model fit for the J0108–0037 UVES spectrum Zn II and Cr II transitions, centred at $z_{\text{abs}} = 1.371$	67
3.4	Data and model fit for the J0226–2857 UVES spectrum Zn II and Cr II transitions, centred at $z_{\text{abs}} = 1.023$	70
3.5	Data and model fit for the J0841+0312 HIRES spectrum Zn II and Cr II transitions, centred at $z_{\text{abs}} = 1.343$	73
3.6	Data and model fit for the J0841+0312 UVES spectrum Zn II and Cr II transitions, centred at $z_{\text{abs}} = 1.343$	74
3.7	Data and model fit for the J1029+1039 HIRES spectrum Zn II and Cr II transitions, centred at $z_{\text{abs}} = 1.622$	77
3.8	Data and model fit for the PHL957 HIRES spectrum Zn II and Cr II transitions, centred at $z_{\text{abs}} = 2.309$	80
3.9	Data and model fit for the PHL957 UVES spectrum Zn II and Cr II transitions, centred at $z_{\text{abs}} = 2.309$	81
3.10	Data and model fit for the Q1755+57 HIRES spectrum Zn II and Cr II transitions, centred at $z_{\text{abs}} = 1.971$	85
3.11	Data and model fit for the Q2206–1958 UVES spectrum Zn II and Cr II transitions, centred at $z_{\text{abs}} = 1.920$	87
3.12	Data and model fit for the J1237+0106 HIRES spectrum Zn II and Cr II transitions, centred at $z_{\text{abs}} = 1.305$	90
3.13	Plot of fiducial $\Delta\alpha/\alpha$ results vs. z_{abs} , the absorption redshift. . . .	94
3.14	Plot of $\Delta\alpha/\alpha_d$ values obtained from artificially distorted spectra sim- ulating short-range intra-order distortions, compared to the fiducial $\Delta\alpha/\alpha$ values.	98

3.15	Plot of fiducial $\Delta\alpha/\alpha$ results overlaid to the best fit spatially varying α dipole of King et al. (2012) vs Θ , the angle from dipole maximum (in degrees).	101
4.1	Sample of the 86 H ₂ and 7 HD lines from the J2123–0050 Keck spectrum on a velocity scale centred at $z_{\text{abs}} = 2.0594$	110
4.2	The sensitivity coefficients, K_i and the distribution of transitions with wavelength according to their J -levels.	117
4.3	All regions of the J2123–0050 Keck spectrum fitted in the analysis.	125
4.4	$\Delta\mu/\mu$ and χ^2 per degree of freedom, χ^2_ν , for different velocity structures characterised by the number of fit absorption components. . .	134
4.5	Composite residual spectra (CRS), formed from 24 relatively unblended H ₂ transitions for 2, 3 and the fiducial 4 component models.	136
4.6	$\Delta\mu/\mu$ measured for subsets of transitions based on H ₂ J -level and HD and groupings thereof.	143
4.7	420 Monte Carlo simulations of the fiducial 4 component absorption model used in the analysis.	144
4.8	Current extragalactic $\Delta\mu/\mu$ constraints.	154
A.1	Data and model fit for the J0058+0051 HIRES spectrum Mg I transitions, centred at $z_{\text{abs}} = 1.072$	176
A.2	Data and model fit for the J0058+0051 UVES spectrum Mg I transitions, centred at $z_{\text{abs}} = 1.072$	177
A.3	Data and model fit for the J0108–0037 UVES spectrum Mg I transitions, centred at $z_{\text{abs}} = 1.371$	179
A.4	Data and model fit for the J0226–2857 UVES spectrum Mg I transitions, centred at $z_{\text{abs}} = 1.023$	181
A.5	Data and model fit for the J0841+0312 HIRES spectrum Mg I transitions, centred at $z_{\text{abs}} = 1.343$	183
A.6	Data and model fit for the J0841+0312 UVES spectrum Mg I transitions, centred at $z_{\text{abs}} = 1.343$	184
A.7	Data and model fit for the J1029+1039 HIRES spectrum Mg I transitions, centred at $z_{\text{abs}} = 1.622$	186

A.8	Data and model fit for the Q1755+57 HIRES spectrum Mg I transitions, centred at $z_{\text{abs}} = 1.971$	189
A.9	Data and model fit for the Q2206–1958 UVES spectrum Mg I transitions, centred at $z_{\text{abs}} = 1.920$	191
A.10	Data and model fit for the J1237+0106 HIRES spectrum Mg I transitions, centred at $z_{\text{abs}} = 1.305$	193

List of Tables

2.1	Target Zn/Cr II systems	29
2.2	Journal of Keck/HIRES observations taken and the additional archival spectra used for this thesis.	32
2.3	Journal of VLT/UVES observations taken and archival spectra used for this thesis.	38
2.4	SNR per pixel of the final combined spectra used for the varying α analysis.	52
3.1	Fiducial fit Zn II and Cr II absorption line parameters and 1- σ statistical uncertainties for the J0058+0051 HIRES spectrum.	63
3.2	Fiducial fit Zn II and Cr II absorption line parameters and 1- σ statistical uncertainties for the J0058+0051 UVES spectrum.	63
3.3	Fiducial fit Zn II and Cr II absorption line parameters and 1- σ statistical uncertainties for the J0108–0037 spectrum.	66
3.4	Fiducial fit Zn II and Cr II absorption line parameters and 1- σ statistical uncertainties for the J0226–2857 spectrum.	69
3.5	Fiducial fit Zn II and Cr II absorption line parameters and 1- σ statistical uncertainties for the J0841+0312 HIRES spectrum.	72
3.6	Fiducial fit Zn II and Cr II absorption line parameters and 1- σ statistical uncertainties for the J0841+0312 UVES spectrum.	72
3.7	Fiducial fit Zn II and Cr II absorption line parameters and 1- σ statistical uncertainties for the J1029+1039 spectrum.	76
3.8	Fiducial fit Zn II and Cr II absorption line parameters and 1- σ statistical uncertainties for the PHL957 HIRES spectrum.	78
3.9	Fiducial fit Zn II and Cr II absorption line parameters and 1- σ statistical uncertainties for the PHL957 UVES spectrum.	79
3.10	Fiducial fit Zn II and Cr II absorption line parameters and 1- σ statistical uncertainties for the Q1755+57 spectrum.	83
3.11	Fiducial fit Zn II and Cr II absorption line parameters and 1- σ statistical uncertainties for the Q2206–1958 spectrum.	86

3.12	Fiducial fit Zn II and Cr II absorption line parameters and 1- σ statistical uncertainties for the J1237+0106 spectrum.	89
3.13	The fiducial $\Delta\alpha/\alpha$ values obtained as a result of the χ^2 minimisation.	93
3.14	The $\Delta\alpha/\alpha_d$ values obtained from artificially distorted spectra simulating short-range intra-order distortions, compared to the fiducial $\Delta\alpha/\alpha$ values.	97
3.15	Table of current QSO absorption-based $\Delta\alpha/\alpha$ constraints.	103
4.1	Compilation of laboratory H ₂ data for all of the H ₂ transitions fit in the spectrum of J2123–0050.	112
4.2	Compilation of laboratory HD data for all of the $J = 0$ HD transitions falling in the spectrum of J2123–0050.	115
4.3	Molecular absorption line parameters and 1- σ statistical uncertainties for the 4-component fiducial fit of J2123–0050 used to constrain $\Delta\mu/\mu$	137
A.1	Fiducial fit Mg I absorption line parameters and 1- σ statistical uncertainties for the J0058+0051 HIRES spectrum.	174
A.2	Fiducial fit Mg I absorption line parameters and 1- σ statistical uncertainties for the J0058+0051 UVES spectrum.	175
A.3	Fiducial fit Mg I absorption line parameters and 1- σ statistical uncertainties for the J0108–0037 spectrum.	178
A.4	Fiducial fit Mg I absorption line parameters and 1- σ statistical uncertainties for the J0226–2857 spectrum.	180
A.5	Fiducial fit Mg I absorption line parameters and 1- σ statistical uncertainties for the J0841+0312 HIRES spectrum.	182
A.6	Fiducial fit Mg I absorption line parameters and 1- σ statistical uncertainties for the J0841+0312 UVES spectrum.	182
A.7	Fiducial fit Mg I absorption line parameters and 1- σ statistical uncertainties for the J1029+1039 spectrum.	185
A.8	Fiducial fit Mg I absorption line parameters and 1- σ statistical uncertainties for the Q1755+57 spectrum.	187
A.9	Fiducial fit Mg I absorption line parameters and 1- σ statistical uncertainties for the Q2206–1958 spectrum.	190

A.10 Fiducial fit Mg I absorption line parameters and $1\text{-}\sigma$ statistical uncertainties for the J1237+0106 spectrum.	192
B.1 Catalogue of the most accurate and precise laboratory parameters for fitting H ₂ absorptions lines.	195

Introduction

Contents

1.1	Fundamental physical constants	2
1.1.1	The primacy of dimensionless constants	2
1.1.2	The fine structure constant – α	4
1.1.3	The proton-to-electron mass ratio – μ	4
1.2	Varying fundamental constants	5
1.2.1	Local constraints	6
1.2.2	Astrophysics as a probe of fundamental constants	7
1.3	QSO constraints on α variation	8
1.3.1	The alkaline-doublet method	8
1.3.2	The many-multiplet method	10
1.4	QSO constraints on μ variation	14
1.4.1	Using molecular hydrogen absorption spectra	15
1.4.2	Using ammonia absorption spectra	17
1.4.3	Other methods	18
1.5	Searches for systematic effects	19
1.6	Thesis outline	21

1.1 Fundamental physical constants

A fundamental physical constant is a physical value believed to be a property of the Universe that is unchanging in space and time. It requires a physical measurement, unlike a mathematical constant, which is derived from first principles. The most commonly recognised constants are the speed of light in vacuum c , the gravitational constant G and the elementary charge e . Other constants are particle masses and coupling constants. Given that most of human observation is of *change* in one form or another, the idea of some fixed, unchanging, constant property of the Universe naturally leads one to ascribe it fundamentality. Our abstract, scientific models require these constants to predict observation, as if they are the link between the abstract, geometrical and the physical. One can think of fundamental physical constants as the fixed parameters at the beginning of a computer program, used throughout the code, and chosen to make the program return the ‘correct’ output. If the reader feels unsatisfied with this, they are not alone. The idea that the values of constants are fixed to some particular values to make the Universe *work* lead one to explanations such as the Anthropic principle¹ or concepts of ‘cosmic providence’. Before resting on any such philosophical conclusions, one should exhaust their scientific inquiry first. Maybe their values are calculable? Maybe they are not constant at all? Maybe their nature is not yet fully understood? One way or the other, their existence and our lack of explanation for them and their values are signposts of our ignorance.

1.1.1 The primacy of dimensionless constants

It is important to distinguish between dimensional constants and dimensionless physical constants. They are not merely categories; the two terms describe two very different types of ‘constants’. Constants such as c , G and e are measured in physical units – they are *dimensional*. Their particular values are a direct result of the chosen unit system and one cannot place significance on their numeric value *per se*. They ‘exist’ only when they relate one measured quantity to another (e.g. time to distance, mass to force) in a given model and they effectively set the

¹The notion that intelligent life would not have developed to measure fundamental constants if the constants were not the exact values required for this to happen.

units of measurable quantities. Constants which are dimensionless are calculated from the ratios of dimensional constants, where the ratio of the units is 1. Examples include coupling constants such as the fine structure constant α , particle masses normalised by the Planck mass or by other fundamental masses, such as the proton-to-electron mass ratio μ and unitary matrix parameters used to describe behaviour of quarks and neutrinos. There are 26 such constants in the Standard Model of particle physics. It is important to stress that these constants are pure numbers, yet are completely specified by physical measurement. One could naively say they permeate the Universe, as they are present wherever the four fundamental interactions occur. This parametrisation ‘ether’ is neither explanatory as a concept nor sophisticated in any way. Yet there is no consensus or evidence for anything better. This lack of understanding, with our avenue of recourse limited to physical measurement was expressed by Edward M. Purcell when he stated “With respect to [the fine structure constant] we are in the rather humiliating position of people who have to wrap a piece of string around a cylinder to determine pi.” (Rigden, 2002).

The importance of dimensionless constants can be demonstrated with a thought experiment involving communication with a distant, extraterrestrial intelligence. In order to establish a common language for information pertaining to local physics on either end, one could exchange the values of important physical constants. Using the speed of light c or any other dimensional constant would involve an exchange describing the unit systems used from either or both parties (especially apparent because c is a defined quantity within the SI). This would have to involve communication of experimental methods and conditions required for the development of these unit systems. If the ‘laws of physics’ are different between both locations (due to, say, yet undiscovered phenomena), one could not reliably consider both methods being comparable. It would be much easier and more direct to communicate the *dimensionless* physical constants. Their mere approximate numerical values should correlate with some part of a sufficiently developed scientific body of knowledge.

This thesis is concerned with two dimensionless constants, the fine structure constant α , and the proton-to-electron mass ratio μ . The key idea behind the work presented here is not too different from the thought experiment just described,

where instead of communication, high-precision observations of physical phenomena are made at large spatial and temporal scales and compared with those here on Earth.

1.1.2 The fine structure constant – α

The fine structure constant is most often defined in terms of other constants as

$$\alpha \equiv \frac{e^2}{4\pi\epsilon_0\hbar c} \approx \frac{1}{137.036}, \quad (1.1)$$

where e is the elementary charge, ϵ_0 is the permittivity of free space, \hbar is the reduced Planck constant and c is the speed of light in vacuum. This dimensionless quantity was originally introduced by Sommerfeld (1911) as a measure of the relativistic correction to the Bohr model of the atom and the scale of the fine-structure splitting in Hydrogen spectral lines. α is now more generally interpreted as a coupling constant that determines the strength of the electromagnetic force. Effectively, it characterises the interactions between light and matter. For example, it is a measure of the strength of interaction between photons and electrons; an $\alpha = 0$ would mean this interaction was null. The presence of α in physics is almost ubiquitous – one only needs the presence of an electrically charged particle and a model that considers quantum and relativistic effects, to find α in the equations. This ubiquity also makes α available for measurement using a wide variety of experiments.

1.1.3 The proton-to-electron mass ratio – μ

The proton-to-electron mass ratio is defined as

$$\mu \equiv \frac{m_p}{m_e} \approx 1836.153, \quad (1.2)$$

where m_p is the mass of the proton and m_e is the mass of the electron. The μ constant characterises the scales of vibrational, rotational, and hyperfine intervals in atomic and molecular spectra (in contrast to α , which characterises the structure of atomic and ionic spectra). The primary source of mass in m_p is the quark-binding gluon field, so the μ constant can be said to be a measure of the chromodynamic

scale relative to the electroweak scale (from the bound electrons and nucleus). More generally, it can be said that μ parameterises the relative strengths of the strong and electroweak forces.

1.2 Varying fundamental constants

In the Standard Model of particle physics α and μ are assumed to be constant in space-time. The Standard Model, however, cannot predict the values of α or μ , which must be established experimentally. This implies that the constancy of α , μ and other parameters that define the Model must also be determined through experiment. Essentially, these fundamental constants are *assumed* to be constant, because their measurements have been found to be consistent between different types of laboratory-based experiments, performed over timescales of the order of years. There is no definitive, commonly accepted theory which answers *why* this consistency exists. Further, can one truly generalise measurements taken over what are *local* Earth-based scales to *cosmological* scales? These unknowns are the motivation behind the search for *varying* fundamental constants. If these fundamental parameters are found to vary in time or space, a more fundamental theory would supplant the Standard Model and perhaps unify the four known physical interactions. One may hope for a surprising, extraordinary experimental result leading to rapid new developments in the theoretical sphere, as has unfolded many times in the past. However, the continued evidence of the constancy of the fundamental constants is just as interesting. It deepens the mystery and significance of these quantities as truly fundamental – future theories would have to predict the nature of the particular values these constants measure. In either case, investigation of the potential variation of fundamental constants informs the development of new theoretical frameworks, as these must be consistent with physical observations.

Throughout this thesis, references will be made to the constraints on fractional variation in values of α and μ on cosmological scales, formalised as

$$\frac{\Delta\alpha}{\alpha} = \frac{\alpha_z - \alpha_{\text{lab}}}{\alpha_{\text{lab}}}, \quad (1.3a)$$

$$\frac{\Delta\mu}{\mu} = \frac{\mu_z - \mu_{\text{lab}}}{\mu_{\text{lab}}}, \quad (1.3b)$$

where α_z is the measured α value at redshift z , and α_{lab} is the local lab-measured value. Similarly for μ . For local constraints, $\dot{\alpha}/\alpha$ and $\dot{\mu}/\mu$ are used, which are fractional time-derivative constraints that assume a linear variation with time.

1.2.1 Local constraints

Before addressing astrophysical constraints of variation of fundamental constants on cosmological scales, local constraints are briefly discussed here. Local constraints on $\Delta\alpha/\alpha$ have been derived from a variety of terrestrial, geological sources, such as meteorite dating and the Oklo natural fission reactor, on timescales of the age of the Earth. These geological constraints vary in precision, from $\delta(\Delta\alpha/\alpha)$ of $\sim 10^{-3}$ to $\sim 10^{-8}$, and notably require consideration of their inherent model-dependencies. In some cases, the constraints are degenerate with weakly-constrained cosmological parameters, meaning they are not independent measures of the constants. See Uzan (2003) for a review. The Oklo natural fission reactor, for example, offers a constraint on varying α but requires assumptions and estimates concerning the physical properties of the reactor in the past, and the result is degenerate with potential variation of the proton gyro-magnetic ratio and the weak coupling constant.

Local varying μ constraints are virtually limited to lab-based atomic clock experiments, which also constrain α variation. These experiments are an active area of research and currently provide the best local bounds for both α and μ variation. The time-derivative form of the results is usually quoted, as these constraints are obtained over year periods. Constraints are currently achieving uncertainties of $\delta(\dot{\alpha}/\alpha) \sim 10^{-17} \text{ year}^{-1}$ and $\delta(\dot{\mu}/\mu) \sim 10^{-16} \text{ year}^{-1}$. Recently Huntemann et al. (2014) measured $\dot{\alpha}/\alpha = (-2.0 \pm 2.0) \times 10^{-17} \text{ year}^{-1}$ and $\dot{\mu}/\mu = (-0.5 \pm 1.6) \times 10^{-16} \text{ year}^{-1}$ using a comparison of a singly-ionised ytterbium atomic clock with a reference to two caesium clocks. These results were derived from measurements obtained in that experiment and other similar studies, using a linear regression fit. In this fit the constraint on μ variation was obtained at the same time as the α constraint and cannot be considered an independent measurement. Godun et al. (2014) measured $\dot{\alpha}/\alpha = (-0.7 \pm 2.1) \times 10^{-17} \text{ year}^{-1}$ and $\dot{\mu}/\mu = (0.2 \pm 1.1) \times 10^{-16} \text{ year}^{-1}$ using a singly-ionised ytterbium atomic clock, without the use of a caesium standard. Measurements were made over a period of about 1 to 2 months and previous results in the field were used in calculat-

ing the final constraint. Single-experiment constraints taken over longer periods have also been obtained, such as those of Rosenband et al. (2008), who found $\dot{\alpha}/\alpha = (-1.6 \pm 2.3) \times 10^{-17} \text{ year}^{-1}$ based on repeated measurements of the frequency ratio of two (singly ionised aluminium and mercury) atomic clocks made over one year.

1.2.2 Astrophysics as a probe of fundamental constants

Observations of astrophysical systems offer an attractive source of constraints on fundamental constants over larger scales than those available in the lab or from geological sources. Arguably, the most powerful of these are those based on QSO (quasi-stellar object, or quasar) spectroscopy, as distinguished by high sensitivity and model independence. QSO constraints on α and μ variation are discussed in detail in the following sections. Note that recent μ constraints are virtually all QSO-based. Other sources of constraints include measurements of the cosmic microwave background (CMB), which involve modelling large-scale structure formation as a function of fundamental constants. These can be used to measure potential α variation (along with m_e , the mass of the electron) through measures of the ionisation cross-section for hydrogen. Recent Planck observations of the CMB (Planck Collaboration et al., 2015) have constrained α to $\Delta\alpha/\alpha = (3.6 \pm 3.7) \times 10^{-3}$ (note that the constraint is less stringent than best QSO-based constraints by 3 orders of magnitude and involves model dependencies). Big Bang nucleosynthesis (BBN) constraints use the dependence of primordial abundances on fundamental physical constants. Abundance ratios D/H, ${}^7\text{Li}/\text{H}$, ${}^3\text{He}/\text{H}$ and ${}^4\text{He}/\text{H}$ can be used to constrain $\Delta\alpha/\alpha$. The precision of these constraints is of similar magnitude to those derived from the CMB, e.g. Ichikawa and Kawasaki (2002), who measured $\Delta\alpha/\alpha = (-2.24 \pm 3.75) \times 10^{-4}$. Like CMB constraints, BBN constraints are highly model-dependent (e.g. on the baryon-to-photon ratio, correlations with other coupling constants). Removing some of these model dependencies weakens the constraints by two orders of magnitude (e.g. Cyburt et al., 2005). The CMB and BBN sources of constraints are suggestive of no variation in α , but are relatively insensitive compared to QSO constraints. For a more detailed overview of the various astrophysical methods used, see Uzan (2003) and Dent et al. (2008).

1.3 QSO constraints on α variation

This section reviews constraints on $\Delta\alpha/\alpha$ using high-resolution spectra of background QSOs, primarily using intervening absorption systems. As described in the following sections, a varying α will correspond to a variation in the energy levels of atomic/ionic transitions. Any such variations on large spatial and temporal scales are therefore observable as relative velocity shifts² between different absorption (or emission) lines along QSO lines of sight (if one momentarily disregards limited measurement precision). To distinguish these velocity shifts as resulting from a variation in α , the calculated magnitude, direction and overall pattern of shifts, based on the relativistic effects for a transition, are taken into account. This approach carries with it a high degree of model-independence because only the atomic/ionic system's response to α variation is modelled, using reliable methods. The approach also limits assumptions to the kinematic properties of the intervening systems, not those directly related to measurements of variation in α (i.e. no assumptions are made involving other constants or cosmological parameters and there is no dependency on the evolution of the QSOs or the intervening absorbers), as is the case for most other types of local and astrophysical constraints.

1.3.1 The alkaline-doublet method

In an alkali doublet the fine-structure splitting of energy levels occurs due to the spin-orbit interaction. The relative doublet separation is proportional to α^2 . Using the separation $(\Delta\lambda)_z$ observed at redshift z and the separation observed in the laboratory $(\Delta\lambda)_0$ one can derive a constraint on a small change (as expected from the wealth of physical observation) in $\Delta\alpha/\alpha$ as follows (Varshalovich et al., 2000)

$$\frac{\Delta\alpha}{\alpha} \simeq \frac{1}{2} \left[\frac{(\Delta\lambda)_z}{(\Delta\lambda)_0} - 1 \right]. \quad (1.4)$$

The first constraint on $\Delta\alpha/\alpha$ using the alkali doublet (AD) method was published by Savedoff (1956), who measured the separation between AD transitions of N II and Ne III observed in a Seyfert galaxy's (Cygnus A) emission spectra. A

²denoted as $\Delta v = (\lambda_n/\lambda_o - 1)c$, where λ_n is the shifted wavelength and λ_o is the original wavelength.

comparable constraint at higher redshift ($z \sim 0.2$) was obtained by Bahcall and Schmidt (1967) who used a pair of O III multiplet lines seen in QSO emission spectrum.

Since one is looking for small velocity shifts, the ideal spectral line would resemble a delta function: the narrower the lines observed, the better the constraint. Almost every current QSO constant constraint relies on intervening metal absorption lines, which are narrower than intrinsic emission lines. Although an order of magnitude weaker than preceding constraints, the limit on $\Delta\alpha/\alpha$ derived by Bahcall et al. (1967) was the first QSO absorption line-based constraint (though the absorption was broad, as it was *intrinsic* to the spectrum of the QSO). Even narrower are intervening absorption lines seen in damped Lyman- α absorbers (DLAs), as used by Wolfe et al. (1976).

The quantity and the sensitivity of the QSO-based varying-constant constraints up until the mid-90s was low when compared to the relatively recent developments in the field. Better limits became available because of the advent of 10m-class telescopes. Cowie and Songaila (1995) used Keck High Resolution Echelle Spectrometer (HIRES) spectra (with $R = 36,000$; considered to be “extremely high-resolution” at the time) of 9 absorption systems with $z_{\text{abs}} = 2.7 - 3.6$ to obtain an improved high-redshift constraint. Varshalovich et al. (1996) used only Si IV doublet lines (Si IV has a widely spaced doublet, and is therefore very sensitive to changes in α), and later Ivanchik et al. (1999) and Varshalovich et al. (2000) used the same method and expanded samples of spectra to achieve relative precision of $\sim 9 \times 10^{-5}$. Murphy et al. (2001c) applied the AD method to spectra of better resolution and signal-to-noise ratio (SNR; an improvement over the spectra used in Varshalovich et al., 2000) with improved laboratory wavelengths. Multi-component Voigt profile fits were constructed to model the velocity structure of the absorbing clouds (for a description of what velocity structure is in the context of profile fitting see Section 3.2.1 and sections therein). Simultaneous χ^2 minimisation between the spectral data and profile fits was then used to obtain a $\Delta\alpha/\alpha$ constraint for each absorber. The combined result was $\Delta\alpha/\alpha = (-0.5 \pm 1.3) \times 10^{-5}$ with $z_{\text{abs}} = 2 - 3$. Martínez Fiorenzano et al. (2003) and later Chand et al. (2005) used Very Large Telescope (VLT) Ultraviolet and Visual Echelle Spectrograph (UVES) data in their AD analysis. Chand et al. claimed the strongest constraint, obtained with the AD

method, using 15 Si IV doublets obtained from a UVES sample. Unfortunately that work suffered from the same serious deficiencies described by Murphy et al. (2008b, discussed in the next section) and cannot be considered reliable at any level.

1.3.2 The many-multiplet method

The many-multiplet (MM) method was introduced by Webb et al. (1999) and Dzuba et al. (1999). The MM method uses the transitions of different multiplets and different atoms/ions associated with the same QSO absorption system.

In an AD analysis, the ‘doublet’ is a result of the fine-structure splitting of energy levels due to the spin–orbit interaction. The method’s weakness is that it compares transitions with the same ground state, since a doublet arises in the same atomic/ionic species. The ground state is important because here the electron is closest to the nucleus. α strongly factors into the relativistic corrections due to the interaction between electron and nucleus, where the common ground state often has the largest relativistic corrections. Comparing transitions with different ground states, that is, of different species, allows one almost an order of magnitude improvement in $\Delta\alpha/\alpha$ sensitivity, in large part due to the greater differences in the ground state relativistic corrections between different species. This is exactly what the MM method achieves, additionally utilising more spectral information than the AD method via the use of more transitions. What makes the MM method readily applicable to QSO spectra is that all relativistic effects for a transition are combined into a single coefficient q , which varies in sign and magnitude depending on the particular transition (this in itself is an advantage, since more complex patterns of q values lead to constraints more resistant to systematic effects). See Murphy et al. (2001b) and the two seminal works cited above for details. The MM method derives a constraint on a small change in $\Delta\alpha/\alpha$ as follows

$$\omega_z = \omega_0 + q \left[\left(\frac{\alpha_z}{\alpha_0} \right)^2 - 1 \right], \quad (1.5)$$

where ω_z is the rest wavenumber of a transition at redshift z and ω_0 is the laboratory

reference wavenumber. This can be expressed as follows

$$\frac{\Delta\alpha}{\alpha} = \sqrt{\frac{\omega_z - \omega_0}{q} + 1} - 1. \quad (1.6)$$

This equation is applied to each transition observed in a QSO spectrum and a joint constraint on $\Delta\alpha/\alpha$ is derived from the pattern of line shifts between those transitions.

First to use the MM method, Webb et al. (1999) found tentative evidence for a smaller α at $z_{\text{abs}} = 0.5 - 1.6$, achieving relative precision of 4×10^{-6} using 30 absorbers from archival Keck/HIRES spectra (i.e. not observed or wavelength calibrated with the specific purpose of measuring $\Delta\alpha/\alpha$). Including additional QSO spectra of 19 DLA absorbers, Murphy et al. (2001b) obtained an even stronger constraint in support of the positive detection of a smaller α in the past, with a result of $\Delta\alpha/\alpha = (-0.72 \pm 0.18) \times 10^{-5}$. The companion work in Murphy et al. (2001a) detailed the comprehensive search by the authors for systematic effects which might explain the result. It was found that correcting for the strongest known systematic effects only reinforced a non-zero $\Delta\alpha/\alpha$. Soon after, Murphy et al. (2003a) further expanded the sample in Murphy et al. (2001b) with more archival Keck/HIRES spectra, analysing a total of 128 absorption systems (in 76 independent QSO lines of sight), also re-analysing the previous samples for consistency of method. By utilising archival spectra from 3 different observing groups, the study analysed more QSO absorbers to constrain $\Delta\alpha/\alpha$ than in previous studies combined. Further, the simultaneously and consistently analysed sample allowed for potential systematic effects to be better studied. The weighted mean of the individual absorber constraints allowed a more precise measurement of $\Delta\alpha/\alpha = (-0.54 \pm 0.10) \times 10^{-5}$ over $z_{\text{abs}} = 0.2 - 3.7$ to be derived, seemingly confirming the prior evidence of a smaller α in the past with $\sim 5\text{-}\sigma$ confidence. A further 15 absorption systems observed using Keck/HIRES at high- z_{abs} (> 1.8), were added to this sample in Murphy et al. (2004), where a total of 143 absorbers were analysed, arriving at the constraint $\Delta\alpha/\alpha = (-0.57 \pm 0.11) \times 10^{-5}$ for $z_{\text{abs}} = 0.5 - 4.2$.

The results spurred further studies, including those incorporating data from VLT/UVES observations. Chand et al. (2004) used VLT/UVES spectra and found $\Delta\alpha/\alpha = (-0.06 \pm 0.06) \times 10^{-5}$ using a sample of 23 absorbers at $z_{\text{abs}} = 0.4 - 2.3$,

conflicting with that of Murphy et al. (2004). The incredible jump in precision, given the significantly smaller number of absorbers without significantly higher SNR, put the results into question. Indeed, the χ^2 curves from the minimisation algorithm reveal faults in the minimisation routine used, which not only led to significant underestimation of the uncertainties derived, but rendered the result completely inconclusive. Murphy et al. (2008b) discussed these problems and used the same, reduced VLT/UVES spectra and fits used by Chand et al. (2004) in a re-analysis. It was found that Chand et al. (2004) measured an uncertainty that was impossible to achieve given the SNR of the data. The result itself was found to be zero-biased because of problems in the χ^2 -minimisation. The re-analysis (using the original, unmodified data and fits) found an uncertainty 6 times larger than originally quoted, with the result now $\Delta\alpha/\alpha = (-0.64 \pm 0.36) \times 10^{-5}$ – neither strongly supportive of a smaller α in the past nor inconsistent with the Murphy et al. (2004) result. Murphy et al. (2008b) also critically reviewed other null constraints based on observations of two individual absorbers observed with VLT/UVES (e.g. Quast et al., 2004; Levshakov et al., 2006, 2007). It was found that some of the studies underestimated uncertainties. The review stressed the importance of fitting enough structure in the absorption models so as to avoid systematic errors.

The potential for spatial, rather than just temporal variation in α , was considered by Murphy et al. (2004). The results were not strongly conclusive, as the Keck-based absorber sample did not offer the necessary level of angular sky coverage. This was fully realised by Webb et al. (2011) and King et al. (2012), who found evidence of spatial variation in α from a combined VLT and Keck absorber sample, where the Keck constraints used were those of Murphy et al. (2004). King et al. (2012) analysed a sample of 153 VLT/UVES absorbers, with resolution and SNR similar to the Keck/HIRES sample of Murphy et al. (2004). The weighted mean of the results over $z_{\text{abs}} = 0.22 - 3.61$ was $\Delta\alpha/\alpha = (0.208 \pm 0.124) \times 10^{-5}$, seemingly contradicting the Keck sample of Murphy et al. (2004) and motivating the spatially varying α fit to the combined sample. King et al. (2012) found a best-fitting dipole model to be $\Delta\alpha/\alpha = A \cos(\Theta) + m$ where $m = (-0.178 \pm 0.084) \times 10^{-5}$, $A = 0.97 \times 10^{-5}$ ($1-\sigma$ confidence range $[0.77, 1.19] \times 10^{-5}$). The angle from the dipole maximum is the Θ parameter (in degrees), where the direction of the dipole

maximum is $\text{RA} = 17.3 \pm 1.0$ h, $\text{Dec.} = -61^\circ \pm 10^\circ$.

Recently, however, all the above results have been called into question by Whitmore and Murphy (2015), who show the positive $\Delta\alpha/\alpha$ VLT results can be wholly attributed to long-range wavelength distortions in UVES spectra. These distortions were found by comparing UVES spectra of ‘solar twin’ stars and asteroids to a reliable laboratory solar spectrum. A long-range, approximately linear velocity offset from the true wavelength values was found to be present across the full wavelength range of each arm (blue and red) of the spectrograph. This distortion was found to mimic the velocity shifts corresponding to a non-zero $\Delta\alpha/\alpha$. Similar distortions were also found in HIRES spectra, and partially explain the negative $\Delta\alpha/\alpha$ results of the Keck-based studies. Systematic errors due to instrumental effects have always been, and continue to be, investigated in the field of varying constants (along with searches in other fields reliant on high-precision spectroscopy, such as those detecting and characterising exoplanets). Recent systematic effect searches are reviewed in their own Section 1.5, as they are relevant to both varying α and μ QSO-based studies that utilise optical telescope data. However, a brief summary of the main steps in this area follows. Valenti et al. (1995) found that the instrument profile (spatial projection of spectrograph slit onto the echelle spectrum) varies across the focal plane of HIRES. Molaro et al. (2008) was the first study to investigate the wavelength accuracy of the UVES spectrograph using asteroid spectra as compared to a reference solar atlas. It found no substantial long-range distortions in the wavelength scale of UVES, at least for the spectra analysed, in stark contrast to the results of Whitmore and Murphy (2015). That the spectra analysed by Molaro et al. (2008) did not have substantial distortions is likely a result of chance, as almost all other UVES spectra do. Griest et al. (2010), Whitmore et al. (2010) and Wendt and Molaro (2012) detected the presence of intra-order distortions in HIRES and UVES spectrographs using similar techniques. However, in these studies, the distortions did not have a long-range component and the intra-order pattern of distortions was essentially repeated from order to order. Rahmani et al. (2013) and Bagdonaite et al. (2014) used comparisons of UVES asteroid spectra and laboratory solar spectra to detect and correct for long-range wavelength distortions in their constraints on varying μ .

A major collaboration, the UVES Large Program for testing fundamental physics,

aiming to resolve the sometimes contradictory α and μ results in the field was commenced in mid-2010. The Program aims to obtain $\Delta\alpha/\alpha$ measurements with ~ 10 ppm precision from each of ~ 25 absorbers in ~ 12 QSO VLT/UVES spectra with higher SNR (~ 80 per pixel) than typically used previously (Molaro et al., 2013). Importantly, this Program is the first large-scale observational campaign with the primary, *a priori* focus on varying- α measurements. As part of the Program, Molaro et al. (2013) analysed a single QSO spectrum of HE 2217–2818, using 5 absorption systems over $z_{\text{abs}} = 0.79 - 1.69$ in that line of sight, measuring $\Delta\alpha/\alpha = (1.3 \pm 2.4_{\text{stat}} \pm 1.0_{\text{sys}}) \times 10^{-6}$. Evans et al. (2014) then analysed another single QSO spectrum, of HS 1549+1919, using 3 absorbers in that line of sight. Keck and Subaru spectra for these absorbers were also used, in addition to the Program’s VLT spectrum, obtaining a weighted mean result of $\Delta\alpha/\alpha = (-5.4 \pm 3.3_{\text{stat}} \pm 1.5_{\text{sys}}) \times 10^{-6}$, suggestive of no variation in α . Additional calibrating asteroid and iodine-cell spectra were used to characterise and correct for long-range distortions in the spectral wavelength scales, making these results the most reliable measurements of $\Delta\alpha/\alpha$ so far. By combining these results with those of Molaro et al. (2013), a constraint of $\Delta\alpha/\alpha = (-0.6 \pm 1.9_{\text{stat}} \pm 0.9_{\text{sys}}) \times 10^{-6}$ was calculated. Note that the Molaro et al. (2013) results did not employ the additional calibration techniques of Evans et al. (2014). Further analyses from the Program’s observations are expected in the near future.

1.4 QSO constraints on μ variation

This section reviews QSO constraints on $\Delta\mu/\mu$ using molecular hydrogen and ammonia absorption spectra and other methods. A majority of these employ precise measurements of shifts in absorption or emission lines, similar to $\Delta\alpha/\alpha$ analyses, and also carry the advantage of model-independence.

Note that the material presented herein is current as of 2010, when the varying μ work presented in this thesis was completed and published (Malec et al., 2010a), and has not been since updated. Significant developments in the field are summarised in Bagdonaite et al. (2014).

1.4.1 Using molecular hydrogen absorption spectra

The first $\Delta\mu/\mu$ constraint based on QSO observations was that of Pagel (1977) who used H I and metal absorption lines. Thompson (1975) was the first work to suggest using ro-vibrational molecular transitions (transitions between rotational sublevels of vibrational levels of an electronic level) as indicators of μ -variation. While molecular hydrogen, H_2 , is by far the most abundant molecule in the universe, the H_2 Lyman and Werner transitions³ are detectable with ground-based telescopes only at redshifts $z_{\text{abs}} > 2$, due to the atmospheric cutoff toward bluer wavelengths. Foltz et al. (1988) used the H_2 absorber at $z_{\text{abs}} = 2.8$ towards the QSO Q 0528–250 to derive an upper limit to μ variation of $|\Delta\mu/\mu| < 2.0 \times 10^{-4}$. The study used Multiple Mirror Telescope (MMT) spectra, of low resolution compared to modern standards (FWHM of $\sim 1 \text{ \AA}$), and was a limited analysis using only two H_2 transitions.

Varshalovich and Levshakov (1993) introduced the sensitivity coefficients, K_i , now ubiquitous in H_2 -based $\Delta\mu/\mu$ studies. As μ varies, ro-vibronic transitions shift in velocity based on their particular dependence on the reduced-mass of the molecule. The magnitude and direction of the velocity shift is characterised by a sensitivity coefficient K_i for each transition i , analogous to the q coefficients used for MM $\Delta\alpha/\alpha$ studies. One may consider a single transition arising in an absorption cloud, whose redshift is established to be z_{abs} , assuming momentarily that the other transitions are insensitive to variations in μ . If μ was the same in the absorption cloud as in the laboratory, one would expect to find transition i at wavelength $\lambda_{\text{lab}}^i(1 + z_{\text{abs}})$. If instead it is measured to be at wavelength $\lambda_i = \lambda_{\text{lab}}^i(1 + z_i)$ (i.e. at redshift $z_i \neq z_{\text{abs}}$), then the shift in redshift, $\Delta z_i \equiv z_i - z_{\text{abs}}$, or velocity, Δv_i , can be ascribed to a variation in μ ,

$$\frac{\Delta v_i}{c} \approx \frac{\Delta z_i}{1 + z_{\text{abs}}} = K_i \frac{\Delta\mu}{\mu}. \quad (1.7)$$

That different transitions have different K_i values enables a differential measurement of $\Delta\mu/\mu$ from two or more transitions.

³Lyman and Werner transitions refer to two electronic transition levels possible from the ground state. These are bands because of different available ro-vibrational levels in the excited state. The Lyman and Werner bands dominate the absorption spectrum of H_2 at laboratory wavelengths $\lambda_{\text{lab}} \lesssim 1150 \text{ \AA}$.

While H_2 is abundant, just as H is abundant, absorbers usable for $\Delta\mu/\mu$ analysis are scarce. The need of a bright background QSO and the requirement of the cold (and therefore more likely to be small) clouds in which H_2 forms on dust grains (Ge and Bechtold, 1999) mean that lines-of-sight that pass through such clouds are uncommon. Further, the H_2 absorption needs to be present at high enough column densities to absorb most of the continuum so that effective line velocity measurements are possible, and needs to occur at high enough redshift ($z_{\text{abs}} > 2$) for the molecular spectrum to fall in the optical range for ground-based observations. As a result, Q 0528–250 and only a handful of other QSOs were used and reused for $\Delta\mu/\mu$ analysis for some time (e.g. Varshalovich and Levshakov, 1993; Cowie and Songaila, 1995; Varshalovich and Potekhin, 1995; Levshakov et al., 2002).

Indications for a significantly positive $\Delta\mu/\mu$ were derived from two H_2 absorbers observed with VLT/UVES by Ivanchik et al. (2005). The study used high resolving power ($R \approx 53000$) and high SNR (≈ 30 –70) UVES spectra of the $z_{\text{abs}} = 2.595$ and 3.025 absorbers towards the QSOs Q 0405–443 and Q 0347–383, respectively. A total of 76 H_2 lines in the two spectra were fit independently of each other (i.e. the so-called ‘line-by-line’ approach) to derive values for λ_i . In this analysis the H_2 absorption profiles in Q 0347–383 were treated as comprising a single cloud. Of the two resolved H_2 features observed in Q 0405–443, only the strongest was fitted. Using two different sets of ‘best’ H_2 laboratory wavelengths (Abgrall et al. 1993 and Philip et al. 2004) Ivanchik et al. derived two sets of z_i values which yielded two $\Delta\mu/\mu$ values, $(+30.5 \pm 7.5) \times 10^{-6}$ and $(+16.5 \pm 7.4) \times 10^{-6}$ respectively.

Reinhold et al. (2006) subsequently improved the laboratory wavelengths and the calculation of the K sensitivity coefficients. Using the same values of λ_i and their uncertainties derived by Ivanchik et al. (2005), Reinhold et al. performed a ‘line-by-line’ analysis to refine the values of $\Delta\mu/\mu$ for each absorber: $(+20.6 \pm 7.9) \times 10^{-6}$ for Q 0347–383 and $(+27.8 \pm 8.8) \times 10^{-6}$ for Q 0405–443. The combined value of $(+24.5 \pm 5.9) \times 10^{-6}$ was presented as an indication for cosmological variation in μ .

King et al. (2008) reanalysed the same raw UVES QSO spectra with improved flux extraction and, more importantly, using the improved wavelength calibration procedures detailed in Murphy et al. (2007). King et al. (2008) used slightly more H_2 transitions and, importantly, a ‘simultaneous fitting’ technique, with explicit

treatment of Lyman- α forest lines (see Section 4.4.1) to constrain the values of $\Delta\mu/\mu$ in the newly reduced and calibrated spectra. This ‘simultaneous fitting’ method works in a similar way to the MM method. That is, it allows the redshift z_{abs} to be determined simultaneously with $\Delta\mu/\mu$.

They found decreased values in both absorbers compared to previous works: $\Delta\mu/\mu = (+8.2 \pm 7.4) \times 10^{-6}$ and $(+10.1 \pm 6.2) \times 10^{-6}$ for Q 0347–383 and Q 0405–443 respectively. King et al. also analysed 64 H_2 lines of a third absorption system, that at $z_{\text{abs}} = 2.811$ towards Q 0528–250, using UVES spectra with $R \approx 45000$ and $\text{SNR} \approx 25\text{--}45$. This provided the tightest constraint of all three absorbers: $\Delta\mu/\mu = (-1.4 \pm 3.9) \times 10^{-6}$. Thus, the combined result, where the slightly positive values for Q 0347–383 and Q 0405–443 are somewhat cancelled by the slightly negative but more precise value for Q 0528–250, was a null constraint of $\Delta\mu/\mu = (+2.6 \pm 3.0) \times 10^{-6}$. The same UVES spectra were also recently studied by Wendt and Reimers (2008) and Thompson et al. (2009) using different data reduction and analysis techniques, generally aimed at avoiding and/or understanding potential systematic errors and biases in $\Delta\mu/\mu$. They also found null constraints, albeit with somewhat larger statistical errors than King et al., due to their more conservative approaches.

A much larger statistical sample is obviously desirable if one is to find confidence in the results, and work is underway in the field to survey high redshift QSO absorbers for H_2 (e.g. Srianand et al., 2012; Balashev et al., 2014).

1.4.2 Using ammonia absorption spectra

At $z < 1$, comparison of the radio inversion transitions of NH_3 – which have enhanced sensitivity to μ -variation (van Veldhoven et al., 2004; Flambaum and Kozlov, 2007) – with less sensitive molecular rotational lines (e.g. HCO^+ , HCN) has yielded two very strong constraints: $\Delta\mu/\mu = (+0.74 \pm 0.47_{\text{stat}} \pm 0.76_{\text{sys}}) \times 10^{-6}$ at $z = 0.685$ (Murphy et al., 2008a) and $(+0.08 \pm 0.47_{\text{sys}}) \times 10^{-6}$ at $z = 0.889$ (Henkel et al., 2009). The radio constraints have superior precision and, by current estimates, smaller potential systematic errors. However, direct comparison of the radio and optical H_2/HD constraints is difficult because of the possibility, in principle, for spatial variations in μ ; i.e. the different molecular species (NH_3 and H_2/HD) trace regions of different densities and, therefore, different spatial

scales and environment. If μ does vary, one does not know what that variation depends on, so one should not give preference to one type of measurement over the other. Indeed, this is highlighted by Levshakov et al. (2008) who studied NH_3 inversion *emission* lines from numerous Galactic molecular clouds. With statistical errors from previous literature of $\sim 0.1 \text{ km s}^{-1}$ they found velocity offsets between the NH_3 inversion and rotational molecular emission of up to $|\Delta v| \sim 0.5 \text{ km s}^{-1}$ in individual systems. This might indicate spatial variations in μ throughout our Galaxy, although intrinsic shifts between emission lines of different molecules are to be expected. The possibility for both space and time-variations in μ is even more important given the different redshift ranges currently probed by the radio and optical constraints.

1.4.3 Other methods

Several other QSO absorption and emission-line techniques for constraining variations in combinations of fundamental constants involving μ are also of note. One approach is to use absorption lines associated with rest-frame UV transitions of heavy element species compared with the rest-frame 21-cm transition of neutral hydrogen. The method constrains the quantity $X \equiv g_p \alpha^2 / \mu$ where g_p is the proton g -factor. A variety of analyses using different metal-ions have been performed (e.g. Wolfe et al., 1976; Tzanavaris et al., 2005; Kanekar et al., 2006), with measurements from 9 absorption systems at $0.23 < z_{\text{abs}} < 2.35$ by Tzanavaris et al. (2007) providing a constraint of $\Delta X/X = (+6.3 \pm 9.9) \times 10^{-6}$. Kanekar et al. (2010b) used two 21-cm and C I absorption systems at $z_{\text{abs}} = 1.4 - 1.6$ to obtain $\Delta X/X = (+6.8 \pm 1.0_{\text{stat}} \pm 6.7_{\text{sys}}) \times 10^{-6}$. Rahmani et al. (2012) used Keck, VLT, Giant Metrewave Radio Telescope and Green Bank Telescope observations of 4 QSO lines of sight over $z_{\text{abs}} = 1.17 - 1.56$ to arrive at the constraint of $\Delta X/X = (-0.1 \pm 1.3) \times 10^{-6}$.

However, the fact that the H I 21-cm and metal-line velocity structures are observationally dissimilar – probably because the radio morphology of most background QSOs is not point-like – means that improvements must come by averaging over many sight-lines and/or carefully selecting QSOs with point-like radio morphologies. Comparing H I 21-cm with the ‘main’ OH 18-cm absorption lines, which constrains $F \equiv g_p(\mu\alpha^2)^{1.57}$ (Chengalur and Kanekar, 2003), suffers less from this

problem because of the similarity of the wavelengths concerned. Kanekar et al. (2005) analysed two absorbers at $z_{\text{abs}} = 0.685$ and 0.765 to obtain the constraint $\Delta F/F = (+4.4 \pm 3.6_{\text{stat}} \pm 10_{\text{sys}}) \times 10^{-6}$. Recently, Kanekar et al. (2012) measured $\Delta F/F = (-5.2 \pm 4.3) \times 10^{-6}$ using the $z_{\text{abs}} = 0.765$ absorption system toward PMN J0134-0931.

One can also use “conjugate” satellite OH 18-cm lines, where one is observed in absorption while the other in emission (arising when the ground state level populations are inverted). The distinct advantage of the method is that both lines typically have the same optical depth profile and are guaranteed to arise in the same gas clouds. Comparing the sum and difference of the optical depth profiles of the 1612 and 1720 MHz conjugate satellite lines constrains $G \equiv g_{\text{p}}(\mu\alpha^2)^{1.85}$ (Chengalur and Kanekar, 2003). With only two such systems known outside our Galaxy, and with their published spectra having low SNR, no definitive constraints on $\Delta G/G$ yet exist (Darling, 2004; Kanekar et al., 2005). Kanekar (2008) presented a preliminary constraint of $|\Delta G/G| < 11 \times 10^{-6}$ for a system (PKS 1413+135) at $z = 0.247$, and also $< 12 \times 10^{-6}$ for a Galactic system, Centaurus A. Recently, Kanekar et al. (2010a) used Westerbork Synthesis Radio Telescope and Arecibo Telescope observations of PKS 1413+135 to obtain $\Delta G/G = (-1.18 \pm 0.46) \times 10^{-5}$.

While these constraints on variations in X , F and G are important in their own right, it is difficult to directly compare them with constraints on $\Delta\mu/\mu$. Predictions for the relationships between variations in, for example, μ and α , are strongly model-dependent (Dent et al., 2008). Currently, there is also no overlap with the redshift range occupied by the H₂/HD constraints on $\Delta\mu/\mu$ and variations in X , F and/or G .

1.5 Searches for systematic effects

Detailed searches for systematic effects are of great significance in the field of QSO-based fundamental constraints. Any detection of a variation in a fundamental constant would hold significant consequences for the current understanding of physics, so it is imperative to understand the extent and role of any important systematic effects in great detail, even in the case of non-detections. While statistical errors are reduced with increasing sample sizes, greater SNR and, in the

long term, better telescopes and instrumentation, characterisation and correction for persistent systematic errors becomes ever more so pressing. This is especially true in this field. Much work has been done in estimating the systematic error component for many of the studies in the field, with some dedicated primarily to the task (e.g. Murphy et al., 2001a, 2003b). While many such previous studies have explored various potential physical sources of systematic error and estimated them, focus has recently shifted towards measuring systematic errors *empirically*. Recent works have performed direct searches for evidence of systematic errors in the most important aspect of calibration of the spectra, the wavelength scale, without first identifying potential causes of the errors. Griest et al. (2010) and Whitmore et al. (2010) compared QSO spectra calibrated using the standard ThAr lamp and those with iodine absorption directly imprinted within the instrumentation⁴. They found pervasive distortion patterns, which vary from exposure to exposure, projected on the 2D echelle spectra of both Keck/HIRES and VLT/UVES instruments. This systematic effect is present on relatively short-wavelength scales. Its cause is yet to be fully identified. It is more important for smaller sample constraints than those derived from large samples, as the systematic effect is effectively random for larger samples. See Section 3.4.3 and Section 4.5.2.3 for discussion of these distortions in the context of the constraints presented in this thesis.

A method of measuring distortions in spectra without the use of additional non-standard calibrations was developed by Evans and Murphy (2013) where spectra of the same object are directly compared with each other. This direct comparison (DC) method was applied to Keck and VLT spectra of J2123–0050, with no detections of significant distortions. The DC method was also used in Evans et al. (2014) for their 3-telescope sample, where long-range distortions between individual exposures were corrected as part of the analysis.

Most recently, significant long-range wavelength distortions were found in UVES and HIRES spectra by Whitmore and Murphy (2015). The work compared spectra of ‘solar twin’ stars and asteroids to a reliable laboratory solar spectrum, allowing for unprecedented characterisation of the wavelength accuracy of the HIRES and

⁴Using iodine cells in the light path of the telescope is a very reliable method of wavelength calibration, but it is costly. It greatly reduces the effective SNR of the QSO spectrum studied and complicates the analysis because of the overlapping iodine and QSO spectra. In contrast, ThAr calibration involves very short (~ 1 second) exposures taken before or after the QSO exposures.

UVES instruments. The long-range distortions are particularly important to varying α and μ studies, and it was found that these distortions largely account for previous non-null varying α results (see Section 1.3.2). The exact nature of these distortions remains elusive, though they are likely caused by a difference in astronomical object and ThAr calibration light paths. The distortions are discussed in the context of the varying α constraint in this work in Section 3.4.2. It is apparent that all future constraints using HIRES and UVES spectra will need to correct for this systematic effect.

1.6 Thesis outline

The developments in the varying α and μ fields summarised in this thesis motivate further investigation, with the hope of reconciling the often conflicting studies through continued observations and improvements to methods. The work presented in this thesis is aligned with this aim and covers two separate studies. One, constraining α variation using a sample of 9 absorption systems, using the novel approach of using a subset of Zn/Cr II transitions, motivated by the method’s resistance to long-range wavelength distortions. The other, constraining μ variation using high-SNR observations of a single absorber with properties that make it exceptional for such a constraint, motivated by the expansion of the sample of absorbers studied, but with the much-improved “comprehensive fitting” approach rather than the “line-by-line” approach.

Chapter 2 describes the 9 target Zn/Cr II systems used for the varying α analysis, including the general observational strategy, a detailed journal of observations taken for the project, a summary of the data reduction performed and improvements to the reduction approach that enable this project. The varying α analysis is detailed in the separate Chapter 3 and covers physical assumptions, profile fitting, results, systematic error considerations, a discussion of implications of the results and a comparison with other recent constraints. Chapter 4 follows the structure of the previous chapter, but for constraining μ variation. Chapter 5 summarises the key conclusions from the two studies and outlines the future work for the studies and more broadly, the field of QSO-based varying constant constraints.

Zn II and Cr II absorption observations and data reduction

Contents

2.1	Foreword	23
2.2	Introduction	24
2.3	Observational and laboratory data	28
2.3.1	Targets and observation strategy	28
2.3.2	Journal of observations and archival spectra	31
2.3.3	Laboratory wavelengths and sensitivity coefficients	44
2.4	Data reduction	44
2.4.1	Standard wavelength calibration and optimal extraction	46
2.4.2	Improved calibration for Keck/HIRES data	47
2.4.3	Combining exposures and fitting a continuum	50

2.1 Foreword

The data reduction for VLT/UVES data was performed by M. Murphy, using the UVES data reduction pipeline, not including the combination of exposures. The reference ThAr line selection for both VLT/UVES and Keck/HIRES data was also performed M. Murphy using the method in Murphy et al. (2007). All other work in this Chapter was performed by the author of this thesis.

2.2 Introduction

The full many-multiplet (MM) method, which uses the transitions of different multiplets and different atoms/ions to constrain $\Delta\alpha/\alpha$, has been applied to large samples of high-quality QSO spectra from 8 & 10-m telescopes and has demonstrated an impressive increase in the statistical precision (to about 1 part per million in Murphy et al., 2004; King et al., 2012). However, it has been long suspected, and recently demonstrated by Whitmore and Murphy (2015), that the evidence of α being different on cosmological scales is almost certainly a result of long-range distortions of the wavelength scale. The effect of these distortions is the introduction of a systematic error in $\Delta\alpha/\alpha$, with a resulting deviation from $\Delta\alpha/\alpha = 0$ of the same sign and similar magnitude to the non-zero α detections. Especially vulnerable are QSO absorption systems at low redshifts where only the Mg I/II and Fe II lines were used. As shown in Figure 2.1 the Fe II lines all shift, as a function of α variation, in a common direction and similar magnitude with respect to the effectively ‘anchored’ Mg lines at longer wavelengths. Therefore, identifying absorption systems in which a subset of transitions can be used to avoid this sensitivity to long-range distortions is highly desirable.

The use of Zn II and Cr II transitions in constraining $\Delta\alpha/\alpha$ is particularly advantageous, having 3 primary benefits over full many-multiplet (MM) fits.

1. The Zn II 2026/2062 (Å) and Cr II 2056/2062/2066 (Å) transitions shift in opposite directions as α varies, as shown in Figure 2.1, allowing for greater sensitivity to α variation. The signature of a varying α in this case is very different to that in the full MM method. For example, in the case of Mg/Fe II transitions, the Fe II transitions are most sensitive to α , shifting in a common direction, while the Mg II transitions remain largely ‘anchored’. But in the Zn/Cr II signature of varying α , the lines shift in opposite directions, meaning there is a greater sensitivity to α variation. Additionally, the Zn II 2062 line interlaces among the Cr II 2056/2062/2066 lines in wavelength, meaning a complex pattern of shifts will exist if α varies – more complicated for a systematic error to mimic – than for the Mg/Fe II signature.
2. The associated lines are close to each other in wavelength, making measure-

ments of $\Delta\alpha/\alpha$ much less prone to long-range wavelength calibration errors than in the full MM method. Because the lines used in previous MM analyses are spread over a wide range of wavelengths, they are sensitive not only to shifts from α variation, but also to long-range wavelength distortions. Whitmore and Murphy (2015) used reliable calibration sources to show that such distortions are present in both the HIRES and UVES spectrographs. The authors hypothesise they are a result of a difference in astronomical object and calibration light paths, showing the distortions largely account for the non-constant α results in the field.

3. Finally, the optical depths of the two sets of transitions are typically very similar in known Zn/Cr II absorbers. This simplifies profile fitting. This becomes apparent when one considers fitting lines with very different optical depths. The lines often have complex spectral structure spread over a range of velocities and depths, a result of the distribution of the properties of the individual ‘clouds’ that make up the absorber along the line of sight. Lines with higher optical depths may display structure that will be beyond the detection threshold of lines with lower optical depths. Further to this, lines with very high optical depths may become saturated (i.e. in part absorb all of the background flux), concealing structure. In such cases profile fitting becomes difficult, because in order to constrain $\Delta\alpha/\alpha$, a common set of profile parameters needs to be used for the different transitions, and if the variation in transition optical depths is great, a common set of profile parameters will be more difficult to obtain and these will ultimately be poorly constrained. These difficulties in obtaining reliable profile parameters can give rise to systematic errors in the final $\Delta\alpha/\alpha$ result, but for Zn/Cr II lines these difficulties are minimal.

The spectra of Zn/Cr II systems are therefore promising for measuring any variation in α , independent of – and qualitatively very different in nature to – previous *and* most, if not all, other future constraints.

Given the advantages over full MM fits a potential disadvantage exists in the form of pervasive short-range wavelength distortion patterns discovered and described by Griest et al. (2010) and Whitmore et al. (2010). These exist on the

scale-length of echelle orders¹, where each order has a similar pattern of distortion to the adjacent ones, though the pattern may vary from exposure to exposure. The distortions are present in spectra from both HIRES and UVES spectrographs. There is still ongoing work in the field to fully characterise and, ideally, correct for these distortions. These short-range distortions are particularly important to this work because they act on scale-lengths of the same order as the separation between many of the Zn/Cr II lines. Their effects on the results presented here are investigated in Section 3.4.3. It is worth noting that the systematic effect of the distortions on $\Delta\alpha/\alpha$ is inversely proportional to the number of transitions fit per absorber and the number of fit systems (see Equation 3.5 as derived by Whitmore et al., 2010) and the relatively small separation between the Zn/Cr II lines is not necessarily suggestive of a significant systematic error on $\Delta\alpha/\alpha$ for the QSO absorber sample in this work.

Unfortunately systems exhibiting Zn II and Cr II lines that are strong enough for varying α analysis are very rare. Only about 100 *metal-strong* absorbers have been found in the huge Sloan Digital Sky Survey (SDSS) QSO database by Herbert-Fort et al. (2006). Metal-strong systems were first named in the context of the SDSS and are defined in terms of Zn II or Si II column densities: $\log N(\text{Zn II}) \geq 13.15$ or $\log N(\text{Si II}) \geq 15.95$. Therefore, there is a direct relationship between an absorber being metal-strong and the Zn II column densities, aiding in identification of candidate systems for varying α analysis. However, only a subset of these is useful for Zn/Cr II-based $\Delta\alpha/\alpha$ analyses. This is because the background QSO may not be bright enough to achieve adequate SNR and some absorption may occur at high enough redshifts to push the Mg I 2852 transition, required for constraining the structure of Mg I 2026 (which blends the Zn II 2026 line; see Section 3.2.1), to regions of low CCD quantum efficiency (typically past 8000 Å, or $z_{\text{abs}} > 1.8$). Therefore, in this work strong Zn/Cr II absorbers are first carefully selected based on their metallicity and then further selected based on observational constraints.

The work in this Chapter is separated into two main sections. Section 2.3 describes how the 9 target Zn/Cr II systems, in which Zn II and Cr II absorption is strong enough to constrain $\Delta\alpha/\alpha$ to a precision of approximately 5 parts per million on their own, were selected and observed. This includes the general observa-

¹See Section 2.4 for a brief description of the echelle spectrum structure.

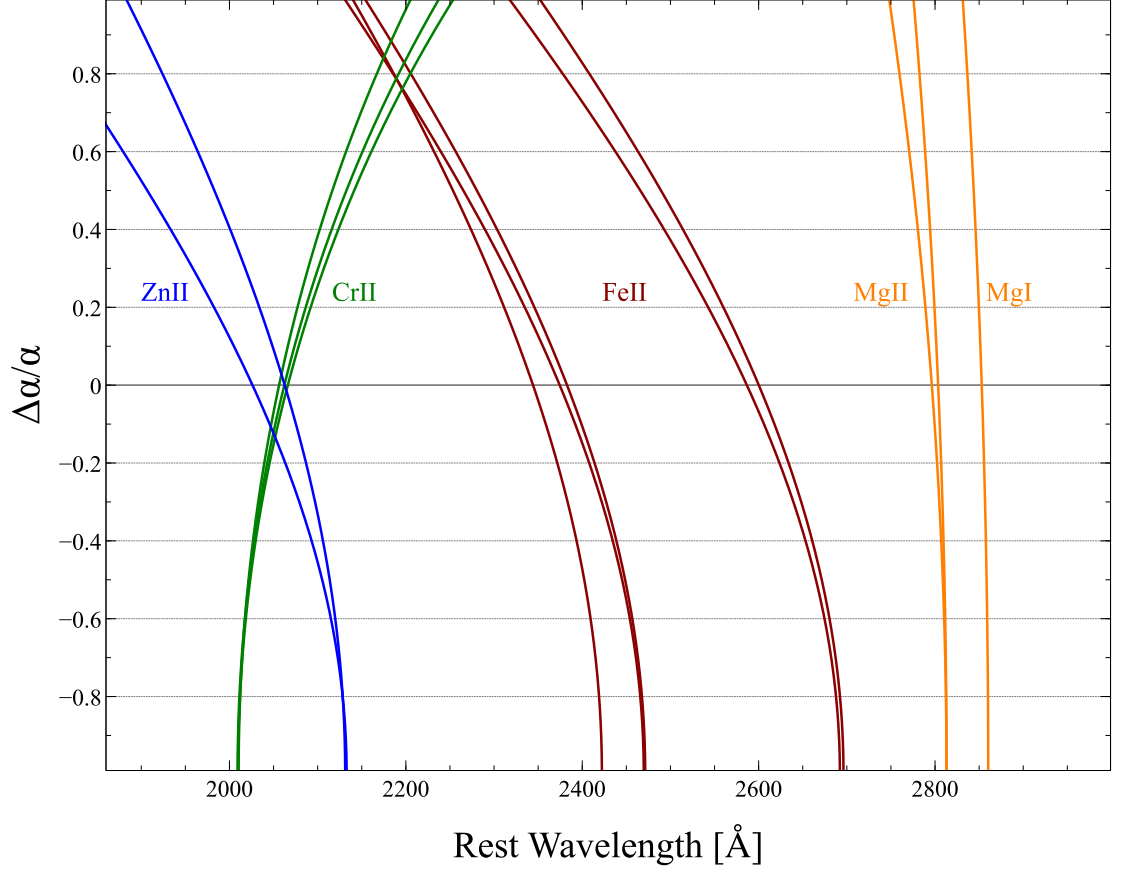


Figure 2.1: Metal-line shifts with varying α . The curves plot the rest wavelengths of various atomic/ionic transitions with respect to relative changes in α , $\Delta\alpha/\alpha$. The blue curves correspond to the Zn II 2026 and 2062 lines, the green curves correspond to Cr II 2066, 2062 and 2056 lines, the red curves correspond to Fe II lines commonly used in $\Delta\alpha/\alpha$ analyses and the orange curves correspond to commonly used Mg I and II lines. Note that the range of the vertical axis is extended to be illustrative of the overall pattern of shifts. The Zn II and Cr II subset of lines shift in opposite directions as α varies in a complex pattern, in contrast to the Fe and Mg lines, which experience a largely monotonic shift. A $\Delta\alpha/\alpha = 10 \times 10^{-6}$ implies a velocity shift between the Mg & Fe II lines of 0.2 km s^{-1} , while in the case of Zn & Cr II lines it implies a velocity shift of 0.4 km s^{-1} . The proximity (often within the same echelle order in the HIRES and UVES spectrographs) of the Zn II and Cr II lines is advantageous, making measurements of $\Delta\alpha/\alpha$ much less prone to long-range wavelength calibration errors than for fits of the full set of transitions.

tional strategy, along with a detailed journal of Keck and VLT observations taken for this project, including archival data, and the reference laboratory transition data used to compare with QSO-based measurements. Section 2.4 summarises the data reduction performed on the observed sample of Zn/Cr II systems, including improvements to the HIRES reduction procedure. The varying α analysis, results and systematic error considerations for these systems are detailed separately in Chapter 3.

2.3 Observational and laboratory data

2.3.1 Targets and observation strategy

The target Zn/Cr II systems were selected as follows. The brightest ($m_r < 17.0$) QSOs amongst the metal-strong systems of Herbert-Fort et al. (2006) were selected so that a SNR of ~ 50 per $\sim 2 \text{ km s}^{-1}$ pixel could be obtained with ~ 10 or fewer hours of observation time on the Keck or VLT telescopes (i.e. approximately one night of observation per system). This selection was then further refined for RA and declination accessibility from Keck and/or VLT telescopes, with a preference for systems with the highest Zn II column density estimates from Herbert-Fort et al. (2006). In some cases archival observations using HIRES or UVES spectrographs were available in the respective public archives or were obtained from collaborator Jason X. Prochaska. While most of these did not have sufficient SNR to readily provide competitive constraints on $\Delta\alpha/\alpha$, they nevertheless allowed an inspection of the spectral structure of the absorber without further observations. Some cases were discarded upon inspection because they exhibited “smooth” absorption profiles, which mean a reduced capacity to constrain $\Delta\alpha/\alpha$. This is because, by nature of the method, a $\Delta\alpha/\alpha$ constraint is entirely reliant on precisely measuring velocity offsets between different lines, which requires the presence of many sharp, narrow features in the absorption profiles. The cases which exhibited such features were further observed to enable measurements of $\Delta\alpha/\alpha$. Note that there were also additional targets, which were not SDSS-selected. For these targets, spectra already existed either as HIRES observations already conducted by Jason X. Prochaska or observations that were available in the UVES data archive.

These target systems, suited for Zn/Cr II-based $\Delta\alpha/\alpha$ constraints and numbering 9 in total, are listed in Table 2.1. Observations of these systems have been completed using the Keck/HIRES and VLT/UVES spectrographs. Observations were supplemented with archival spectra, but the bulk of the exposures were taken specifically for this work. Of the 9 systems, 3 have spectra from both telescopes, 3 from UVES only and 3 from HIRES only. The journal of observations in Section 2.3.2 provides details of the exposures used in this thesis.

Table 2.1: Target Zn/Cr II systems. The first column is the object name, as referred to in this thesis. The second and third columns are the right ascension and declination, respectively, in J2000 coordinates. The fourth and fifth columns are the emission and absorption redshifts, respectively. The absorption redshifts are only of the systems used to constrain $\Delta\alpha/\alpha$ in this work. The final column is the r magnitude of the QSO (using the approximate conversions where necessary as per Atlee and Gould, 2007).

Object	RA	Dec.	z_{em}	z_{abs}	m_r
J0058+0051	00 58 24.750	+00 41 13.64	1.92	1.072	16.97
J0108−0037	01 08 26.843	−00 37 24.17	1.373	1.371	17.44
J0226−2857	02 26 20.502	−28 57 50.78	2.17	1.023	18.13
J0841+0312	08 41 06.775	+03 12 06.60	1.94	1.342	16.36
J1029+1039	10 29 04.149	+10 39 01.59	1.79	1.622	17.57
PHL957	01 03 11.268	+13 16 17.74	2.68	2.309	16.11
Q1755+57	17 56 03.628	+57 48 48.00	2.11	1.971	18.3
Q2206-1958	22 08 52.07	−19 44 00.0	2.56	1.921	17.1
J1237+0106	12 37 24.51	+01 06 15.4	2.02	1.305	17.92

QSO observations, where archival spectra were not used (see Section 2.3.2) were performed in grey time. QSO exposures were always immediately followed by ThAr comparison exposures for wavelength calibration (with the exception of some VLT/UVES exposures taken in service mode²). This was done to minimise any

²Service mode observing is performed by ESO staff at the VLT. It is executed when observing criteria (such as fractional lunar illumination, sky brightness, object accessibility, etc.) defined

potential systematic error in the instrument resulting from drifts in the ambient conditions (such as temperature and pressure) within the spectrographs over the observing nights. The choice of cross-disperser and echelle angle settings³ were always such that the Zn II, Cr II and Mg I lines were recorded in a single exposure, ensuring efficient use of observing time. Because the Mg I 2852 line is separated in wavelength from the other lines of interest, this was not always possible (specifically in the case of J0108–0037 observed on the VLT) and two different settings had to be used in order to achieve full coverage. Pixel binnings⁴ of 2×1 and 2×2 were used for HIRES and UVES, respectively (with the exception of a set of UVES service mode observations performed using 1×1 binning).

For archival spectra, only exposures that were adequately calibrated were used. Adequately calibrated, in the context of this work, refers to the presence of ThAr exposures taken directly before or after and in the same setting as the QSO exposures, for reliable wavelength calibration. In a small number of cases, archival data sets had a ThAr exposure not taken directly before or after the QSO exposure, but with one other exposure proceeding or following it with the same setting. In those cases the exposures were still used. For UVES archival spectra, settings which cover the red end of the spectrograph range (i.e. 760-nm and 860-nm settings) result in heavy saturation of the CCD when the ThAr lamp is used, which requires additional time to clear. Because of this, the ThAr exposures for such settings are usually taken separately at the end of the night. Because only the Mg I 2852 line is

in the observing proposal are met. It allows for more efficient use of telescope time overall and is suited for when the proposing scientist does not need to make real-time decisions during the night. In such cases visitor mode observing is granted.

³These settings correspond to the configurable angles of the cross-disperser and echelle gratings. To understand their effect one may consider a simplified model of an echelle spectrograph. In this model, light from the telescope passes through a slit and is collimated onto an echelle grating, which diffracts the incident light into orders of progressive wavelength ranges, which are further separated using another grating, commonly referred to as the cross-disperser. Note that one can substitute gratings for prisms, however the spectrographs in this thesis use gratings. The effect of these optical elements is to produce a 2D image composed of lines (orders) of sub-spectra. This is akin to breaking text into multiple lines of characters, making efficient use of the page. The ‘page’ here is a CCD detector, which digitally records the spectra. Only a window of the full 2D spectrum image is captured by the CCD. In order to observe specific wavelength regions, the echelle and cross-disperser angles are adjusted, effectively shifting the image in the x-y plane.

⁴Binning is performed at the hardware level of the CCD pixel array, where charges from adjacent pixels are combined, offering reduced readout noise at the cost of reduced spatial or spectral resolution. For the spectrographs in this thesis, the number of binned pixels is denoted as *spatial* \times *spectral*.

affected by this and does not require as much wavelength accuracy as the others (it is not used to constrain $\Delta\alpha/\alpha$, but to constrain interfering velocity structure; see Section 3.2.1.1) this is not considered to be an issue and the exposures are still used. The HIRES spectrograph’s single chip archival spectra were not used (i.e. spectra taken before the upgrade to a 3-chip CCD mosaic in 2004), primarily because the spectra were almost never calibrated with ThAr exposures before or after the QSO exposures and in some cases were not wavelength calibrated at all. Flux standards were not taken or used, as the work in this thesis is concerned primarily with constraining the wavelengths of absorbing atomic species for constraining $\Delta\alpha/\alpha$.

2.3.2 Journal of observations and archival spectra

This section includes chronologically ordered tables of all of the Keck/HIRES and VLT/UVES exposures used for this project, including the ThAr arc lamp exposures used for wavelength calibration. Archival exposures that were not taken as part of this project are denoted as such and are listed at the end of each table.

The journal of observations covers a total of 8 observing runs, 6 using Keck and 2 using VLT (one of which was service mode allocation) conducted between mid-2008 and early 2010. A total of 7 nights were Keck nights, with 1 night (2009/03/09) lost to ice and snow at the summit and around 50% of two nights lost to high humidity (2009/05/17-18). Two half-nights were spent on the VLT, with further observations in service mode between 2009/10/12 and 2010/01/09 (using about 1.5 night’s worth of observing time). A total of ~ 47 hours were spent on Keck/HIRES exposures of the QSO targets used in this work, excluding archival exposures. This does not include time spent on setup, calibration and other targets⁵. A total of ~ 15 hours were spent on VLT/UVES exposures, with most of the UVES spectra used in this project being archival.

⁵While the nights were scheduled such that at least one Zn II and Cr II QSO was accessible through each night, this was not always possible and the time was spent on short exposures of other targets of interest to varying α studies.

2.3.2.1 Keck/HIRES

Table 2.2: Journal of Keck/HIRES observations taken and the additional archival spectra used for this thesis. The rows are individual QSO and ThAr arc lamp exposures, ordered chronologically (the archival exposures used are listed at the end of the table). The rows are separated by headers that indicate the UTC date the exposures were taken on, followed by observer/PI details. Spectrograph settings, such as the cross-disperser or slit width used, are usually common to all of the exposures for a night and are included under the headers. The columns are, in order: the object name or the calibration lamp used, the exposure time in seconds, the UTC hour, minute and second the exposure was started, the HIRES echelle and cross-disperser angles in degrees, the airmass (the amount of air the light from the object traverses normalised by that at the zenith) recorded in the FITS header of the exposure and the seeing in arcseconds, if it was recorded. The note marks which appear in the table are explained below.

*The C5/1.148" decker was used for the QSO and following ThAr arc lamp calibration exposure because of poor seeing.

†The atmospheric conditions during this observing night were unstable with seeing $> 1.0''$.

‡The seeing was unstable throughout the night, values represent average seeing.

Object <i>or</i> lamp	Expo- sure [s]	Time [UTC]	Echelle ang. [°]	XD ang. [°]	Air- mass	See- ing ["]
2008/07/08						
Observers: A. L. Malec, M. T. Murphy (PI)						
Using red cross-disperser, C1/0.861" decker, 2×1 binning, WG360 filter, THAR1 lamp, NG3 lamp filter throughout.						
Q1755+578	3600	06:50:42	0.450	0.00	1.43	—
ThAr	1	07:52:21	0.450	0.00		
Q1755+578	3600	07:54:31	0.450	0.00	1.31	
ThAr	1	08:56:16	0.450	0.00		
Q1755+578	3600	08:58:23	0.450	0.00	1.27	
ThAr	1	10:00:03	0.450	0.00		
Q1755+578	3600	10:02:00	0.450	0.00	1.29	
ThAr	1	11:03:39	0.450	0.00		
Q1755+578	3600	11:06:15	0.450	0.00	1.38	
ThAr	1	12:07:50	0.450	0.00		

Continued on next page

Table 2.2: *Continued from previous page*

Object or lamp	Expo- sure [s]	Time [UTC]	Echelle ang. [°]	XD ang. [°]	Air- mass	See- ing ["]
2008/08/20 – 22						
Observer: M. T. Murphy (PI)						
Using red cross-disperser, C1/0.861" decker, 2×1 binning, WG360 filter, THAr1 lamp, NG3 lamp filter throughout.						
— <i>Night 1</i> —						
PHL957	3000	10:30:45	0.326	0.00	1.37	—
ThAr	1	11:22:38	0.326	0.00		
PHL957	3000	11:24:24	0.326	0.00	1.16	
ThAr	1	12:16:00	0.326	0.00		
— <i>Night 2</i> —						
PHL957	3000	10:28:22	0.326	0.00	1.36	
ThAr	1	11:19:34	0.326	0.00		
PHL957	3000	11:21:25	0.326	0.00	1.16	
ThAr	1	12:12:50	0.326	0.00		
PHL957	3000	12:15:08	0.326	0.00	1.05	
ThAr	1	13:15:46	0.326	0.00		
PHL957	3000	13:20:47	0.326	0.00	1.01	
ThAr	1	14:17:13	0.326	0.00		
PHL957	2701	14:19:01	0.326	0.00	1.03	
ThAr	1	15:09:21	0.326	0.00		
— <i>Night 3</i> —						
PHL957	1201	09:48:12	0.326	0.00	1.60	
ThAr	1	10:10:23	0.326	0.00		
PHL957*	3301	11:17:43	0.326	0.00	1.16	
ThAr	1	12:13:54	0.326	0.00		
PHL957	2821	12:15:25	0.326	0.00	1.05	
ThAr	1	13:05:43	0.326	0.00		
PHL957	3600	14:03:40	0.324	0.00	1.02	

Continued on next page

Table 2.2: *Continued from previous page*

Object <i>or</i> lamp	Expo- sure [s]	Time [UTC]	Echelle ang. [°]	XD ang. [°]	Air- mass	See- ing ["]
ThAr	1	15:04:54	0.324	0.00		
2009/02/01						
Observers: A. L. Malec, M. T. Murphy (PI)						
Using red cross-disperser, C1/0.861" decker, 2×1 binning, WG360 filter, THAR1 lamp, NG3 lamp filter throughout.						
J0058+0041	3300	05:09:51	−0.077	0.00	1.35	—
ThAr	1	06:07:07	−0.077	0.00		
J0841+0312	3600	07:26:09	0.281	−0.15	1.41	
ThAr	1	08:28:48	0.281	−0.15		
J0841+0312	3000	09:33:07	0.281	−0.15	1.06	
ThAr	1	10:24:35	0.281	−0.15		
J0841+0312	3300	10:25:56	0.281	−0.15	1.04	
ThAr	1	11:22:20	0.281	−0.15		
J1029+1039	3600	11:27:54	0.450	0.00	1.03	
ThAr	1	12:29:15	0.450	0.00		
J1029+1039	3600	12:31:14	0.450	0.00	1.02	
ThAr	1	13:32:37	0.451	0.00		
J1029+1039	3600	13:34:30	0.451	0.00	1.09	
ThAr	1	14:36:04	0.451	0.00		
J1237+0106	1604	14:41:04	0.451	0.00	1.06	
J1237+0106	2500	15:09:41	0.225	−0.15	1.09	
ThAr	1	15:52:38	0.225	−0.15		
2009/05/19						
Observers: G. G. Kacprzak, A. L. Malec, M. T. Murphy (PI)						
Using red cross-disperser, C1/0.861" decker, 2×1 binning, WG360 filter, THAR1 lamp, NG3 lamp filter throughout.						
J1029+1039	3600	06:36:35	0.451	0.00	1.10	†

Continued on next page

Table 2.2: *Continued from previous page*

Object <i>or</i> lamp	Expo- sure [s]	Time [UTC]	Echelle ang. [°]	XD ang. [°]	Air- mass	See- ing ["]
ThAr	1	07:39:22	0.451	0.00		
J1237+0106	3300	07:48:42	0.225	−0.15	1.07	
ThAr	1	08:46:08	0.226	−0.15		
J1237+0106	3300	08:47:31	0.226	−0.15	1.16	
ThAr	1	09:43:42	0.226	−0.15		
J1237+0106	2700	09:45:35	0.226	−0.15	1.35	
ThAr	1	10:31:49	0.226	−0.15		
Q1755+578	3300	10:46:08	0.451	0.00	1.35	
ThAr	1	11:42:21	0.451	0.00		
Q1755+578	3300	11:43:17	0.451	0.00	1.28	
ThAr	1	12:39:28	0.451	0.00		
Q1755+578	3300	12:41:30	0.451	0.00	1.27	
ThAr	1	13:37:49	0.451	0.00		
Q1755+578	3300	13:38:59	0.451	0.00	1.31	
2009/11/03						
Observers: A. L. Malec, M. T. Murphy (PI)						
Using red cross-disperser, C1/0.861" decker, 2×1 binning, WG360 filter, THAR1 lamp, NG3 lamp filter throughout.						
J0058+0041	3300	05:08:20	0.078	0.00	1.66	0.7 [‡]
ThAr	1	06:05:05	0.078	0.00		
J0058+0041	3300	06:07:22	0.078	0.00	1.30	
ThAr	1	07:03:47	0.078	0.00		
J0058+0041	3300	07:05:05	0.078	0.00	1.13	
ThAr	1	08:01:45	0.078	0.00		
J0058+0041	3300	08:04:09	0.078	0.00	1.06	
ThAr	1	09:02:20	0.078	0.00		
J0058+0041	3300	09:04:28	0.078	0.00	1.07	0.67
ThAr	1	10:01:13	0.078	0.00		

Continued on next page

Table 2.2: *Continued from previous page*

Object <i>or</i> lamp	Expo- sure [s]	Time [UTC]	Echelle ang. [°]	XD ang. [°]	Air- mass	See- ing ["]
J0058+0041	3300	10:03:07	0.078	0.00	1.15	
ThAr	1	10:59:46	0.078	0.00		
J0058+0041	3300	11:01:44	0.078	0.00	1.34	
ThAr	1	11:58:16	0.078	0.00		
J0841+0312	2400	13:04:42	0.283	−0.15	1.51	
ThAr	1	13:46:05	0.283	−0.15		
J0841+0312	2400	13:47:33	0.283	−0.15	1.28	
ThAr	1	14:29:16	0.283	−0.15		
J0841+0312	3000	14:31:17	0.283	−0.15	1.15	0.73
ThAr	1	15:22:51	0.283	−0.15		
2009/12/29						
Observers: A. L. Malec, M. T. Murphy (PI)						
Using red cross-disperser, C1/0.861" decker, 2×1 binning, WG360 filter, THAR1 lamp, NG3 lamp filter throughout.						
J0058+0041	3600	04:56:15	0.079	0.00	1.06	0.7
ThAr	1	05:57:35	0.079	0.00		
J0058+0041	3600	06:02:46	0.079	0.00	1.11	0.95
ThAr	1	07:04:16	0.079	0.00		
J0058+0041	3600	07:06:10	0.079	0.00	1.28	
ThAr	1	08:07:28	0.079	0.00		
J0841+0312	2400	09:15:39	0.282	−0.15	1.57	0.8
ThAr	1	09:57:07	0.282	−0.15		
J0841+0312	2400	09:58:19	0.282	−0.15	1.32	
ThAr	1	10:39:40	0.282	−0.15		
J1029+1039	3600	10:42:52	0.450	0.00	1.65	0.75
ThAr	1	11:44:26	0.451	0.00		
J1029+1039	3600	11:46:09	0.451	0.00	1.27	
ThAr	1	12:47:56	0.451	0.00		

Continued on next page

Table 2.2: *Continued from previous page*

Object <i>or</i> lamp	Expo- sure [s]	Time [UTC]	Echelle ang. [°]	XD ang. [°]	Air- mass	See- ing ["]
J1237+0106	3300	12:51:49	0.226	−0.15	1.78	0.6
ThAr	1	13:48:24	0.226	−0.15		
J1237+0106	3600	13:50:06	0.226	−0.15	1.36	
ThAr	1	14:51:49	0.226	−0.15		
J1237+0106	3600	14:53:36	0.226	−0.15	1.15	0.8
ThAr	1	15:54:57	0.226	−0.15		

ARCHIVAL DATA – J. X. Prochaska (PI)

Observers: G. E. Prochter, M. Dessauges-Zavadsky, J. M. O’Meara

Using blue cross-disperser, C1/0.861" decker, 2×1 binning, THAR2 lamp, NG3 lamp filter throughout.

— 2004/09/09 —						
Q1755+57	5400	06:38:21	1.176	0.00	1.34	—
ThAr	1	08:12:03	1.176	0.00		
— 2006/08/19 —						
Q1755+578	4500	06:50:13	1.176	0.00	1.27	
Q1755+578	4500	08:06:05	1.176	0.00	1.34	
ThAr	1	09:22:05	1.175	0.00		
— 2006/08/20 —						
Q1755+578	4500	06:52:10	1.176	0.00	1.27	
Q1755+578	4500	08:08:03	1.176	0.00	1.35	
ThAr	1	09:24:01	1.176	0.00		
— 2006/06/02 —						
Q1755+578	4400	13:02:37	1.175	0.00	1.33	
ThAr	1	14:18:25	1.175	0.00		
— 2006/06/03 —						
Q1755+578	4400	13:01:52	1.176	0.00	1.33	
ThAr	1	14:18:05	1.176	0.00		

2.3.2.2 VLT/UVES

Table 2.3: Journal of VLT/UVES observations taken and archival spectra used for this thesis. The rows are individual QSO and ThAr arc lamp exposures, ordered chronologically. The rows are separated by headers that indicate the UTC date the exposures were taken on, followed by PI/Co-I details. Spectrograph settings, such as the central wavelength or slit width used, are usually common to all of the exposures for a night and are included under the headers. The dichroic beam splitter was used for all observations, enabling simultaneous use of both arms of the spectrograph. The columns are, in order: the object name or the calibration lamp used, the exposure time in seconds, the UTC hour, minute and second the exposure was started, the UVES setting used, the airmass recorded in the FITS header of the exposure and the seeing in arcseconds, if it was recorded. The note marks which appear in the table are explained below.

[†]Used the 1.0'' slit for this QSO exposure and the following ThAr arc lamp calibration exposure.

Object <i>or</i> lamp	Expo- sure [s]	Time [UTC]	Setting	Air- mass	See- ing ["]
2009/10/12 – 2010/01/09					
PI/Co-Is: A. L. Malec, M. T. Murphy, R. F. Carswell					
Program ID 084.A-0136(B); Service mode					
0.8'' slit, 1×1 binning, standard setting filters throughout.					
Wavelength calibrations taken separately for red arm for J0841+0312.					
— 2009/10/12 —					
J0058+0041	2886	03:28:10	390+564	1.12	0.75
ThAr	18	04:17:25	390+564		
J0058+0041	2886	04:20:51	390+564	1.12	0.78
— 2009/10/17 —					
J0058+0041	2886	04:09:44	390+564	1.13	0.82
ThAr	18	04:58:58	390+564		
J0058+0041	2886	05:00:33	390+564	1.20	1.31
— 2009/10/18 —					
J0058+0041	2886	02:49:40	390+564	1.13	0.89
ThAr	18	03:38:55	390+564		

Continued on next page

Table 2.3: *Continued from previous page*

Object <i>or</i> lamp	Expo- sure [s]	Time [UTC]	Setting	Air- mass	See- ing ["]
J0058+0041	2886	03:44:42	390+564	1.12	0.76
— 2009/12/15 —					
J0841+0312	2896	07:08:50	437+760	1.14	0.81
ThAr	18	07:58:22	437		
ThAr	5	15:03:48	760		
— 2009/12/27 —					
J0841+0312	2896	05:33:35	437+760	1.18	0.66
ThAr	18	06:23:04	437		
ThAr	5	11:47:40	760		
— 2010/01/09 —					
J0841+0312	2896	03:36:24	437+760	1.35	0.91
ThAr	18	04:25:54	437		
J0841+0312	2896	04:33:27	437+760	1.20	0.63
ThAr	18	05:22:57	437		
ThAr	5	14:46:12	760		
2009/12/08 – 09					
PI/Co-Is: A. L. Malec, M. T. Murphy, R. F. Carswell					
Program ID 084.A-0136(A); Visitor mode					
0.8" slit, 2×2 binning, standard setting filters throughout.					
— <i>Night 1</i> —					
J0226–2857	2914	00:38:54	390+564	1.03	0.59
ThAr	1	01:28:41	390+564		
J0226–2857	3300	01:33:01	390+564	1.01	0.56
ThAr	1	02:29:14	390+564		
J0226–2857	3300	02:35:45	390+564	1.04	0.58
ThAr	1	03:31:58	390+564		
J0226–2857	3600	03:36:53	437+760	1.15	0.57
ThAr	1	04:38:06	437+760		

Continued on next page

Table 2.3: *Continued from previous page*

Object <i>or</i> lamp	Expo- sure [s]	Time [UTC]	Setting	Air- mass	See- ing ["]
<i>— Night 2 —</i>					
J0226–2857	3300	00:34:23	390+564	1.03	0.70
ThAr	1	01:30:37	390+564		
J0226–2857	3300	01:35:07	437+760	1.01	0.76
J0226–2857	2461	02:39:00	437+760	1.04	0.43
ThAr	1	03:21:15	437+760		
J0226–2857	4200	03:34:21	437+760	1.17	0.34
ThAr	1	04:45:34	437+760		
ARCHIVAL DATA 2000/05/29 – 31					
PI/Co-Is: M. Pettini, J. Bergeron, P. Petitjean					
Program ID 65.O-0158(A); Visitor mode					
1.0" slit, 2×2 binning, standard setting filters throughout.					
<i>— Night 1 —</i>					
Q2206–1958	3600	07:57:33	390+564	1.13	0.56
ThAr	1	08:58:47	390+564		
Q2206–1958	3600	09:02:32	437+860	1.03	0.49
ThAr	1	10:03:47	437+860		
<i>— Night 2 —</i>					
Q2206–1958	3600	07:30:54	390+564	1.19	0.41
ThAr	1	08:32:18	390+564		
Q2206–1958	4200	08:35:31	437+860	1.05	0.72
ThAr	1	09:46:43	437+860		
<i>— Night 3 —</i>					
Q2206–1958	3600	07:16:58	390+564	1.23	0.51
ThAr	1	08:18:11	390+564		
Q2206–1958	3600	08:19:52	390+564	1.07	1.19
Q2206–1958	2700	09:21:22	390+564	1.02	1.02

Continued on next page

Table 2.3: *Continued from previous page*

Object or lamp	Expo- sure [s]	Time [UTC]	Setting	Air- mass	See- ing ["]
ARCHIVAL DATA 2001/09/16 – 17					
PI/Co-Is: S. D’Odorico, M. Dessauges-Zavadsky, J. X. Prochaska					
Program ID 67.A-0022(A); Service mode					
1.0" slit for blue, 0.9" slit for red, 2×2 binning, standard setting					filters
throughout. Wavelength calibrations taken separately for red arm.					
— <i>Night 1</i> —					
PHL957	3600	07:46:02	390+860	1.58	0.96
ThAr	1	08:47:19	390		
ThAr	1	10:47:09	860		
— <i>2Night 2</i> —					
PHL957	3600	05:46:07	390+860	1.28	0.87
ThAr	1	06:47:24	390		
ThAr	1	14:41:13	860		
ARCHIVAL DATA 2003/10/29					
PI/Co-Is: C. Ledoux, P. Petitjean, R. Srianand					
Program ID 072.A-0346(A); Visitor mode					
1.0" slit, 2×2 binning, standard setting filters throughout.					
Wavelength calibrations taken at the end of the night.					
Q2206–1958	4500	23:58:01	346+580	1.02	1.20
Q2206–1958	4500	01:13:50	346+580	1.09	0.68
ThAr	1	12:20:01	346+580		
ARCHIVAL DATA 2004/10/08 – 09					
PI/Co-Is: R. Srianand, P. Petitjean, H. Chand, B. Aracil, C. Ledoux					
Program ID 074.A-0201(A); Visitor mode					
0.9" slit, 2×2 binning, standard setting filters throughout.					
— <i>Night 1</i> —					

Continued on next page

Table 2.3: *Continued from previous page*

Object <i>or</i> lamp	Expo- sure [s]	Time [UTC]	Setting	Air- mass	See- ing ["]
Q2206–1958	5403	00:05:05	455+850	1.05	1.12
ThAr	1	01:36:24	455+850		
Q2206–1958	5000	01:44:46	455+850	1.04	0.93
PHL957	5000	03:24:24	390+590	1.31	1.02
ThAr	1	04:48:59	390+590		
ThAr	1	04:49:51	390+590		
PHL957	5000	04:52:44	390+590	1.34	1.34
— <i>Night 2</i> —					
Q2206–1958	5000	02:01:55	455+850	1.06	0.77
ThAr	1	03:26:31	455+850		
Q2206–1958	4200	03:31:07	455+850	1.24	1.34
PHL957 [†]	5400	04:56:36	390+590	1.37	1.40
ThAr	1	06:29:45	390+590		
ARCHIVAL DATA 2007/07/25 – 09/05					
PI/Co-Is: N. Bouche, C. Peroux, M. T. Murphy					
Program ID 079.A-0600(B); Service mode					
1.2" slit, 2×2 binning, standard setting filters throughout.					
Wavelength calibrations taken at the end of the night.					
— 2007/07/25 —					
J0226–2857	3005	08:17:23	390+580	1.17	1.24
ThAr	1	11:46:36	390+580		
— 2007/07/28 —					
J0226–2857	3005	08:03:28	390+580	1.17	0.87
ThAr	1	12:14:10	390+580		
— 2007/09/05 —					
J0226–2857	3005	08:26:16	390+580	1.02	1.84
ThAr	1	12:14:43	390+580		

Continued on next page

Table 2.3: *Continued from previous page*

Object <i>or</i> lamp	Expo- sure [s]	Time [UTC]	Setting	Air- mass	See- ing ["]
ARCHIVAL DATA 2008/11/05					
PI/Co-Is: M. Dessauges-Zavadsky, D. Schaerer, S. D’Odorico, A. Ferrara, C. Tapken					
Program ID 082.A-0682(A); Visitor mode					
1.0" slit, 2×2 binning, standard setting filters throughout.					
J0058+0041	3300	00:16:47	437+760	1.29	1.70
ThAr	1	01:13:01	437+760		
J0058+0041	3600	01:15:52	437+760	1.15	1.38
ThAr	1	02:17:06	437+760		
J0058+0041	3000	02:19:17	437+760	1.11	1.69
ThAr	1	03:10:31	437+760		
J0058+0041	3000	03:12:41	437+760	1.15	1.41
ARCHIVAL DATA 2008/11/21 – 12/03					
PI/Co-Is: R. Srianand, P. Petitjean, P. Noterdaeme, N. Gupta, H. Chand					
Program ID 082.A-0569(A); Service mode					
1.0" slit, 2×2 binning, standard setting filters throughout.					
— 2008/11/21 —					
J0108–0037	3700	01:14:58	390+580	1.11	0.88
ThAr	1	02:17:52	390+580		
— 2008/11/23 —					
J0108–0037	3700	02:41:41	390+580	1.20	0.77
ThAr	1	03:44:35	390+580		
— 2008/11/25 —					
J0108–0037	3700	01:52:04	390+580	1.13	0.69
ThAr	1	02:54:58	390+580		
— 2008/12/03 —					
J0108–0037	3690	01:11:10	390+580	1.12	0.72

Continued on next page

Table 2.3: *Continued from previous page*

Object or lamp	Expo- sure [s]	Time [UTC]	Setting	Air- mass	See- ing ["]
ThAr	1	02:13:54	390+580		
ARCHIVAL DATA 2009/08/20 – 24					
PI/Co-Is: F. Miniati, M. L. Bernet, S. J. Lilly, P. P. Kronberg, M. Dessauges-Zavadsky					
Program ID 083.A-0874(A); Service mode					
1.0" slit, 2×2 binning, standard setting filters throughout.					
Wavelength calibrations taken at the end of the night.					
— 2009/08/20 —					
J0108–0037	430	09:30:38	346+580	1.21	1.19
J0108–0037	430	09:38:51	346+580	1.23	1.21
ThAr	1	11:20:30	346+580		
— 2009/08/24 —					
J0108–0037	430	08:43:07	437+860	1.14	1.42
J0108–0037	430	08:51:35	437+860	1.16	1.26
ThAr	1	16:44:14	437+860		

2.3.3 Laboratory wavelengths and sensitivity coefficients

The q sensitivity coefficients (see Section 1.3.2) used in this work are from Murphy et al. (2003a). The laboratory rest wavelengths λ_0 and oscillator strengths f are from Murphy and Berengut (2014).

2.4 Data reduction

This section is a general description of the data reduction performed. Sections 2.4.1 and 2.4.2 discuss the most important aspects of the data reduction and how they’ve been improved for this work.

Both the Keck and UVES spectrographs are echelle spectrographs, where an echelle grating is used in tandem with a cross-disperser (used to separate overlapping echelle orders) to produce what is effectively a linear spectrum compactly ‘broken’ into echelle diffraction orders across the 2D CCD plane. The UVES spectrograph is comprised of two cross-dispersed arms with a dichroic beam splitter, allowing for simultaneous observations in ranges of 3000 to 5000 Å (blue arm; single CCD) and 4200 to 11000 Å (red arm, 2 CCD mosaic). The HIRES spectrograph is a single arm spectrograph (using a 3 CCD mosaic) and allows observations in the 3000 to 10000 Å range.

The reduction of the raw CCD data from the HIRES spectrographs is performed using the HIRES REDUX package⁶ written and maintained by Jason X. Prochaska. For the UVES spectrograph data the official ESO UVES Data Reduction Pipeline⁷ is used. Generally speaking, both packages process calibration files to create a model of the echelle order structure, including wavelength solutions. Slit profiles (profiles of the cross-dispersed slit image in the spatial direction, used in extracting sky and object flux) are created from the flat-field (i.e. quartz lamp) spectra. The QSO spectra are optimally extracted using the slit profiles as weights from the QSO exposures, including sky subtraction. The UVES data reduction pipeline uses a model of the spectrograph to obtain initial solutions to the data reduction parameters (e.g. echelle order structure, varying slit tilts across echelle orders). The HIRES REDUX package generally calculates these reduction parameters directly from the data, which in some cases necessitates manual intervention during the data reduction process.

For multiple exposures of the same object, the wavelengths of the fluxes falling on each pixel in a detector will be different from exposure to exposure, due to the varying velocity shift imparted by the motion of the Earth relative to the object being observed. Changing spectrograph settings (i.e. the echelle and cross-disperser angles) will also place the detected spectrum elsewhere on the detector pixel grid. For HIRES spectra, HIRES REDUX always re-disperses its output flux onto a fixed velocity scale. For UVES, this is taken into account when re-dispersing the individual QSO exposures onto a common wavelength scale (performed after

⁶<http://www.ucolick.org/~xavier/HIRedux/>

⁷<http://www.eso.org/sci/software/pipelines/>

and outside of the UVES data reduction pipeline, as discussed below).

This process of combining exposures from *both* HIRES and UVES spectrographs onto a common one dimensional wavelength scale, and further adjustments including pixel clipping, order scaling and continuum fitting, is performed using UVES POPLER⁸, written and maintained by Michael T. Murphy. It is worthwhile noting that in both cases of HIRES and UVES spectra the re-dispersion onto a common wavelength scale is performed only once (by HIRES REDUX for HIRES spectra and by UVES POPLER for UVES spectra), in order to minimise inter-pixel correlations, which may produce systematic errors in the analysis. As part of the re-dispersion process the wavelength solutions for each exposure are corrected to vacuum wavelengths from the original air wavelength values, using the Edlen (1966) formula (this is because ThAr line-lists, from which the wavelength calibration is established, are traditionally presented as air wavelengths). The HIRES REDUX pipeline was modified by the author of this thesis to use the inverse of the Edlen (1966) formula (that formula having been used to convert the ThAr line-lists from vacuum to air wavelengths in the first place) in order to make it consistent with its application in UVES POPLER. The UVES POPLER software operates on individual reduced echelle orders and automatically scales overlapping orders to a common magnitude, as weighted by their inverse variance, before combining their flux. It also includes automated cosmic ray rejection and low-order polynomial continuum fitting. The UVES POPLER data combination process also allows for manual adjustment of all of these stages. This important process is further discussed in Section 2.4.3. The output spectra are in the form of flux and flux error arrays versus wavelength, and are used in the varying α analysis in Chapter 3.

2.4.1 Standard wavelength calibration and optimal extraction

The QSO exposures are calibrated using ThAr lamp spectra with the same spectrograph set-up (including grating angles, slit width, on-chip binning etc.) as the QSO exposures. Because the wavelengths of the thorium and argon lines are precisely measured in laboratory tests, they serve as a reference for associating pixel locations

⁸<http://astronomy.swin.edu.au/~mmurphy/UVES-popler/>

with wavelength values. The reference ThAr line selection for both VLT/UVES and Keck/HIRES data is performed using the method in Murphy et al. (2007), who achieved a factor of $\gtrsim 3$ improvement in the wavelength calibration residuals. The RMS residual obtained with the standard ThAr line list is $\sim 130 \text{ m s}^{-1}$, which the method reduces to $\sim 30 \text{ m s}^{-1}$ using the improved ThAr line selection.

Both HIRES and UVES spectra are recovered from the CCD image using optimal extraction (Horne, 1986), as implemented in their respective data reduction pipelines. While the end-result of spectroscopic data reduction is a 1D flux (and error) versus wavelength array, each raw echelle order is a 2D image. This image is a stack of a number of sources: the CCD read noise, dark current, the sky spectrum which enters the entirety of the spectrograph slit (and therefore projects onto the entire spatial extent of the echelle order), incident cosmic rays and the object spectrum itself, which for a point source (such as a QSO) projects only onto the (approximate) centre of the echelle order with a spatial extent dominated by the apparent seeing. Optimal extraction maximises the SNR of the flux from the astronomical source by using a nonuniform object profile in the spatial axis (i.e. perpendicular to the dispersion axis, or the ‘wavelength axis’). This means that pixels where the object flux is the strongest are weighted more than pixels far from the peak of the projected spatial object profile. In addition to the optimal extraction of the object flux, the method allows one the opportunity to identify and reject outlying pixels, such as those caused by cosmic rays. The sum of sky and object fluxes in the 2D echelle order is very different from that produced by a cosmic ray impact on the CCD, which is more easily detected when the object profile is modelled.

2.4.2 Improved calibration for Keck/HIRES data

The HIRES REDUX data reduction package was modified by the author for the work in this thesis, with the intention of making the later process of exposure combination require less manual adjustment and, more importantly, was also modified to improve the quality of the wavelength calibration. The latter modification aims to minimise the presence of systematic errors due to distortions in the wavelength scale. This work was motivated by the presence of artefacts in the intermediate data reduction outputs, difficulties in obtaining automated wavelength scale so-

lutions, and apparent distortions and high residuals in these solutions due to the effects of outliers.

The first modification improves the blaze flux extraction, simplifying continuum fitting using UVES POPLER at the later stages of the data reduction process (see Section 2.4.3). The UVES POPLER software includes blaze fitting routines. The blaze function defines the amplitude of the spectral continuum of each individual echelle order, specific to the blazed grating of the instrument. The amplitude, or signal strength, is highest in the central wavelengths of the echelle order (i.e. at the blaze wavelength), and falls off on either edge of the order. Without taking into account the blaze function, the spectral continuum of an individual exposure oscillates, and does not ‘align’ in amplitude where there are overlapping wavelengths between neighbouring echelle orders. The extracted flux needs to be ‘straightened’ in order to simplify the combination of flux from overlapping orders and subsequent fitting of a continuum to the combined spectrum. Because a QSO spectrum is not the best source of instrumental profile information (being relatively low in SNR and ‘feature rich’ in terms of absorption and emission) the calibrating quartz lamp flat exposures are used to approximate the blaze function. In order to be more closely representative of the blaze function the QSO exposures are subject to, the object profile from the optimal extraction stage is used for extracting the blaze data from the flat. The object profile along the slit (i.e. in the spatial direction) does not fall off to exactly zero at the top or bottom of the slit’s length. For high SNR sources (i.e. a calibrating quartz lamp exposure) this distorts the blaze extraction, imparting a stepping pattern, which may cause problems if the order of the subsequent polynomial fit to the blaze data is high enough. This is because, at higher SNR levels, the non-zero weights of individual pixels at the edge of the object profile used (in the spatial axis) mean that those pixels significantly contribute to the flux extraction, in contrast to actual QSO exposures, where the signal is effectively zero at the edges of the object profile. To mark which pixels belong to which echelle order, a pixel order mask is employed, where the pixel values are integers corresponding to order numbers. The actual orders cross the grid of pixels on the spectrograph on an angle, where they project only fractionally onto pixels corresponding to order edges. The order mask is effectively binary in the case of a single echelle order and does not account for fractional illumination

of the pixels. This spatial aliasing is the underlying cause of the observed stepping pattern in the blaze extraction. To reduce this effect, the object profile has been modified with an additional weighting as follows

$$P_w(x) = \begin{cases} P(x) \left[1 - \left(\frac{|x|}{w} \right)^3 \right]^3 & \text{if } |x| < w \\ 0 & \text{otherwise,} \end{cases} \quad (2.1)$$

where $P_w(x)$ is the weighted profile, $P(x)$ is the original object profile and w is some fraction of the profile width to be included (0.8 is used in this work). This is similar in effect to anti-aliasing the order mask and more straightforward to implement.

The second modification is more significant in that it optimises the wavelength solution in HIRES REDUX and reduces the wavelength calibration residuals. This is implemented in the form of an additional routine to be run after the standard wavelength calibration procedure. It works on the complete 2D wavelength solution (i.e. all orders on a given CCD), as opposed to a given 1D solution (i.e. a single order on a given CCD). This approach uses information from adjacent echelle orders, not just a given order. This allows a further benefit of resistance to sporadic errors in solutions in individual echelle orders due to misidentification of arc lines. The wavelength solution optimisation routine performs the following steps:

1. Identifies potential arc lines in each order and assigns wavelengths based on the current 2D wavelength solution.
2. Matches lines in the reference line list with potential arc lines in each order. The lines have to match to within a velocity offset parameter set by the user (500 m s^{-1} was used in this work).
3. Performs an initial sigma rejection⁹ of outlying arc lines, based on the current 2D wavelength solution ($2.5\text{-}\sigma$ was used in this work). Recalculates the 2D wavelength solution.
4. Optionally performs a further, *iterative* sigma rejection of outlying arc lines ($2.0\text{-}\sigma$ was used in this work). Recalculates the 2D wavelength solution in each iteration.

⁹Sigma rejection is the removal of outliers based on how many standard deviations they lie from the current solution.

5. Optionally, iteratively crops lines from the fit to within a velocity offset parameter and refits every iteration. Allows one to define a desired maximum velocity residual for the arc lines about the fit at the expense of potentially fitting fewer lines (this option was used in this work, with the maximum velocity residuals set to achieve the RMS residuals below).
6. Outputs diagnostic files for inspection.

The routine itself is designed to be run multiple times, iteratively improving the solution with each call. It is robust in that it is by-design insensitive to outlying arc lines and line mis-identifications. The use of the routine generally halves the RMS of the wavelength calibration residuals of the standard reduction. RMS residuals of 30, 40 and 50 m s^{-1} or better were consistently obtained for the blue, green and red chips of HIRES, respectively, while fitting approximately the same number of lines as the standard reduction¹⁰. This makes the quality of the wavelength solution in HIRES REDUX consistent with the UVES data reduction pipeline. The IDL code for the routine is available online¹¹.

2.4.3 Combining exposures and fitting a continuum

The individual extracted echelle orders for a given QSO, from all exposures, are combined using the UVES POPLER software (see Section 2.4). Note that observations of the same object taken with both Keck and VLT are processed separately, with separate output spectra (to be analysed separately as discussed in Section 3.2.1.2). This process is in part automated, where UVES POPLER performs the initial detection of spurious pixels (performed using sigma rejection, usually resulting from cosmic rays not removed in the prior stages of the data reduction, but also spurious or persistent sensor artefacts), blaze profile fitting, scaling of the orders to a common flux level and the first guess of the spectral continuum. All of these stages are open to manual adjustment after visual inspection of the individual orders and the combined spectrum. These adjustments are executed in a repeatable fashion as each user action is recorded by the software, effectively creating a history of operations performed on the data. For the spectra in this work,

¹⁰Note that the results quoted are based on cases of spectra where no pixel binning was used.

¹¹https://github.com/amalec/hiredux_mods

the entirety of each spectrum was inspected and ‘cleaned’, with special attention given to the regions of interest (locations of the Zn II, Cr II and Mg I lines). The majority of the actions performed fall into three categories. The first is the fitting of polynomial ‘continua’ to individual echelle orders of the exposures. These are often affected by the noise at the blue and red extremes of each order, where the noise dominates. These noisy regions are ‘clipped’ (removed from the combined spectrum), allowing for a more reliable fit to the individual order ‘continua’. This is also important because the blaze function extracted from the data may not always be reliable. The second is the removal of outlying pixels, based on visual inspection of the combined spectrum (i.e. the mean flux of all the individual flux values contributed by the exposures). The last category is the final adjustment of the object continuum, where regions of absorption are manually marked as not contributing to the continuum. The work in this thesis is not concerned with the absolute flux of the final spectra and flux arrays normalised by the fit continuum are used in the analysis.

Table 2.4 summarises the final data quality obtained after reducing and combining the exposures listed in Section 2.3.2. The average SNR is 43 per 1.3 km s^{-1} pixel at $\lambda_{\text{rest}} = 2026, 2060 \text{ \AA}$ (where the Zn II and Cr II transitions of interest to constraining $\Delta\alpha/\alpha$ are located), with a standard deviation of 20. At the redder $\lambda_{\text{rest}} = 2852 \text{ \AA}$, the average SNR is 36 per 1.3 km s^{-1} pixel, with a standard deviation of 29. The SNR is highly variable for the transitions of interest, but on average it is close to the target SNR of 50 per 1.3 km s^{-1} pixel. This non-uniformity is likely due to the mix of data from dedicated observations and archival sources and in part due to incidental loss of observing time due to poor weather conditions (e.g. in the case of Q1755+57). The data quality is approximately even between the Keck and VLT telescopes. Overall the SNR is high enough for competitive constraints on $\Delta\alpha/\alpha$.

Table 2.4: SNR per pixel of the final combined spectra used for the varying α analysis at the wavelengths where the Zn II, Cr II and Mg I lines of interest fall. The SNR was measured in continuum regions with no absorption, adjacent to the absorption lines. The first column is the object name, where H superscript denotes Keck/HIRES observations and the U superscript denotes VLT/UVES observations of an object. The second through to fifth columns are measured SNR values at approximately $\lambda_{\text{rest}} = 2026, 2060, 2852 \text{ \AA}$. The final column is the pixel width in km s^{-1} of the final spectra. Note the PHL957 Mg I 2852 lines were not used in the analysis (see Section 3.2.2.6) and the SNR values are either not available or not relevant.

Object	SNR per pixel at $\lambda_{\text{rest}} \sim$			Pixel width [km s^{-1}]
	2026 \AA	2060 \AA	2852 \AA	
J0058+0051 ^H	44	50	68	1.3
J0058+0051 ^U	27	29	31	1.3
J0108–0037	54	48	58	2.5
J0226–2857	32	35	46	2.5
J0841+0312 ^H	85	85	100	1.3
J0841+0312 ^U	44	41	72	1.3
J1029+1039	33	36	29	1.3
PHL957 ^H	78	74	–	1.3
PHL957 ^U	93	95	–	2.5
Q1755+57	34	29	34	1.3
Q2206–1958	90	97	25	2.5
J1237+0106	40	30	36	1.3

3

Constraints on $\Delta\alpha/\alpha$ using Zn II and Cr II transitions

Contents

3.1	Introduction	54
3.2	Analysis	54
3.2.1	Profile fitting and optimisation	54
3.2.2	Fiducial absorption models	60
3.3	Results	91
3.4	Systematic error analysis	93
3.4.1	ThAr wavelength calibration errors	93
3.4.2	Long-range wavelength distortions	95
3.4.3	Short-range intra-order wavelength distortions	96
3.5	Discussion	100
3.5.1	Temporal variation in α	100
3.5.2	Spatial variation in α	100
3.5.3	Comparison to previous $\Delta\alpha/\alpha$ constraints	101

3.1 Introduction

The QSO absorption line data in Chapter 2 is analysed in this chapter, as motivated by the benefits of using only Zn II and Cr II transitions to constrain $\Delta\alpha/\alpha$. These are detailed in Section 2.2, and can be briefly summarised as follows. Using only Zn II and Cr II transitions allows a robust and sensitive measure of $\Delta\alpha/\alpha$ because of the unique pattern of shifts the lines have with varying α . The wavelength separation between the 5 transitions is small, allowing the analysis to be much less prone to long-range wavelength calibration errors than in any other many-multiplet (MM) analyses. And finally, the transitions have similar optical depths, which aids in profile fitting. In this Chapter, spectral models are constructed, where the transitions of interest are ‘simultaneously fit’. The models are then subject to χ^2 minimisation, with variation in α incorporated as a free parameter. This process measures individual $\Delta\alpha/\alpha$ values for each spectrum, along with statistical errors on the values. Estimates of major sources of systematic error are performed and the final weighted mean result is compared to previous $\Delta\alpha/\alpha$ constraints in the field.

The work presented here is separated into four main sections. Section 3.2 outlines the physical assumptions, profile fitting and optimisation method, along with descriptions of each model fit. The $\Delta\alpha/\alpha$ results are presented in Section 3.3 and the systematic error contribution is estimated in Section 3.4. Finally, the implications of the results for temporal and spatial variation of α are discussed, and comparisons are made to other $\Delta\alpha/\alpha$ constraints in Section 3.5.

3.2 Analysis

3.2.1 Profile fitting and optimisation

All of the absorbers in the Zn & Cr II sample used in this thesis display some form of velocity structure with various degrees of complexity. This means the absorption ‘cloud’ is actually made up of several clouds, or a ‘continuum of clouds’ with similar redshifts and different optical depths and Doppler widths. Further,

in most cases the Zn II 2026 absorption blends or overlaps with Mg I 2026 (the velocity difference is $\Delta v = 50 \text{ km s}^{-1}$, which is narrower than the velocity structure observed in most of the absorber sample). The Zn II 2062 lines also heavily blend with Cr II 2062 ($\Delta v = 62 \text{ km s}^{-1}$). Their structure is resolved via the unblended Cr II 2056, 2066 and Mg I 2852 transitions (available for all absorbers in the sample, with the exception of Mg I 2852 in PHL957 for both telescopes; see Section 3.2.2.6 for discussion).

These complications are addressed by ‘simultaneous fitting’, where the Cr II, Zn II and Mg I transitions are fit at the same time in a single, comprehensive fit. The process behind constructing each fiducial fit is an iterative one. Because of the huge parameter space, an initial guess is made, where structure is added until the residuals show no evidence of unfit absorption. Structure, in the context of fitting absorption model to data, refers to the combined effect of one or more, often overlapping, velocity components (each modelled with the Voigt profile; see Section 3.2.1.1). Each velocity component represents an absorbing ‘cloud’ along the observed sightline and the combination of these clouds, each at slightly different velocities, represents a part of, or the full observed ‘shape’ or ‘structure’ of the profile of a particular transition in the absorption system. Throughout the process of fitting, where the final, stable model has not been reached, the $\Delta\alpha/\alpha$ parameter is not included in the fit. It is only once convergence on the $\Delta\alpha/\alpha$ -free model is achieved, and the fit is stable (i.e. no velocity components are disregarded by the fitting software during optimisation), that the variation in α is allowed in the model.

When minimising χ^2 , the uncertainties in the model fit parameters take into account degeneracies resulting from overlapping lines, providing a robust constraint on the $\Delta\alpha/\alpha$ parameter incorporated into the model. The benefits described in the previous chapter (see Section 2.2) could not be realised if not for the simultaneous fitting when performing χ^2 minimisation, as the Zn II transitions are in almost all cases blended with Mg I and Cr II transitions.

3.2.1.1 Absorption model parameters and physical assumptions

The basic unit of an absorption model that is fitted to the observations is the Voigt profile of a single absorption line – the convolution of Gaussian Doppler broadening

and the transition's natural line-shape, a Lorentzian profile. An absorption line is parameterised by its redshift, z_{abs} , logarithmic column density $\log N$ (cm^{-2}) and broadening parameter b (km s^{-1}). The b parameter describes both thermal and turbulent broadening. Each individual line constitutes what is referred to as a velocity component.

To measure $\Delta\alpha/\alpha$ the z_{abs} parameters of Zn II and Cr II transitions are tied together, that is, the individual ‘clouds’ which make up the observed absorption have the same intrinsic redshift. This assumes the proper motion between the absorbing gas ‘clouds’ of different atomic species is negligible. Even if this was not the case, and there existed spatial offsets between the singly ionised Zn II and Cr II, any such offsets should occur randomly for different sight-lines in the sample, and therefore the resulting individual departures from a true $\Delta\alpha/\alpha$ value would not be a systematic effect overall.

To reduce the number of free parameters, the broadening b parameter is assumed to be purely turbulent. Line broadening is a function of thermal broadening and turbulent broadening¹. Purely thermal broadening implies the turbulent motion of the absorbing gas is negligible and the b parameter effectively defines the temperature of the gas. Fitting with purely turbulent broadening implies the thermal component is null. While this is unlikely to be the case in reality, purely turbulent broadening is an approximation, where the turbulent component is assumed to dominate the thermal component to the effect the latter can be ignored. Murphy (2002) found $\Delta\alpha/\alpha$ values derived from either entirely thermal, entirely turbulent or a combination of both types of broadening are in almost all cases consistent with each other. Murphy et al. (2003a) note that fitting for both broadening types is computationally intensive (given both types are fit, while being strongly degenerate with each other) and the resulting thermal and turbulent b parameters are poorly constrained. More recently, King et al. (2012) found a purely turbulent fit to be preferred in 71 percent of their 154 absorber sample (with the caveat that all of the initial fits were first constructed using purely turbulent broadening). The same work also notes that any given effect on $\Delta\alpha/\alpha$ will be random between different absorbers. This suggests a potential source of additional scatter in the $\Delta\alpha/\alpha$ results,

¹Formally $b = \sqrt{2kT/m + b_{\text{turb}}^2}$, where k is the Boltzmann constant, T is the kinetic temperature of the gas cloud, m is the mass of the ionic species and b_{turb} is the turbulent motion component, independent of the ionic species.

but not any systematic deflection away from the true mean in $\Delta\alpha/\alpha$. With the benefit of a simpler model, the line broadening mechanism is therefore parametrised as purely turbulent in the work presented here. The minimum allowed value for the b parameters is 0.5 km s^{-1} . This is below the resolution of the spectra and the effective velocity component shape is the instrumental profile. Such narrow velocity components allow the fits to account for unresolved velocity structure.

The oscillator strengths for the different transitions and their column densities N , along with the b parameters, determine the shapes of the individual velocity components, where, broadly speaking, the b parameter controls the width and the N parameter controls the depth. The Voigt profile function is symmetrical about its minimum (in the case of absorption). The profile can ‘saturate’ at high enough N , corresponding to complete absorption at a range of wavelengths about its centre. Asymmetry and structure in the spectral features present in the absorption profile is modelled through a combination of overlapping velocity components. The individual velocity components are also convolved with the instrumental profile, with a velocity width corresponding to the instrumental resolution (i.e. determined mainly by the slit-width of the spectrograph). The instrumental profile is modelled as a Gaussian function. One cannot assume the same abundances of Zn and Cr in the absorbers and so the N parameters of the velocity components are independent. This is necessary given the different abundances of Zn and Cr and the potential for differential dust depletion of the elements (Herbert-Fort et al., 2006, find evidence of dust depletion in a handful of absorbers in their metal-strong sample). Both Zn and Cr may be depleted out of the gas phase (e.g. Roth and Blades, 1995), though in DLAs Zn is almost undepleted and Cr is heavily depleted, particularly in DLAs that host observable molecular hydrogen content (Pettini et al., 1994). The presence or the magnitude of depletion onto dust grains is not investigated in this work as it does not affect the $\Delta\alpha/\alpha$ constraints, as long as differences in column densities between Zn II and Cr II are permitted in the fitted models. As previously mentioned, this is facilitated by fitting the N parameters between the different species independently.

Finally, the free parameter $\Delta\alpha/\alpha$ is introduced for the Zn II and Cr II transitions. The Mg I transitions, which blend with Zn II at 2026 \AA are fit with all of the parameters not linked to Zn II and Cr II. This is because the Mg I transitions

are not being used to constrain $\Delta\alpha/\alpha$. Tying Mg I with the target transitions may introduce a systematic error in the presence of a long-range distortion of the wavelength scale. This would cause a shift between the Mg I 2852 and 2026 lines which, if the velocity structure of Mg I is tied to that of Zn II and Cr II, would propagate into $\Delta\alpha/\alpha$. By decoupling these transitions, the Mg I 2026 line is constrained only by Mg I 2852, which reduces any systematic error in the $\Delta\alpha/\alpha$ constraint. An improvement to this approach is to allow for a velocity shift between the 2026 and 2852 Å fitting regions to decouple the two Mg I transitions, not just Mg I and Zn/Cr II. However, this was not available as a working, tested option in the VPFIT software used for fitting (see Section 3.2.1.2) until recently and it will be implemented in the near future to further refine the analysis of $\Delta\alpha/\alpha$ presented here.

3.2.1.2 Minimising χ^2 to constrain $\Delta\alpha/\alpha$

The absorption model is constructed with the free parameters described above and the χ^2 between it and the spectral data is minimised using the program VPFIT². This is a non-linear least-squares χ^2 minimisation package written specifically for modelling complex, possibly interrelated, ‘tied’ absorption lines with a series of Voigt profiles. To aid in the modelling process the author of this thesis created the FITCMP³ tool, an extended interface for VPFIT, used throughout all stages of profile fitting here. The functionality employed in χ^2 minimisation is purely that of VPFIT, however, and the FITCMP tool is not necessary to reproduce the results in this Chapter.

In cases where exposures of a single QSO target were obtained using both the HIRES and UVES spectrographs, separate model fits were constructed. While VPFIT is designed to allow a single model to be fit to multiple data sources, there is potential for differences in data quality and instrumental profile between the HIRES and UVES science exposures to lead to unexpected issues, as this method has neither been fully tested nor verified. Additionally, fitting the data from both telescopes separately allows for the results to be directly compared. Potential future work includes fitting simulated and actual data from both telescopes with separate

²<http://www.ast.cam.ac.uk/~rfc/vpfit.html>

³<https://github.com/amalec/fitcmp>

and single models to verify both approaches.

The model fits are convolved with instrumental resolution functions for comparison with the real spectra. A Gaussian function parameterised by the FWHM was used to match the resolution inferred from the extracted ThAr exposures, which use the same slit width as the science exposures⁴. In some cases, different slit-widths (i.e. resolving powers) were used in separate exposures of the same QSO. While all exposures of a given QSO were initially combined together into a “master” spectrum with a common continuum (note that exposures from different telescopes, were reduced, combined and fit separately), the exposures were then grouped according to the slit-widths (i.e. resolving powers) and output to separate data-files, or “sub-spectra” of the master. The same process was also followed when differently binned exposures were used. These sub-spectra are fit simultaneously using a common absorption model, where this data separation allows for separate resolving powers to be used for each sub-spectrum, according to the slit-width and binning used. This additional fit complexity, where data is fit separately but simultaneously, is justified because re-dispersion introduces inter-pixel correlations in the fluxes and errors, which VPFIT assumes are uncorrelated in neighbouring pixel bins – a source of potential systematic error. For UVES fits, the FWHM used was greater for the redder Mg I 2852 spectrum regions by 7.5% to account for the difference in the resolution between the two spectrograph arms⁵.

That VPFIT returns the correct values of $\Delta\alpha/\alpha$ and their uncertainties has been tested with a variety of simulations, including models with many strongly overlapping velocity components which are, in some cases, blended with transitions from unrelated absorption clouds (e.g. Murphy et al., 2003a, 2008a,b; King et al., 2012). The $1-\sigma$ uncertainties on the best fitting parameters are derived by VPFIT from the appropriate diagonal terms of the final parameter covariance matrix. Given a particular absorption model, these errors represent only the formal statistical uncertainties derived from the flux error arrays of the fitted spectral regions. They do

⁴The FWHM values were set according to the resolving power associated with a given slit-width. In the calculation, the resolving power was increased by 5%. When the modelled absorption structures are unsaturated it is safer to over-estimate the resolving power, as the fitted b parameters will become overestimated in response. An under-estimated resolving power can broaden the model fit to the extent that it cannot adequately fit the narrower features in the absorption profile. The effect of slightly over-estimated b parameters on $\Delta\alpha/\alpha$ is negligibly small.

⁵This is based on the ratio of the resolution-slit product of the blue and red arms of UVES, 41400 and 38700 respectively.

not reflect additional sources of error, like wavelength calibration uncertainties (see Section 3.4.1). As mentioned previously in this section, VPFIT assumes that the fluxes (and flux errors) in neighbouring spectral pixels are uncorrelated. This is not true here because the different QSO exposures were re-binned onto the same final wavelength grid for combination into a single spectrum (see Section 2.4.3). The correlation is reduced by averaging these exposures. The effect is not detected by comparing the RMS flux variations in unabsorbed regions of the sample absorbers with the final error spectra. The values are consistent for all absorbers.

3.2.2 Fiducial absorption models

The following sections describe the fiducial absorption models of the Zn II, Cr II, and Mg I transitions that were constructed to constrain $\Delta\alpha/\alpha$, using the assumptions described in Section 3.2.1.1. The fiducial fits are obtained by minimising the model χ^2 (see Section 3.2.1.2). This is performed with the $\Delta\alpha/\alpha$ parameter initially fixed to zero. These fits are referred to as the fiducial fits or models. They are used at the starting point of any further tests or consistency checks. The minimisation process is repeated with a free $\Delta\alpha/\alpha$ and the result is referred to as the fiducial $\Delta\alpha/\alpha$ result (these results are presented in Section 3.3). Each section concerns an individual absorption system separately. The Zn II and Cr II transition spectra are plotted with overlaid fiducial model fits. For those transitions composite residual spectra (CRS) are also plotted.

A CRS is constructed by normalising the residuals between the data and the model fit by the flux error arrays for many transitions, shifting them to a common velocity scale and averaging them together. The CRS allows one to visually inspect the sum residual structure between the model and the data, serving as a diagnostic of model inadequacies. The best example of this is under-fitting, where the CRS will depart from within its $\pm 1\text{-}\sigma$ range for several pixels, indicating that there exists structure in the absorption profile which has not been incorporated into the model. Further details of the CRS, and exemplary plots, are presented in Section 4.4.2.

Tables with model parameters and errors are also presented in each absorption system's section. Note that the plots and tables of Mg I fits and parameters are omitted for brevity, especially as the Mg I transitions are not used to constrain $\Delta\alpha/\alpha$. Plots of blending Mg I fits and fit parameters are contained in Appendix A.

3.2.2.1 J0058+0051

The J0058+0051 $z_{\text{abs}} = 1.072$ absorber extends over 120 km s^{-1} . It is dominated by 3 major absorption features at -30 , 0 and 30 km s^{-1} as plotted in Figure 3.1, where the central feature is the strongest. The blending Mg I 2026 velocity structure extends over the whole of the fit Zn II 2026 transition. Both HIRES and UVES exposures are fit separately, showing a consistent velocity structure. The UVES set is composed of 1×1 and 2×2 binned exposures. As described in Section 3.2.1.2, these were fit separately but simultaneously. Visual inspection of Figure 3.2 shows no evidence of gross inconsistencies in the data between the two differently binned sets.

One velocity component, at -20 km s^{-1} , is present in the HIRES but not in the UVES model. It may be unnecessary, as the adjacent broad lines effectively fit the shallow feature in that location in the UVES model.

The red-most velocity component could not be justified in Zn II and was consistently rejected by VPFIT optimisation. Its presence in both HIRES and UVES models confirms that it is indeed a feature of the absorber, but given the SNR of the spectra, it cannot be effectively fit for the Zn II transitions. The effect of such broad features on the validity of the $\Delta\alpha/\alpha$ result is small, given their low constraining power on velocity shifts, as long as the model is not under-fit. Attempts at introducing additional velocity components were unsuccessful (deemed suboptimal by VPFIT optimisation) and it is concluded that the complexity of the model is sufficient as to be deemed adequate, given the data SNR.

The CRS of the HIRES fit, presented in the top panel of Figure 3.1, shows no evidence of unfit velocity structure. The fit has a normalised chi-squared value of $\chi^2_\nu = 0.91$ (where $\chi^2 = 422.93$ and $\nu = 467$).

The UVES fit converges in the first instance, when not fitting for varying α , but fails to do so when a $\Delta\alpha/\alpha$ is added as an additional degree of freedom. The fitting program VPFIT outputs a high normalised chi-squared value of $\chi^2_\nu = 1.45$ (where $\chi^2 = 1212.03$ and $\nu = 836$). The fit to the blending Mg I 2026 structure, as resolved by the Mg I 2852 transition, is adequate and comparable to that of the HIRES spectrum. Further, as the Mg I 2026 velocity components are not tied to the $\Delta\alpha/\alpha$ parameter in the first place (see Section 3.2.1.1), they should have no bearing when fitting for $\Delta\alpha/\alpha$. Comparing the errors on the fit parameters,

especially z_{abs} and b in Table 3.2 with Table 3.1, one can see that the errors in the UVES fit are generally at least double the HIRES fit. This is surprising, given the SNR quality of the two data sets is not significantly dissimilar. Adding more velocity components in various parts of the absorption structure, the first course of action one would take when χ^2_ν is well over the optimal value of 1, has been unsuccessful. VPFIT removes any such additions to the velocity structure.

The CRS of the Zn II and Cr II transitions as shown in the top panel of Figure 3.2 is not indicative of any gross unfit structure. Note that the composite residual values are binned onto a velocity scale with wider bins of the 2×2 spectra.

Overall, it is difficult to make conclusions as to why $\Delta\alpha/\alpha$ does not converge for the J0058+0051 UVES spectrum. It is possible that VPFIT is being prevented from converging towards a final solution because of a large degeneracy between parameters and/or because χ^2 is particularly insensitive to one or more of the model parameters (e.g. a very low N or very small b parameter). No $\Delta\alpha/\alpha$ constraint could be obtained for the J0058+0051 UVES spectrum and therefore it is disregarded in further analysis.

Table 3.1: Fiducial fit Zn II and Cr II absorption line parameters and $1\text{-}\sigma$ statistical uncertainties for the J0058+0051 HIRES spectrum. The errors are given in units of the least significant digit of the measurement itself; for example, $b = 3.68(109)$ implies a $1\text{-}\sigma$ error of 1.09 km s^{-1} . The number of significant figures in the error values presented exceeds one; this is to permit a compact record of the parameter values at a precision which facilitates reproducibility of the fits. This is the same for all subsequent tables.

	z_{abs}	b [km s^{-1}]	$\log N(\text{Cr II})$ [cm^{-2}]	$\log N(\text{Zn II})$ [cm^{-2}]
a	1.0716582(49)	3.68(109)	11.74(36)	11.50(12)
b	1.0717482(295)	7.99(423)	12.84(32)	12.06(31)
c	1.0717870(46)	2.67(171)	12.58(45)	11.65(61)
d	1.0718339(45)	4.71(129)	12.91(12)	12.21(10)
e	1.0718898(43)	1.49(222)	12.12(29)	10.87(75)
f	1.0719585(55)	7.10(148)	13.10(9)	12.21(10)
g	1.0720081(9)	2.40(33)	12.60(14)	12.34(4)
h	1.0720609(77)	7.94(308)	12.97(16)	12.18(17)
i	1.0721328(46)	2.66(174)	12.19(32)	11.15(56)
j	1.0722302(24)	8.40(65)	12.73(2)	11.70(4)
k	1.0723862(89)	7.06(211)	11.97(9)	

Table 3.2: Fiducial fit Zn II and Cr II absorption line parameters and $1\text{-}\sigma$ statistical uncertainties for the J0058+0051 UVES spectrum.

	z_{abs}	b [km s^{-1}]	$\log N(\text{Cr II})$ [cm^{-2}]	$\log N(\text{Zn II})$ [cm^{-2}]
a	1.0716491(163)	3.47(259)	12.04(23)	10.91(44)
b	1.0717190(217)	4.87(339)	12.51(52)	11.77(44)
c	1.0717900(175)	5.91(466)	13.08(39)	12.24(41)
d	1.0718321(98)	0.98(236)	11.67(308)	11.64(47)
e	1.0718506(380)	4.08(509)	12.70(103)	11.85(105)
f	1.0719540(92)	8.41(260)	13.16(14)	12.23(16)
g	1.0720058(236)	2.97(47)	12.59(17)	12.44(4)
h	1.0720749(103)	9.48(168)	13.03(11)	12.21(12)
i	1.0722323(93)	8.72(89)	12.79(4)	11.77(7)
j	1.0723749(98)	1.50(284)	11.86(11)	

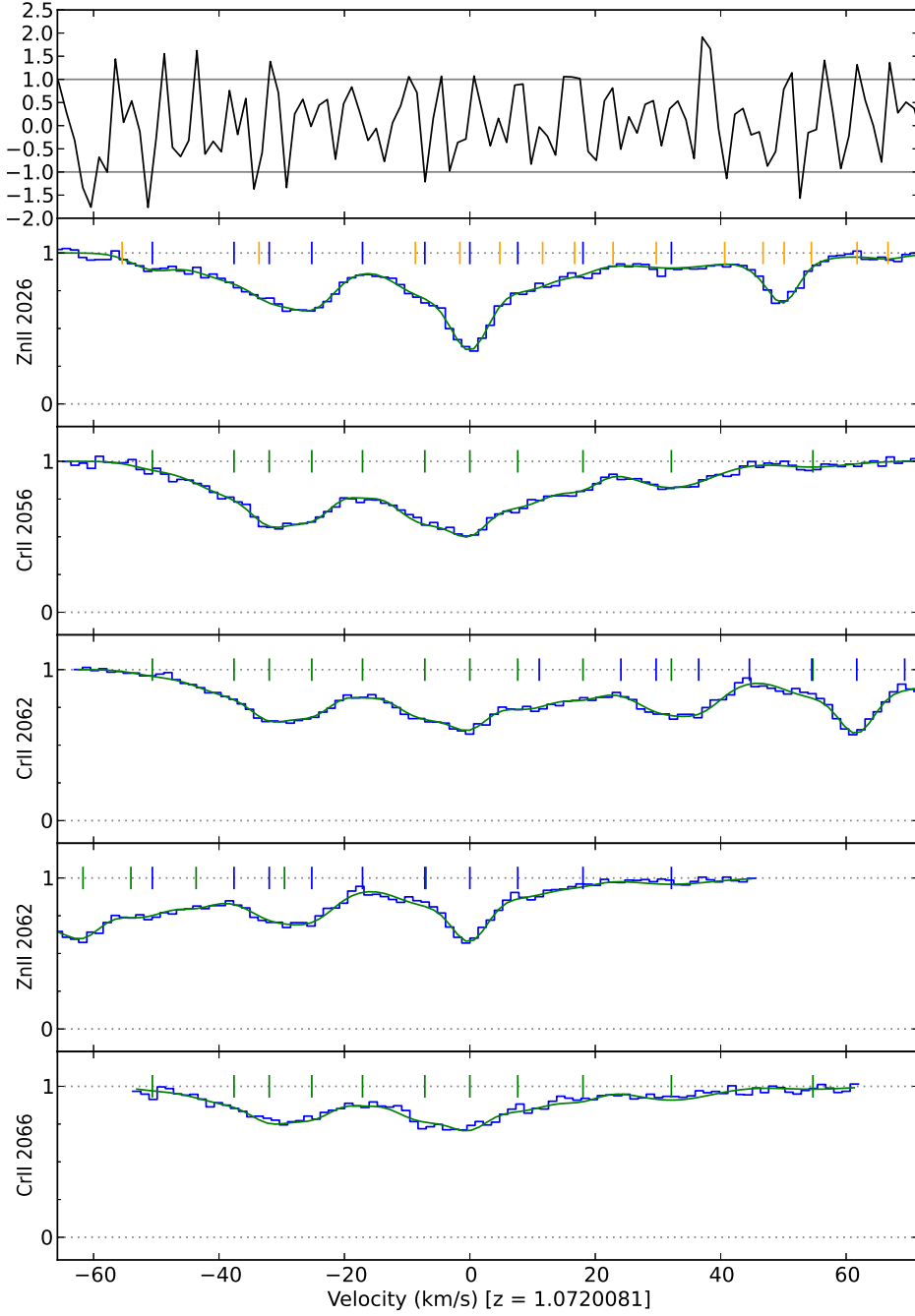


Figure 3.1: Data and model fit for the J0058+0051 HIRES spectrum Zn II and Cr II transitions, centred at $z_{\text{abs}} = 1.072$. The fit (continuous green line) is overlaid on the normalised spectrum (blue histogram). Each transition is labelled on the vertical axis for that panel. The vertical tick marks indicate the positions of the fit Zn II (blue), Cr II (green) and Mg I (orange) velocity components. The top panel is the composite residual spectrum formed by the Zn II and Cr II transitions (see Section 3.2.2). This is the same for all subsequent figures.

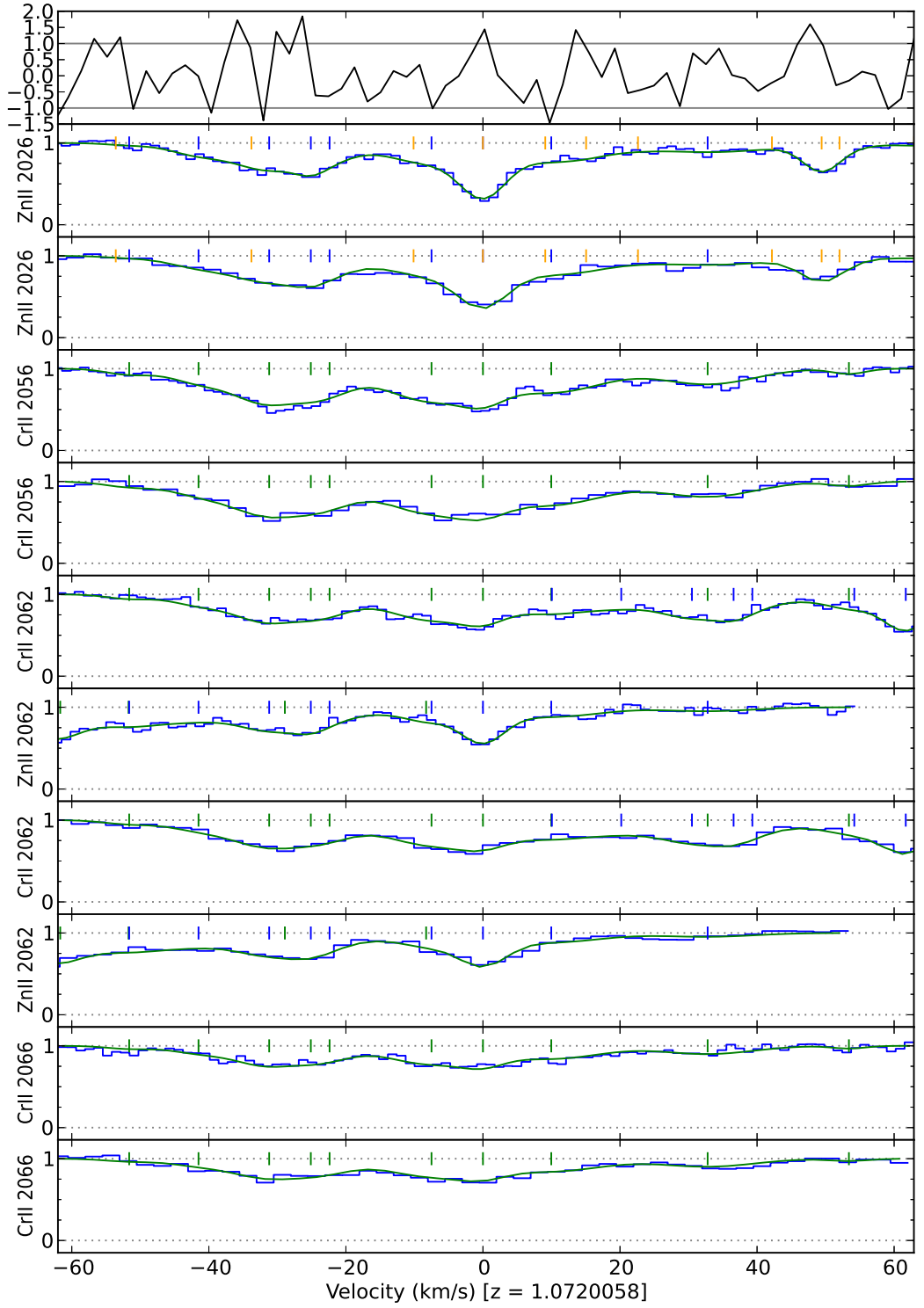


Figure 3.2: Data and model fit for the J0058+0051 UVES spectrum Zn II and Cr II transitions, centred at $z_{\text{abs}} = 1.072$. The alternating panels are 1×1 and 2×2 binned spectra.

3.2.2.2 J0108–0037

The J0108–0037 $z_{\text{abs}} = 1.371$ absorber extends over approximately 40 km s^{-1} . The UVES spectrum shows 2 broad features, approximately 15 km s^{-1} apart, as plotted in Figure 3.3. The blending of the Zn II 2026 transition by Mg I 2026 is minimal, limited only to the weak, red-most absorption structure.

Similar to J0058+0051, the red-most velocity component could not be justified in Zn II (also see Table 3.3). The component coincides in velocity with the one blending Mg I 2026 velocity component (their positions are both approximately 11 km s^{-1} ; note that the Mg I 2026 velocity structure is constrained with the observed Mg I 2852 transition). Combined with how weakly the flux is absorbed in that spectral region (given the SNR) and how, by inspection, the Zn II 2062 transition does not strongly justify additional velocity structure, one can see why it was consistently rejected by VPFIT optimisation. Again, such broad and shallow features are largely inconsequential for constraining $\Delta\alpha/\alpha$, provided the velocity structure is adequately fit.

In that regard, the CRS in Figure 3.3 does not suggest unfit velocity structure. Instead it may even be indicative of over-fitting of the bluer absorption structure, as the CRS is very close to 0.0 at around -15 km s^{-1} . The normalised chi-squared value of $\chi^2_\nu = 1.17$ (where $\chi^2 = 159.78$ and $\nu = 137$) is acceptable.

Table 3.3: Fiducial fit Zn II and Cr II absorption line parameters and $1\text{-}\sigma$ statistical uncertainties for the J0108–0037 spectrum.

	z_{abs}	b [km s^{-1}]	$\log N(\text{Cr II})$ [cm^{-2}]	$\log N(\text{Zn II})$ [cm^{-2}]
a	1.3709241(102)	4.79(188)	13.21(54)	12.33(37)
b	1.3709560(235)	9.29(277)	13.49(29)	12.01(93)
c	1.3709783(47)	1.01(41)	12.56(32)	12.17(10)
d	1.3710523(23)	4.84(29)	13.59(5)	12.67(4)
e	1.3711361(142)	0.50(1025)	11.61(52)	

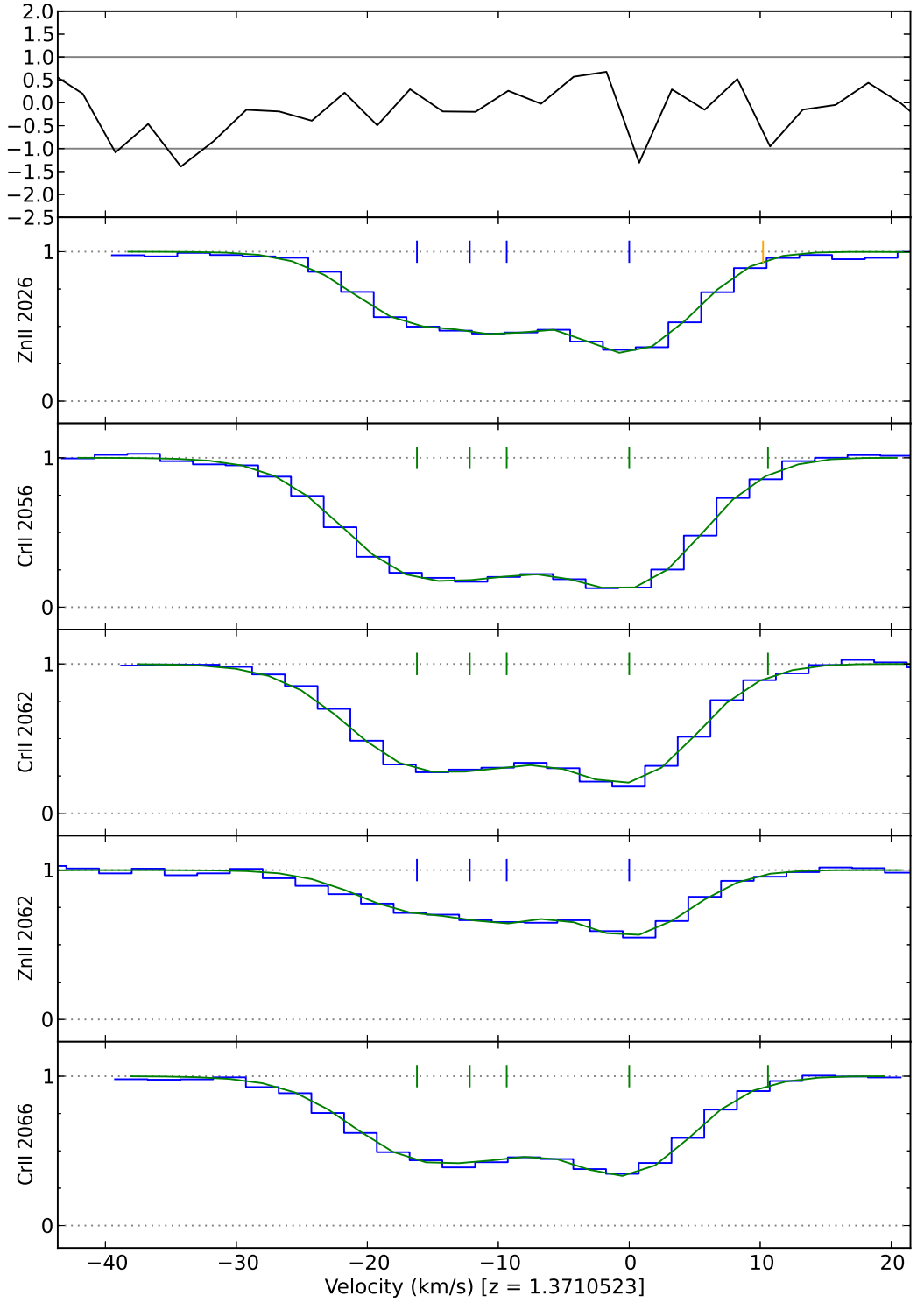


Figure 3.3: Data and model fit for the J0108-0037 UVES spectrum Zn II and Cr II transitions, centred at $z_{\text{abs}} = 1.371$.

3.2.2.3 J0226–2857

The J0226–2857 $z_{\text{abs}} = 1.023$ absorber extends over approximately 170 km s^{-1} . The UVES spectrum shows a strong, complex velocity structure, as plotted in Figure 3.4, making this absorber particularly suited for constraining $\Delta\alpha/\alpha$. The data set is composed of both $0.8''$ and $1.2''$ slit data, fit separately but simultaneously with the same model, as described in Section 3.2.1.2. The VPFIT program output no evidence of convergence problems, unlike the issue with the J0058+0051 1×1 and 2×2 binned UVES exposures in Section 3.2.2.1.

The blending of the Zn II 2026 transition by Mg I 2026 extends over the whole of the Zn II 2026 absorption. Modelling both Zn II 2062 and Mg I 2852 allows this complex blending structure to be successfully resolved. The column densities of both Zn II and Cr II are particularly similar (see Table 3.4), unlike for most absorbers in this sample.

The CRS in Figure 3.4 does not suggest unfit velocity structure. The normalised chi-squared value of $\chi^2_\nu = 1.27$ (where $\chi^2 = 1046.67$ and $\nu = 826$) is typical of the sample UVES χ^2_ν values, which are in most cases higher than the HIRES values. To verify that this is not a symptom of an underlying problem in the flux error arrays, the RMS flux and the mean error array values in regions of unabsorbed flux were compared. This was done in areas adjacent to the fitted regions and revealed no inconsistency.

Overall, this absorber is exemplary, in absorption strength, complexity of structure and data SNR.

Table 3.4: Fiducial fit Zn II and Cr II absorption line parameters and 1- σ statistical uncertainties for the J0226–2857 spectrum.

	z_{abs}	b [km s ⁻¹]	$\log N(\text{Cr II})$ [cm ⁻²]	$\log N(\text{Zn II})$ [cm ⁻²]
a	1.0220203(59)	7.59(139)	12.23(7)	11.64(7)
b	1.0221652(54)	3.28(159)	11.97(10)	11.22(15)
c	1.0222535(50)	0.50(384)	11.88(38)	10.85(54)
d	1.0223357(168)	8.71(473)	12.21(21)	11.89(20)
e	1.0224340(190)	4.64(310)	12.64(35)	12.29(35)
f	1.0224603(52)	0.69(74)	12.39(35)	12.30(22)
g	1.0224920(46)	1.52(70)	12.95(15)	12.68(14)
h	1.0225284(53)	3.04(205)	13.02(28)	12.76(25)
i	1.0225828(134)	4.26(332)	13.24(45)	12.88(52)
j	1.0226239(110)	4.47(151)	13.45(23)	13.27(18)
k	1.0226622(37)	1.04(73)	12.91(15)	12.61(32)
l	1.0227197(167)	5.17(551)	12.65(41)	12.28(46)
m	1.0227639(45)	2.70(181)	12.40(73)	12.36(38)
n	1.0228031(114)	2.41(320)	12.71(43)	12.28(52)
o	1.0228417(84)	2.48(302)	12.85(50)	12.52(42)
p	1.0228814(222)	3.20(455)	12.61(57)	12.20(60)
q	1.0229252(50)	0.91(132)	12.30(16)	11.88(18)
r	1.0229746(36)	0.50(108)	12.25(31)	10.92(75)
s	1.0230290(48)	9.01(91)	12.90(4)	12.33(4)

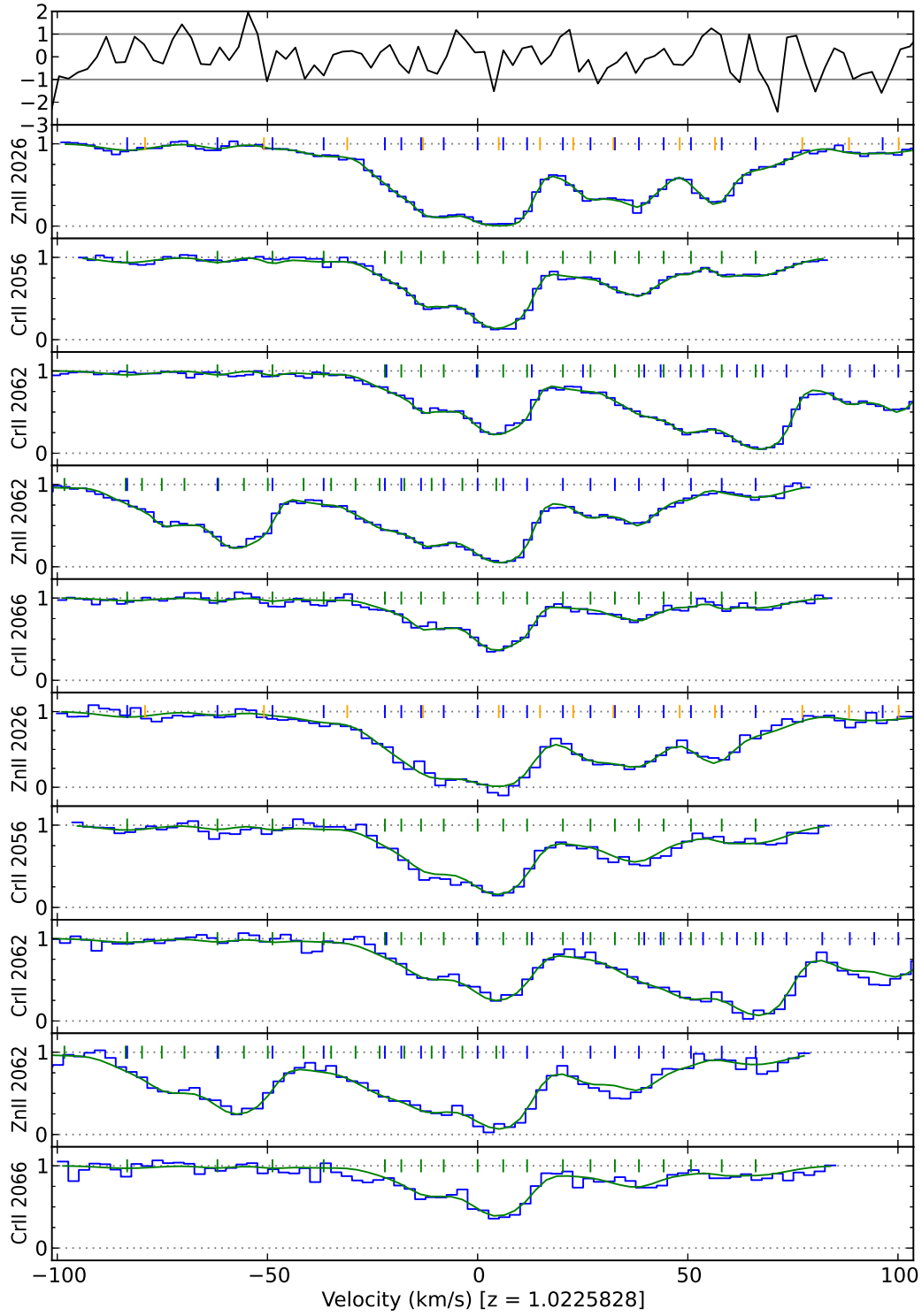


Figure 3.4: Data and model fit for the J0226–2857 UVES spectrum Zn II and Cr II transitions, centred at $z_{\text{abs}} = 1.023$. Top and bottom panels show $0.8''$ and $1.2''$ slit data, respectively.

3.2.2.4 J0841+0312

The J0841+0312 $z_{\text{abs}} = 1.342$ absorber extends over approximately 90 km s^{-1} . The spectrum shows 2 broad features, approximately 55 km s^{-1} apart, as plotted in Figures 3.5 and 3.6.

The absorber sample has both HIRES and UVES data, both of which are very comparable in SNR (see Figures 3.5 and 3.6) and their fiducial model fits (see Tables 3.5 and 3.6). The velocity structure is smooth, with two main broad absorption features at -50 km s^{-1} and 0 km s^{-1} , as plotted. The redder feature is stronger and has more structure fit as a result. The blending of the Zn II 2026 transition by Mg I 2026 is moderate.

Three (HIRES) and two (UVES) velocity components on the blue side of the absorption could not be justified in Zn II (also see Table 3.5). This is not surprising, given the blue-most absorption feature is relatively weak and the Cr II transitions are observed to be stronger in the sample. This has little or no effect on constraining $\Delta\alpha/\alpha$, as for the previously discussed absorbers.

The CRS plots for both HIRES and UVES fits are very similar, as to be expected given the similarity in the underlying data SNR. The plots do not suggest unfit velocity structure. For the HIRES model, the normalised χ^2 test value is $\chi^2_\nu = 0.79$ (where $\chi^2 = 288.66$ and $\nu = 365$). For the UVES model, the normalised chi-squared value is $\chi^2_\nu = 1.02$ (where $\chi^2 = 351.94$ and $\nu = 346$). Both are representative of fits with an appropriate level of modelled structure. Interestingly, given the similarities of the models and data SNR, the UVES χ^2 is somewhat larger (also noted in Section 3.2.2.3).

Table 3.5: Fiducial fit Zn II and Cr II absorption line parameters and 1- σ statistical uncertainties for the J0841+0312 HIRES spectrum.

	z_{abs}	b [km s ⁻¹]	$\log N(\text{Cr II})$ [cm ⁻²]	$\log N(\text{Zn II})$ [cm ⁻²]
a	1.3421294(188)	0.50(2893)	10.89(68)	
b	1.3422072(53)	0.53(602)	11.50(17)	
c	1.3422523(3223)	87.83(9163)	12.03(95)	11.58(38)
d	1.3422893(34)	8.68(88)	12.55(6)	11.31(8)
e	1.3424648(82)	5.05(245)	11.72(22)	
f	1.3425436(64)	0.50(298)	11.68(25)	10.93(14)
g	1.3425810(61)	0.57(196)	11.96(91)	11.19(31)
h	1.3426215(725)	3.76(1168)	12.59(176)	11.53(179)
i	1.3426523(177)	2.67(158)	12.58(156)	11.74(97)
j	1.3427063(19)	3.65(65)	13.09(6)	12.31(5)
k	1.3427656(58)	1.47(352)	12.04(52)	11.25(55)
l	1.3428067(59)	0.50(132)	11.92(22)	11.11(37)
m	1.3428217(1375)	9.50(1564)	11.99(113)	11.18(131)
n	1.3429679(3713)	18.22(6132)	10.92(387)	10.68(180)

Table 3.6: Fiducial fit Zn II and Cr II absorption line parameters and 1- σ statistical uncertainties for the J0841+0312 UVES spectrum.

	z_{abs}	b [km s ⁻¹]	$\log N(\text{Cr II})$ [cm ⁻²]	$\log N(\text{Zn II})$ [cm ⁻²]
a	1.3421285(134)	3.90(354)	11.67(19)	
b	1.3422074(56)	0.66(396)	11.92(22)	
c	1.3422771(81)	4.83(185)	12.44(14)	11.24(18)
d	1.3423592(198)	5.10(415)	12.06(33)	11.05(33)
e	1.3424847(174)	6.96(591)	11.93(27)	11.12(27)
f	1.3425563(104)	0.50(309)	11.85(28)	11.02(25)
g	1.3426128(129)	3.31(293)	12.59(28)	11.72(27)
h	1.3426487(47)	0.82(61)	12.65(18)	11.63(27)
i	1.3427026(11)	3.97(42)	13.15(2)	12.37(2)
j	1.3427748(34)	1.94(136)	12.26(9)	11.50(10)
k	1.3428274(71)	0.50(209)	11.75(17)	11.28(27)
l	1.3428717(142)	0.50(1184)	11.11(41)	10.85(44)

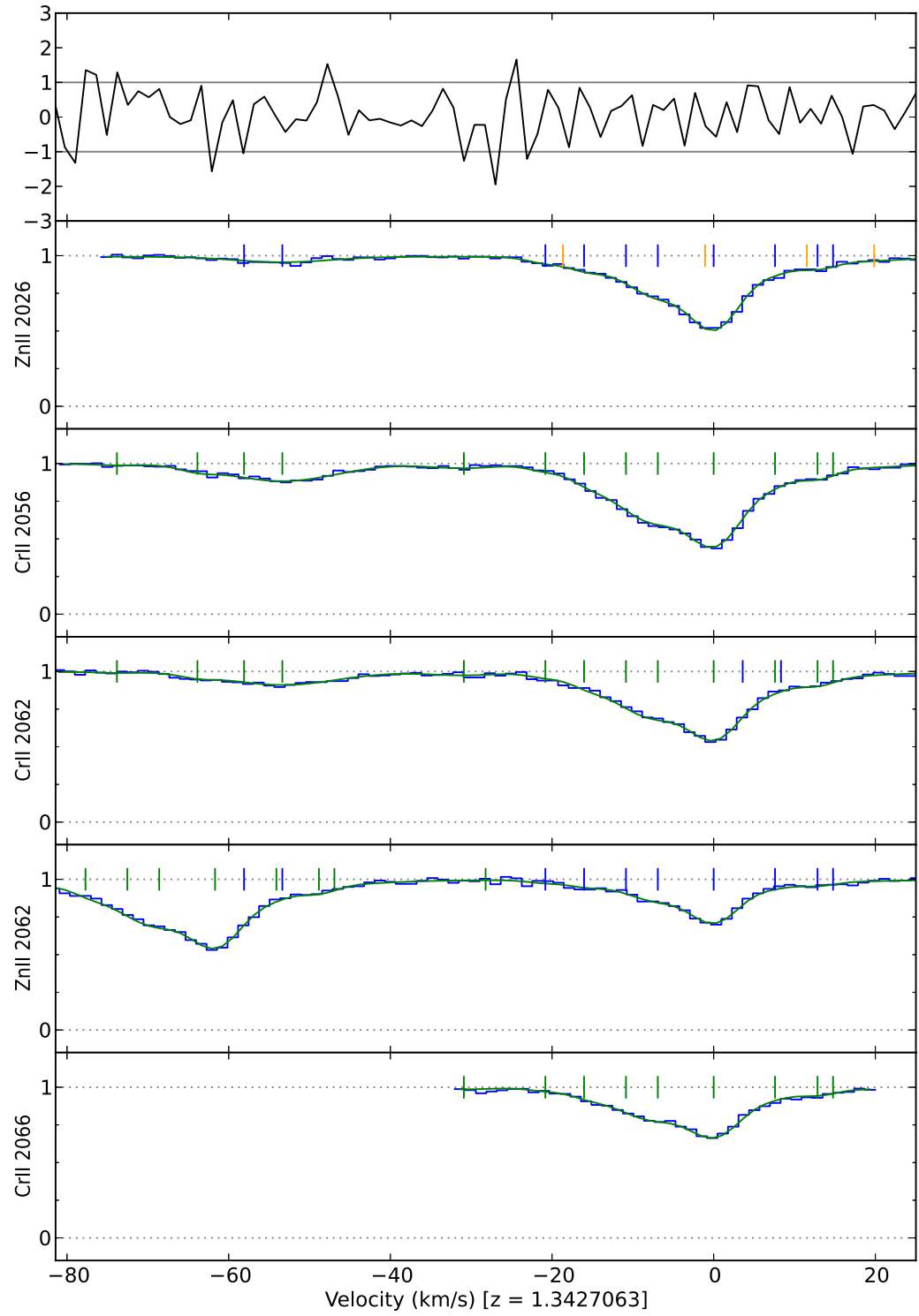


Figure 3.5: Data and model fit for the J0841+0312 HIRES spectrum Zn II and Cr II transitions, centred at $z_{\text{abs}} = 1.023$.

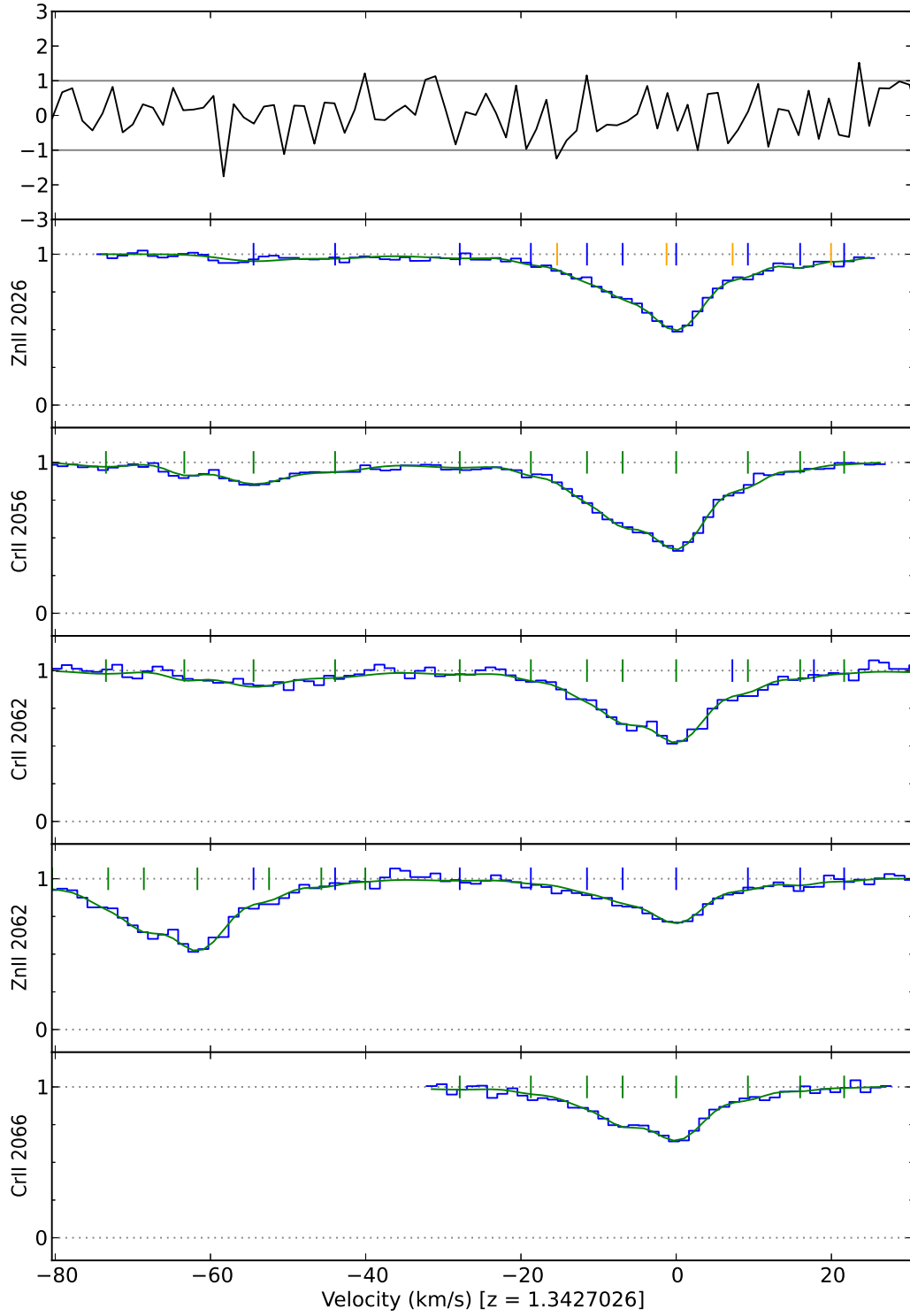


Figure 3.6: Data and model fit for the J0841+0312 UVES spectrum Zn II and Cr II transitions, centred at $z_{\text{abs}} = 1.343$.

3.2.2.5 J1029+1039

The J1029+1039 $z_{\text{abs}} = 1.622$ absorber extends over approximately 250 km s^{-1} . The HIRES spectrum shows a strong, extended and complex velocity structure, as plotted in Figure 3.7. The blending of the Zn II 2026 transition by Mg I 2026 extends over the whole of the Zn II 2026 absorption. Modelling both Zn II 2062 and Mg I 2852 allows this complex blending structure to be successfully resolved.

Two velocity components present in Cr II could not be justified in Zn II (see Table 3.7). In the case of the redder component, at approximately 170 km s^{-1} , this is due to the weakness of absorption at that velocity, and given the data SNR, one cannot be confident that it is even truly present in Cr II. The effect of such shallow absorption on the $\Delta\alpha/\alpha$ constraint is minimal.

The bluer Zn II velocity component, at approximately 50 km s^{-1} , present in Cr II, was consistently removed by VPFIT optimisation, most likely due to how relatively weak it would have to be, and especially because the Zn II and Cr II largely overlap in this extended absorption system. Given the relatively low SNR for this spectrum, the overlapping components are somewhat degenerate with each other. Essentially, the Cr II velocity model easily incorporates the weak, blended structure of the Zn II transitions. The effect of these slight differences between the Zn II and Cr II parameters on $\Delta\alpha/\alpha$ has to be minimal, as most of the constraining power lies in the strong and sharp features at 0 and 70 km s^{-1} . As a potential, but not entirely necessary solution, one could remove velocity components to simplify the fit, effectively giving greater weight to the individual components, especially as the CRS is suggestive of an over-fit model. In this situation one has to weigh the benefits of perfect consistency and the dangers of potentially under-fitting the very complex velocity structure of this absorber.

The normalised chi-squared is consistent with the CRS, with a value of $\chi^2_\nu = 0.69$ (where $\chi^2 = 595.984$ and $\nu = 861$). This lower χ^2_ν may indicate some degree of over-fitting, but it is not very different to the χ^2_ν found for other HIRES fits. Note that this absorber has the second largest error in the $\Delta\alpha/\alpha$ parameter, as shown in the following results chapter. This is likely a result of the absorption profile being relatively ‘smooth’. The high degree of blending between the Zn II and Cr II lines is also a contributing factor. It is worth stressing that over-fitting low SNR data increases the errors on the parameters via degeneracies between

adjacent components, but ensures that the model is not under-fit, which would lead to spurious $\Delta\alpha/\alpha$ measurements. The effects of over-fitting have been considered most explicitly in Murphy et al. (2008b) and Murphy et al. (2008a), where it was shown that by over-fitting one only gets a somewhat larger error on $\Delta\alpha/\alpha$ than is optimal (at most greater by 10%), but one does not introduce a spurious shift to $\Delta\alpha/\alpha$.

Table 3.7: Fiducial fit Zn II and Cr II absorption line parameters and $1\text{-}\sigma$ statistical uncertainties for the J1029+1039 spectrum.

	z_{abs}	b [km s ⁻¹]	$\log N(\text{Cr II})$ [cm ⁻²]	$\log N(\text{Zn II})$ [cm ⁻²]
a	1.6213470(3128)	8.00(3079)	11.38(289)	11.45(254)
b	1.6213937(121)	4.10(214)	12.38(24)	11.68(100)
c	1.6214610(148)	3.31(329)	12.23(70)	11.86(66)
d	1.6215612(1032)	6.74(1205)	12.88(115)	12.44(119)
e	1.6216212(279)	4.88(252)	12.42(2884)	12.68(553)
f	1.6216484(3799)	5.31(2256)	13.00(692)	12.51(753)
g	1.6217260(69)	2.80(232)	12.56(58)	12.39(37)
h	1.6217695(110)	1.09(305)	12.34(53)	11.79(95)
i	1.6218039(252)	2.75(421)	12.30(77)	11.98(64)
j	1.6218874(162)	8.11(394)	12.71(19)	12.22(19)
k	1.6219981(115)	2.82(300)	12.08(32)	11.45(40)
l	1.6220529(128)	1.17(525)	11.85(34)	
m	1.6221678(487)	9.60(1038)	12.31(151)	11.54(426)
n	1.6222479(2100)	13.59(1545)	12.36(142)	12.15(112)
o	1.6223086(28)	0.50(92)	12.17(23)	11.80(26)
p	1.6224189(161)	8.02(182)	12.42(19)	12.10(21)
q	1.6226340(134)	2.50(344)	11.65(23)	10.29(95)
r	1.6227222(78)	2.97(183)	11.38(36)	11.30(11)
s	1.6229935(103)	0.50(844)	11.48(37)	10.81(40)
t	1.6230813(73)	0.50(386)	11.60(34)	11.16(41)
u	1.6231176(125)	0.50(693)	11.71(41)	
v	1.6232013(52)	4.42(107)	12.13(8)	11.50(7)

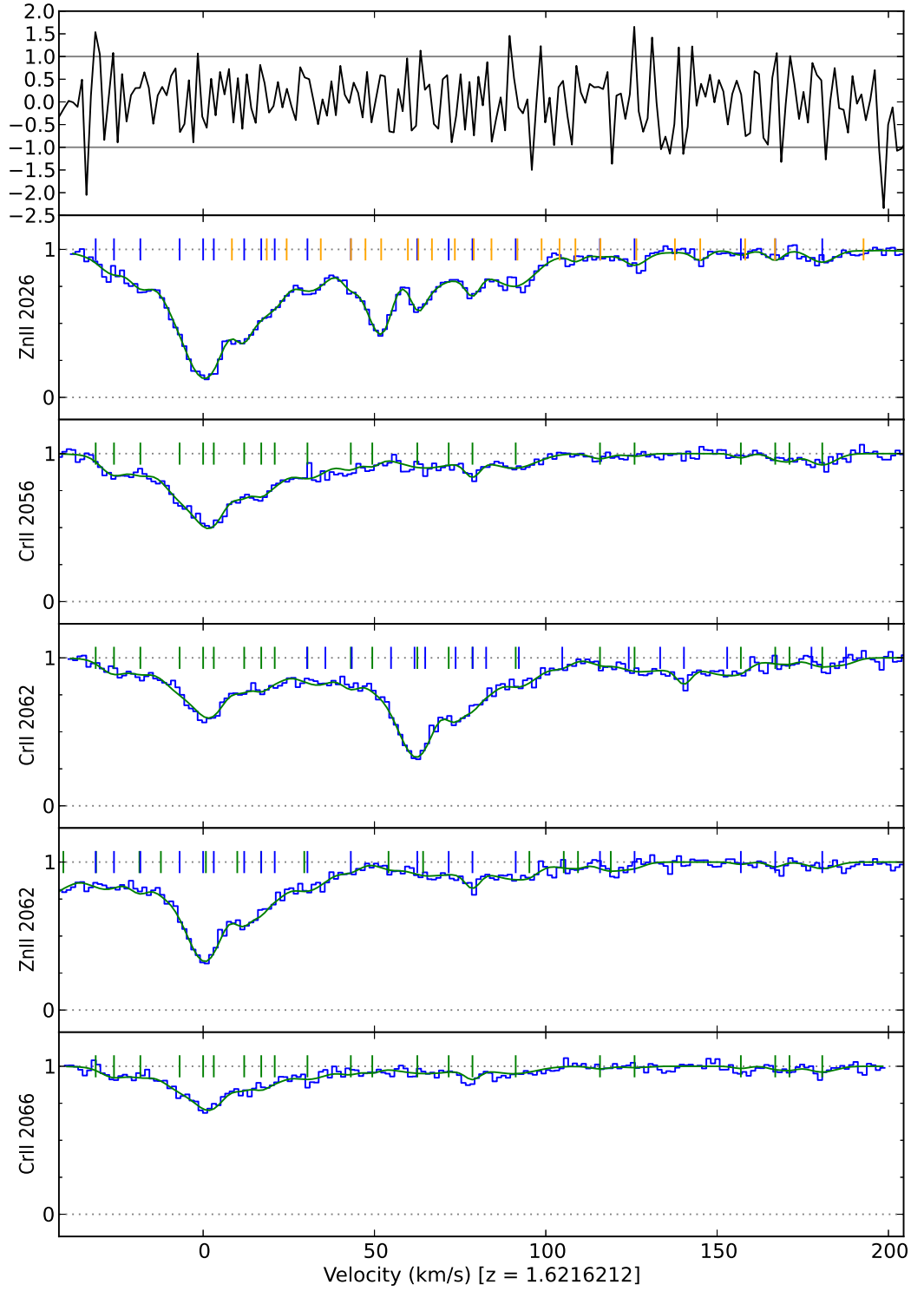


Figure 3.7: Data and model fit for the J1029+1039 HIRES spectrum Zn II and Cr II transitions, centred at $z_{\text{abs}} = 1.622$.

3.2.2.6 PHL957

The PHL957 $z_{\text{abs}} = 2.309$ absorber extends over approximately 70 km s^{-1} , with the bulk of the absorption within a 30 km s^{-1} range. Both HIRES and UVES data are in the absorber sample. While it is one of the structurally simpler absorption systems in the sample (see Figure 3.8 or Figure 3.9), PHL957’s brightness ($m_v = 16.57$) allows for high SNR to be achieved with short exposures. It also has the highest absorption redshift of the sample ($z_{\text{abs}} = 2.309$). Unfortunately this high redshift means no observations of the Mg I 2852 transition are available⁶ for constraining the blend with Zn II. Fortunately the bulk of the absorption lies in a relatively narrow 30 km s^{-1} window, and there is no evidence that Mg I 2026 extends over Zn II 2062, hence the Zn II regions are trimmed on the red side.

The UVES and HIRES fits are structurally consistent (see Table 3.8 and Table 3.9). The lack of the red-most velocity components in Zn II is easily explained by the above-mentioned trimming of the Zn II regions.

Neither CRS (top panels of Figure 3.8 and Figure 3.9) suggest unfit velocity structure. The HIRES model’s normalised chi-squared value is $\chi^2_\nu = 0.98$ (where $\chi^2 = 208.6585$ and $\nu = 214$). The UVES model’s normalised chi-squared value is $\chi^2_\nu = 1.38$ (where $\chi^2 = 129.43$ and $\nu = 94$). Again, the UVES χ^2_ν is consistently higher than for the HIRES data and model.

Table 3.8: Fiducial fit Zn II and Cr II absorption line parameters and $1\text{-}\sigma$ statistical uncertainties for the PHL957 HIRES spectrum.

	z_{abs}	b [km s^{-1}]	$\log N(\text{Cr II})$ [cm^{-2}]	$\log N(\text{Zn II})$ [cm^{-2}]
a	2.3089730(169)	3.25(84)	12.58(38)	11.70(33)
b	2.3090403(94)	4.20(187)	13.03(18)	12.06(20)
c	2.3090991(60)	0.50(58)	12.27(23)	11.19(34)
d	2.3091670(34)	4.35(48)	12.90(6)	11.90(13)
e	2.3092891(1086)	14.14(2742)	11.87(102)	11.47(79)
f	2.3094807(222)	12.00(249)	12.24(18)	
g	2.3097223(97)	0.50(672)	11.38(19)	

⁶In the case of UVES data, the Mg I 2852 transition is within the range of the observed wavelengths, however it is strongly overlapped by telluric absorption lines. For HIRES, it was not observed because the atmospheric interference reduces the usefulness of observing that region of the spectrum.

Table 3.9: Fiducial fit Zn II and Cr II absorption line parameters and 1- σ statistical uncertainties for the PHL957 UVES spectrum.

	z_{abs}	b [km s ⁻¹]	$\log N(\text{Cr II})$ [cm ⁻²]	$\log N(\text{Zn II})$ [cm ⁻²]
a	2.3089836(292)	2.97(154)	12.72(61)	11.74(67)
b	2.3090528(176)	4.00(469)	13.01(46)	12.08(43)
c	2.3091286(128)	2.08(393)	12.49(87)	11.32(143)
d	2.3091818(176)	3.14(169)	12.71(32)	11.83(28)
e	2.3093172(735)	13.03(3114)	12.22(102)	11.40(93)
f	2.3094871(505)	7.59(585)	11.84(129)	

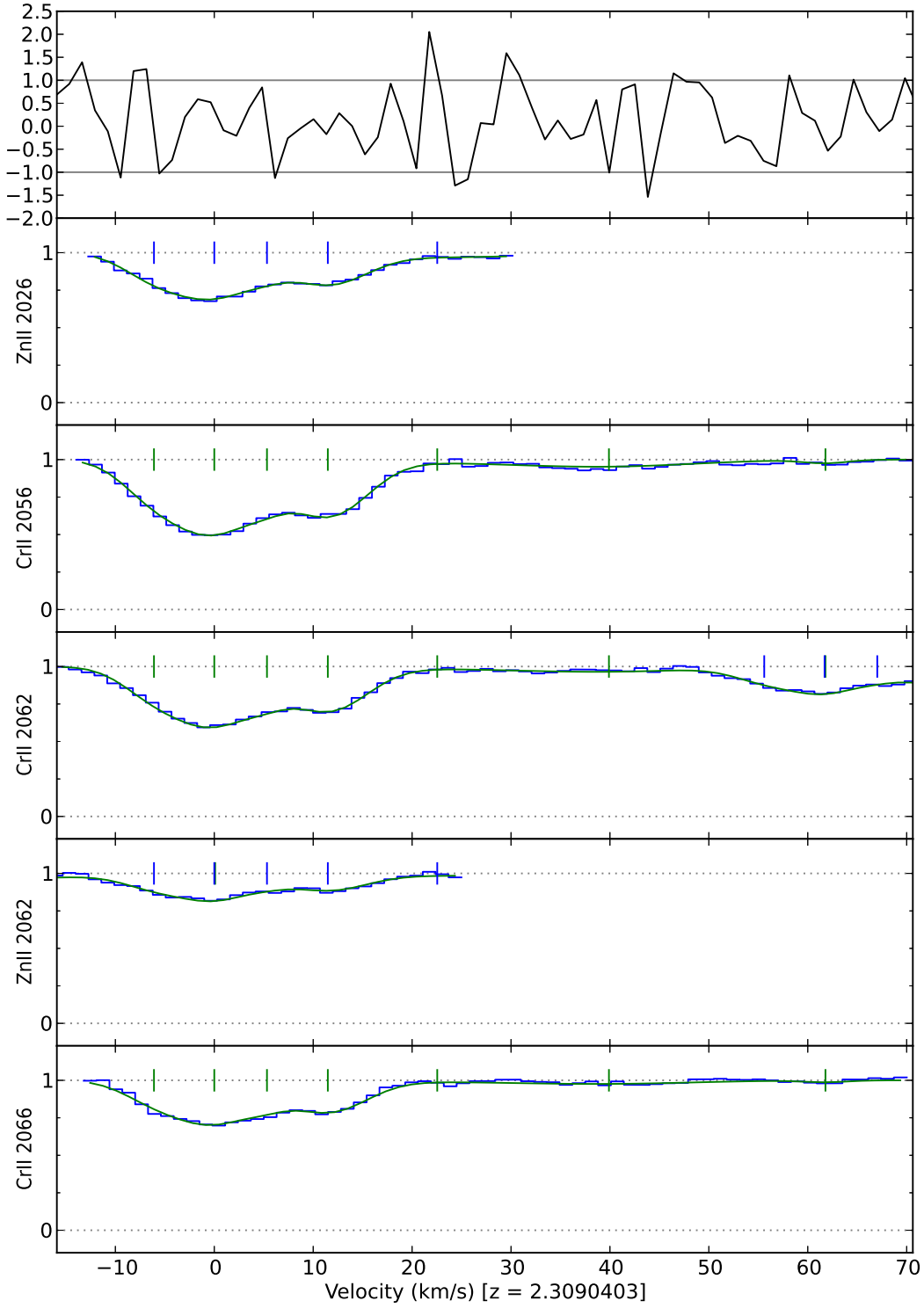


Figure 3.8: Data and model fit for the PHL957 HIRES spectrum Zn II and Cr II transitions, centred at $z_{\text{abs}} = 2.309$.

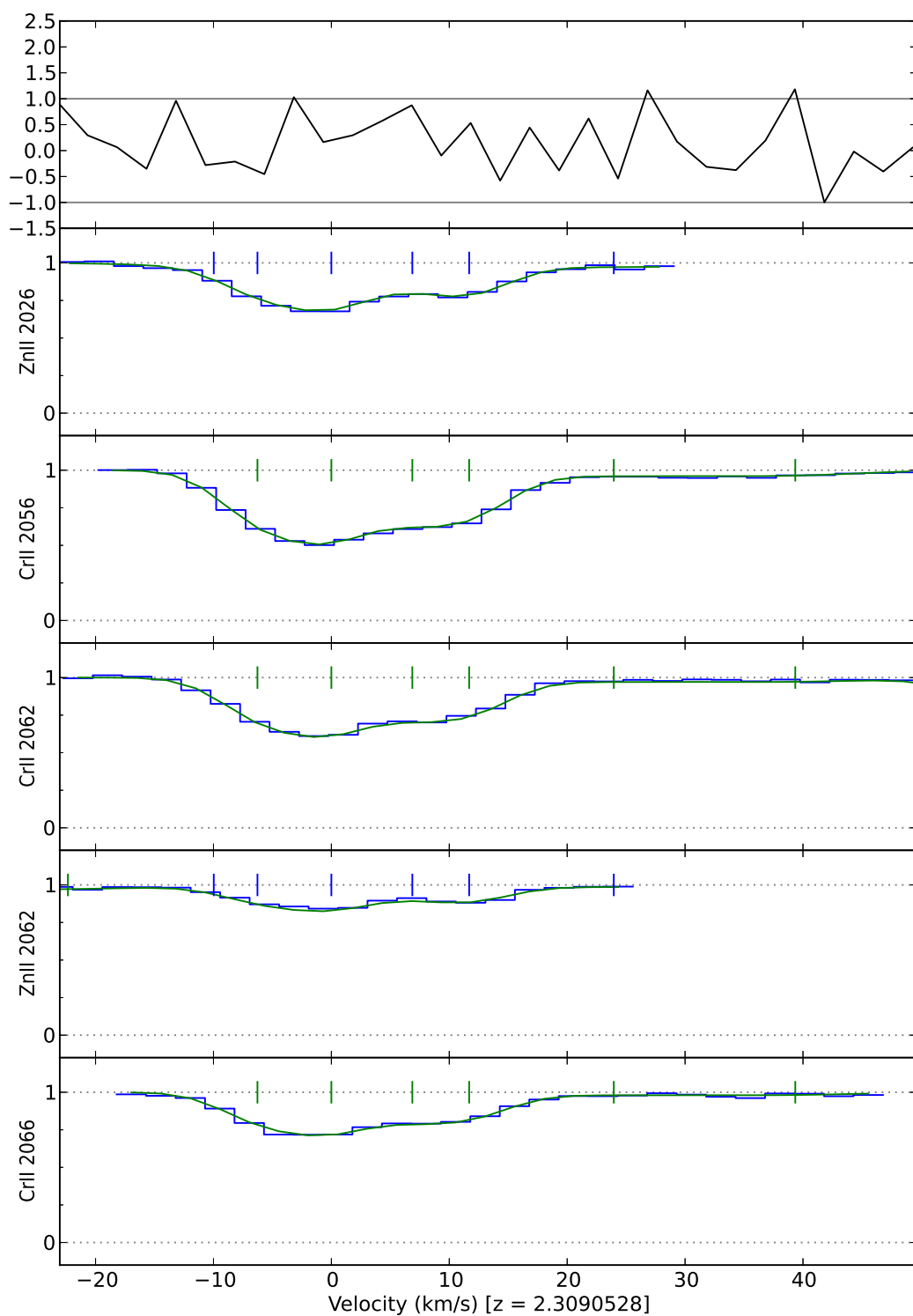


Figure 3.9: Data and model fit for the PHL957 UVES spectrum Zn II and Cr II transitions, centred at $z_{\text{abs}} = 2.309$.

3.2.2.7 Q1755+57

The Q1755+57 $z_{\text{abs}} = 1.971$ absorber extends over approximately 400 km s^{-1} . The HIRES spectrum shows a strong, incredibly complex velocity structure, as plotted in Figure 3.10, making this absorber suitable for constraining $\Delta\alpha/\alpha$ even at lower SNR (given that $m_r = 18.3$). The velocity structure features multiple absorption peaks and these were modelled with the most complex fit in the whole sample (see Table 3.10)

The blending of the Zn II 2026 transition by Mg I 2026 extends over the whole of the Zn II 2026 absorption, and is quite significant. The absorption feature blending with Zn II 2026 at approximately -130 km s^{-1} , for example, is entirely due to the Mg I transition. Because the Mg I 2852 absorption was in part saturated, its structure was also strongly constrained by Mg I 2026. Modelling both Zn II 2062 and Mg I 2852 with a suitably complex fit was essential to reducing any potential systematic modelling errors on $\Delta\alpha/\alpha$.

Three components present in Cr II could not be justified in Zn II for similar reasons as in the case of another strong, complex absorber, J1029+1039 (see Section 3.2.2.5), i.e. due to the weakness of Zn II absorption at that velocity and its heavy overlap with Cr II and Mg I.

The CRS in Figure 3.10 does not suggest unfit velocity structure. The normalised chi-squared value of $\chi_\nu^2 = 0.86$ (where $\chi^2 = 1337.80$ and $\nu = 1548$) is consistent with the CRS.

Table 3.10: Fiducial fit Zn II and Cr II absorption line parameters and 1- σ statistical uncertainties for the Q1755+57 spectrum.

	z_{abs}	b [km s ⁻¹]	$\log N(\text{Cr II})$ [cm ⁻²]	$\log N(\text{Zn II})$ [cm ⁻²]
a	1.9690122(505)	6.10(530)	12.05(37)	11.48(44)
b	1.9690762(49)	1.81(165)	11.78(140)	11.75(20)
c	1.9691217(683)	3.83(1200)	11.95(103)	
d	1.9692007(25)	0.50(19)	12.28(38)	14.69(43)
e	1.9692216(141)	5.98(137)	12.87(5)	12.59(14)
f	1.9693235(97)	2.92(196)	12.27(25)	11.93(26)
g	1.9694047(80)	1.17(358)	11.89(19)	11.58(11)
h	1.9694639(165)	0.73(771)	11.62(25)	11.20(23)
i	1.9695458(138)	1.76(463)	11.38(43)	11.06(23)
j	1.9696410(99)	1.02(392)	11.63(22)	11.26(24)
k	1.9701772(102)	0.67(599)	11.79(24)	10.64(48)
l	1.9703221(296)	9.11(381)	12.18(20)	11.53(18)
m	1.9703669(137)	0.50(863)	11.71(46)	10.77(54)
n	1.9704773(56)	0.50(136)	11.80(20)	11.51(36)
o	1.9705473(55)	0.50(158)	12.09(28)	11.57(51)
p	1.9706126(121)	1.27(269)	12.00(32)	11.80(15)
q	1.9706629(133)	1.55(344)	12.21(45)	11.78(36)
r	1.9707318(268)	4.36(614)	12.49(65)	11.88(82)
s	1.9707985(437)	4.65(910)	12.00(229)	11.73(129)
t	1.9708736(166)	4.07(409)	12.46(42)	11.69(72)
u	1.9709456(126)	3.33(167)	12.55(22)	12.27(21)
v	1.9710233(40)	3.77(62)	13.08(6)	12.92(5)
w	1.9711123(119)	1.67(138)	12.79(28)	12.37(23)
x	1.9711587(115)	2.09(208)	12.88(28)	12.36(36)
y	1.9712199(76)	4.46(185)	12.92(69)	12.70(45)
z	1.9712878(1724)	8.09(1871)	12.67(140)	12.21(150)
ba	1.9714335(67)	5.02(145)	12.74(19)	12.51(13)
bb	1.9715178(131)	2.62(265)	12.55(31)	11.90(58)
bc	1.9715715(48)	2.43(98)	12.70(61)	12.85(18)
bd	1.9716134(376)	3.14(512)	12.58(68)	12.15(86)
be	1.9716939(66)	3.00(152)	12.57(46)	12.34(29)
bf	1.9717686(957)	9.99(1762)	12.61(78)	12.14(80)
bg	1.9719254(374)	4.39(429)	12.34(64)	11.78(58)
bh	1.9719925(295)	3.86(289)	12.37(46)	11.60(63)
bi	1.9721556(120)	5.45(158)	12.73(12)	12.08(13)

Continued on next page

Table 3.10: *Continued from previous page*

	z_{abs}	b [km s ⁻¹]	$\log N(\text{Cr II})$ [cm ⁻²]	$\log N(\text{Zn II})$ [cm ⁻²]
bj	1.9722478(56)	4.30(58)	12.86(8)	12.31(7)
bk	1.9723465(95)	0.86(446)	11.94(14)	
bl	1.9724388(354)	3.19(604)	12.11(153)	10.88(259)
bm	1.9725024(1040)	5.92(886)	12.33(95)	11.39(78)
bn	1.9726829(188)	5.33(346)	11.99(18)	
bo	1.9728587(207)	4.26(398)	11.85(22)	10.32(105)
bp	1.9729591(86)	0.65(468)	11.96(27)	10.97(82)
bq	1.9730092(219)	5.27(233)	12.23(22)	11.73(20)
br	1.9731766(86)	7.06(140)	12.43(7)	11.60(8)

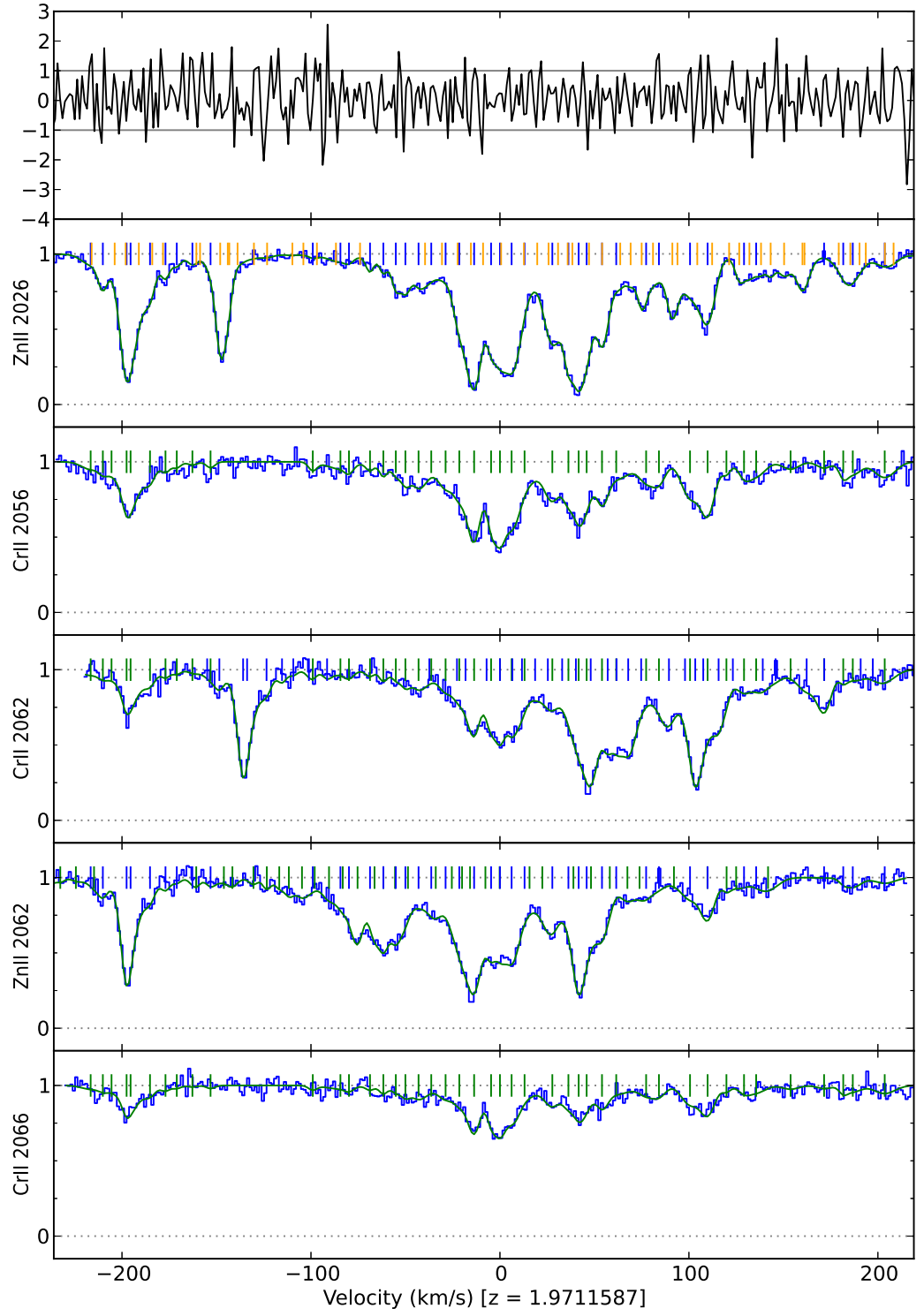


Figure 3.10: Data and model fit for the Q1755+57 HIRES spectrum Zn II and Cr II transitions, centred at $z_{\text{abs}} = 1.971$.

3.2.2.8 Q2206–1958

The Q2206–1958 $z_{\text{abs}} = 1.921$ absorber extends over approximately 190 km s^{-1} . The UVES spectrum shows this to be a relatively weak absorber, with two main absorption features at 0 and 60 km s^{-1} , as plotted in Figure 3.11. The weak blending by Mg I 2026 (constrained by the observed Mg I 2852 line) extends over most of the Zn II 2026 absorption. The same number of Zn II and Cr II components were fit.

The CRS in Figure 3.11 does not suggest unfit velocity structure and the fit has a normalised chi-squared value of $\chi^2_\nu = 1.08$ (where $\chi^2 = 344.36$ and $\nu = 320$).

Table 3.11: Fiducial fit Zn II and Cr II absorption line parameters and $1\text{-}\sigma$ statistical uncertainties for the Q2206–1958 spectrum.

	z_{abs}	b [km s^{-1}]	$\log N(\text{Cr II})$ [cm^{-2}]	$\log N(\text{Zn II})$ [cm^{-2}]
a	1.9197186(133)	0.50(1096)	11.39(33)	10.77(42)
b	1.9199065(649)	9.57(559)	12.48(38)	11.66(39)
c	1.9200016(41)	5.13(77)	12.88(15)	12.10(14)
d	1.9201855(100)	13.08(282)	12.52(7)	11.88(7)
e	1.9203912(40)	4.66(88)	12.43(7)	11.66(8)
f	1.9206040(70)	13.45(138)	13.15(4)	12.39(4)
g	1.9206961(45)	0.50(52)	12.30(15)	11.36(16)
h	1.9207943(107)	4.26(217)	12.30(27)	11.60(23)
i	1.9209036(148)	7.14(347)	12.47(26)	11.63(32)
j	1.9210697(314)	13.19(469)	12.54(17)	11.85(15)
k	1.9213018(220)	5.44(414)	11.75(25)	10.81(36)

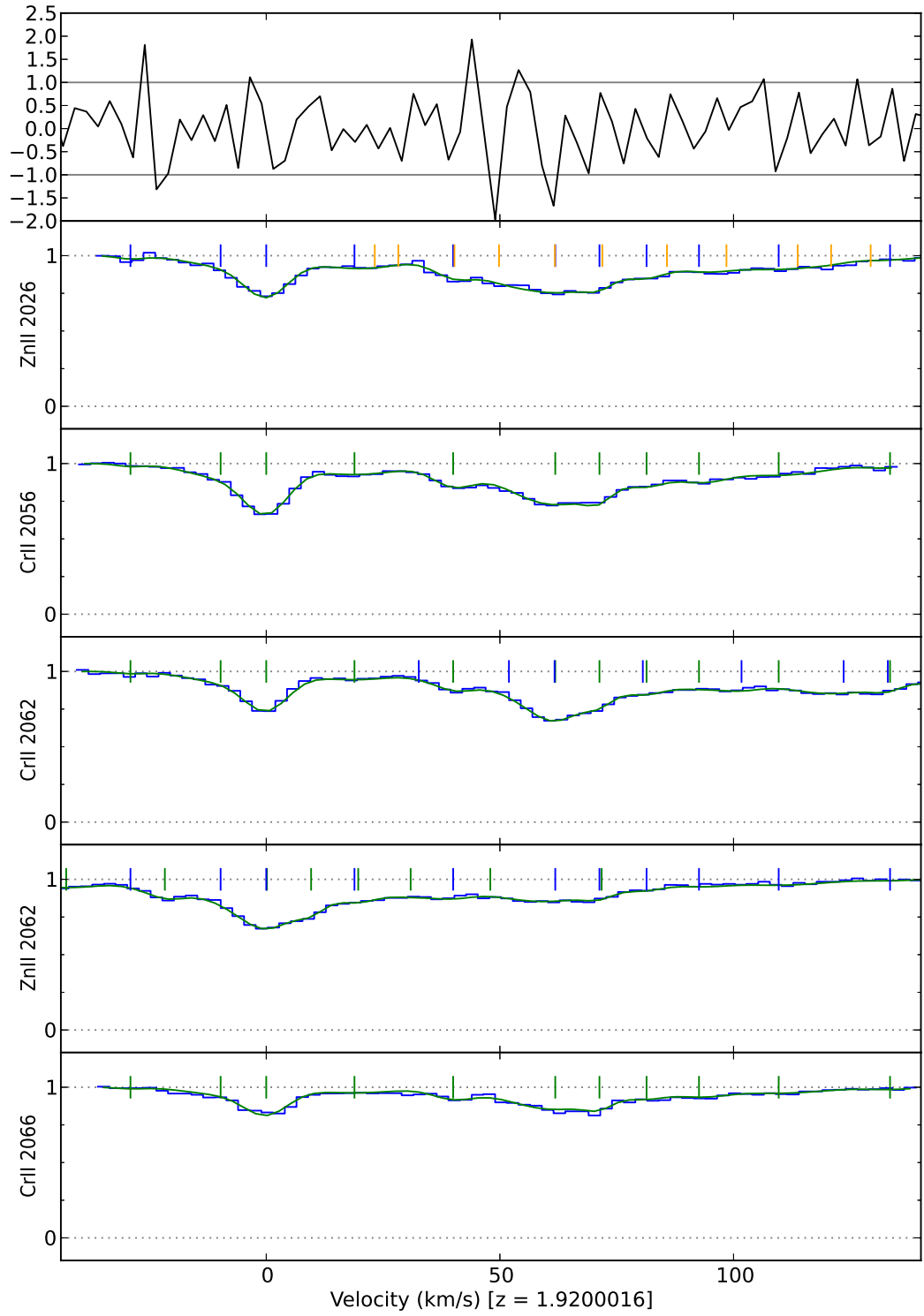


Figure 3.11: Data and model fit for the Q2206–1958 UVES spectrum Zn II and Cr II transitions, centred at $z_{\text{abs}} = 1.920$.

3.2.2.9 J1237+0106

The J1237+0106 $z_{\text{abs}} = 1.305$ absorber extends over approximately 200 km s^{-1} . The HIRES spectrum in Figure 3.12 shows it to be an extended, moderately weak (within the context of the sample), but a complex absorption system, with two major absorption peaks at approximately -20 and 140 km s^{-1} . The Mg I 2026 transition blend (constrained by the observed Mg I 2852 line) extends over most of the Zn II 2026 absorption.

The CRS in Figure 3.12 suggests no unfit structure, with a normalised chi-squared value of $\chi^2_\nu = 0.73$ (where $\chi^2 = 594.31$ and $\nu = 810$). However, the model deviates from the data over numerous successive pixels in regions of Cr II 2062 and 2066 transitions at 60 , 90 and $\sim 140 \text{ km s}^{-1}$. This inconsistency could not be successfully removed with more complex models and it is concluded that the spectra may be spurious in those regions. Therefore the J1237+0106 absorber is excluded from final analysis and the $\Delta\alpha/\alpha$ sample.

Table 3.12: Fiducial fit Zn II and Cr II absorption line parameters and 1- σ statistical uncertainties for the J1237+0106 spectrum.

	z_{abs}	b [km s ⁻¹]	$\log N(\text{Cr II})$ [cm ⁻²]	$\log N(\text{Zn II})$ [cm ⁻²]
a	1.3044282(100)	0.50(874)	11.21(45)	10.97(55)
b	1.3045403(44)	8.30(110)	12.41(5)	11.94(4)
c	1.3046932(59)	4.38(76)	12.62(11)	12.39(8)
d	1.3047356(108)	2.68(318)	12.19(54)	11.23(175)
e	1.3047759(165)	2.97(350)	11.99(61)	11.59(39)
f	1.3048652(27)	5.29(70)	13.11(4)	12.32(6)
g	1.3049348(97)	3.14(184)	12.49(41)	12.09(28)
h	1.3049858(231)	3.48(579)	12.53(93)	11.88(117)
i	1.3050286(224)	3.49(465)	12.55(79)	12.07(66)
j	1.3050695(98)	0.51(63)	12.44(22)	11.67(41)
k	1.3051084(117)	2.28(364)	12.23(29)	11.44(32)
l	1.3051624(82)	0.50(165)	12.12(32)	
m	1.3052204(93)	5.18(249)	12.54(19)	10.51(298)
n	1.3053114(62)	6.30(223)	12.76(14)	11.86(11)
o	1.3053722(86)	0.50(286)	11.96(35)	
p	1.3054386(75)	7.00(304)	12.67(15)	11.75(15)
q	1.3055062(62)	0.50(59)	12.39(21)	11.13(27)
r	1.3055532(93)	2.99(369)	12.42(70)	11.46(84)
s	1.3056352(434)	7.74(1590)	12.81(84)	11.96(82)
t	1.3056729(75)	0.52(71)	12.62(24)	11.48(54)
u	1.3057055(70)	1.36(157)	12.78(38)	11.81(42)
v	1.3057423(308)	4.45(652)	12.72(77)	11.69(92)
w	1.3058303(440)	5.92(1456)	12.48(114)	11.67(99)
x	1.3058785(247)	2.82(600)	12.18(191)	10.90(452)
y	1.3059270(244)	4.12(873)	12.46(101)	11.51(90)
z	1.3059851(549)	4.36(502)	12.30(91)	11.30(94)

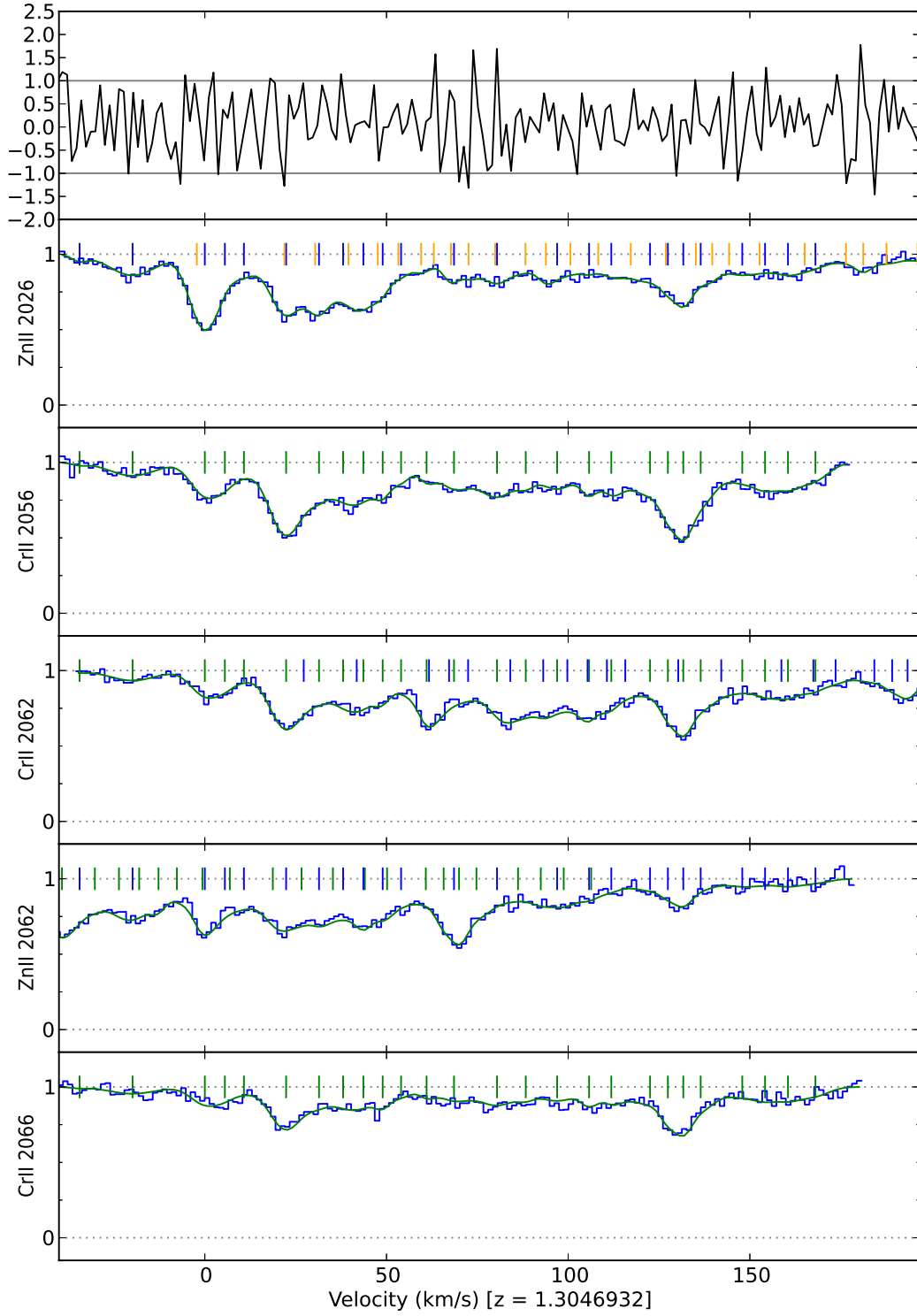


Figure 3.12: Data and model fit for the J1237+0106 HIRES spectrum Zn II and Cr II transitions, centred at $z_{\text{abs}} = 1.305$.

3.3 Results

The fiducial $\Delta\alpha/\alpha$ values obtained as a result of the χ^2 minimisation described in Section 3.2.1.2 are presented in Table 3.13 and plotted in Figure 3.13. The results for J0058+0051 (UVES) and J1237–0106 (UVES) could not be reliably obtained and are omitted, as discussed in Section 3.2.2.1 and Section 3.2.2.9.

Inspection of the individual results reveals no significant deviations away from a zero $\Delta\alpha/\alpha$ (with the exception of J0108–0037, which deviates negatively from a null $\Delta\alpha/\alpha$ with $2\text{-}\sigma$ significance). This is the case even though none of results are corrected for any types of systematic error and their error bars are only statistical. The statistical errors in this work range from approximately 4 to 10×10^{-6} , with a mean error of 6.6×10^{-6} . This can be compared to the large combined HIRES and VLT sample of 295 absorbers in King et al. (2012), which includes the Keck sample of results from Murphy et al. (2004). Here the errors range from approximately 2 to 160×10^{-6} , with a mean error of 21×10^{-6} (and a median of 15×10^{-6} , which may be more representative of such a large sample). For Evans et al. (2014) who studied the same 3 absorbers along one QSO line of sight with 3 different telescopes (Keck, VLT and Subaru), the errors range from approximately 2.5 to 24×10^{-6} , with a mean error of 8.5×10^{-6} . The individual constraints presented here are therefore highly competitive with full many-multiplet constraints.

The weighted mean and $1\text{-}\sigma$ statistical error of the 10 measurements obtained is

$$\Delta\alpha/\alpha = (0.04 \pm 1.69_{\text{stat}}) \times 10^{-6}. \quad (3.1)$$

The weighted mean uses $1/\sigma_i^2$ weights, where σ_i is the $1\text{-}\sigma$ statistical error for the individual measurements. The unweighted mean is $(-0.36 \pm 2.03) \times 10^{-6}$. The two estimates are consistent with each other. Note that the statistical error derives only from the photon statistics in the individual spectra and not from systematic errors (which are considered in Section 3.4). The sample mean and error show no evidence for variation in α at a statistical precision of under 2 parts per million (ppm). The final result, with the systematic error component, is presented in Section 3.5.1 and comparison with other measurements in the literature is presented in Section 3.5.3.

By splitting the results into two subsamples, Keck/HIRES and VLT/UVES data, and calculating their weighted means and $1\text{-}\sigma$ errors, the following constraints

are obtained,

$$\Delta\alpha/\alpha_{\text{Keck}} = (0.89 \pm 2.27_{\text{stat}}) \times 10^{-6} \quad (3.2)$$

and

$$\Delta\alpha/\alpha_{\text{VLT}} = (-1.01 \pm 2.52_{\text{stat}}) \times 10^{-6}. \quad (3.3)$$

The weighted means are different by 1.9×10^{-6} . This difference is within their individual $1\text{-}\sigma$ errors suggesting the two results are consistent. The similarity in the error values is indicative of the two subsamples having comparable constraining power for $\Delta\alpha/\alpha$.

The error on the weighted mean is calculated using only $1\text{-}\sigma$ errors of the individual measurements and is not reflective of the scatter in the sample. The root-mean-square deviation from the mean $\Delta\alpha/\alpha$ (RMSD) is representative of the scatter and should be consistent with the mean of the individual errors, $\langle\delta(\Delta\alpha/\alpha)\rangle$. For the full sample (error of 1.69×10^{-6}), $\text{RMSD} = 6.07$ and $\langle\delta(\Delta\alpha/\alpha)\rangle = 6.57$, suggesting no inconsistency. The χ^2_ν value around the weighed mean is 1.44. This corresponds to a (left-tail) probability of 84%, confirming the observed scatter in the $\Delta\alpha/\alpha$ values of the full sample is not unexpected. For the Keck subsample (error of 2.27×10^{-6}), $\text{RMSD} = 3.13$ and $\langle\delta(\Delta\alpha/\alpha)\rangle = 6.03$, indicating little scatter in the results, reflected also in its χ^2_ν of 0.47 (probability of 24%). For the VLT subsample (error of 2.52×10^{-6}), $\text{RMSD} = 7.99$ and $\langle\delta(\Delta\alpha/\alpha)\rangle = 7.10$, with a χ^2_ν of 2.70 (probability of 97%). This latter result may indicate some evidence for additional scatter, beyond that expected from the individual errors, in the VLT sample, though that evidence is not highly significant (the 97% probability corresponds to $2.2\text{-}\sigma$ significance).

In the two cases where constraints are available from both Keck and VLT telescopes (J0841+0312 and PHL957) the $\Delta\alpha/\alpha$ results are consistent with each other within their $1\text{-}\sigma$ errors. The analysis of 3 absorbers in the same line of sight with 3 telescopes, including Keck and VLT, in Evans et al. (2014), also found consistency at the $1\text{-}\sigma$ level (after detecting and removing long-range wavelength scale distortions). In the large samples of King et al. (2012) and Murphy et al. (2004) there were 7 absorbers with data from both Keck and VLT – again, with the same consistency.

Table 3.13: The fiducial $\Delta\alpha/\alpha$ values obtained as a result of the χ^2 minimisation described in Section 3.2.1.2. The columns are: the object name, marked with superscript H for Keck/HIRES data and U for VLT/UVES data; the absorption redshift z_{abs} ; the $\Delta\alpha/\alpha$ result with $1\text{-}\sigma$ statistical error; and the model fit normalised chi-squared value χ^2_ν . The results for J0058+0051^U and J1237–0106^U could not be reliably obtained and are omitted, as discussed in Section 3.2.2.1 and Section 3.2.2.9. The results in this table are plotted in Figure 3.13.

Object	z_{abs}	$\Delta\alpha/\alpha$ [10^{-6}]			χ^2_ν
J0058+0051 ^H	1.072	−1.063	±	6.609	0.91
J0108–0037 ^U	1.371	−10.380	±	4.632	1.17
J0226–2857 ^U	1.023	10.732	±	6.903	1.27
J0841+0312 ^H	1.342	1.507	±	3.668	0.79
J0841+0312 ^U	1.342	5.466	±	4.149	1.02
J1029+1039 ^H	1.622	−2.485	±	10.088	0.69
PHL957 ^H	2.309	−4.233	±	5.475	0.97
PHL957 ^U	2.309	0.311	±	13.716	1.38
Q1755+57 ^H	1.971	4.687	±	4.325	0.86
Q2206–1958 ^U	1.921	−8.184	±	6.110	1.08

3.4 Systematic error analysis

What follows in this section is a simple and preliminary systematic error analysis of the results presented in Section 3.3. Wavelength calibration errors are considered, followed by an investigation of the effects of the long and short-range wavelength distortions found in UVES and HIRES spectra (Whitmore and Murphy, 2015; Griest et al., 2010; Whitmore et al., 2010).

3.4.1 ThAr wavelength calibration errors

Because the $\Delta\alpha/\alpha$ constraint is sensitive to velocity shifts between the subset of transitions fit, distortions in the wavelength scale due to errors in the ThAr calibration process are a source of systematic error. Inspection of the wavelength scale

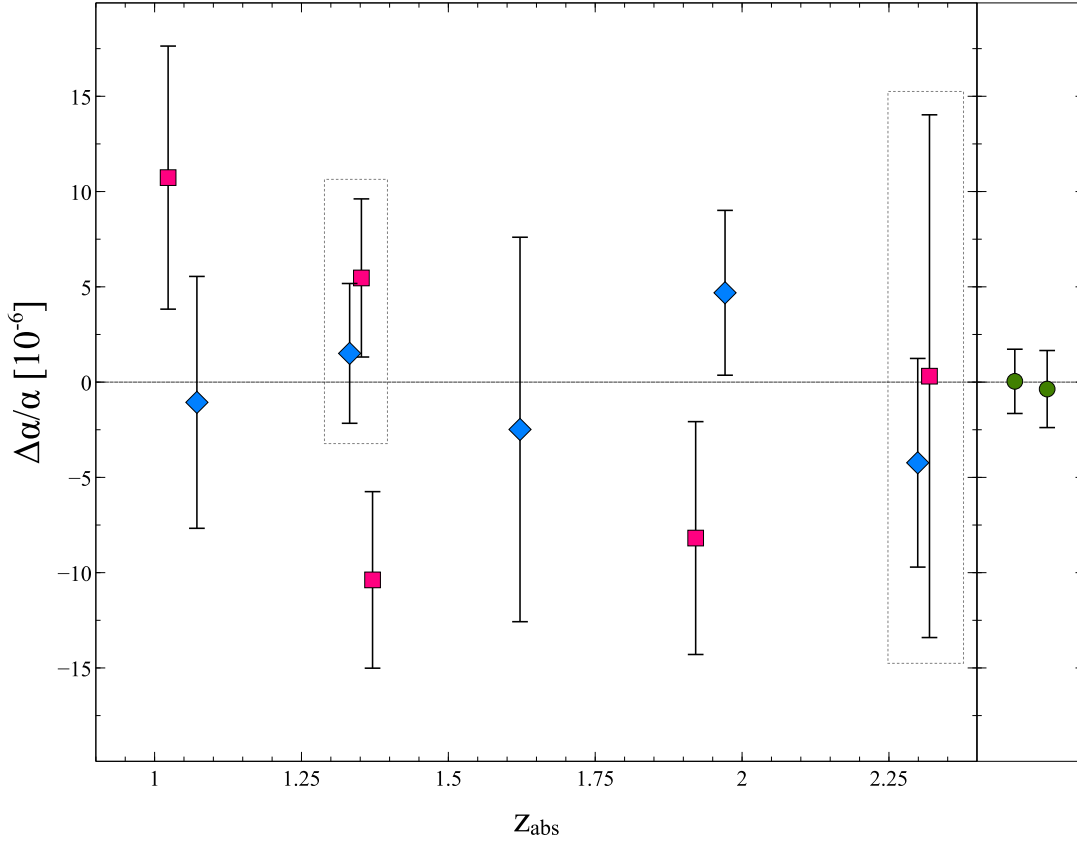


Figure 3.13: Plot of fiducial $\Delta\alpha/\alpha$ results as presented in Table 3.13 vs. z_{abs} , the absorption redshift. *Left:* the HIRES $\Delta\alpha/\alpha$ results rendered as blue diamonds, the UVES $\Delta\alpha/\alpha$ results as fuchsia squares and the error bars are their statistical 1- σ errors. The double data points enclosed by dotted rectangles are results from the same object, with data from both Keck and VLT telescopes. *Right:* the averaged results. The left point is the weighted mean of the $\Delta\alpha/\alpha$ constraints in this sample, $\Delta\alpha/\alpha_w = (0.04 \pm 1.69) \times 10^{-6}$. The right point is the unweighted mean, $\Delta\alpha/\alpha_u = (-0.36 \pm 2.03) \times 10^{-6}$. Both error bars are the 1- σ statistical error.

solution and residuals produced by the calibrating ThAr exposures showed no evidence of structure. The resulting residuals for the spectra used here in the regions where the Zn II and Cr II lines fall are typically $\text{RMS} \sim 30 - 50 \text{ m s}^{-1}$ and are symmetrically distributed around the final wavelength solution at all wavelengths. If the wavelength solution may be imagined to depart by as much as this RMS from the true value, as Murphy et al. (2007) found to be possible in some cases, it corresponds to an approximate systematic error in $\Delta\alpha/\alpha$ of $\pm 0.51 \times 10^{-6}$ *per individual absorber*. Because most of the sample has different absorption redshifts, resulting in the fit Zn II and Cr II transitions falling on different parts of the wavelength scale, the effect on the final fiducial constraint is even less and is considered negligible.

3.4.2 Long-range wavelength distortions

One of the justifying benefits of using the Zn II 2026/2062 and Cr II 2056/2062/2066 subset of transitions is that they are close to each other in wavelength (see Figure 2.1), rendering measurements of $\Delta\alpha/\alpha$ less sensitive to the effects of long-range wavelength calibration errors than for a full fit involving a wide range of transitions. The effect of these distortions of the wavelength scale should be small and can be characterised in a simple fashion, as below.

Assuming the presence of the typical long-range wavelength distortion found in UVES and HIRES spectra of $v_{\text{dist}} \sim \pm 200 \text{ m s}^{-1}$ per 1000 Å (Whitmore and Murphy, 2015), one can estimate the effect on $\Delta\alpha/\alpha$ by considering the two transitions Zn II 2026 and Cr II 2066, which have the greatest separation in wavelength of any in the subset ($\Delta\lambda \sim 40 \text{ Å}$), and also have the greatest difference in q coefficients ($\Delta q = 2920 \text{ cm}^{-1}$). If one assumes the distortion to be a simple linear, monotonic velocity shift the effect on $\Delta\alpha/\alpha$ will be greater when z_{abs} is large. PHL957 has the highest absorption redshift in our sample of $z_{\text{abs}} = 2.309$, which makes for a conservative estimate. Using Equation 1.5, this corresponds to a systematic error in $\Delta\alpha/\alpha$ as a result of long-range distortions in the wavelength scale of $\pm 0.75 \times 10^{-6}$. This is small compared to the 1- σ statistical error in this work (1.92×10^{-6}). It is also expected that this simple estimate is an upper limit to any real effect because the pattern of shifts expected among all Zn II and Cr II transitions if α varies is more complex than a simple linear function (see Figure 2.1). It is therefore con-

cluded that the choice of Zn II and Cr II transitions effectively suppresses the errors from long-range distortions in this work’s sample.

3.4.3 Short-range intra-order wavelength distortions

The methodology used in this project, where only a subset of wavelength-proximate, highly $\Delta\alpha/\alpha$ sensitive transitions are used, was justified by a reduced reaction to long-range wavelength distortions. However, this leaves the measurements here open to another significant source of systematic error – the presence of short-range intra-order wavelength distortions in both the HIRES and UVES spectrographs. These were found by Griest et al. (2010) and Whitmore et al. (2010) by comparing QSO spectra calibrated using the standard ThAr method and those with iodine absorption directly imprinted within the instrumentation.

The distortions are considered in detail in the before-mentioned studies, and can be described as pervasive velocity shift patterns. These are projected on the spectrograph echelle order structure (i.e. each order has a similar pattern of distortion to the adjacent ones) and are clearly an instrumentation-based systematic. The distortions vary in structure from exposure to exposure. While the amplitude of the velocity shifts varies between the instruments, the typical magnitude of distortion is $\sim 300 \text{ ms}^{-1}$ peak-to-peak for both HIRES and UVES instruments. See Section 4.5.2.3 for further discussion of the distortions, as considered for constraining $\Delta\mu/\mu$. The effect on large samples of hundreds of QSO absorbers should be negligible given that different absorbers are at different redshifts and the transitions of interest fall at different positions along echelle orders (i.e. relative to the ‘phase’ of the intra-order distortion pattern). The effect is therefore random and reduces in magnitude as the sample size increases. Nevertheless, for the final sample of 10 spectra in this work, the effect may be important.

Because the source of this systematic error has not yet been fully identified and it may not be possible to correct for its effects, one may only estimate its impact on the $\Delta\alpha/\alpha$ constraint presented here. To do this effectively the echelle structure of the orders has to be considered, along with the location of the fit absorption lines on this structure and the SNR at those wavelengths. This is most directly done by imposing a similar velocity distortion onto the individual exposures during the data reduction stage, for each absorber in the sample, then

re-fitting the fiducial model and re-fitting it again with $\Delta\alpha/\alpha$ as a free parameter. This is done here using a modification of the UVES_POPLER software, where each combined order receives a $\pm 200 \text{ m s}^{-1}$ saw-tooth wavelength distortion (400 m s^{-1} peak-to-peak). The magnitude is greater than the typical $\sim 300 \text{ m s}^{-1}$ peak-to-peak distortion observed in both instruments, allowing a more conservative estimate of the effect it has on $\Delta\alpha/\alpha$. The magnitude of the observed distortion is actually smaller for UVES, but using the same, conservative value allows for comparisons of the effect on absorption data from the different instruments. It is also worth noting that the actual observed distortion structure varies from exposure to exposure, and that here an identical velocity shift pattern is imprinted onto each reduced order – the effect should be amplified in this test, rather than suppressed.

The results of this test are summarised in Table 3.14 as compared to the fiducial results in Table 3.13 and plotted in Figure 3.14.

Table 3.14: The $\Delta\alpha/\alpha_d$ values obtained from artificially distorted spectra simulating short-range intra-order distortions, compared to the fiducial $\Delta\alpha/\alpha$ values. The columns are: the object name, marked with superscript H for Keck/HIRES data and U for VLT/UVES data; the $\Delta\alpha/\alpha_d$ value obtained for the artificially distorted spectra with statistical error; the fiducial $\Delta\alpha/\alpha$ result; and the difference between the two results. The results in this table are plotted in Figure 3.14.

Object	$\Delta\alpha/\alpha$ [10^{-6}]			$\Delta\alpha/\alpha_d$ [10^{-6}]			Diff.
J0058+0051 ^H	−1.063	±	6.609	−6.432	±	6.686	−5.369
J0108−0037 ^U	−10.380	±	4.632	−10.131	±	4.711	0.249
J0226−2857 ^U	10.732	±	6.903	9.457	±	7.421	−1.275
J0841+0312 ^H	1.507	±	3.668	1.053	±	3.388	−0.454
J0841+0312 ^U	5.466	±	4.149	8.206	±	4.331	2.740
J1029+1039 ^H	−2.485	±	10.088	−2.504	±	10.155	−0.019
PHL957 ^H	−4.233	±	5.475	−1.494	±	6.451	2.739
PHL957 ^U	0.311	±	13.716	−2.152	±	14.266	−2.463
Q1755+57 ^H	4.687	±	4.325	0.502	±	5.222	−4.720
Q2206−1958 ^U	−8.184	±	6.110	−8.481	±	6.149	−0.297

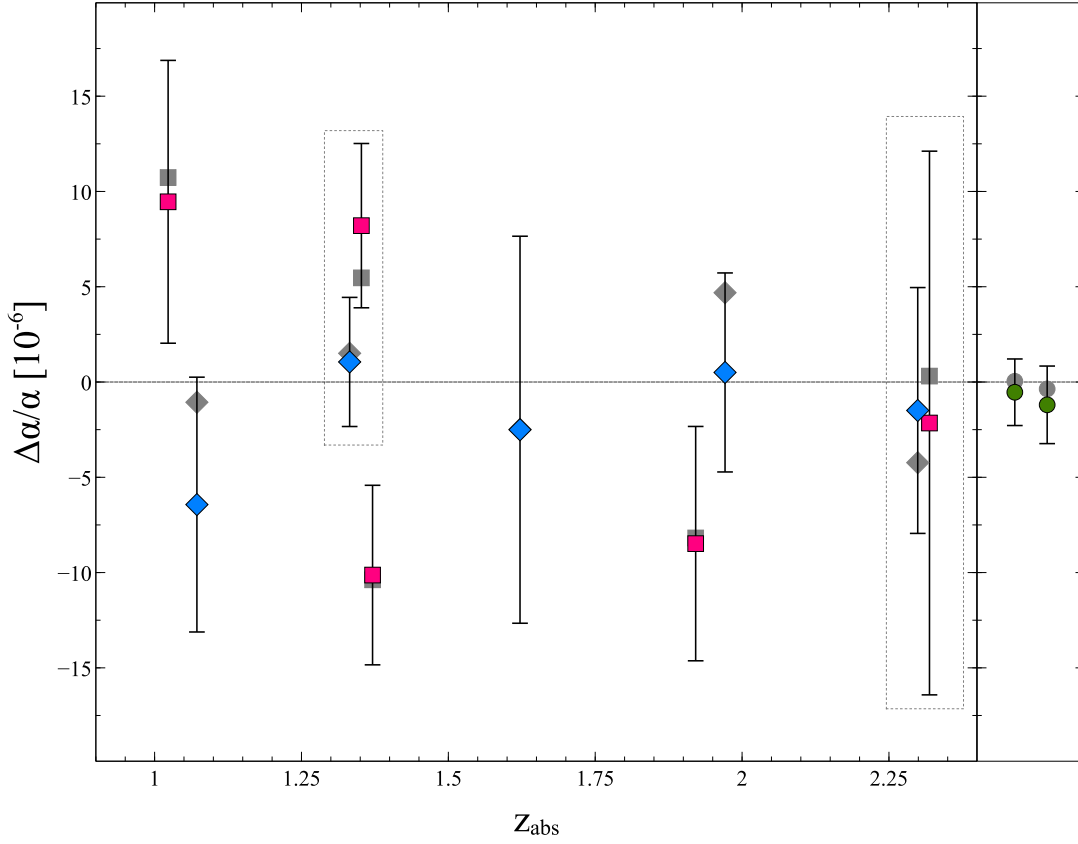


Figure 3.14: Plot of $\Delta\alpha/\alpha_d$ values obtained from artificially distorted spectra simulating short-range intra-order distortions, compared to the fiducial $\Delta\alpha/\alpha$ values, tabulated in Table 3.14. *Left:* the HIRES $\Delta\alpha/\alpha_d$ results rendered as blue diamonds, the UVES $\Delta\alpha/\alpha_d$ results as fuchsia squares and the error bars are their statistical $1-\sigma$ errors. The fiducial results from Figure 3.13 are plotted as grey points without error bars, as the error values between the two sets of results are very similar (as expected). The double data points enclosed by dotted rectangles are results from the same object, with data from both Keck and VLT telescopes. *Right:* the averaged results from the artificially distorted sample. The fiducial results are plotted in grey. The left point is the weighted mean of the $\Delta\alpha/\alpha_d$ result and the right point is the unweighted mean. Both error bars are the $1-\sigma$ statistical errors of the distorted sample.

The weighted mean and $1-\sigma$ error of the distorted sample is

$$\Delta\alpha/\alpha_d = (-0.54 \pm 1.75) \times 10^{-6}. \quad (3.4)$$

The difference between the distorted and fiducial weighted mean results is -0.58×10^{-6} and the errors are effectively identical. This difference is smaller than either constraint's error and is comparable to the systematic error due to long range wavelength distortions in Section 3.4.2 of $\pm 0.75 \times 10^{-6}$.

While the direct difference can be taken as the systematic error component due to short-range intra-order wavelength distortions, another viable estimate is based on the scatter of the differences of the individual absorber results (right-most column in Table 3.14). The standard error on the mean of these differences is 0.86×10^{-6} , comparable to the direct difference in the means.

Whitmore et al. (2010) presented a formula for estimating the standard deviation of the scatter due to the short-range distortions in $\Delta\alpha/\alpha$, based on Monte Carlo simulations of distorted spectra and fits

$$\sigma(\Delta\alpha/\alpha) = 7.5 \times 10^{-8} C_{\text{Nt}} \frac{\sigma(v)}{(N_{\text{sys}} N_{\text{tran}})^{\frac{1}{2}}}. \quad (3.5)$$

For the sample in this work, $\sigma(v)$, the standard deviation of the distorting velocity offsets is taken to be 200 m s^{-1} , the C_{Nt} factor is 1.3 for the $N_{\text{tran}} = 5$ α -sensitive transitions fit per absorber and the number of fit systems is $N_{\text{sys}} = 10$. This returns a standard error value of

$$\sigma_{\text{err}}(\Delta\alpha/\alpha) = 0.87 \times 10^{-6}, \quad (3.6)$$

which is comparable to the difference between distorted and fiducial weighted mean results and is indicative of the reliability of both methods in estimating the systematic effect of these short-range distortions on $\Delta\alpha/\alpha$ constraints.

Motivated by this consistency, and taking the most conservative estimate of all three, the systematic error due to short-range intra-order distortions is estimated as 0.87×10^{-6} .

3.5 Discussion

3.5.1 Temporal variation in α

By adding the two main known sources of systematic error in quadrature – the long (Section 3.4.2) and short-range (Section 3.4.3) distortions of the wavelength scale – the systematic error on the fiducial $\Delta\alpha/\alpha$ constraint is 1.15×10^{-6} . Therefore the final constraint on $\Delta\alpha/\alpha$ using the fiducial 10-sample Zn II and Cr II χ^2 -minimised fits is

$$\Delta\alpha/\alpha = (0.04 \pm 1.69_{\text{stat}} \pm 1.15_{\text{sys}}) \times 10^{-6}, \quad (3.7)$$

which is consistent with no temporal variation in α for the range of absorption redshifts in this sample ($z_{\text{abs}} = 1.072 - 2.308$), for the given precision. This null result is suggestive of no variation with cosmological time.

3.5.2 Spatial variation in α

Evidence of spatial variation in α from a combined VLT and Keck QSO sample was found by Webb et al. (2011) and King et al. (2012), who found a best-fitting dipole model $\Delta\alpha/\alpha = A \cos(\Theta) + m$ where $m = (-0.178 \pm 0.084) \times 10^{-5}$, $A = 0.97 \times 10^{-5}$ ($1\text{-}\sigma$ confidence range $[0.77, 1.19] \times 10^{-5}$). The angle from the dipole maximum here is the Θ parameter (in degrees), where the direction of the dipole maximum is RA = 17.3 ± 1.0 h, Dec. = $-61^\circ \pm 10^\circ$. While the work of Whitmore and Murphy (2015) shows strong evidence for a long-range systematic wavelength distortion in at least the VLT/UVES component being responsible for the positive dipole result, it is still considered here.

Figure 3.15 overlays the fiducial results on the $\Delta\alpha/\alpha$ dipole found by Webb et al. (2011) and King et al. (2012). The sample is clearly clustered in a narrow range of Θ values ($100^\circ - 120^\circ$), with two outlying UVES measurements (outlying in this context meaning to lie outside the narrow angular range in which the sample of this work is clustered, not ‘statistical outliers’). Overall it is hard to draw conclusions given the low angular separation of the sample. However, a rudimentary indication is gained by comparing the χ^2_ν values of a non-varying ‘model’ where $\Delta\alpha/\alpha = 0$ for all z_{abs} , with that of an angular variation model as defined by the King et al.

(2012) dipole (where both ‘models’ have zero free parameters). The non-varying $\chi^2_\nu = 1.30$ has a probability of 5.6%, while the varying $\chi^2_\nu = 2.48$ has a probability of 0.2%. Alternatively, the probability that the χ^2_ν in the non-varying case is smaller than that measured is 78%, while in the varying case it is 99%, indicating the non-varying case to be marginally preferred.

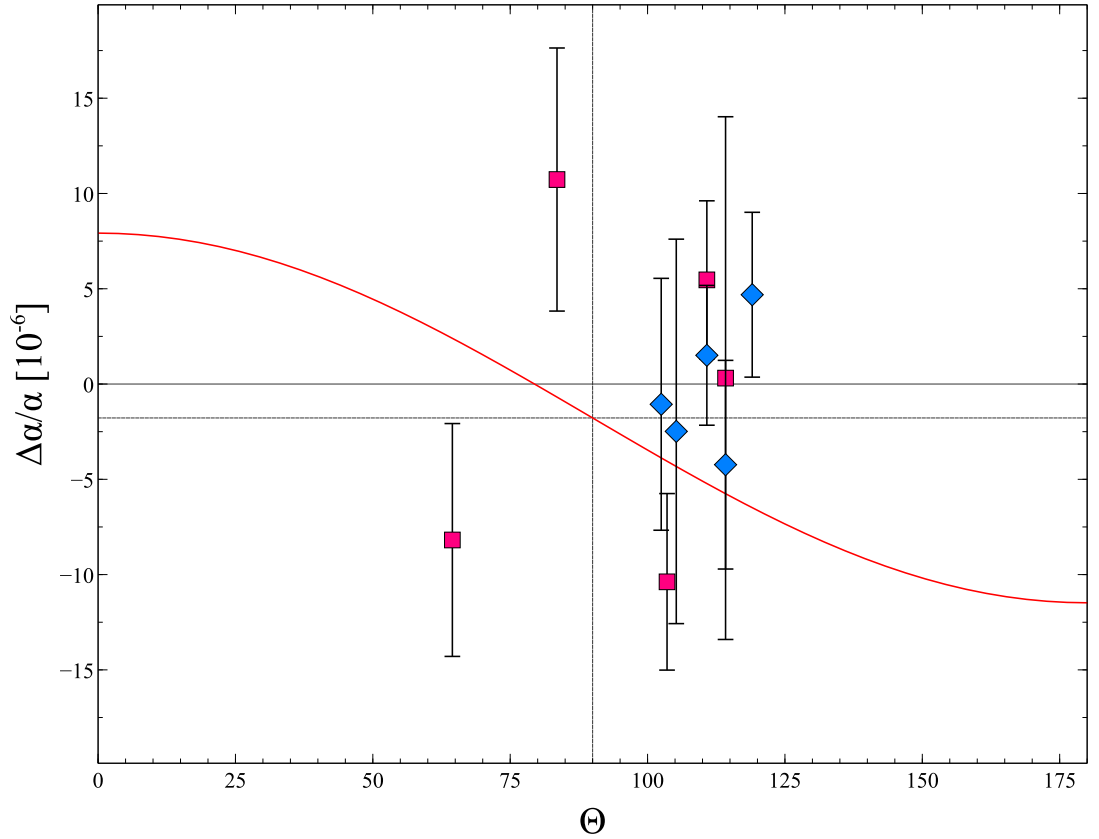


Figure 3.15: Plot of fiducial $\Delta\alpha/\alpha$ results overlaid to the best fit spatially varying α dipole (red curve) of King et al. (2012) vs Θ , the angle from dipole maximum (in degrees). The HIRES $\Delta\alpha/\alpha$ results rendered as blue diamonds, the UVES $\Delta\alpha/\alpha$ results as fuchsia squares and the error bars are their statistical $1\text{-}\sigma$ errors.








3.5.3 Comparison to previous $\Delta\alpha/\alpha$ constraints

The $\Delta\alpha/\alpha$ constraint obtained in this work is compared to previous results in Table 3.15. The work of Evans et al. (2014) is the only study to correct for long-range distortions of the wavelength scale. It is such distortions that the work in this

thesis is uniquely resistant to, and the only work currently in the field to use only a subset of transitions which lie close to each other in wavelength for its analysis. This work and Evans et al. (2014) are consistent with each other and suggest no variation in α at the combined precision of 2×10^{-6} (where the statistical and systematic errors were simply combined in quadrature), which is the best currently available to the astronomical community. The error on the result in this thesis is competitive with other small-sample studies, especially given the small number of transitions fit, and the moderate SNR of the spectra (~ 40 , compared to the > 100 of the single absorber studies). The large-sample studies have statistical errors of around only one-half of that presented in this work, but have sample sizes of more than an order of magnitude greater. This is not surprising, given the overall SNR of their individual absorbers is lower and the sensitivity to varying α of the Cr II and Zn II transitions used here is very high.

Because of the rare nature of metal-strong Zn II and Cr II absorbers that are suitable for varying α analyses, this work may be the only study of its kind for some time to come. Future analyses will need to correct for, or avoid, the systematics that have plagued the field, particularly the long-range distortions of the wavelength scale in the slit-based spectrographs used here, and verify results using multiple telescopes, where available.

Table 3.15: Table of current QSO absorption-based $\Delta\alpha/\alpha$ constraints. The first column is the referenced study; the second column is a plot of the $\Delta\alpha/\alpha$ result in units of parts per million (ppm), where the error bars are the 1- σ statistical errors and the extended error bars are the statistical and systematic errors (where estimated); the result itself is quoted next, also in ppm; the final column is the absorber sample size used in the study. The Evans et al. (2014) result is the weighted mean of the 3 absorbers studied using 3 different telescopes. The King et al. (2012) result is the weighted mean of the VLT sample in that study.

Ref.	$\Delta\alpha/\alpha$ [10^{-6}]	N
This work	 $+0.04 \pm 1.69_{\text{stat}} \pm 1.15_{\text{sys}}$	10
Evans et al. (2014)	 $-5.4 \pm 3.3_{\text{stat}} \pm 1.5_{\text{sys}}$	9
Molaro et al. (2013)	 $+1.3 \pm 2.4_{\text{stat}} \pm 1.0_{\text{sys}}$	5
King et al. (2012)	 $+2.08 \pm 1.24_{\text{stat}}$	153
Levshakov et al. (2007)	 $+5.4 \pm 2.5_{\text{stat}}$	1
Quast et al. (2004)	 $-0.4 \pm 1.9_{\text{stat}} \pm 2.7_{\text{sys}}$	1
Murphy et al. (2004)	 $-5.7 \pm 1.1_{\text{stat}}$	143

4

Robust $\Delta\mu/\mu$ constraint from molecular absorption spectra

Contents

4.1	Foreword	106
4.2	Introduction	106
4.3	Data	107
4.3.1	Keck spectrum of J2123–0050	107
4.3.2	Laboratory wavelengths for H ₂ and HD transitions	109
4.3.3	Sensitivity coefficients, K	116
4.4	Analysis and results	116
4.4.1	χ^2 minimisation analysis	116
4.4.2	Fiducial absorption model	124
4.4.3	Fiducial result	138
4.5	Internal consistency and systematic errors	138
4.5.1	Consistency tests	138
4.5.2	Systematic errors	145
4.6	Discussion	151
4.6.1	Comparison to other astrophysical $\Delta\mu/\mu$ constraints	152
4.6.2	Reanalysis using VLT data for J2123–0050	153

4.1 Foreword

The material presented herein is current as of 2010, when it was published in Malec et al. (2010a) and has not been updated. Significant developments in the field are summarised in Bagdonaite et al. (2014). The author of this thesis was not involved in the observations and the initial data reduction of the object studied here.

4.2 Introduction

While some analyses have indicated a varying μ (e.g. Reinhold et al., 2006), reanalyses of the three well-documented and high-quality H_2 absorption spectra at $z > 2$ (see Section 1.4.1) did not provide evidence for cosmological variation in μ . A much larger statistical sample is desirable, deriving from several telescopes and spectrographs, for definitive results and to provide measurements over a larger redshift range. However, the scarcity of known H_2 absorbers has hampered such progress: >1000 absorption systems rich in neutral hydrogen – i.e. damped Lyman- α systems, with H I column densities $N(\text{H I}) \geq 2 \times 10^{20} \text{ cm}^{-2}$ – are known (e.g. Prochaska and Wolfe, 2009) but in systematic searches for H_2 conducted in <100 systems (e.g. Ledoux et al., 2003) only ~ 15 were found to harbour detectable column densities of H_2 (Noterdaeme et al., 2008a). Furthermore, for varying- μ analyses, H_2 absorbers must

1. be at $z > 2$ to shift enough Lyman and Werner transitions above the atmospheric cutoff ($\sim 3000 \text{ \AA}$),
2. have bright background QSOs to enable high-SNR, high resolution spectroscopy and
3. have high enough H_2 column densities so that individual transitions absorb significant fractions of the QSO continuum.

In these respects, and others, the absorber studied here – at $z_{\text{abs}} = 2.059$ towards the $z_{\text{em}} = 2.261$ QSO SDSS J212329.46–005052.9 (hereafter J2123–0050; Milutinovic et al., 2010) – is exceptional. It is the first studied with the High Resolution Echelle Spectrometer (HIRES; Vogt and et al., 1994) on the Keck telescope in Hawaii to provide constraints of similar precision to the three VLT

ones¹. J2123–0050 is unusually bright (r -band magnitude ≈ 16.5 mag), providing a high SNR spectrum in just 6 hours observation with a high spectral resolution for an H₂ absorber to date: $R \approx 110000$ or full-width-at-half-maximum FWHM $\approx 2.7 \text{ km s}^{-1}$. HIRES’s high ultraviolet (UV) throughput provides 86 H₂ transitions for constraining μ -variation, the largest number in an individual absorber so far. Also, for the first time, (7) hydrogen deuteride (HD) transitions are used to constrain μ -variation; HD has been observed in just two other high-redshift absorbers (Varshalovich et al., 2001; Noterdaeme et al., 2008b).

As mentioned in Section 1.4.1 variations in μ should shift the ro-vibronic transition frequencies in molecular spectra. This mass-dependent shift is quantified by a sensitivity coefficient, K_i , for each transition i (see Equation 1.7).

The work presented here is separated into four main sections. Section 4.3 provides an overview of the QSO absorption spectrum used and local lab-based molecular data used for comparison with cosmological observations. Section 4.4 contains the method used to construct a spectral model of the data and constrain $\Delta\mu/\mu$, along with the raw, fiducial result. Section 4.5 consists of a series of robust consistency tests and systematic error estimates. Section 4.6 summarises the previous sections and compares the results to other astrophysical $\Delta\mu/\mu$ constraints.

4.3 Data

4.3.1 Keck spectrum of J2123–0050

The sub-DLA at $z_{\text{abs}} = 2.059$ towards J2123–0050 ($z_{\text{em}} = 2.26$), was observed using the HIRES instrument on the Keck I telescope as a result of a follow-up survey of absorbers by Milutinovic et al. (2010), based on a sub-sample of metal-strong DLAs algorithmically identified by Herbert-Fort et al. (2006) in the Sloan Digital Sky Survey (SDSS) Data Release 3 QSO sample (Prochaska et al., 2005). Presented here are properties of the data particularly pertinent to a varying- μ analysis. Some further details are available in Milutinovic et al. (2010), who focus on the study of abundances and photoionisation, rather than any fundamental constant constraint.

¹Cowie and Songaila (1995) previously analysed Keck/HIRES spectra of Q 0528–250 to derive a comparatively weak constraint of $\Delta\mu/\mu = (-80 \pm 313) \times 10^{-6}$.

The final J2123–0050 HIRES data is composed of 2 sets of 3×1 -hr exposures, corresponding to the nights of 19 and 20 August 2007. The exposures were taken consecutively each night, with a thorium–argon (ThAr) lamp exposure taken before or after a set to calibrate the data. The excellent seeing ($0''.3$ – $0''.5$ at ~ 6000 Å) and brightness of the QSO ($m_r = 16.44$) allowed for a $0''.4$ -wide slit to be used. Spectrograph temperature and atmospheric pressure shifts between the QSO and ThAr exposures were < 1 K and < 1 mbar respectively.

The raw spectra were reduced using the HIRES REDUX software package (described in Section 2.4), following standard procedure for the flux extraction. In order to ensure accurate wavelength calibration ThAr lines were pre-selected with the procedures described in Murphy et al. (2007). At the time the HIRES REDUX ThAr line centroiding code was enhanced to perform Gaussian fitting to ensure more reliable results. The root-mean-square (RMS) of the wavelength calibration residuals, i.e. the RMS error in any given wavelength, was ~ 80 m s $^{-1}$.

The exposures were combined using the UVES_POPLER software to form the final spectrum (see Section 2.4.3 for details), spanning the vacuum–heliocentric wavelengths² of 3071–5896 Å. Because the local continuum was later modelled and fitted simultaneously with most H₂/HD and Lyman- α forest absorption lines (see Section 4.4.1) the global QSO continuum fit performed at this stage served simply as a nominal, fixed starting guess in most cases.

The quality of the final spectrum is relatively high, with the SNR in the nominal continuum ranging from 7 per 1.3 km s $^{-1}$ pixel at ~ 3075 Å to 25 at ~ 3420 Å (all of the H₂/HD fall bluewards of this wavelength). A manual check was performed around each H₂/HD transition to ensure consistency between the final RMS flux variations and the uncertainty expected from the individual flux error arrays as obtained from the extraction. Visual inspection revealed no significant wavelength or velocity shifts between the individual exposures.

Figure 4.3 shows the region of the final spectrum containing H₂/HD lines (3071–3421 Å) and a region redwards of the Lyman- α emission line (4905–4926 Å) containing metal lines which are required in the fit, as described in Section 4.4.1.

Figure 4.1 highlights some of the H₂ and HD transitions covering the observed

²Referring to wavelengths that have been corrected from air to vacuum and to the heliocentric frame of reference.

range of overall line-strengths, SNRs and ground-state rotational levels, characterised by the quantum number J (J -levels'). H_2 lines are observed in the $\text{B}^1\Sigma_u^+ - \text{X}^1\Sigma_g^+$ Lyman and $\text{C}^1\Pi_u - \text{X}^1\Sigma_g^+$ Werner bands, for $J \in [0, 5]$. HD is observed in six R0 Lyman lines and one R0 Werner line. The molecular absorption shows two distinct spectral features (SFs), separated by $\approx 20 \text{ km s}^{-1}$. Figure 4.3 shows that the strong left-hand SF appears saturated for most low- J transitions, while the weaker right-hand SF appears unsaturated in almost all transitions. Only the left-hand SF is detected in the HD transitions.

The non-trivial absorption profile with lines of different strengths and presence of blending with the Lyman- α forest, along with variable SNR and potential background continuum-placement errors all must be taken into account to obtain the final uncertainty on $\Delta\mu/\mu$. This is achieved using a χ^2 minimisation fitting technique (Section 4.4.1), combined with a detailed model of the absorption profile (Section 4.4.2).

4.3.2 Laboratory wavelengths for H_2 and HD transitions

The velocity shifts between different H_2/HD transitions, along with the sensitivity coefficients K can be related to a varying μ (see Equation 1.7). This is only true, however, if the current, local laboratory wavelengths of those transitions are measured to a high enough precision – that matching the precision of the astronomical spectra. As challenging as laboratory measurements in the $\lambda_{\text{lab}} \lesssim 1150 \text{ \AA}$ regime are, these have been improved over time and today precise laboratory wavelengths for all of the H_2/HD transitions relevant in μ -variation studies are available.

The classical data of the Meudon group reached fractional wavelength accuracies of $\delta\lambda/\lambda \sim 10^{-6}$ (Abgrall et al., 1993), soon followed by the first laser calibration study using a pulsed dye laser system (Hinnen et al., 1994), which reached similar or somewhat improved accuracies of 6×10^{-7} . Ubachs et al. (1997) pushed for a further order of magnitude improvement using an implementation of Fourier transform-limited laser pulses in the harmonic conversion processes. Subsequent studies used this technique to narrow the Lyman and Werner transition wavelengths to fractional accuracies of 5×10^{-8} (Philip et al., 2004; Ubachs and Reinhold, 2004). Recently, this impressive progress has continued to produce even more accurate

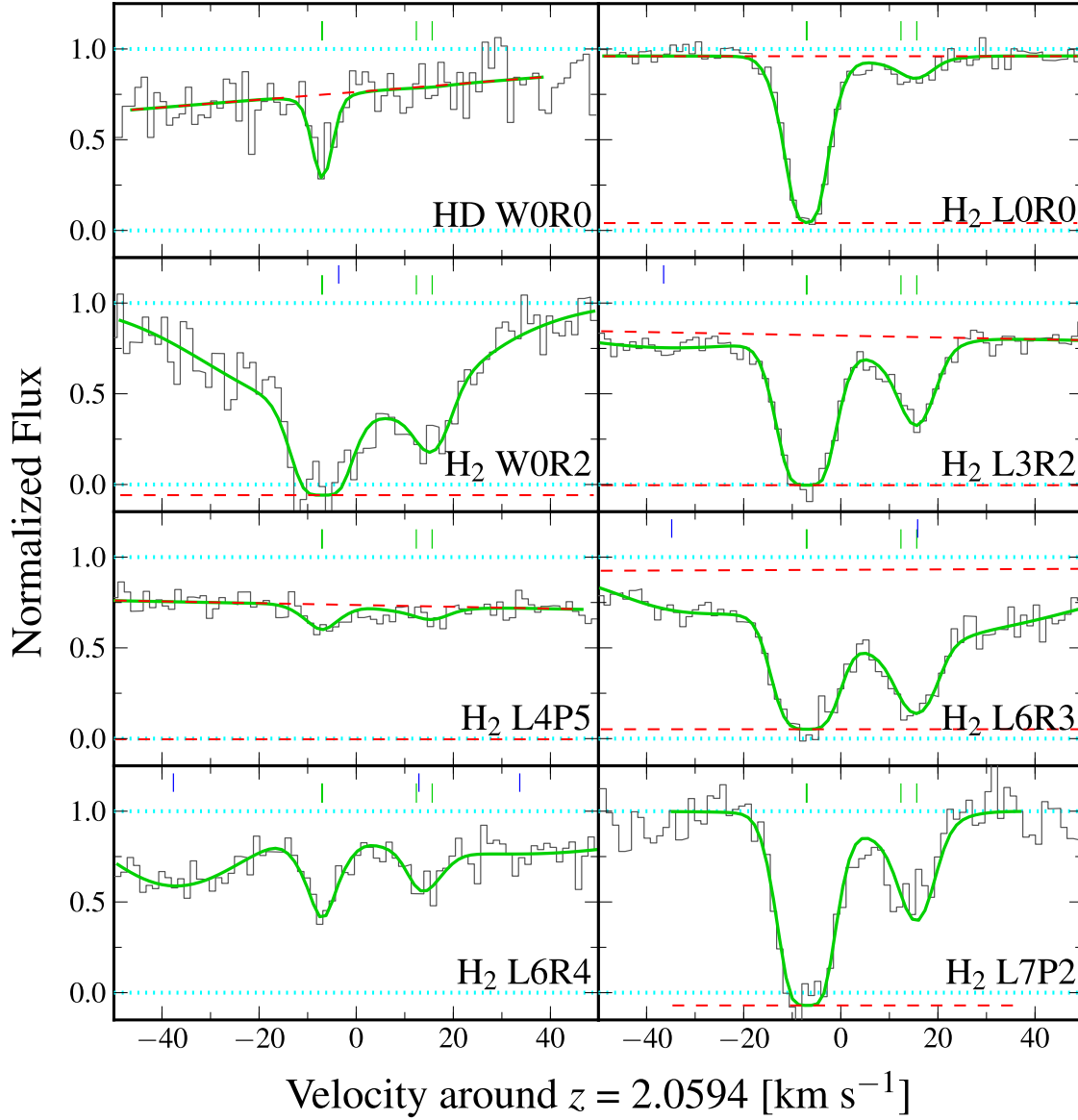


Figure 4.1: Sample of the 86 H_2 and 7 HD lines from the J2123–0050 Keck spectrum on a velocity scale centred at $z_{\text{abs}} = 2.0594$. The spectrum (black histogram) is normalised by a nominal continuum (upper dotted line). Local linear continua (upper dashed lines) and zero levels (lower dashed lines) are fitted simultaneously with the molecular and broader Lyman- α lines, the positions of which are indicated with, respectively, lighter and darker tick marks (offset vertically from each other) above the spectrum. The 4-component fiducial fit is the solid curve. Note that the two left-most components are nearly coincident in velocity.

values, with fractional accuracies of 5×10^{-9} for most Lyman transitions and $1-2 \times 10^{-8}$ for Werner transitions, obtained from combining two-photon excitation results with Fourier-transform studies of emission lines between H_2 excited states (Salumbides et al., 2008). The most precise wavelengths from these studies are used for each H_2 transition detected in this work's spectrum of J2123–0050.

Table 4.1 is a compilation of the most precise laboratory H_2 transition wavelength data for all of the H_2 transitions fit in the analysis (see Figure 4.3). It is only a subset of a larger, complete catalogue for all allowed Lyman and Werner H_2 transitions between the lowest 8 rotational levels in the ground and excited states with wavelengths generally above the hydrogen Lyman limit (more specifically, to the first 20 and 6 excited vibrational levels for Lyman and Werner transitions, respectively). Most important to μ -variation studies such as this one are the wavelengths and sensitivity coefficients (see below), but also included is the other laboratory data required for fitting the H_2 absorption lines seen in astronomical spectra, such as oscillator strengths. This table is presented in full in Appendix B and has been submitted to the VizieR Online Data Catalog (Malec et al., 2010b) as a useful reference catalogue for other astronomical studies.

The HD transition wavelengths used here are those recently measured via direct extreme UV laser excitation to a relative accuracy of $\approx 5 \times 10^{-8}$ by Hollenstein et al. (2006) and Ivanov et al. (2008). Table 4.2 provides the laboratory data for the 7 HD transitions fit in the analysis presented in this thesis.

Table 4.1: Compilation of laboratory H_2 data for all of the H_2 transitions fit in the spectrum of J2123–0050. The first column provides a short-hand notation for the transition: letters denote a Lyman (L) or Werner (W) line and the branch, where P, Q and R represent $J' - J = -1, 0$ and 1 , respectively, for J and J' the ground state and excited state J -levels, respectively; the first integer is the excited state vibrational quantum number and the second is J . The second column gives the most precise reported laboratory wavelength and its $1\text{-}\sigma$ uncertainty. Note that almost all wavelength data is sourced from Bailly et al. (2010), the note mark 3 indicates data from Abgrall et al. (1993) for the excited state energy levels with ground states derived directly from Jennings et al. (1984), for consistency with the full table of molecular data presented in Appendix B. The third column gives the oscillator strengths which were calculated from the Einstein A coefficients given by Abgrall et al. (1994). The fourth column gives the (natural) damping coefficients which were calculated from the total transition probabilities (A_t) in Abgrall et al. (2000). The final column gives the sensitivity coefficients calculated in Ubachs et al. (2007) which have estimated uncertainties of typically $< 5 \times 10^{-4}$ (see Section 4.3.3).

Trans.	λ_{lab} [\AA]	f [10^{-2}]	Γ [10^9 s^{-1}]	K
L0P2	1112.495989(3)	0.0691459	1.86	−0.01190946
L0P3	1115.895530(3)	0.0738064	1.86	−0.01491660
L0R0	1108.127317(2)	0.166457	1.86	−0.00800319
L0R1	1108.633244(3)	0.1077	1.86	−0.00846231
L0R3	1112.583944(5)	0.0846784	1.84	−0.01201537
L0R4	1116.014618(7)	0.0777988	1.83	−0.01507444
L1P1	1094.051949(3)	0.196852	1.74	−0.00259287
L1P2	1096.438914(5)	0.236713	1.74	−0.00474693
L1P3	1099.787177(5)	0.252569	1.73	−0.00774742
L1P4	1104.083933(7)	0.259547	1.73	−0.01155644
L1P5	1109.313238(4)	0.261585	1.72	−0.01612812
L1R0	1092.195201(4)	0.578358	1.74	−0.00092454
L1R1	1092.732382(4)	0.378015	1.73	−0.00143170
L1R2	1094.244560(7)	0.33148	1.73	−0.00282772
L1R3	1096.725316(4)	0.305571	1.72	−0.00509470
L1R5	1104.548705(5)	0.267606	1.70	−0.01212508
L2P1	1078.925400(3)	0.392257	1.63	0.00397218

Continued on next page

Table 4.1: *Continued from previous page*

Trans.	λ_{lab} [Å]	f [10^{-2}]	Γ [10^9 s^{-1}]	K
L2P2	1081.265950(4)	0.469983	1.63	0.00183764
L2P4	1088.795369(4)	0.515046	1.62	−0.00494895
L2P5	1093.954976(3)	0.520673	1.61	−0.00951288
L2R0	1077.138656(3)	1.16679	1.63	0.00558220
L2R2	1079.225425(4)	0.681799	1.62	0.00360188
L2R3	1081.711274(3)	0.636247	1.61	0.00129543
L2R5	1089.513848(5)	0.573951	1.59	−0.00579408
L3P1	1064.605318(4)	0.594138	1.54	0.01000951
L3P3	1070.140818(3)	0.753828	1.53	0.00492550
L3P4	1074.312899(5)	0.774358	1.53	0.00114033
L3P5	1079.400450(4)	0.783446	1.52	−0.00340979
L3R0	1062.882074(4)	1.78952	1.53	0.01156759
L3R1	1063.460086(3)	1.19024	1.53	0.01099293
L3R2	1064.994759(4)	1.06482	1.53	0.00952560
L3R3	1067.478598(4)	1.00421	1.52	0.00718891
L3R4	1070.900286(6)	0.962639	1.51	0.00401739
L3R5	1075.244947(6)	0.928142	1.50	0.00005478
L4P1	1051.032451(5)	0.760153	1.45	0.01555697
L4P2	1053.284210(4)	0.902223	1.45	0.01346322
L4P3	1056.471373(3)	0.955567	1.45	0.01051153
L4P4	1060.580970(4)	0.979364	1.44	0.00674295
L4P5	1065.596570(4)	0.990006	1.43	0.00220871
L4R0	1049.367383(4)	2.31929	1.45	0.01706801
L4R1	1049.959704(3)	1.55494	1.45	0.01646751
L4R2	1051.498512(4)	1.40303	1.44	0.01497399
L4R3	1053.976051(4)	1.33569	1.43	0.01261209
L4R4	1057.380706(7)	1.29372	1.43	0.00941815
L4R5	1061.697413(5)	1.26059	1.42	0.00543822
L5P1	1038.157044(4)	0.866057	1.37	0.02064400
L5P2	1040.367202(3)	1.02228	1.37	0.01856997

Continued on next page

Table 4.1: *Continued from previous page*

Trans.	λ_{lab} [Å]	f [10^{-2}]	Γ [10^9 s^{-1}]	K
L5P3	1043.503090(4)	1.07672	1.37	0.01563663
L5P4	1047.551786(4)	1.09902	1.36	0.01188511
L5P5	1052.496918(4)	1.10794	1.36	0.00736695
L5R2	1038.690179(3)	1.6503	1.36	0.01997239
L5R3	1041.158832(4)	1.58464	1.36	0.01758824
L5R4	1044.543977(5)	1.54839	1.35	0.01437358
L6P2	1028.105875(7)	1.06298	1.30	0.02324105
L6P3	1031.192672(4)	1.11102	1.30	0.02032577
L6P4	1035.182762(5)	1.12657	1.29	0.01659124
L6R0	1024.373738(6)	2.87085	1.30	0.02672449
L6R2	1026.528323(5)	1.79656	1.29	0.02454448
L6R3	1028.986607(4)	1.73884	1.29	0.02214038
L6R4	1032.350972(8)	1.71203	1.28	0.01890632
L7P1	1014.327128(6)	0.898222	1.24	0.02953792
L7P2	1016.461136(5)	1.02323	1.24	0.02750099
L7P3	1019.502139(3)	1.04758	1.23	0.02460346
L7P4	1023.436799(5)	1.04924	1.23	0.02088590
L7P5	1028.248570(4)	1.04684	1.22	0.01639930
L7R0	1012.812914(4)	2.9702	1.24	0.03092982
L7R1	1013.436916(2)	2.05043	1.23	0.03026841
L7R2	1014.976843(5)	1.89365	1.23	0.02871411
L7R3	1017.424212(4)	1.83845	1.22	0.02629246
L8P2	1005.393086(5)	0.991071	1.18	0.03137464
L8P3	1008.386075(3)	1.04293	1.17	0.02849467
L8P4	1012.262348(5)	1.07544	1.17	0.02479431
L8R2	1003.985377(5)	1.66161	1.17	0.03250586
L8R4	1009.71969(2)	1.41081	1.16	0.02664915
W0P2	1012.16946(2)	0.878387	1.18	−0.00830958
W0P3	1014.504259(5)	1.1105	1.18	−0.01056398
W0P4	1017.385588(5)	1.22766	1.18	−0.01330997

Continued on next page

Table 4.1: *Continued from previous page*

Trans.	λ_{lab} [Å]	f [10^{-2}]	Γ [10^9 s^{-1}]	K
W0Q1	1009.770899(6)	2.38007	1.18	−0.00595909
W0Q2	1010.938509(8)	2.38098	1.18	−0.00709859
W0Q3	1012.679615(6)	2.38304	1.18	−0.00878174
W0Q4	1014.98244(3)	2.38617	1.17	−0.01097807
W0Q5	1017.83147(3)	2.38871	1.17	−0.01364833
W0R0	1008.55192(2)	1.53493	1.18	−0.00476718
W0R1	1008.498181(5)	1.28722	1.18	−0.00471844
W0R2	1009.024969(5)	1.16636	1.18	−0.00524664
W0R5	1014.2425(11) ³	2.29175	1.16	0.00022003

Table 4.2: Laboratory data for $J = 0$ HD transitions falling in (but not necessarily detected or fitted in) the spectrum of J2123−0050. The columns have the same descriptions as in Table 4.1 except for the following. The laboratory wavelength references for the first 3 rows are Hollenstein et al. (2006), the rest are Ivanov et al. (2008). The oscillator strengths (f) and damping coefficients (Γ) were calculated from the Einstein A coefficients and total transition probabilities (A_t), respectively, given by Abgrall and Roueff (2006). The sensitivity coefficients (K) were calculated by Ivanov et al. (2008) and have estimated uncertainties of typically $< 1.5 \times 10^{-4}$.

Trans.	λ_{lab} [Å]	f [10^{-2}]	Γ [10^9 s^{-1}]	K
L0R0	1105.840555(57)	0.07436	1.87	−0.0065
L1R0	1092.001264(58)	0.29669	1.76	−0.0004
L2R0	1078.831044(61)	0.67473	1.67	0.0053
L3R0	1066.27568(6)	1.14500	1.58	0.0106
L4R0	1054.29354(6)	1.63570	1.50	0.0156
L5R0	1042.85005(6)	2.05477	1.43	0.0201
L6R0	1031.91493(6)	2.35911	1.36	0.0244
L7R0	1021.46045(6)	2.53491	1.30	0.0283
L8R0	1011.46180(6)	2.61849	1.25	0.0319
L9R0	1001.89413(6)	2.47212	1.19	0.0353

Continued on next page

Table 4.2: *Continued from previous page*

Trans.	λ_{lab} [Å]	f [10^{-2}]	Γ [10^9 s^{-1}]	K
W0R0	1007.29020(6)	3.25368	1.18	−0.0039

4.3.3 Sensitivity coefficients, K

The K coefficients, which determine the sensitivity of a transition to a varying μ (see Equation 1.7), were calculated via a semi-empirical analysis by Ubachs et al. (2007). The results of this analysis are in agreement to within 1% with the independent *ab initio* calculations by Meshkov et al. (2006). The margin corresponds to the estimated uncertainties in both studies, each of which can be considered reliable. The K coefficients for the H_2 transitions are included in Table 4.1. The K coefficients for HD were derived via *ab initio* calculations by Ivanov et al. (2008) and are given in Table 4.2.

Figure 4.2 (upper panel) shows the K values, which occupy the range $-0.02 < K < +0.03$, for all detected molecular transitions. Here, the broad pattern of K values increases for bluer Lyman transitions and could potentially be simulated by a long-range distortion in the wavelength scale of the data. This would be of major concern if not for the Werner transitions below $\lambda_{\text{lab}} = 1020 \text{ Å}$ which help render a more complicated signature of a varying μ – that is, they shift in the opposite direction to the Lyman transitions at similar wavelengths. This is important when considering possible systematic effects and is discussed in detail in Section 4.5.2.

4.4 Analysis and results

4.4.1 χ^2 minimisation analysis

One may consider a simple, hypothetical case where molecular absorption occurs at a single redshift in a single absorbing cloud, with nothing else in the line of sight between the observer and the background QSO. Measuring $\Delta\mu/\mu$ is straightforward: determine each molecular line’s redshift from a fit against a well-defined

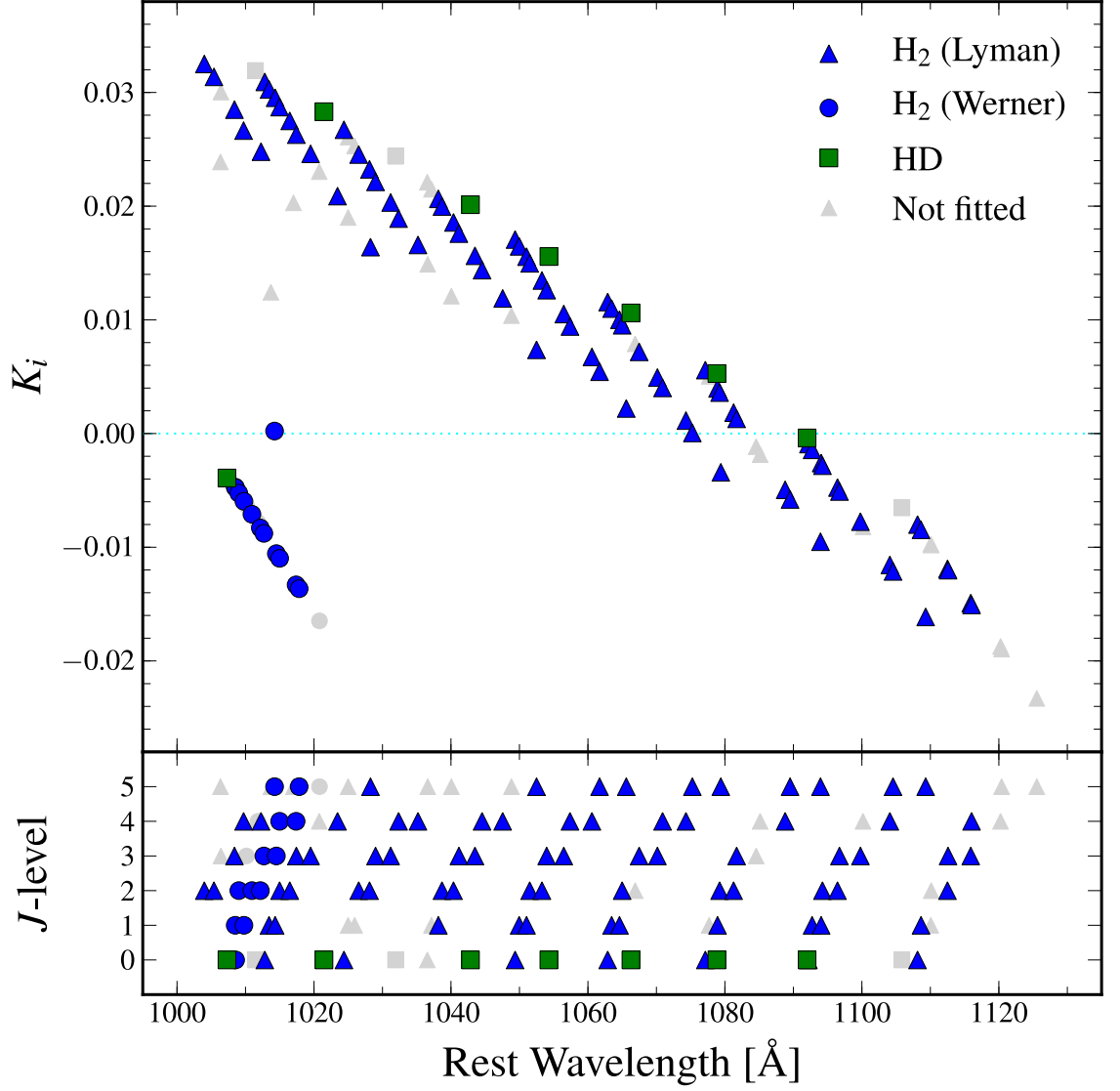


Figure 4.2: *Upper panel:* The sensitivity coefficients, K_i , for the $J=0-5$ HD and H₂ Lyman and Werner transitions, i , used in the analysis (dark/coloured points) and those not detected or fitted (light grey points). The legend explains the symbols used in both panels. *Lower panel:* The distribution of transitions with wavelength according to their J -levels.

background continuum and plot its relative deviation from some arbitrary redshift against its K coefficient. Equation 1.7, in which the deviation term $\Delta z_i/(1 + z_{\text{abs}})$ is generally referred to as the reduced redshift, implies that $\Delta\mu/\mu$ would simply be the slope of such a plot.

For the absorber studied here such a linear fit is not possible because of two complicating factors:

1. The molecular lines show ‘velocity structure’ – meaning the absorption cloud is actually made up of several clouds with similar redshifts and different optical depths and Doppler widths. The two main spectral features (SFs) highlighted in Figure 4.1 can be clearly seen, and are actually each comprised of more than one absorbing velocity component (VC) as discussed in Section 4.4.2.
2. All of the molecular lines fall in the Lyman- α forest, the series of relatively broad H I Lyman- α absorption lines randomly distributed in optical depth and redshift bluewards of the QSO’s Lyman- α emission line. Many molecular lines fall within the absorption profile of one or more forest lines (see Figures 4.3 and 4.1). The forest absorption is insensitive to changes in μ and can be thought of as another layer contributing to the background QSO continuum in the context of a varying $\Delta\mu/\mu$ and must also be fitted.

These complications are robustly addressed by ‘simultaneous fitting’, where all detected H₂ and HD absorption lines, together with the broader Lyman- α lines are fit together, at the same time in a single, comprehensive fit. When minimising χ^2 , uncertainties in the Lyman- α forest parameters contribute naturally to uncertainties in $\Delta\mu/\mu$ – they provide additional degrees of freedom to the absorption model and can only increase the final measurement uncertainty. While seemingly more complex than the earlier ‘line-by-line’ fitting approach, the payoff is that systems with complex velocity structures can be fit in the first place (indeed, the more complex a velocity structure the more ‘constraining power’ a system has), and lines subject to various blends in the absorption can be included in an analysis, allowing for a greater use of the available data and a much more precise measurement of $\Delta\mu/\mu$. Other advantages of this technique are outlined by King et al. (2008).

4.4.1.1 Free parameters and physical assumptions

Both the $\Delta\mu/\mu$ and $\Delta\alpha/\alpha$ analyses in this thesis apply the same, general approach: measuring a pattern of velocity shifts between narrow absorption lines that correspond to a variation in a fundamental constant. While the particulars vary, such as assumptions of what parameters are ‘tied’ to common values across different transitions, the modelling of the individual absorption line is the same. The same three familiar parameters describe each absorption lines’s properties: column density, N , Doppler width, b , and redshift, z_{abs} . The most precise available rest wavelengths, oscillator strengths and natural line-widths are used for each transition. Their values are presented in Tables 4.1 and 4.2.

Out of the parameter assumptions made for constraining $\Delta\mu/\mu$ for this particular absorber, the simplest case is that of the parameters of the fitted Lyman- α lines – they are independent of each other. The different molecular transitions, however, share these parameters in ways that have physical significance. For H_2 and HD, each J -level has a different ground state population, so all transitions from the same J -level have the same, single value of N for each corresponding VC within their velocity structure. This is also true for the b and z_{abs} values. A further assumption is that the velocity structure is the same in all transitions, meaning a particular VC has the same z_{abs} value, for all J -levels. It is also assumed that a given VC is characterised by the same, single value of b in all J -levels. Physically, these assumptions imply that the structure of the absorbing molecular cloud is the same for all ground state rotational levels; however, these levels may be populated differently. In relating the absorption model parameters of different transitions in these physically meaningful ways, the number of free parameters is minimised. This is similar to the analysis in King et al. (2008), though they fitted the molecular oscillator strengths, f , as free parameters as well. Finally, because the HD transitions are few and relatively weak (only the left-hand spectral feature is detected, though both are still fit) it is assumed that the ratio of an HD VC’s column density to that of the corresponding VC in the H_2 $J=0$ transitions is the same for all VCs. As can be seen from Figure 4.3, there is no strong evidence against this assumption. These assumptions are removed or relaxed in Section 4.5.1 and are found to have little impact on the results in Section 4.4.3.

While several Fe II transitions with $\lambda_{\text{lab}} < 1150 \text{ \AA}$ in the $z_{\text{abs}} = 2.059$ absorber

appear as weak absorption, the velocity structure extends over $\sim 400 \text{ km s}^{-1}$. These transitions effectively ‘contaminate’ any H_2 lines that happen to have wavelengths in the vicinity. The velocity components in these Fe II transitions are marked in Figure 4.3. This velocity structure can be strongly constrained by using the Fe II 1608 Å transition, which falls redwards of the Lyman- α forest and so has a well-defined continuum. The transition itself is blended with weak, broad C IV 1550 absorption associated with the QSO itself (Hamann et al., 2011). The velocity structure of C IV 1550 can be constrained by the C IV 1548 absorption. This situation may appear complex, but is easily resolved by fitting both the metal line species together with the molecular lines, to obtain a complete and a reliable absorption model, as shown in Figure 4.3. The H_2 fits are insensitive to those of the metal lines.

As noted in Section 4.3.1, a nominal continuum was initially fit to the Lyman- α forest region during the data reduction process. Simple, low-order polynomial fits connecting seemingly unabsorbed regions of the spectrum, typically spaced apart by $\gtrsim 5000 \text{ km s}^{-1}$, provided a qualitatively realistic continuum. As described above, the absorption model connects the properties of molecular lines to each other to minimise the number of free parameters and it is important to recognise that this approximate but *fixed* QSO continuum is unlikely to allow very good fits to the many molecular transitions simultaneously. This is especially true for any continuum fits in regions of Lyman- α forest absorption. It is therefore important in such cases to fit local continua around transitions where the nominal continuum is particularly uncertain. These local continua are shown in Figures 4.3 and 4.1.

In regions where Lyman- α lines and local continua are fit, one can expect strong degeneracies between the parameters of these features. This implies that the local continua need only a polynomial degree of, at most, unity – they are either constants or straight lines in wavelength space. The fitting code indicates the cases where the degeneracies are so strong that a local continuum fit serves the same purpose as the Lyman- α lines. Because all of the fit parameters are varied simultaneously in the χ^2 minimisation process, the uncertainties due to the degeneracies contribute to the uncertainties in the molecular lines naturally. One can expect the magnitude of this effect on $\Delta\mu/\mu$ to be small because of the different domains the molecular lines (which constrain $\Delta\mu/\mu$) and Lyman- α lines or local continuum adjustments (which do not have any direct influence on $\Delta\mu/\mu$) occupy in the pa-

parameter space – narrow and broad, respectively. Most previous works (excluding, e.g., King et al., 2008) effectively determined fixed, local continua before fitting the molecular lines. This means that uncertainties in the continuum fits do not propagate through to $\Delta\mu/\mu$ – and while only a small effect, as described, the uncertainty in $\Delta\mu/\mu$ would be underestimated with such an approach.

When inspecting Figure 4.3 one may see instances of saturated Lyman- α features which have non-zero average flux (either positive or, usually, negative) in their flat-bottomed line cores (e.g. features near 3107, 3137, 3171, 3317 and 3350 Å). These systematic uncertainties in the zero flux level are a product of the initial flux extraction process, where weak night sky emission is nominally subtracted. This issue is rectified by including the zero level as a free parameter when fitting regions of spectrum which included nearly saturated absorption lines (either Lyman- α and/or molecular).

In what is likely a special case, applicable to this QSO absorption system and not necessarily others, the list of free model parameters is expanded to include the oscillator strengths for the 10 H₂ transitions with $J=0-3$ falling in the wavelength range $\lambda_{\text{obs}} = 3345-3415$ Å. While establishing the fit, these transitions were observed to have noticeably higher optical depths in the data than predicted by the absorption model. For this reason the oscillator strengths f for these transitions are left as free parameters to be determined in the χ^2 minimisation process. Their fitted-to-calculated oscillator strength ratios, $f_{\text{fit}}/f_{\text{calc}}$, determined using the fiducial model (see Section 4.4.2), range from 1.5 to 2.0

It is unlikely that the published oscillator strengths for these transitions are incorrect (all molecular transition f values used here are calculated rather than experimentally measured) because these transitions are not affected by interference between multiple interacting H₂ states. Fits to H₂ transitions, which included some of these transitions, in other QSO absorbers also suggests their published oscillator strengths are reliable (J. King, private communication). A follow up study by van Weerdenburg et al. (2011) of the same QSO absorption system, but using spectra from VLT/UVES spectrograph yields the same inconsistency between f , model N 's and optical depth – confirming that this cannot be a data reduction issue. The cause is most likely a physical phenomenon. The affected transitions all fall on the combined O VI/Lyman- β QSO emission line at $\lambda_{\text{lab}} \approx 1025-1045$ Å – there

may be some inhomogeneity in the H_2 column density on the scale of the QSO broad emission-line region. While such a scenario would have no impact on the $\Delta\mu/\mu$ measurement, the effect of these transitions on the final results is checked in Section 4.5.1.

Once the absorption model described thus far is optimised (to minimise χ^2 between it and the spectral data; see the next section), the best-fitting values for the parameters are obtained. The final free parameter is now added to the model, it is the one parameter ultimately motivating the study – $\Delta\mu/\mu$. Only a single value of $\Delta\mu/\mu$ describes all molecular transitions, including all their constituent VCs.

Equation 1.7 states that a change in μ manifests itself as a pattern of relative shifts between the different molecular transitions. The covariance between $\Delta\mu/\mu$ and the other model parameters is small thanks to the diversity of K values (see Figure 4.2), or, in other words, the pattern of shifts is not degenerate with the other parameters of the fit (e.g. the individual VC redshifts).

4.4.1.2 Minimising χ^2 to constrain $\Delta\mu/\mu$

Once the absorption model is constructed as prescribed in the previous section, the χ^2 between the J2123–0050 spectral data and the model is minimised using the VPFIT software described in Section 3.2.1. The absorption model is convolved with an instrumental resolution function – a Gaussian function with $\text{FWHM} = 2.7 \text{ km s}^{-1}$ to match the resolution inferred from the line widths of the ThAr lines in the calibration exposures (these use the same slit width as the science exposures).

The fit is configured in a manner that allows VPFIT to satisfy the conditions and relationships listed in the previous section³. The software ‘understands’ that

³For the interested reader seeking to reproduce this configuration a practical summary of how this is achieved follows. It is assumed that the reader is familiar with the basics of fitting with VPFIT. The atomic data file is structured such that all H_2 transitions with the same J -level share the same label (e.g. ‘H2J1’), with the exception of the 10 transitions which require optical depth correction (see Section 4.4.1.1) – these have their own separate labels and are effectively fit as separate J -levels. The HD transitions all have a single common label. The z and b parameters are tied between the different J -level transitions, including the HD transitions; the N values are set to share the same pattern (but not absolute values) using VPFIT’s common pattern relative abundance feature. Within this scheme the HD VC shares the abundance pattern of the $J = 0$ level and the transitions requiring optical depth correction share the abundance pattern of their respective J -level transitions. A common $\Delta\mu/\mu$ parameter is used for all molecular transitions and VCs.

many molecular transitions can arise from the same J -level (i.e. that they have the same N) and the ability to link physically related parameters, such as b and z_{abs} values, across many transitions is inherent in its design.

The operation of a varying μ on the molecular lines is functionally the same as the action of a varying α on metal lines. Murphy et al. (2003a) has used simulations of spectra to verify the reliability of VPFIT for $\Delta\alpha/\alpha$ constraints and uncertainties, which also apply for $\Delta\mu/\mu$. This included absorption models with ‘challenging’ features, present in this work’s $\Delta\mu/\mu$ fit: strong overlapping (i.e. blended) metal lines (and therefore effectively molecular lines) and blends with unrelated absorption. The model used here, however, has a much greater number of transitions and links between these transitions than a metal-line fit. To test VPFIT with such a complex fit a Monte Carlo simulation of the actual absorption model is used to create many realisations of the spectral data (see the relevant part of Section 4.5.1). The sum of all the systematic error and consistency tests in Section 4.5 also testifies to the reliability of the method and software used.

The $1\text{-}\sigma$ uncertainties on the best fitting parameters output by VPFIT represent only the statistical uncertainties derived from the spectral data flux errors, as described in Section 3.2.1. An important source of further uncertainty arises from *model* errors. There are in principle many different absorption models that could be created to fit a particular spectral dataset – the uncertainties in the flux values (i.e. a non-infinite SNR) and the ‘smoothing’ by a spectrograph’s instrumental profile allow for this. In many cases, one model may be statistically preferred over the other, but there may also be cases where this preference is not significant enough to choose a particular one. One could imagine a case of a spectrum that is almost completely dominated by noise – while such a dataset would probably not be scientifically useful, it does illustrate a case where one could fit a variety of different models, without a clear ‘winner’. This effect becomes less strong as the quality of the data improves. Data that is ‘perfect’ does not exist however, and this effect will always be present to some degree. Additional sources of uncertainty, such as calibration errors and inter-pixel correlations due to flux re-binning⁴ are also important. A discussion of the selection of the ‘best’ fitting model can be

⁴Comparing the RMS flux variations in unabsorbed regions with the final error spectrum does not directly indicate the presence of significant inter-pixel correlations. Nonetheless, potential systematic errors as a result of re-binning are quantified in Section 4.5.2.5.

found in Section 4.4.2 and the non-statistical sources of uncertainty are quantified in Section 4.5.2.

4.4.2 Fiducial absorption model

A total of 86 H_2 transitions and 7 HD transitions are included in the fiducial fit. See Figure 4.3 for the complete fit. A small number of transitions detected in the spectrum of J2123–0050 cannot be reliably fit and therefore are not included in the model. These transitions have absorption profiles that are heavily blended with either nearby Lyman- α lines and/or suspected metal lines from one or more absorption systems (e.g. the LOP1 H_2 transition falling at $\lambda_{\text{obs}} \approx 3396.2$ in Figure 4.3).

The full spectrum is not modelled, only the small regions of interest around the molecular absorption and any blending metal-line transitions. Each region contains only as much of the surrounding Lyman- α forest absorption to define the effective continuum against which the molecular lines can be fit. Some molecular lines are ‘connected’ by one or more Lyman- α forest lines and in such cases are fit as part of the same region. For most regions, a single local continuum adjustment (effectively a straight-line) is present. A zero level adjustment is also included where necessary.

In order to create the initial model of the Lyman- α forest lines, local continua and zero levels, a 2-component model of the molecular absorption is initially assumed. This is a good base assumption as the absorption profiles in Figure 4.1 show two distinct spectral features (SFs). This model is then refined into the effective continuum against which the molecular lines are fit – a structure that can be used as a starting point in subsequent fits to determine the molecular velocity structure more accurately.

Given the large number of molecular transitions available, more information than merely seen ‘by eye’ in a single transition is available for constraining the parameters of the fit. It is likely that the profiles comprise more than the 2 VCs initially assumed. The additional VCs, which may be statistically significant when all transitions are considered simultaneously, could result in systematic errors in the results when ignored. Previous studies have demonstrated that ‘under-fitting’ – fitting too few VCs – causes strong systematic errors in quantities like $\Delta\alpha/\alpha$ (Mur-

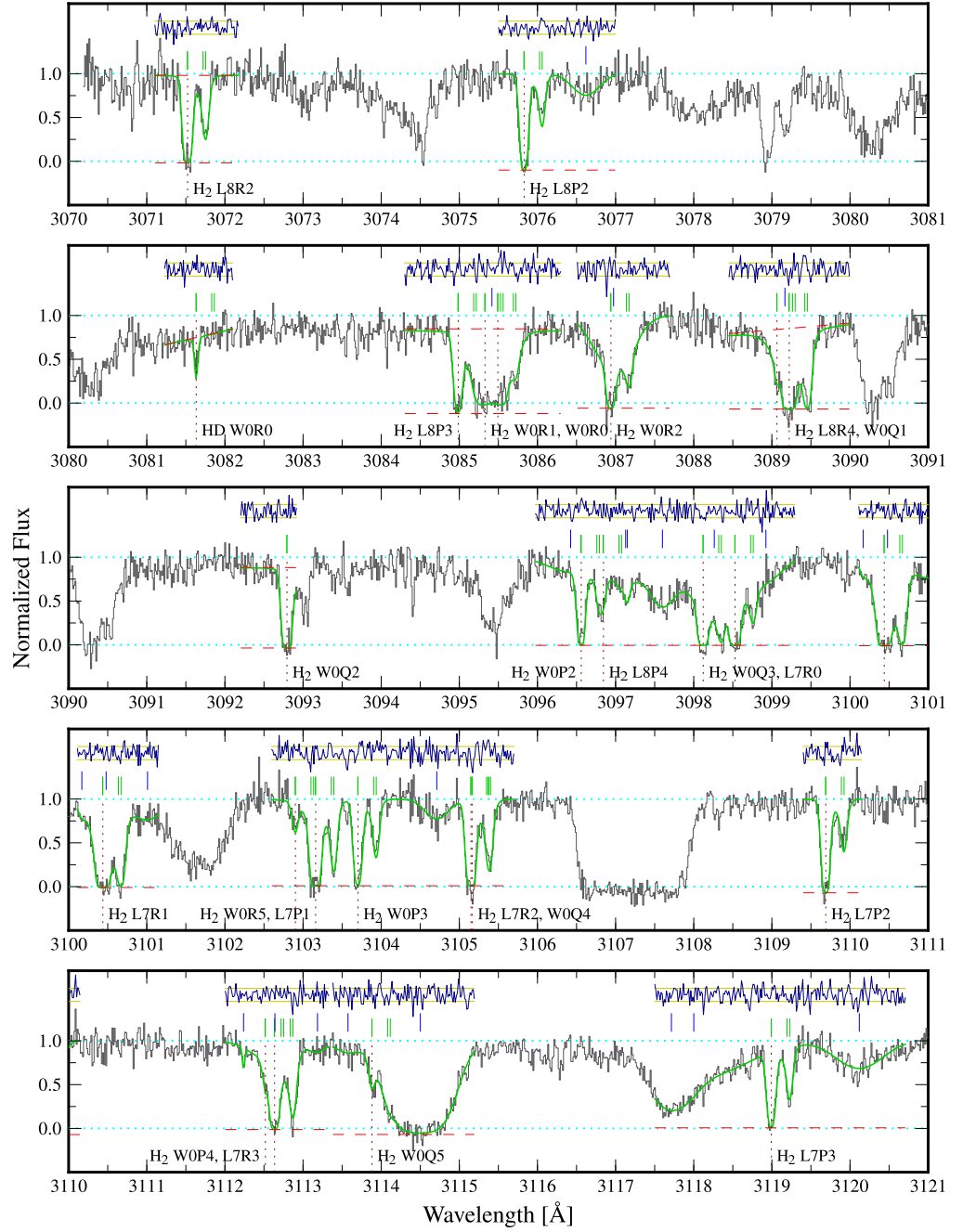


Figure 4.3: All regions of the J2123–0050 Keck spectrum fitted simultaneously in the analysis. The spectrum (black histogram) is normalised by a nominal continuum (upper dotted line) fitted over large spectral scales. Local linear continua (upper dashed lines) and zero levels (lower dashed lines) are fitted simultaneously with the H_2 /HD and broader Lyman- α lines. *Text continued on next page*

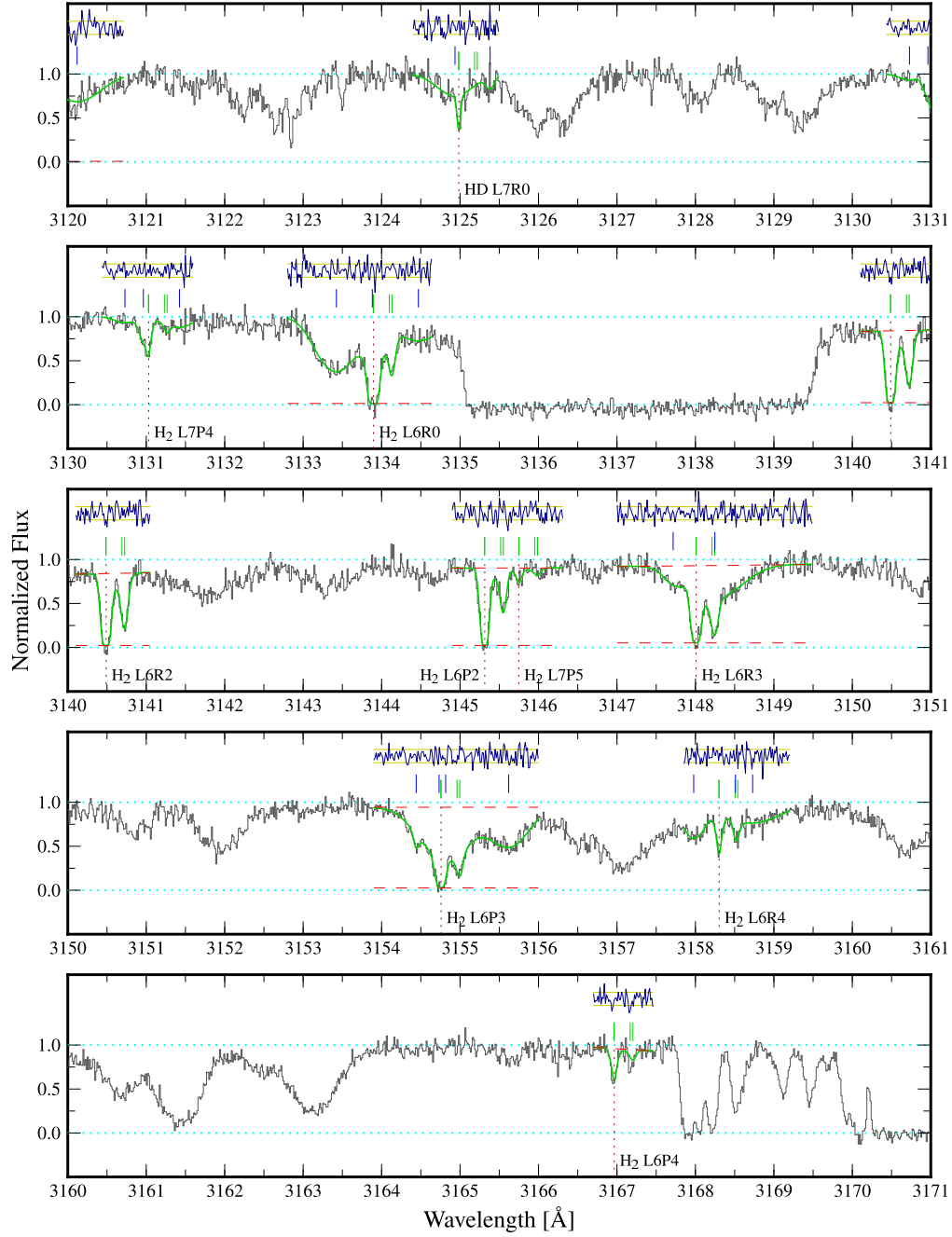


Figure 4.3: (*continued*) The fits are shown with solid grey/green lines. H_2/HD transitions are labelled and their constituent velocity components are indicated by grey/green tick-marks immediately above the spectrum. Higher above the spectrum are tick-marks indicating the positions of Lyman- α lines (blue) and Fe II lines (red). *Text continued on next page*

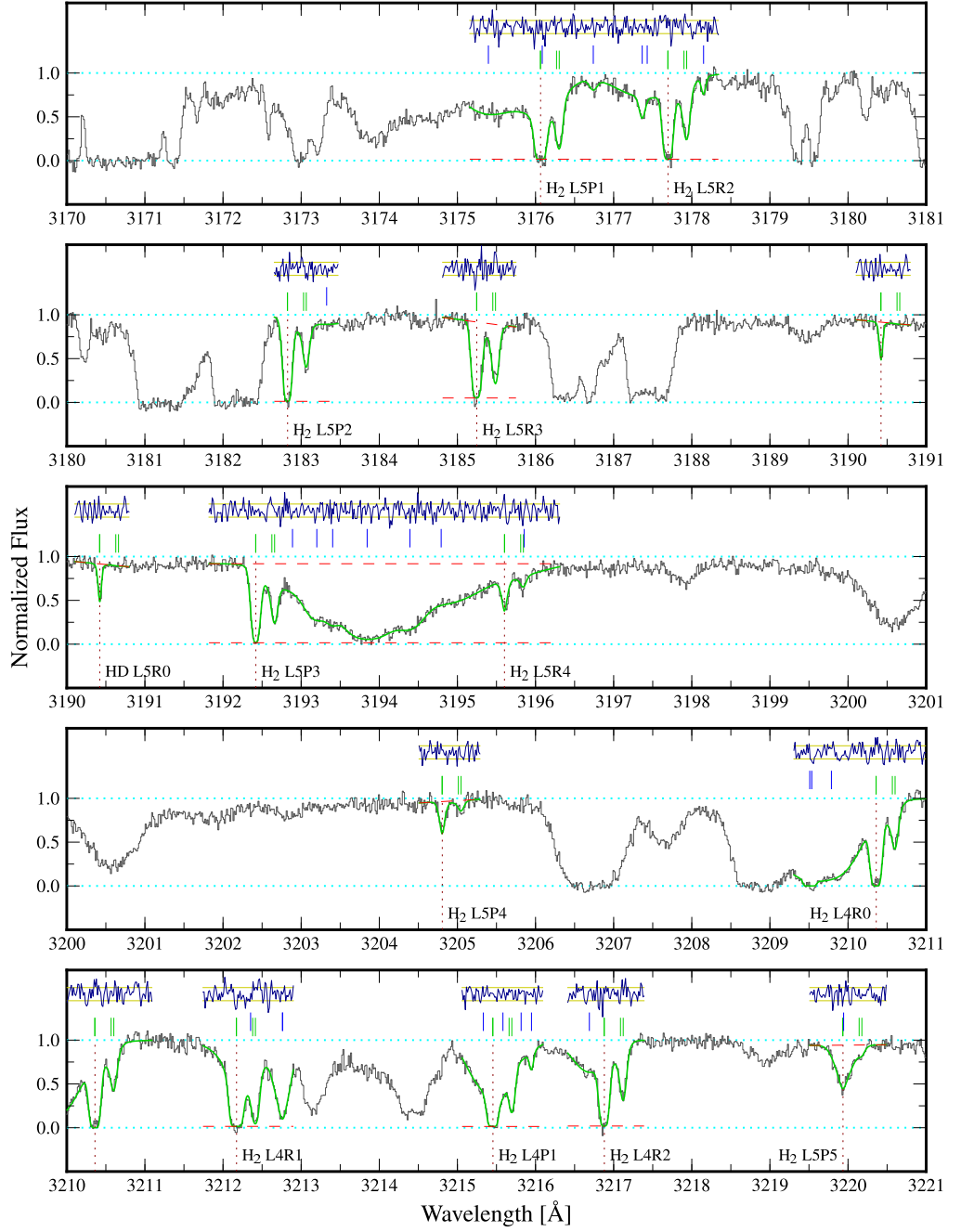


Figure 4.3: (*continued*) Note that the metal-line velocity structure is constrained with the Fe II 1608 transition shown in the final panel of the figure. The residual spectrum (i.e. [data] – [fit]), normalised to the 1- σ errors (faint, horizontal solid lines), is shown above the tick-marks.

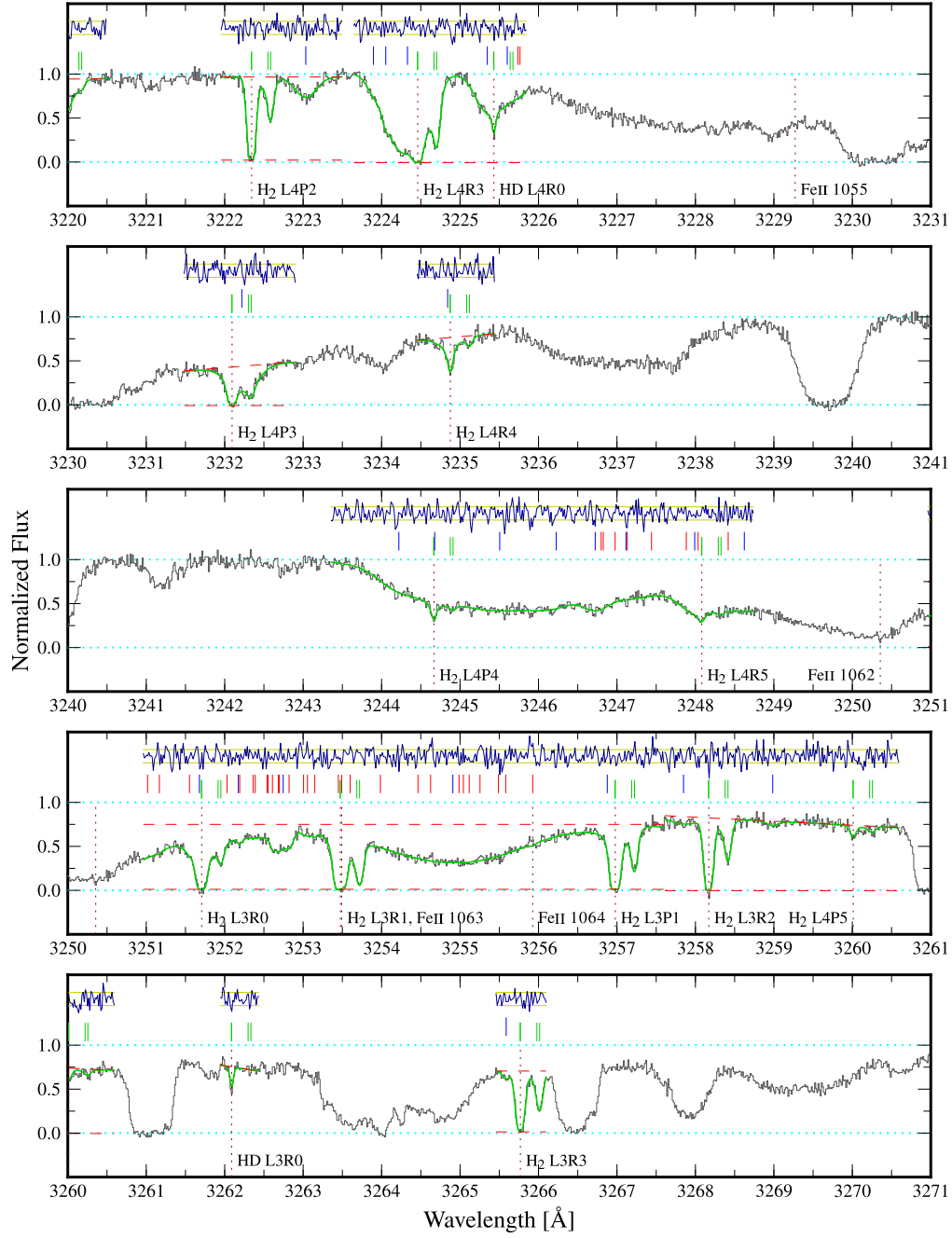


Figure 4.3: (continued)

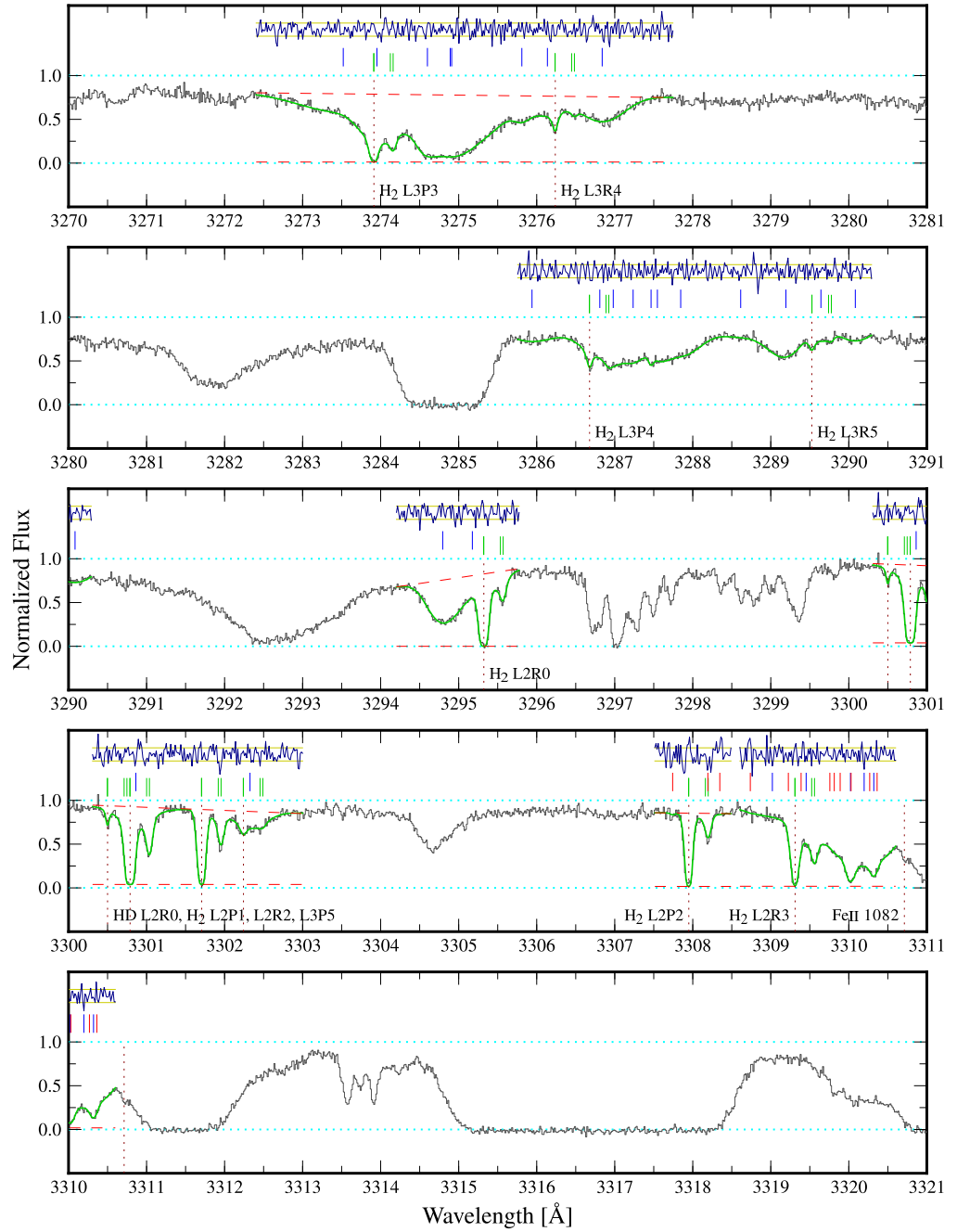


Figure 4.3: (continued)

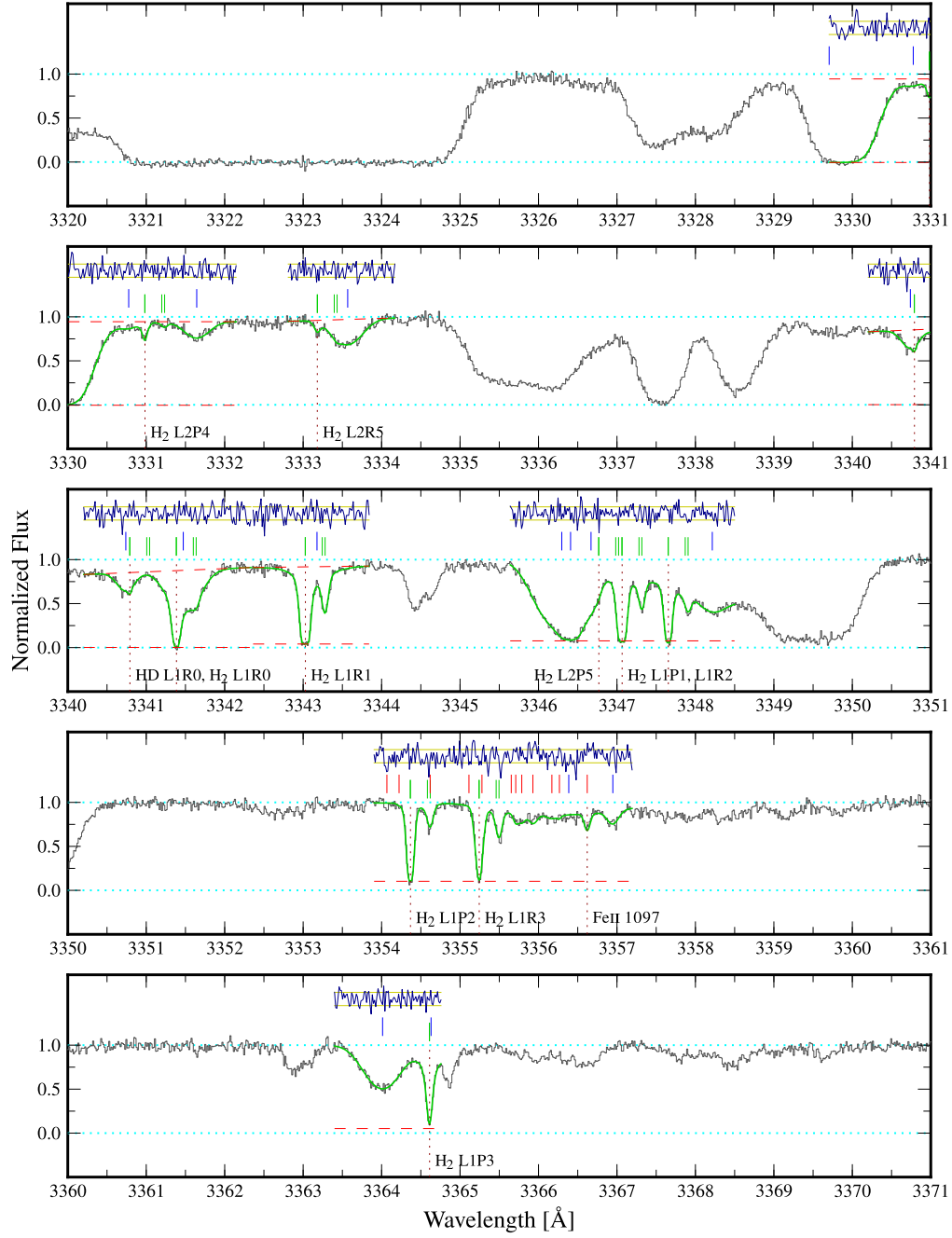


Figure 4.3: (continued)

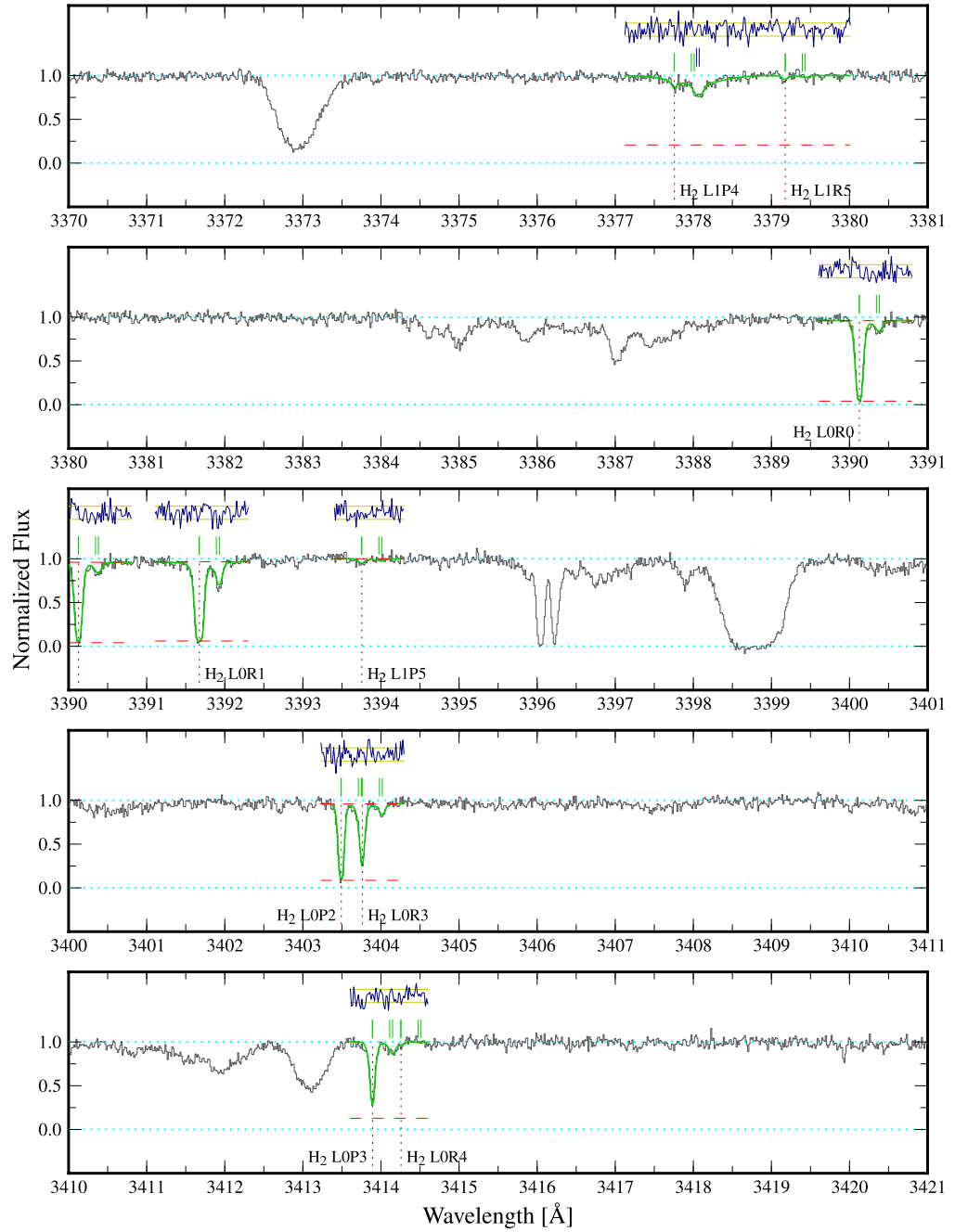


Figure 4.3: (continued)

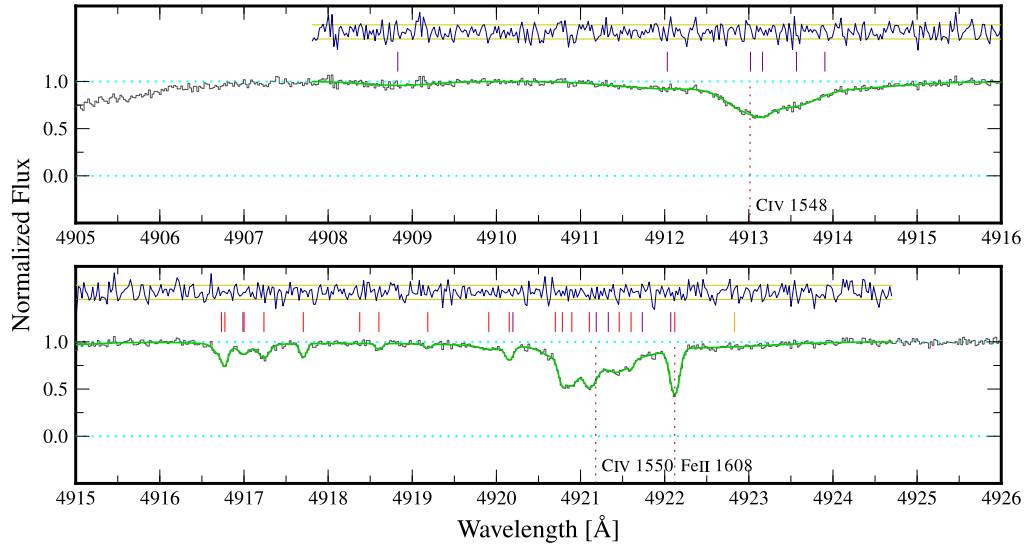


Figure 4.3: *(continued)*

phy et al., 2008b) and $\Delta\mu/\mu$ (Murphy et al., 2008a) when derived from individual absorption systems.

Motivated by this, the velocity structure best representing the molecular absorption profile is determined by fitting models with increasing numbers of molecular VCs and selecting the one with the smallest χ^2 per degree of freedom, χ_ν^2 . This is a simple method for discriminating between different models in χ^2 analyses, but other, similar ‘information criteria’ can also be used (e.g. Liddle, 2007). Key here is the idea that the minimised χ^2 itself must always decrease when more free parameters are added to a model, but χ_ν^2 will begin to *increase* when the additional parameters are not statistically justified. Figure 4.4 (lower panel) shows χ_ν^2 versus the number of molecular VCs in the fit. The 4-component model has a lower χ_ν^2 than the 3-component models and so is statistically preferred. Attempting 5 and 6-component fits results in the additional components being statistically unnecessary – that is, during the χ^2 minimisation process VPFIT finds that the model can be improved by making the additional VCs so weak (i.e. their N parameter values so small) that χ^2 becomes insensitive to *all* of the parameters of these VCs, causing them to be removed. The alternative is to keep the additional VCs in the fit, making it sub-optimal and the final, reduced χ_ν^2 larger than for the fiducial 4-component fit.

Further evidence for a 4-component fit, over 2 and 3-component ones is shown in Figure 4.5, where composite residual spectra (CRS)⁵ are presented for the different fits. For 24 relatively unblended H₂ transitions, the residuals between the data and the model fit are normalised by the flux error arrays, shifted to a common velocity scale and averaged together

$$R_c(v) \equiv \frac{1}{\sqrt{N}} \sum_x \frac{D_x(v) - F_x(v)}{E_x(v)}, \quad (4.1)$$

where v is the common velocity scale, R_c is the CRS, x denotes an included transition, N is the number of transitions, D is the data (i.e. the flux), F is the fit and E is the 1- σ flux error array. The CRS allows one to visually inspect the sum residual structure between the model and the data, serving as a diagnostic of model inadequacies, such as under-fitting. As can be seen in Figure 4.5 the 2-component

⁵Initially described in Section 3.2.2, and described here once more for convenience.

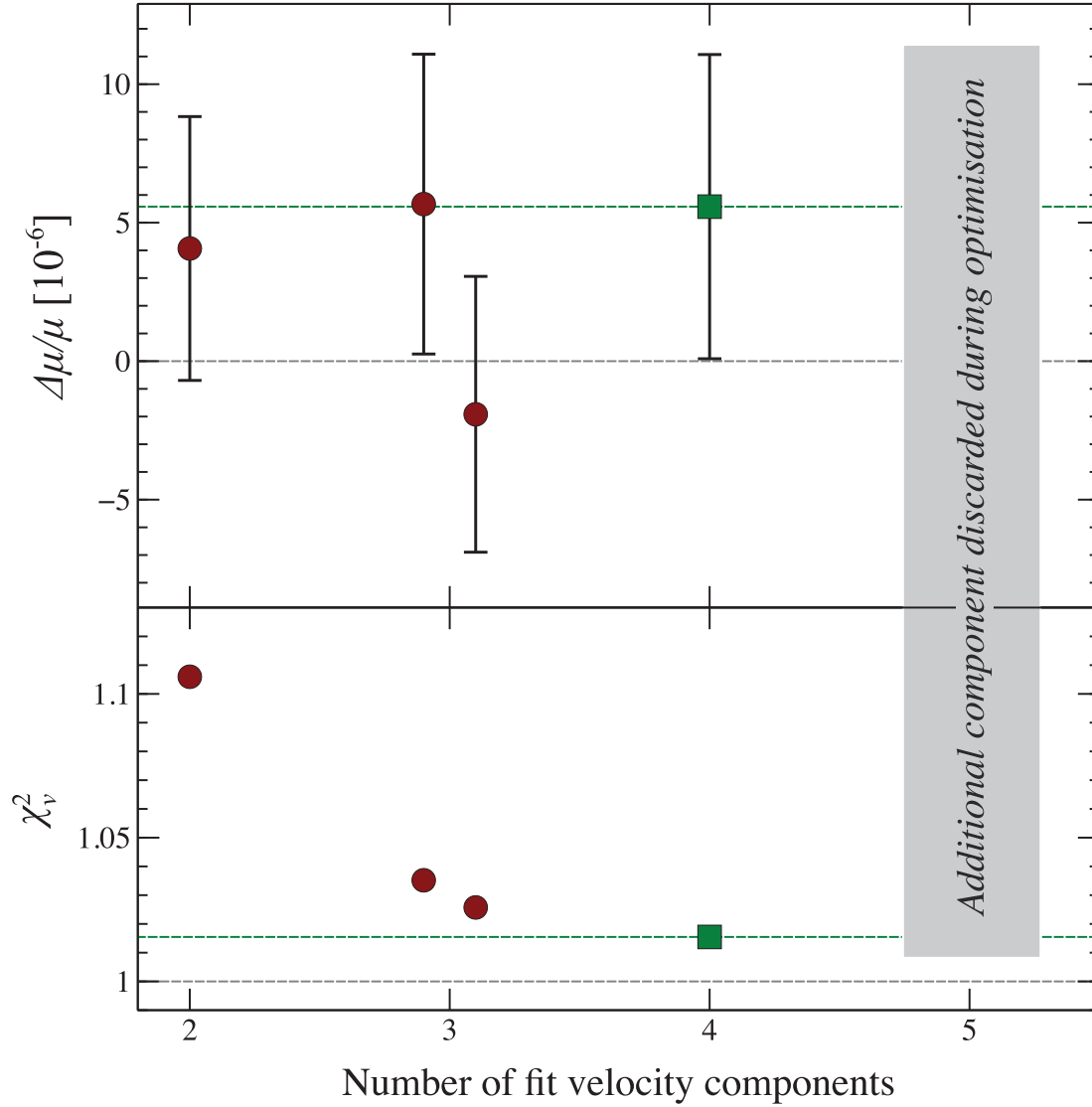


Figure 4.4: $\Delta\mu/\mu$ (upper panel) and χ^2 per degree of freedom, χ^2_ν (lower panel), for different velocity structures characterised by the number of fit absorption components. The 4-component fit, highlighted with square points, has the lowest χ^2_ν and is therefore the statistically preferred model. Two qualitatively different 3-component fits were possible; their results are horizontally offset here for clarity. Note the very different values of $\Delta\mu/\mu$ they return, exemplifying the inherent systematic effects associated with ‘under-fitting’ the absorption profile. The error bars represent 1- σ statistical uncertainties only; systematic errors are discussed in Section 4.5.2.

model fails to reproduce the real absorption profile, with many multi-pixel excursions outside the expected residual range. This is also true for the 3-component fit. Such consistent multi-pixel excursions are indicative of unfit velocity structure in the absorption profile – alleviated by fitting additional VCs. In contrast, the 4-component model leaves no obvious evidence for unmodelled, statistically significant structure.

Figures 4.3 and 4.1 show the fiducial 4-component fit. Table 4.3 provides the molecular cloud properties – z_{abs} , b and the column densities in H_2 and HD – and their formal $1\text{-}\sigma$ statistical uncertainties in all relevant J -levels for each of the 4 VCs.

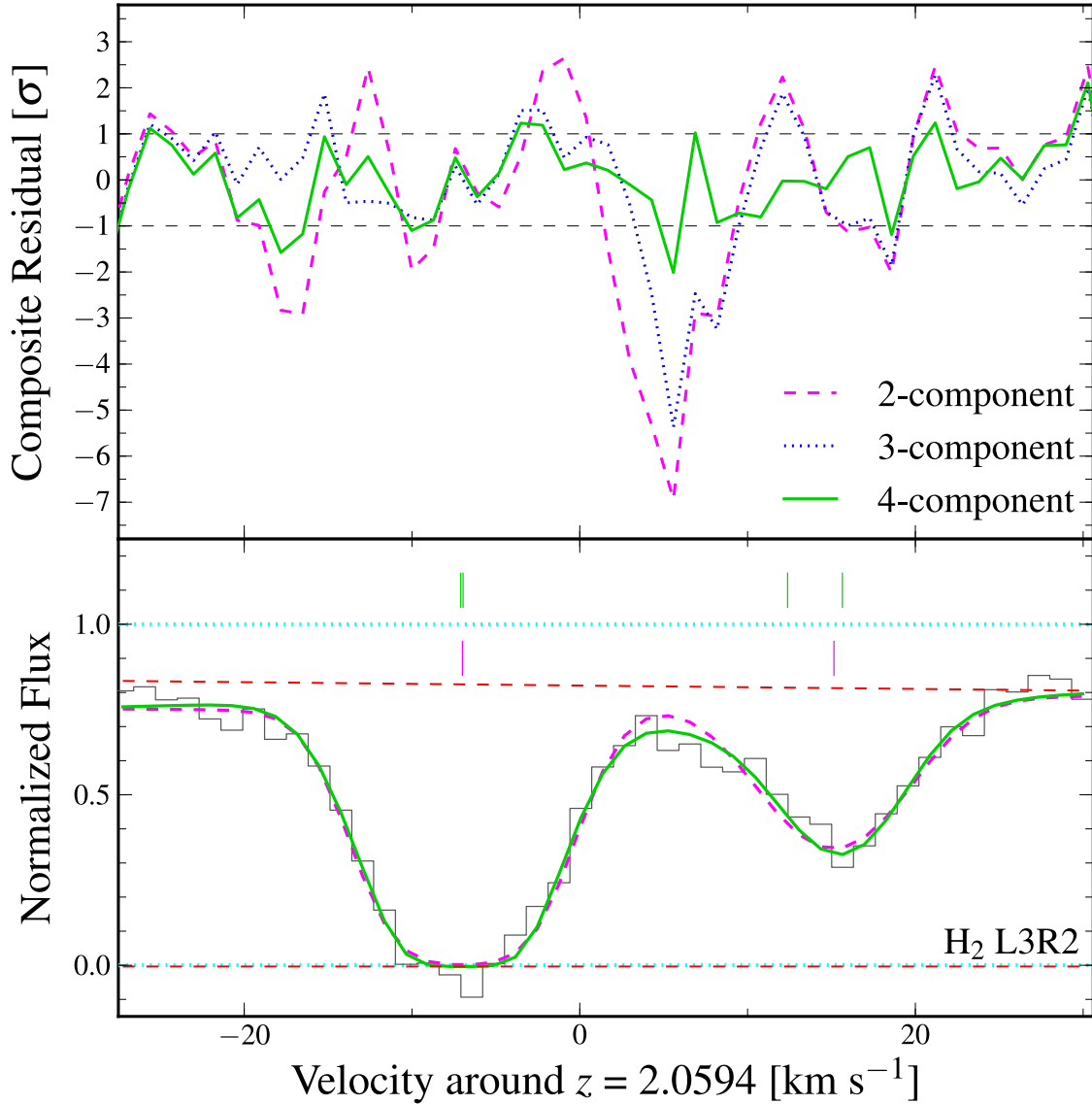


Figure 4.5: Composite residual spectra (CRS), formed from 24 relatively unblended H₂ transitions. *Bottom panel:* An example H₂ transition fitted with the 2 and fiducial 4-component models (dashed and solid curves, respectively). Only a small difference is noticeable by eye. However, the CRS panel above shows how significant the additional components are. *Upper panel:* CRS for the 4-component fiducial model (solid line) and the 2 and 3-component models (dashed and dotted lines, respectively; for clarity only one of the two possible 3-component models is shown here). Note the large, many-pixel excursions outside the $\pm 1\text{-}\sigma$ range for the 2 and 3-component models, indicating unmodelled velocity structure. No such features exist for the 4-component model, as expected.

Table 4.3: Molecular absorption line parameters and $1\text{-}\sigma$ statistical uncertainties for the 4-component fiducial fit in Figure 4.3 and Figure 4.1. Note the assumptions discussed in Section 4.4.1.1 which minimise the number of free parameters. In particular, the ratio of the HD ($J = 0$) velocity component column densities to those of the corresponding H₂ $J=0$ components is the same for all components. The total column density for each H₂ J level and for HD is also provided.

Com- ponent	z_{abs}	b [km s ⁻¹]	$\log N$ [cm ⁻²]	
			H ₂ , $J = 0$	H ₂ , $J = 1$
1	2.0593276(5)	5.14(11)	15.06(3)	15.38(6)
2	2.0593290(4)	1.92(6)	15.80(40)	17.52(4)
3	2.0595264(76)	9.66(90)	13.90(8)	14.30(7)
4	2.0595597(8)	4.02(16)	13.81(6)	14.69(3)
Total			15.88(14)	17.53(4)
			H ₂ , $J = 2$	H ₂ , $J = 3$
1			15.01(3)	15.03(2)
2			16.23(16)	15.16(25)
3			14.10(5)	14.11(7)
4			14.26(4)	14.39(4)
Total			16.26(11)	15.46(4)
			H ₂ , $J = 4$	H ₂ , $J = 5$
1			13.98(4)	13.76(6)
2			13.45(9)	12.78(37)
3			13.31(22)	13.47(15)
4			13.41(9)	13.22(15)
Total			14.23(3)	14.04(4)
			HD, $J = 0$	
1			12.95(3)	
2			13.69(5)	
3				
4				
Total			13.77(3)	

4.4.3 Fiducial result

Once the χ^2 of the absorption model has been minimised, $\Delta\mu/\mu$ is added as a free parameter and the model is χ^2 -minimised once again (as described in Section 4.4.1). For the 4-component fiducial model this gives the result

$$\Delta\mu/\mu = (+5.6 \pm 5.5_{\text{stat}}) \times 10^{-6}. \quad (4.2)$$

It is important to emphasise again that the $1\text{-}\sigma$ uncertainty derives only from the spectrum's photon statistics and is calculated from the relevant diagonal term of the final parameter covariance matrix. Given the range of K coefficients involved (~ 0.05 ; see Figure 4.2), Equation 1.7 implies that this uncertainty corresponds to a velocity precision of $\sim 80 \text{ m s}^{-1}$, or ~ 0.06 spectral pixels.

Figure 4.4 (upper panel) shows the values of $\Delta\mu/\mu$ for different models of the molecular velocity structure as characterised by the number of fit VCs. The two different 3-component fits possible in this system give quite different $\Delta\mu/\mu$ values. Because the different models fit the same transitions and use the same spectra, they are not independent and the statistical error bars cannot be used as a guide of determining the significance of the difference in results. For such highly correlated results one would expect the 3-component fits to lie very closely to each other. The large observed deviation is evidence of a systematic model error, a consequence of ‘under-fitting’. The 2-component model may seem adequate as $\chi^2_\nu \sim 1$, but in comparison to the 4-component fit its χ^2_ν is much larger, and it cannot be preferred in any objective sense. This is also true of the two different 3-component fits.

4.5 Internal consistency and systematic errors

4.5.1 Consistency tests

The consistency and robustness of the result in Section 4.4.3 is explored with a simple convergence test, relaxations of the various assumptions made in Section 4.4.1 and a Monte Carlo test of the fitting algorithm itself.

4.5.1.1 Convergence test

Reliability of the χ^2 minimisation process is confirmed by fitting the real data with a range of starting values to ensure that VPFIT arrived at the same value of $\Delta\mu/\mu$. The default starting value for all the results quoted in this chapter is zero, but starting values of, e.g., ± 10 and $\pm 5 \times 10^{-6}$ gave the same results.

4.5.1.2 Removing blended transitions

The fiducial model in Section 4.4.2 includes all detected molecular transitions that can be fitted reliably. Data quality and degree of Lyman- α blending naturally weights each transition's contribution to $\Delta\mu/\mu$. This is a more objective approach than selecting transitions that are considered the 'best' to fit, or those which are expected, *a priori*, to provide the strongest constraint on $\Delta\mu/\mu$ – a strongly subjective exercise. Nevertheless, as a consistency check, spectral regions containing either no detectable Lyman- α blending or very simple and weak blending are fit. Transitions blended with the Fe II lines described in Section 4.4.1 are also excluded. With 53 H₂ and 5 HD remaining transitions, a 4-component model is statistically preferred and returns $\Delta\mu/\mu = (+5.0 \pm 5.9) \times 10^{-6}$.

4.5.1.3 Removing high J -level transitions

One could argue that because the $J = 4$ and 5 H₂ transitions are weak (typically absorbing < 30% of the local continuum) unmodelled structure in the nearby Lyman- α forest lines and/or local continua for these transitions will have a greater weight on the velocity structure and may therefore influence $\Delta\mu/\mu$. One could also argue this is unlikely because of the low constraining power of weak or shallow absorption lines. To test this, a 4-component fit was constructed, where the 28 $J = 4$ and 5 transitions are prevented from directly influencing $\Delta\mu/\mu$, effectively by setting their K values to zero⁶, returns $\Delta\mu/\mu = (+4.8 \pm 5.6) \times 10^{-6}$. The incremental increase in the statistical uncertainty compared to Equation 4.2 illustrates

⁶Setting $K = 0$ to disable a transition may appear redundant compared to removing the transition from the model altogether. The reader should recall that several molecular transitions are often connected together into one contiguous fitting region because they are in close proximity to each other or blended with the same Lyman- α forest lines (see Section 4.4.2 and Figure 4.3). To remove some individual molecular transitions from the model, entire fitting regions might need to be removed, along with further molecular transitions.

how weak the effect of the $J = 4$ and 5 transitions is on the final $\Delta\mu/\mu$ result, which is expected due to the transitions' low optical depth. The same test, where the μ dependence of the HD transitions is removed in a 4-component model, returns a comparable $\Delta\mu/\mu = (+4.1 \pm 5.8) \times 10^{-6}$. Any effect of the unmodelled structure in the proximate effective continua for these lines is negligible.

4.5.1.4 Free oscillator strengths

In the description of the free parameters and physical assumptions of Section 4.4.1 it is noted that the predicted optical depths for the $J=0-3$ H_2 transitions falling at $\lambda_{\text{obs}} = 3345-3415 \text{ \AA}$ are too low⁷. To take this into account the affected transitions' oscillator strengths were set to be free parameters. This may motivate one to explore the effect these transitions have on the $\Delta\mu/\mu$ results. Removing the μ -dependence of the appropriate transitions, as described in the previous test gives $\Delta\mu/\mu = (+7.0 \pm 6.7) \times 10^{-6}$ for a 4-component fit. The increased statistical error is not unexpected as the $J=0-3$ H_2 transitions removed are strong (the narrower and deeper a transition the more strongly it constrains a velocity shift).

At this point one may be further motivated to test the effect of using fixed (calculated) oscillator strengths for the majority of the transitions. This constraint can be relaxed by allowing *all* 86 H_2 transitions independent oscillator strengths. This is implemented in the same way as for the transitions with the optical depth inconsistency (see Section 4.4.1.1). As before, the pattern of column density values for the individual velocity components is still the same per a given J -level. The weak 7 HD transitions are still associated with the $J = 0$ H_2 transitions. Relaxing constraints like this with a 4-component fit yields $\Delta\mu/\mu = (+5.4 \pm 5.5) \times 10^{-6}$. The statistical uncertainty does not increase discernibly, even though the number of fit parameters has been increased significantly. One could expect this because the many N parameters for the molecular velocity components of each transition have very little influence on the fitted line wavelengths and velocities – the primary source of a $\Delta\mu/\mu$ constraint.

⁷To remind the reader of the suspected cause for this: because the affected transitions fall on the Lyman- β /O IV QSO emission line, it is likely that the inconsistency is a result of some inhomogeneity in the H_2 column density on the angular scale of the QSO broad line region.

4.5.1.5 Free broadening parameters for different J -levels

In the absorption model it is assumed that a given molecular VC has the same b parameter in all J -levels. One can envisage different physical effects which may invalidate this particular model assumption. The approach taken here, one of building up the fit to the molecular lines by adding VCs until all the statistical structure in the molecular line profiles is modelled, may not lend itself to detecting such an effect. While there is no obvious evidence to the contrary in the data, it must be stressed that for a measurement not perceivable ‘by-eye’, such as the $\Delta\mu/\mu$ measurement performed here, one cannot just take into account inconsistencies that may be clearly visible. To relax the b parameter assumption in order to test its effect on the resulting value of $\Delta\mu/\mu$, different sets of b parameters are allowed for different J -levels. This yields $\Delta\mu/\mu = (+7.9 \pm 5.6) \times 10^{-6}$. This change in the value of $\Delta\mu/\mu$ with respect to the fiducial value in equation (Equation 4.2) implies that the b parameter assumptions do have an influence on the results, but that this effect is not great. It is worth noting that relaxing the b parameter assumptions does not resolve the optical depth inconsistency previously discussed.

4.5.1.6 Separate $\Delta\mu/\mu$ parameters for different J -levels

It is possible to measure $\Delta\mu/\mu$ for subsets of transitions at the same time. This is more useful as a test of the robustness of the result itself than as a test of what would have to be an exotic variation in μ . The different J -levels are a natural choice for a set of subsets, where the HD transitions are also considered separately. The resulting values of $\Delta\mu/\mu$ are plotted in Figure 4.6 (left panel). This test is further useful in that it exposes the relative contributions to the final uncertainty on $\Delta\mu/\mu$ from the different sets of H₂ J -level and HD transitions. As per the original model assumptions, which are left intact, the velocity structure is assumed to be the same in all transitions, so the different $\Delta\mu/\mu$ values are not strictly independent. Nevertheless, one can note the general agreement, especially for the H₂ $J=1-3$ transitions. Since the error bars are relatively large for the other J -levels and HD, less uncertain values are obtained by grouping the HD and H₂ $J=0-1$ transitions separately from the H₂ $J=2-5$ transitions, which gives a similar value of $\Delta\mu/\mu$. Note that these results come not from merely a re-binning or averaging of the

previous results, they are two distinct realisations of the absorption model. These results are plotted in Figure 4.6 (right panel).

4.5.1.7 Monte Carlo test of fitting algorithm to determine $\Delta\mu/\mu$

The fiducial fit used to determine $\Delta\mu/\mu$ in the spectrum of J2123–0050 is large and complex. It contains more fitted spectral pixels and more fitted parameters than most, if not all, previous fits of its kind in the literature. The fitted parameters are not all free and independent, but are tied together in a variety of physically meaningful ways, further increasing the complexity of the model. To ensure that the fitting code VPFIT determines $\Delta\mu/\mu$ correctly in this context, a Monte Carlo test is performed using simulated spectra produced from the fiducial fit that was established to the real data. That is, each simulated spectrum is produced simply by taking the fit with 4 molecular velocity components, plus all the fitted Lyman- α forest lines, interloping metal lines, local continuum and zero flux level adjustments, and adding Gaussian noise with a σ of 0.8 times the error array of the real spectrum. This artificially high simulated SNR ensures that Lyman- α blends that are only marginally statistically required in the fit to the real spectrum are not removed when fitting the simulated versions.

Each simulated spectrum is then fitted with VPFIT with initial guess parameters set to be those used to produce the simulated spectrum. An input value of $\Delta\mu/\mu = +5 \times 10^{-6}$ is used to test whether VPFIT recovers that value when started from an initial guess of zero (as is the case in the fits to the real data). Figure 4.7 shows the results of fitting 420 simulated spectra. The mean $1\text{-}\sigma$ uncertainty on individual $\Delta\mu/\mu$ measurements is 4.4×10^{-6} which is the expected value given the value of 5.5×10^{-6} from the real spectrum and a scaling of 0.8 times its flux errors. This corresponds well to the RMS of 4.1×10^{-6} for the 420 $\Delta\mu/\mu$ measurements; it may even be that the individual uncertainties returned by VPFIT are slightly conservative. The mean $\Delta\mu/\mu$ value retrieved is 4.8×10^{-6} and agrees well with expectations.

4.5.1.8 Summary

The above consistency tests indicate that the fiducial value of $\Delta\mu/\mu$ is not strongly dependent on the assumptions made in the 4-component fit. Individually relaxing

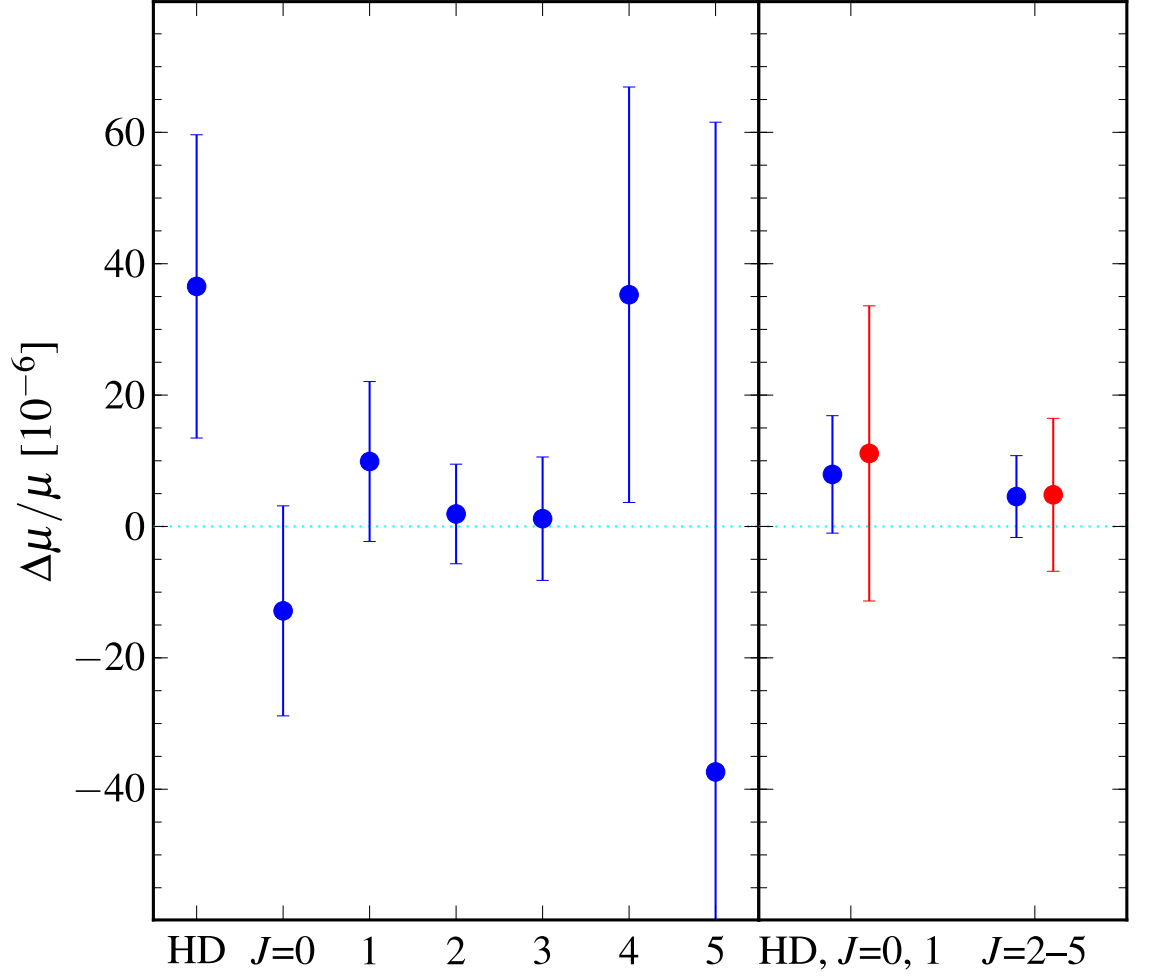


Figure 4.6: *Left panel:* $\Delta\mu/\mu$ for each H_2 J -level and HD, assuming they all have the same 4-component velocity structure. *Right panel:* $\Delta\mu/\mu$ for two groups of transitions, HD plus H_2 $J=0-1$ and H_2 $J=2-5$. The dark/blue points derive from a model assuming the same velocity structure in both groups, whereas the light/red points (offset to the right for clarity) allow the velocity structure for the two groups to differ. Both groups were fitted with a 4-component model in both cases.

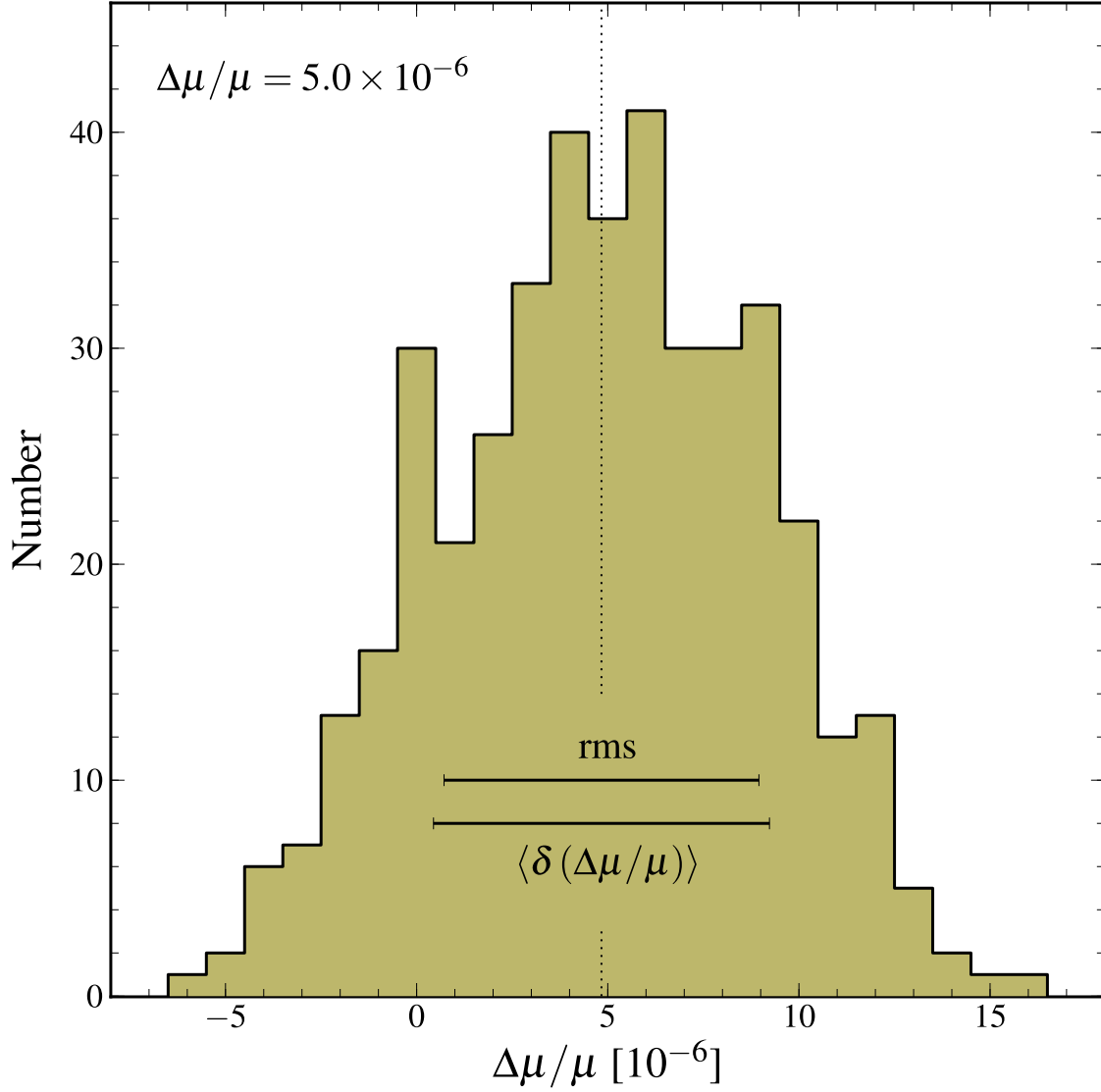


Figure 4.7: 420 Monte Carlo simulations of the fiducial 4 component absorption model used in the analysis. The value of $\Delta\mu/\mu$ returned from the simulated spectra (vertical dotted line) corresponds well to the input value, $+5 \times 10^{-6}$. The mean $1\text{-}\sigma$ error and the standard deviation are shown to be consistent.

these assumptions produces little change in the measured value of $\Delta\mu/\mu$. This is also consistent with there being no important problems with the data, or the analysis presented in this chapter.

4.5.2 Systematic errors

4.5.2.1 ThAr wavelength calibration errors

A varying μ would result in velocity shifts between molecular transitions. Any spurious distortions in the wavelength scale could interfere with the measurement of these shifts and are an important potential source of systematic errors in a $\Delta\mu/\mu$ measurement. Calibration errors in the ThAr calibration process are one such source. It is worth pointing out that as implied by Equation 1.7 the effects which shift the wavelength scale by a constant velocity at all wavelengths are generally unimportant⁸. A simple check of the wavelength scale resulting from ThAr exposures can be obtained from looking at the wavelength calibration residuals. The resulting residuals for the data used here are $\text{RMS} \sim 80 \text{ m s}^{-1}$, and are consistent with being symmetrically distributed around the final wavelength solution at all wavelengths. Because many H_2/HD transitions are used, over a wide range of wavelengths, the overall calibration error is reduced. For the 12 HIRES echelle orders covering the wavelength range where the molecular lines fall (3071–3421 Å), 150–200 ThAr lines are used for wavelength calibration. Systematic trends in the calibration residuals are still possible. Using the same technique employed in Murphy et al. (2007) to track systematic patterns in the ThAr calibration residuals, the possible distortion in the wavelength scale between 3070 and 3430 Å is $<30 \text{ m s}^{-1}$. This corresponds to a systematic error in $\Delta\mu/\mu$ of $\pm 2.0 \times 10^{-6}$ at most.

4.5.2.2 Temperature and atmospheric pressure drifts

The wavelength solutions resulting from the ThAr calibration process are applied to the corresponding QSO exposures. Drifts in the refractive index of air inside HIRES between the ThAr and QSO exposures will therefore cause miscalibrations.

⁸This is not strictly true when many QSO exposures are combined, as is the case here. If different velocity shifts are applied to the different QSO exposures, and if the relative weights of the exposures (e.g. SNRs) vary with wavelength when forming the final, combined spectrum, then small relative velocity shifts will be measured between transitions at different wavelengths.

The temperature and atmospheric pressure drifts during the observations were <1 K and < 1 mbar respectively. According to the Edlen (1966) formula for the refractive index of air, this would cause *differential* velocity shifts between 3070 and 3430 Å of <10 m s⁻¹, which are negligible.

4.5.2.3 Intra-order wavelength distortions

The QSO and ThAr light traverse similar but not identical paths through the HIRES instrument. The ThAr light illuminates the slit almost uniformly, while the QSO light is centrally concentrated and passes through the telescope itself. Different distortions of the wavelength scale may therefore occur in the QSO and corresponding ThAr exposures. Distortions may appear in individual echelle orders (intra-order distortions) and over longer wavelength ranges (long-range distortions).

Griest et al. (2010) have identified the presence of intra-order distortions in HIRES (see Section 3.4.3 for discussion as relevant for the $\Delta\alpha/\alpha$ constraint in this thesis). They compared the wavelength scales established using ThAr exposures with those imprinted on QSO exposures by an iodine absorption cell. The distortions are such that, for different transitions at the same redshift in a QSO spectrum, those at the echelle order edges (the extreme wavelengths of a given echelle order) appear at positive velocities with respect to transitions at the order centres when calibrated with a ThAr exposure. The peak-to-peak velocity distortion is ~ 500 m s⁻¹ at ~ 5600 Å and may grow for redder wavelengths (and conversely shrink for bluer wavelengths) see Figure 4 of Griest et al. (2010). The effect is of similar, but not identical, shape for all echelle orders in the wavelength range ~ 5000 – 6200 Å covered by the iodine cell absorption. It is assumed that such distortions are present in the same form and amplitude at much bluer wavelengths, and that similar intra-order distortions apply to the HIRES spectra of J2123–0050 used here. Because the molecular transitions of interest lie at different positions along different echelle orders, one should expect the effect on $\Delta\mu/\mu$ to be suppressed. To illustrate this, a very crude estimate of the ‘residual’ velocity distortion is just the observed ~ 500 m s⁻¹ peak-to-peak intra-order value reduced according to the number of molecular transitions observed, i.e. ~ 500 m s⁻¹/ $\sqrt{93} \approx 52$ m s⁻¹. This corresponds to a systematic error in $\Delta\mu/\mu$ of approximately $\pm 3.5 \times 10^{-6}$.

However, this calculation fails to take into account the strong variation in the

spectral SNR across the wavelength range containing the H₂/HD transitions, their different sensitivities to μ variation, where they fall with respect to echelle order edges in the data and other factors such as the degree of blending with Lyman- α forest lines of each molecular transition. A simple Monte Carlo simulation which takes into account the first two of these effects, SNR and K for each transition, is performed as follows. Each realisation comprises a velocity shift, Δv_i , chosen randomly for each transition, i , from the 500 m s^{-1} peak-to-peak interval spanned by the intra-order distortions identified by Griest et al. (2010). The square of the SNR of the spectral data surrounding the molecular transitions is then used as a weight in a linear least squares fit of the $\Delta v_i/c$ versus K values, the slope of which provides a value of $\Delta\mu/\mu$ for that realisation (see Equation 1.7). The distribution of values for $\Delta\mu/\mu$ over hundreds of thousands of Monte Carlo realisations is close to Gaussian with an RMS of 4.8×10^{-6} .

Another approach, one that offers a more direct and realistic calculation of the possible systematic effect on $\Delta\mu/\mu$ and takes into account all remaining effects (e.g. positions of transitions with respect to order edges, line blending etc.), can be obtained by attempting to remove the intra-order distortions from the individual QSO exposures. To this end, a -250 m s^{-1} velocity shift is applied to the wavelengths of all echelle order centres for all of the QSO exposures. The shift is reduced linearly with distance from the order centres to reach $+250 \text{ m s}^{-1}$ at the order edges. The spectra are recombined again to form a final 1-dimensional spectrum to which the 4-component model was fit as before. The value of $\Delta\mu/\mu$ derived from this ‘corrected’ spectrum is $(+3.7 \pm 5.5) \times 10^{-6}$. Compared with the fiducial 4-component result of $(+5.6 \pm 5.3) \times 10^{-6}$, this represents a smaller effect, approximately $\pm 1.9 \times 10^{-6}$, than expected from the cruder estimates above. The main assumption in this estimate is that the Griest et al. intra-order distortions are being modelled reliably. Because the physical explanation for those distortions is not yet known, it is not yet reliably known whether, for example, the phase and pattern of the distortions is the same, varies or itself follows some function across all QSO exposures taken at different times and with different telescope and observational conditions (e.g. telescope pointing direction, seeing etc.). What is known is that these distortions are ever-present in the exposures across all observed wavelengths. These important questions should be resolved with future observations and

careful re-calibrations of HIRES. Concluding, it is thus important to state that the estimate of $\pm 1.9 \times 10^{-6}$ for the systematic error due to intra-order distortions may also itself be subject to model errors.

4.5.2.4 General, unknown wavelength calibration errors

The general pattern in Figure 4.2 is one of a decrease in the K coefficients with increasing wavelength, for the fitted *Lyman* H₂ transitions. Because of this, a systematic, long range, monotonic distortion of the wavelength scale could be mistaken for or mask a result, i.e. a shift in μ for the Lyman lines. This strong systematic effect on $\Delta\mu/\mu$ is only possible if the Lyman H₂ transitions are fit without other transitions to break the degeneracy. Therefore, it is important to fit the Werner transitions as well: the pattern of the Werner K values is different to the Lyman K values at similar wavelengths, improving resistance to systematic errors. If the μ -dependence of the 12 H₂ and 1 HD Werner transitions are removed in the fit a 4-component model is statistically preferred and returns $\Delta\mu/\mu = (+5.2 \pm 5.6) \times 10^{-6}$, a result very similar to the fiducial result in Equation 4.2.

However, the SNR at bluer wavelengths where the Werner transitions fall is much lower than for the reddest Lyman transitions, so the effect of the Werner transitions in breaking this degeneracy between $\Delta\mu/\mu$ and long-range wavelength distortions is reduced. To illustrate this such a distortion is inserted into a simulated version of the spectrum. The wavelength scale for one of the Monte Carlo realisations from Section 4.5.1 was compressed according to

$$\frac{\Delta v_j}{c} = \left(\frac{\Delta\mu}{\mu} \right)_{\text{sys}} (a\lambda_j + b) , \quad (4.3)$$

where λ_j is the initial (observed) wavelength of a given pixel, Δv_j is the velocity shift applied to it, $(\Delta\mu/\mu)_{\text{sys}}$ is the systematic error in $\Delta\mu/\mu$ that is being mimicked, and the constants a and b are set to mimic the general decrease in K with increasing wavelength for the Lyman transitions (see Figure 4.2). To obtain a spurious shift in $\Delta\mu/\mu$ of approximately $+15 \times 10^{-6}$, $(\Delta\mu/\mu)_{\text{sys}}$ is set to 15×10^{-6} , $a = -1.3 \times 10^{-4} \text{ \AA}^{-1}$ and $b = 0.4345$. When this spectrum is fit with the fiducial model used to generate it, $\Delta\mu/\mu$ shifts from 4.0×10^{-6} before compression to 16.2×10^{-6} after compression, as expected from the design of this experiment. When the μ -

dependence of the 12 H₂ and 1 HD Werner transitions is removed when fitting the compressed spectrum, $\Delta\mu/\mu$ changes only by a small amount to 17.3×10^{-6} . This confirms that simply removing the Werner transitions' dependence on μ is not a very effective test for long-range distortions of the wavelength scale.

A more meaningful test is to fit only the Lyman and Werner transitions in the bluest part of the spectrum and not the redder Lyman transitions. If the 51 Werner and Lyman lines bluewards of $\lambda_{\text{obs}} = 3230 \text{ \AA}$ are fit in the simulated spectrum, $\Delta\mu/\mu$ only shifts from 6.1 to 7.4×10^{-6} when the compression is introduced, indicative of the expected resistance to this systematic error. Still using the simulated spectrum, when the μ -dependence of the 12 H₂ and 1 HD Werner transitions is removed in the fit, $\Delta\mu/\mu$ changes from 7.6 before compression to 11.3×10^{-6} after compression. This suggests that if there indeed exists a long-range, monotonic distortion of the wavelength scale, one should expect a substantial shift in $\Delta\mu/\mu$ when the μ -dependence of the Werner transitions is removed. When this test is applied to the real spectrum, a value of $\Delta\mu/\mu = (+12.1 \pm 11.7) \times 10^{-6}$ is derived when only the Lyman and Werner lines bluewards of $\lambda_{\text{obs}} = 3230 \text{ \AA}$ are fit. When the μ -dependence of the Werner transitions is removed, this result changes to $\Delta\mu/\mu = (+12.8 \pm 14.3) \times 10^{-6}$. This robust test for long-range distortions of the wavelength scale does not suggest such an effect is present in the spectrum of J2123–0050 used here.

4.5.2.5 Errors from spectral re-binning

The VPFIT software used for fitting the data assumes the fluxes (and flux uncertainties) in neighbouring spectral pixels are uncorrelated. This is not true in practice. The spectrum to which the absorption model is fit is the weighted mean of several individual QSO exposures. In combining these spectra, the different QSO exposures are *re-binned* onto the same final wavelength grid for combination into a single spectrum (this is also referred to as re-dispersion). Note that the data reduction procedure used by HIRES REDUX ensures that each exposure is only re-binned once. Nonetheless, the re-binning introduces inter-pixel correlations in the fluxes and their errors. Note that the correlations are not increased by the process of taking the weighted mean of the re-binned the exposures – if anything, the autocorrelation of the final spectrum is actually smaller than that of individual

exposures. In principle, the re-binning should have a small effect on the fitted centroid of any spectral feature and so, even though many molecular lines are fit simultaneously, a residual effect on $\Delta\mu/\mu$ may exist. To test the possible size of this effect the QSO exposures are further re-combined onto a variety of slightly different wavelength grids with different dispersions (i.e. km s^{-1} per pixel) and wavelength zero points. The values of $\Delta\mu/\mu$ derived from these different versions of the final combined spectrum varied by $\pm 0.8 \times 10^{-6}$ at most – a small systematic effect.

4.5.2.6 Velocity structure uncertainties

One of the assumptions made in constructing the fiducial absorption model is that the molecular velocity structure is the same in all J -levels. In a Galactic line of sight with H_2 absorption, Jenkins and Peimbert (1997) found that (part of) the absorption profile becomes broader and systematically shifts in velocity with increasing J . In such cases the absorption profiles actually have many velocity components (VCs), spanning velocities greater than the broadening and shifting observed. This is, in fact, consistent with the velocity structure being the same in all J -levels where some constituent VCs have low optical depths in the low- J transitions but are relatively strong in the higher- J transitions. If the fit velocity structure used as many VCs as required to model all the statistically significant structure in the observed line profiles, the individual VCs might not necessarily broaden or shift with increasing J . Instead, the relative column densities of neighbouring VCs would change with increasing J . However, if any significant unmodelled structure remains, and its effective optical depth varies as a function of J , it may cause a systematic effect in $\Delta\mu/\mu$. An example of this effect in an H_2 -bearing QSO absorber was identified by Noterdaeme et al. (2007).

Ivanchik et al. (2005) considered this possibility, pointing out that the potential effect on $\Delta\mu/\mu$ is diminished because transitions of different J are interspersed in wavelength space. This is evident in Figure 4.2 (lower panel). While Figures 4.4 and 4.5 demonstrate that all the statistically significant structure in the molecular transitions has been modelled, a direct test for this effect can still be performed by allowing $\Delta\mu/\mu$ and the velocity structure to be different for different H_2 J -levels and HD. In Section 4.5.1 only the former assumption is tested. It has to be noted again that for a test to be stringent, with relatively small statistical uncertainties,

grouping together different H₂ J -level and HD transitions is necessary. For this test, the assumption of a common velocity structure is relaxed by introducing different VC redshifts as free parameters. This is expected to lead to even larger uncertainties than previous tests, because now the z_{abs} parameter values, which up to this point have been kept ‘tied’, are now going to be allowed some level of independence for the different H₂ J -levels and HD (or groups thereof). As in Section 4.5.1 two separate $\Delta\mu/\mu$ results are obtained from the same data by grouping the transitions into two groups: low- J (HD and H₂ $J=0-1$) transitions and high- J (H₂ $J=2-5$) transitions. Each has a different 4-component model and $\Delta\mu/\mu$. Both groups are fit simultaneously with the same assumptions about N parameters as for the fiducial model. The two resulting values are shown in Fig. 4.6 (right panel), with no strong evidence for the effects of unmodelled velocity structure as a function of species (H₂ J -level or HD).

4.6 Discussion

The final result for the $z_{\text{abs}} = 2.059$ absorber observed in the Keck spectrum of J2123–0050 is

$$\Delta\mu/\mu = (+5.6 \pm 5.5_{\text{stat}} \pm 2.9_{\text{sys}}) \times 10^{-6}. \quad (4.4)$$

This includes the $1-\sigma$ statistical error (see Equation 4.2) and the quadrature addition of the three main potential systematic errors discussed in Section 4.5.2: long and short-range wavelength calibration errors and effects from re-dispersion of the spectra. It is difficult to estimate the confidence level represented by the quoted systematic error component, though it is likely to represent a higher confidence (i.e. >68 per cent) than the $1-\sigma$ level represented by the quoted statistical uncertainty. Note that the systematic error estimate for short-range calibration errors is based only on the limited information about intra-order wavelength distortions currently accessible (Griest et al., 2010). This estimate is therefore model-dependent and may under or over-estimate the true effect⁹.

The result in Equation 4.4 is based on fitting an absorption profile model to

⁹The reader is reminded that the material presented in this chapter is current as of 2010, as noted in the Foreword. Significant long-range distortions have now been found to be common in Keck and VLT spectra (Whitmore and Murphy, 2015) and taken into account in some recent analyses of H₂ for constraining $\Delta\mu/\mu$ (e.g. Bagdonaite et al., 2014; Rahmani et al., 2013).

the spectrum of J2123–0050, utilising a total of 86 H₂ and 7 HD transitions. Most of these are blended to varying extents with broader Lyman- α forest lines. A few blend with well-constrained, weak metal absorption. All these lines, together with any necessary local continua and zero flux level adjustments, are fitted simultaneously to determine a single, best-fit value of $\Delta\mu/\mu$. To reduce the number of free parameters in the fit, two main physically motivated assumptions are made about the molecular transitions: that the velocity structure is the same for all J -levels and that individual velocity components have the same Doppler broadening parameter in all J -levels. As the HD lines are weak, it is assumed that the HD ($J = 0$) velocity components follow the same relative optical depth pattern as the H₂ $J = 0$ transitions. Finally, the oscillator strengths of some H₂ transitions are effectively treated as free parameters because their optical depths are higher than expected based on the fiducial absorption model. After individually relaxing these assumptions, the fiducial result in Equation 4.4 is found to remain robust.

4.6.1 Comparison to other astrophysical $\Delta\mu/\mu$ constraints

Figure 4.8 compares the contemporary astronomical $\Delta\mu/\mu$ constraints outside the Galaxy. The new constraint presented in this work is the first from Keck with precision comparable to those from the VLT. Agreement is seen between the Keck result and the three VLT constraints from King et al. (2008) who used similar calibration and fitting techniques to those described here. Such consistency is encouraging, allowing a weighted mean¹⁰ value of $\Delta\mu/\mu = (+3.5 \pm 2.8) \times 10^{-6}$ for redshifts $z = 2.0$ – 3.1 . Statistical errors are shown as thinner error bars with shorter terminators in Figure 4.8. Although the statistical error in this work’s new measurement is slightly smaller than for two of the King et al. (2008) absorbers, it is slightly worse than for the $z_{\text{abs}} = 2.811$ absorber towards Q 0528–250, i.e. 3.9×10^{-6} . The main reason for this is the lower SNR of the Keck spectrum of J2123–0050 used here, despite the fact that its spectral resolution is higher and more molecular transitions were utilised in the analysis. Since J2123–0050 is relatively bright, improvements in both the statistical and systematic uncertainties can be achieved

¹⁰The statistical and systematic error components of this work’s results were added in quadrature for this calculation. No systematic error estimates are available for the King et al. results.

with new observations of moderate duration¹¹.

At $z < 1$, comparison of the radio inversion transitions of NH_3 – which have enhanced sensitivity to μ -variation (van Veldhoven et al., 2004; Flambaum and Kozlov, 2007) – with less sensitive molecular rotational lines (e.g. HCO^+ , HCN), has yielded two very strong constraints, $\Delta\mu/\mu = (+0.74 \pm 0.47_{\text{stat}} \pm 0.76_{\text{sys}}) \times 10^{-6}$ at $z = 0.685$ (Murphy et al., 2008a) and $(+0.08 \pm 0.47_{\text{sys}}) \times 10^{-6}$ at $z = 0.889$ (Henkel et al., 2009). These results are plotted in Figure 4.8 for comparison with the higher redshift H_2/HD constraints. It is clear that the radio constraints have superior precision and, by current estimates, smaller potential systematic errors. However, direct comparison of the radio and optical constraints is difficult because of the possibility, in principle, for spatial variations in μ : the different molecular species (NH_3 and H_2/HD) trace regions of different densities and, therefore, different spatial scales and environment. If μ does vary, one does not know what that variation depends on, so it is presumptuous to prefer one type of measurement over the other. Indeed, this is highlighted by Levshakov et al. (2008) who studied NH_3 inversion *emission* lines from numerous Galactic molecular clouds. With statistical errors from previous literature of $\sim 0.1 \text{ km s}^{-1}$ they find velocity offsets between the NH_3 inversion and rotational molecular emission of up to $|\Delta v| \sim 0.5 \text{ km s}^{-1}$ in individual systems. This might indicate spatial variations in μ throughout the Galaxy, although intrinsic shifts between emission lines of different molecules are to be expected. The possibility for both space and time-variations in μ is even more important given the different redshift ranges currently probed by the radio and optical constraints.

4.6.2 Reanalysis using VLT data for J2123–0050

Since it is located near the celestial equator, J2123–0050 enables analysis using data from two independent telescopes, as it can be observed from both Keck and VLT. This is realised in van Weerdenburg et al. (2011) with a VLT-based constraint of $\Delta\mu/\mu = (+8.5 \pm 3.6_{\text{stat}} \pm 2.2_{\text{sys}}) \times 10^{-6}$. This is in agreement with the final result in this work (Equation 4.4), and provides perhaps the best consistency check of the

¹¹As demonstrated by van Weerdenburg et al. (2011), who obtain a statistical error of 3.6×10^{-6} using VLT observations of the object (see Section 4.6.2).

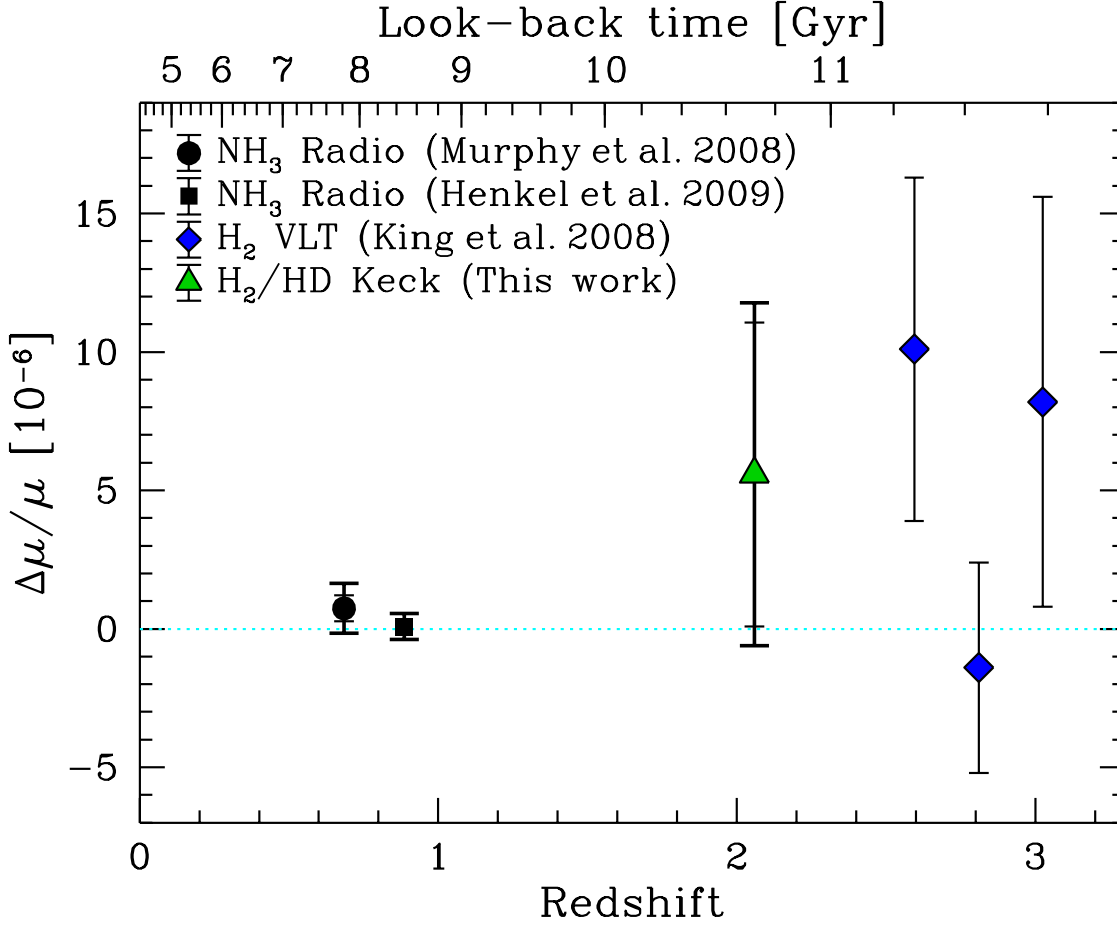


Figure 4.8: Current extragalactic $\Delta\mu/\mu$ constraints. The legend gives the reference for each point and the method used, i.e. H₂ or NH₃ QSO absorption lines. $1\text{-}\sigma$ statistical uncertainties are indicated with thinner error bars with shorter terminators while the thicker error bars with longer terminators show the systematic error added in quadrature with the statistical ones. Diamonds represent the VLT constraints; the new measurement presented in this work is the only one from Keck. Note that two of the King et al. (2008) absorbers use the same raw VLT data as those analysed previously by Ivanchik et al. (2005) and Reinhold et al. (2006). The results of those two studies are omitted, assuming that the improved analysis in King et al. has yielded more reliable results. For clarity, the other recent re-analyses of the same two absorbers by Wendt and Reimers (2008) and Thompson et al. (2009) are also omitted; these works also yielded null results with somewhat larger errors than reported by King et al.. A reminder to the reader that this is the data as at the time Malec et al. (2010a) was published, as noted in the Foreword.

work in this chapter¹².

¹²The methodology in van Weerdenburg et al. (2011) was largely based on Malec et al. (2010a) and therefore this thesis chapter. One can assume the results to be very comparable but still independent. The author of this thesis co-authored the van Weerdenburg et al. (2011) study and assisted in the fitting of the VLT data.

5

Conclusions

Contents

5.1 Summary	157
5.2 Future work	160

5.1 Summary

In this thesis QSO absorption spectra were used to constrain variations of two fundamental constants: α , the fine structure constant and μ , the proton-to-electron mass ratio. Spectra from observations specifically performed for this thesis and archival spectra from Keck/HIRES and VLT/UVES were analysed, suggesting no variation in α or μ at high redshift, to precisions of order parts per million. The main conclusions of this work are summarised below.

1. In Chapter 2 the exclusive use of Zn II and Cr II transitions in constraining $\Delta\alpha/\alpha$ was investigated, in contrast to full many-multiplet (MM) fits, where all available transitions are used. This approach carries significant advantages. The Zn/Cr II transitions shift in opposite directions as α varies, with the Zn II 2062 line interlacing with the Cr II transitions. This complex pattern of shifts is unlikely to be systematically mimicked by wavelength scale distortions in spectra, in contrast to MM fits relying on Mg/Fe II transitions, which render $\Delta\alpha/\alpha$ analyses vulnerable to systematic errors due to long-range wavelength distortions. The Zn/Cr II transitions have similar wavelengths, where

full MM fits use transitions over a wide range of wavelengths. This further reduces the effects of long-range wavelength distortions on $\Delta\alpha/\alpha$ analyses, proven to be ubiquitous in both HIRES and UVES by Whitmore and Murphy (2015). Finally, the optical depths of the two sets of transitions are typically very similar in known Zn/Cr II absorbers, allowing for more consistent and reliable parameterisation of the fits. While short-range wavelength distortions (Griest et al., 2010; Whitmore et al., 2010) are expected to affect $\Delta\alpha/\alpha$ measurements utilising the relatively small number of Zn/Cr II transitions, it was not expected that these would be significant for the QSO absorber sample of this work. To demonstrate this, the systematic errors due to both the long and short-range wavelength distortions were quantified for the sample presented in this work. The error due to long and short-range wavelength distortions was estimated to be $\delta(\Delta\alpha/\alpha)_{\text{long}} = 0.75 \times 10^{-6}$ and $\delta(\Delta\alpha/\alpha)_{\text{short}} = 0.87 \times 10^{-6}$, respectively. These two errors were the main contributors to the systematic error budget.

2. Systems exhibiting Zn II and Cr II lines that are strong enough for varying α analyses are known to be very rare, as found in “metal-strong” surveys for such systems (e.g. Herbert-Fort et al., 2006). Only a subset of these are found to be adequate for Zn/Cr II-based $\Delta\alpha/\alpha$ analyses, due to observational constraints. Keck/HIRES and/or VLT/UVES observations and archival data of 9 systems suitable for effective $\Delta\alpha/\alpha$ constraints were reduced, with particular attention given to calibration of the spectral wavelength scales. The rarity of these systems, along with their unique advantages for constraining $\Delta\alpha/\alpha$, suggests that any such constraint will be qualitatively very different in nature to previous and most, if not all, other future constraints. The work presented here demonstrated that such high-value absorbers can be selected from the existing spectra and metal-strong surveys. It was demonstrated that such systems can yield competitive constraints compared to full MM analyses or larger samples, with precisions for each absorber ranging from 3.7 to 13.7 parts per million, given the range in SNR of the spectra (27 to 100 per 1.3 km s^{-1} pixel).
3. In Chapter 3 the Zn/Cr II absorption in the 9 systems was modelled using

Voigt profile fits, and individual $\Delta\alpha/\alpha$ constraints were obtained using the MM method with the subset of Zn/Cr II lines. The final constraint was measured to be $\Delta\alpha/\alpha = (0.04 \pm 1.69_{\text{stat}} \pm 1.15_{\text{sys}}) \times 10^{-6}$ and is consistent with no temporal variation in α for the range of absorption redshifts in this sample ($z_{\text{abs}} = 1.072 - 2.308$) for the given precision. The result uses a weighted mean of the individual constraints, statistical errors derived from the flux error arrays of the fitted spectral regions and conservative estimates of systematic errors on the whole sample due to known long and short-range distortions of the wavelength scale added in quadrature. This null result is suggestive of no variation with cosmological time. Because of the low angular separations amongst the sample, it was not possible to derive a meaningful constraint on the spatial variation of α . The result presented here will benefit from a further, exhaustive exploration of systematic effects as noted in Section 5.2; however, the major noise sources are expected to be already included in the error terms here, and so the final result is not expected to differ greatly.

4. In Chapter 4 an absorption profile model was fit to the molecular absorption of a Keck/HIRES spectrum of J2123–0050 at $z_{\text{abs}} = 2.059$, utilising a total of 86 H₂ and 7 HD transitions. As part of the fit, broad Lyman- α forest lines, some weak, blending metal absorption lines, along with local continua and zero flux level adjustments, were also fitted simultaneously to determine a single, best-fit value of $\Delta\mu/\mu$. To reduce the great number of free parameters in the fit, physically motivated assumptions were made about the molecular transitions. The systematic error term was calculated as the quadrature addition of the three main potential systematic errors discussed: long and short-range wavelength calibration errors and effects from re-dispersion of the spectra. The final constraint was measured to be $\Delta\mu/\mu = (+5.6 \pm 5.5_{\text{stat}} \pm 2.9_{\text{sys}}) \times 10^{-6}$, and is consistent with no temporal variation in μ for the given precision. The result uses statistical errors derived from the flux error arrays of the fitted spectral regions and the before-mentioned systematic error term.
5. A wide suite of consistency tests were performed, including relaxing the assumptions used in constraining $\Delta\mu/\mu$, convergence tests of the χ^2 minimisation procedure, removing subsets of transitions and Monte Carlo verification

of the fitting process. Further, a thorough search for systematic errors was conducted, including wavelength calibration errors, distortions of the wavelength scale, errors from spectral re-binning and errors due to uncertainties in the fitted velocity structure. The above $\Delta\mu/\mu$ result was found to remain robust after all of these tests. This battery of tests has become standard in subsequent H_2/HD varying μ studies (e.g. Bagdonaite et al., 2014). The analysis in van Weerdenburg et al. (2011), of a UVES spectrum of the same J2123–0050 sightline studied here, followed the same approach developed in this thesis. The results were found to be in agreement with the constraint presented here.

5.2 Future work

The $\Delta\alpha/\alpha$ constraint presented in this work may be the only of its kind for some time to come, because of the rarity of metal-strong Zn II and Cr II absorbers that are suitable for varying α analyses. A number of the exceptional absorbers in this sample could benefit from additional observations to increase the SNR, as this is the most direct path to improving the statistical precision of the measurements. More importantly, future analyses will need to correct for the short and long-range distortions of the wavelength scale in the HIRES and UVES spectrographs. This is likely to be realised through calibration techniques used by Whitmore et al. (2010), Evans and Murphy (2013), Evans et al. (2014), and Whitmore and Murphy (2015), including those used in the UVES Large Program, which are expected to become standard in the field. This would ensure results from full MM fits of the sample in this work (which are very promising in terms of constraining power) are not polluted by wavelength calibration distortions. Verification using results from multiple telescopes, where available, will also be important (e.g. studies like those of Evans et al., 2014). More immediately, more work would be beneficial on the more extensive estimation of other potential systematics in the sample presented in this thesis, including cosmological variations in the isotopic abundances of the ionic species fit and tests of velocity structure-related systematics.

The $\Delta\mu/\mu$ constraint in this work is one of the few direct μ measurements outside the Galaxy. This is in stark contrast to the 143 constraints on α -variation in

Murphy et al. (2004) and the 153 constraints in King et al. (2012). More NH_3 and H_2/HD constraints, in overlapping redshift ranges, would allow additional tests for systematic errors and stronger conclusions to be drawn. Increasing the SNR of the optical H_2/HD spectra is also important, to allow more direct comparisons with the radio observations of molecular absorption. Correction of the instrumental systematics leading to short and long range-wavelength distortions is just as important as in varying α studies and would help establish the reliability of the optical results. Another avenue is increasing the number of H_2/HD absorbers for measuring $\Delta\mu/\mu$ through targeted surveys (e.g. Ledoux et al., 2003; Petitjean et al., 2006; Noterdaeme et al., 2008a; Srianand et al., 2012; Balashev et al., 2014) in order to approach the precisions of the NH_3 sample constraints. The current NH_3 sample of 2 absorbers would also benefit from further additions, especially at $z_{\text{abs}} > 1$ for overlap with H_2/HD constraints.

While detection and characterisation of instrumental systematic effects is currently being investigated in the field, new instrumentation can be designed to minimise or altogether avoid these effects. In this regard, the soon to be commissioned VLT instrument, the Echelle Spectrograph for Rocky Exoplanets and Stable Spectroscopic Observations (ESPRESSO), holds much promise. The high-resolution (up to $R = 225,000$) echelle spectrograph will be fibre-fed, which will eliminate the likely origin of the short and long-range wavelength distortions (angular and PSF differences between the quasar and wavelength calibration light paths). It will be calibrated with a laser frequency comb (a spectrum featuring regularly-spaced lines produced by the pulse train of a mode locked laser, where the frequencies of the lines are known to a high-precision; see Steinmetz et al., 2008, for an example of application of frequency comb spectra to wavelength calibration of astronomical observations), allowing radial velocity measures of accuracy $< 10 \text{ cm s}^{-1}$. ESPRESSO is estimated to provide an order of magnitude improvement in precision over current VLT/UVES and Keck/HIRES constraints of $\Delta\alpha/\alpha$ and $\Delta\mu/\mu$ (Pepe et al., 2013).

6

References

- Abgrall, H. and Roueff, E.: 2006, *A&A* **445**, 361
- Abgrall, H., Roueff, E., and Drira, I.: 2000, *A&AS* **141**, 297
- Abgrall, H., Roueff, E., Launay, F., and Roncin, J.-Y.: 1994, *Canadian J. Phys.* **72**, 856
- Abgrall, H., Roueff, E., Launay, F., Roncin, J. Y., and Subtil, J. L.: 1993, *J. Molecular Spectrosc.* **157**, 512
- Atlee, D. W. and Gould, A.: 2007, *ApJ* **664**, 53
- Bagdonaite, J., Ubachs, W., Murphy, M. T., and Whitmore, J. B.: 2014, *ApJ* **782**, 10
- Bahcall, J. N., Sargent, W. L. W., and Schmidt, M.: 1967, *ApJ* **149**, L11
- Bahcall, J. N. and Schmidt, M.: 1967, *Phys. Rev. Lett.* **19**, 1294
- Bailly, D., Salumbides, E. J., Vervloet, M., and Ubachs, W.: 2010, *Molecular Physics* **108**, 827
- Balashev, S. A., Klimenko, V. V., Ivanchik, A. V., Varshalovich, D. A., Petitjean, P., and Noterdaeme, P.: 2014, *MNRAS* **440**, 225
- Chand, H., Petitjean, P., Srianand, R., and Aracil, B.: 2005, *A&A* **430**, 47
- Chand, H., Srianand, R., Petitjean, P., and Aracil, B.: 2004, *A&A* **417**, 853
- Chengalur, J. N. and Kanekar, N.: 2003, *Phys. Rev. Lett.* **91**(24), 241302
- Cowie, L. L. and Songaila, A.: 1995, *ApJ* **453**, 596

- Cyburt, R. H., Fields, B. D., Olive, K. A., and Skillman, E.: 2005, *Astroparticle Physics* **23**, 313
- Darling, J.: 2004, *ApJ* **612**, 58
- Dent, T., Stern, S., and Wetterich, C.: 2008, *Phys. Rev. D* **78(10)**, 103518
- Dzuba, V. A., Flambaum, V. V., and Webb, J. K.: 1999, *Phys. Rev. A* **59**, 230
- Edlen, B.: 1966, *Metrologia* **2**, 71
- Evans, T. M. and Murphy, M. T.: 2013, *ApJ* **778**, 173
- Evans, T. M., Murphy, M. T., Whitmore, J. B., Misawa, T., Centurion, M., D’Odorico, S., Lopez, S., Martins, C. J. A. P., Molaro, P., Petitjean, P., Rahmani, H., Srianand, R., and Wendt, M.: 2014, *MNRAS* **445**, 128
- Flambaum, V. V. and Kozlov, M. G.: 2007, *Phys. Rev. Lett.* **98(24)**, 240801
- Foltz, C. B., Chaffee, F. H., and Black, J. H.: 1988, *ApJ* **324**, 267
- Ge, J. and Bechtold, J.: 1999, in C. L. Carilli, S. J. E. Radford, K. M. Menten, and G. I. Langstom (eds.), *Highly Redshifted Radio Lines*, Vol. 156 of *ASP Conf. Ser.*, p. 121, Astron. Soc. Pac., San Francisco, CA, U.S.A
- Godun, R. M., Nisbet-Jones, P. B. R., Jones, J. M., King, S. A., Johnson, L. A. M., Margolis, H. S., Szymaniec, K., Lea, S. N., Bongs, K., and Gill, P.: 2014, *Physical Review Letters* **113(21)**, 210801
- Griest, K., Whitmore, J. B., Wolfe, A. M., Prochaska, J. X., Howk, J. C., and Marcy, G. W.: 2010, *ApJ* **708**, 158
- Hamann, F., Kanekar, N., Prochaska, J. X., Murphy, M. T., Ellison, S., Malec, A. L., Milutinovic, N., and Ubachs, W.: 2011, *MNRAS* **410**, 1957
- Henkel, C., Menten, K. M., Murphy, M. T., Jethava, N., Flambaum, V. V., Braatz, J. A., Muller, S., Ott, J., and Mao, R. Q.: 2009, *A&A* **500**, 725
- Herbert-Fort, S., Prochaska, J. X., Dessauges-Zavadsky, M., Ellison, S. L., Howk, J. C., Wolfe, A. M., and Prochter, G. E.: 2006, *PASP* **118**, 1077

-
- Hinnen, P. C., Hogervorst, W., Stolte, S., and Ubachs, W.: 1994, *Canadian Journal of Physics* **72**, 1032
- Hollenstein, U., Reinhold, E., de Lange, C. A., and Ubachs, W.: 2006, *J. Phys. B* **39**, L195
- Horne, K.: 1986, *PASP* **98**, 609
- Huntemann, N., Lipphardt, B., Tamm, C., Gerginov, V., Weyers, S., and Peik, E.: 2014, *Physical Review Letters* **113**(21), 210802
- Ichikawa, K. and Kawasaki, M.: 2002, *Phys. Rev. D* **65**, 123511
- Ivanchik, A., Petitjean, P., Varshalovich, D., Aracil, B., Srianand, R., Chand, H., Ledoux, C., and Boissé, P.: 2005, *A&A* **440**, 45
- Ivanchik, A. V., Potekhin, A. Y., and Varshalovich, D. A.: 1999, *A&A* **343**, 439
- Ivanov, T. I., Roudjane, M., Vieitez, M. O., de Lange, C. A., Tchang-Brillet, W.-Ü. L., and Ubachs, W.: 2008, *Phys. Rev. Lett.* **100**(9), 093007
- Jenkins, E. B. and Peimbert, A.: 1997, *ApJ* **477**, 265
- Jennings, D. E., Bragg, S. L., and Brault, J. W.: 1984, *ApJ* **282**, L85
- Kanekar, N.: 2008, *Mod. Phys. Lett. A* **23**, 2711
- Kanekar, N., Carilli, C. L., Langston, G. I., Rocha, G., Combes, F., Subrahmanyam, R., Stocke, J. T., Menten, K. M., Briggs, F. H., and Wiklind, T.: 2005, *Phys. Rev. Lett.* **95**(26), 261301
- Kanekar, N., Chengalur, J. N., and Ghosh, T.: 2010a, *ApJ* **716**, L23
- Kanekar, N., Langston, G. I., Stocke, J. T., Carilli, C. L., and Menten, K. M.: 2012, *ApJ* **746**, L16
- Kanekar, N., Prochaska, J. X., Ellison, S. L., and Chengalur, J. N.: 2010b, *ApJ* **712**, L148
- Kanekar, N., Subrahmanyam, R., Ellison, S. L., Lane, W. M., and Chengalur, J. N.: 2006, *MNRAS* **370**, L46

- King, J. A., Webb, J. K., Murphy, M. T., and Carswell, R. F.: 2008, *Phys. Rev. Lett.* **101**(25), 251304
- King, J. A., Webb, J. K., Murphy, M. T., Flambaum, V. V., Carswell, R. F., Bainbridge, M. B., Wilczynska, M. R., and Koch, F. E.: 2012, *MNRAS* **422**, 3370
- Ledoux, C., Petitjean, P., and Srianand, R.: 2003, *MNRAS* **346**, 209
- Levshakov, S. A., Centurión, M., Molaro, P., D’Odorico, S., Reimers, D., Quast, R., and Pollmann, M.: 2006, *A&A* **449**, 879
- Levshakov, S. A., Dessauges-Zavadsky, M., D’Odorico, S., and Molaro, P.: 2002, *ApJ* **565**, 696
- Levshakov, S. A., Molaro, P., and Kozlov, M. G.: 2008, *On spatial variations of the electron-to-proton mass ratio in the Milky Way*, preprint (arXiv:0808.0583)
- Levshakov, S. A., Molaro, P., Lopez, S., D’Odorico, S., Centurión, M., Bonifacio, P., Agafonova, I. I., and Reimers, D.: 2007, *A&A* **466**, 1077
- Liddle, A. R.: 2007, *MNRAS* **377**, L74
- Malec, A. L., Buning, R., Murphy, M. T., Milutinovic, N., Ellison, S. L., Prochaska, J. X., Kaper, L., Tumlinson, J., Carswell, R. F., and Ubachs, W.: 2010a, *MNRAS* **403**, 1541
- Malec, A. L., Buning, R., Murphy, M. T., Milutinovic, N., Ellison, S. L., Prochaska, J. X., Kaper, L., Tumlinson, J., Carswell, R. F., and Ubachs, W.: 2010b, *VizieR Online Data Catalog* **740**, 31541
- Martínez Fiorenzano, A. F., Vladilo, G., and Bonifacio, P.: 2003, *Mem. Soc. Astron. Ital.* **3**, 252
- Meshkov, V. V., Stolyarov, A. V., Ivanchik, A. V., and Varshalovich, D. A.: 2006, *Sov. Phys. JETP Lett.* **83**, 303
- Milutinovic, N., Ellison, S. L., Prochaska, J. X., and Tumlinson, J.: 2010, *MNRAS* **408**, 2071

-
- Molaro, P., Centuri3n, M., Whitmore, J. B., Evans, T. M., Murphy, M. T., Agafonova, I. I., Bonifacio, P., D’Odorico, S., Levshakov, S. A., Lopez, S., Martins, C. J. A. P., Petitjean, P., Rahmani, H., Reimers, D., Srianand, R., Vladilo, G., and Wendt, M.: 2013, *A&A* **555**, A68
- Molaro, P., Levshakov, S. A., Monai, S., Centuri3n, M., Bonifacio, P., D’Odorico, S., and Monaco, L.: 2008, *A&A* **481**, 559
- Murphy, M. T.: 2002, *Ph.D. thesis*, University of New South Wales, University of New South Wales
- Murphy, M. T. and Berengut, J. C.: 2014, *MNRAS* **438**, 388
- Murphy, M. T., Flambaum, V. V., Muller, S., and Henkel, C.: 2008a, *Sci* **320**, 1611
- Murphy, M. T., Flambaum, V. V., Webb, J. K., Dzuba, V. V., Prochaska, J. X., and Wolfe, A. M.: 2004, *Lecture Notes Phys.* **648**, 131
- Murphy, M. T., Tzanavaris, P., Webb, J. K., and Lovis, C.: 2007, *MNRAS* **378**, 221
- Murphy, M. T., Webb, J. K., and Flambaum, V. V.: 2003a, *MNRAS* **345**, 609
- Murphy, M. T., Webb, J. K., and Flambaum, V. V.: 2008b, *MNRAS* **384**, 1053
- Murphy, M. T., Webb, J. K., Flambaum, V. V., Churchill, C. W., and Prochaska, J. X.: 2001a, *MNRAS* **327**, 1223
- Murphy, M. T., Webb, J. K., Flambaum, V. V., and Curran, S. J.: 2003b, *ApJSS* **283**, 577
- Murphy, M. T., Webb, J. K., Flambaum, V. V., Dzuba, V. A., Churchill, C. W., Prochaska, J. X., Barrow, J. D., and Wolfe, A. M.: 2001b, *MNRAS* **327**, 1208
- Murphy, M. T., Webb, J. K., Flambaum, V. V., Prochaska, J. X., and Wolfe, A. M.: 2001c, *MNRAS* **327**, 1237
- Noterdaeme, P., Ledoux, C., Petitjean, P., Le Petit, F., Srianand, R., and Smette, A.: 2007, *A&A* **474**, 393

- Noterdaeme, P., Ledoux, C., Petitjean, P., and Srianand, R.: 2008a, *A&A* **481**, 327
- Noterdaeme, P., Petitjean, P., Ledoux, C., Srianand, R., and Ivanchik, A.: 2008b, *A&A* **491**, 397
- Pagel, B. E. J.: 1977, *MNRAS* **179**, 81P
- Pepe, F., Cristiani, S., Rebolo, R., Santos, N. C., Dekker, H., Mégevand, D., Zerbi, F. M., Cabral, A., Molaro, P., Di Marcantonio, P., Abreu, M., Affolter, M., Aliverti, M., Allende Prieto, C., Amate, M., Avila, G., Baldini, V., Bristow, P., Broeg, C., Cirami, R., Coelho, J., Conconi, P., Coretti, I., Cupani, G., D’Odorico, V., De Caprio, V., Delabre, B., Dorn, R., Figueira, P., Frago, A., Galeotta, S., Genolet, L., Gomes, R., González Hernández, J. I., Hughes, I., Iwert, O., Kerber, F., Landoni, M., Lizon, J.-L., Lovis, C., Maire, C., Mannetta, M., Martins, C., Monteiro, M. A., Oliveira, A., Poretti, E., Rasilla, J. L., Riva, M., Santana Tschudi, S., Santos, P., Sosnowska, D., Sousa, S., Spanò, P., Tenegi, F., Toso, G., Vanzella, E., Viel, M., and Zapatero Osorio, M. R.: 2013, *The Messenger* **153**, 6
- Petitjean, P., Ledoux, C., Noterdaeme, P., and Srianand, R.: 2006, *A&A* **456**, L9
- Pettini, M., Smith, L. J., Hunstead, R. W., and King, D. L.: 1994, *ApJ* **426**, 79
- Philip, J., Sprengers, J. P., Pielage, T., de Lange, C. A., Ubachs, W., and Reinhold, E.: 2004, *Canadian J. Chem.* **82**, 713
- Planck Collaboration, Ade, P. A. R., Aghanim, N., Arnaud, M., Ashdown, M., Aumont, J., Baccigalupi, C., Banday, A. J., Barreiro, R. B., Battaner, E., Benabed, K., Benoit-Lévy, A., Bernard, J.-P., Bersanelli, M., Bielewicz, P., Bond, J. R., Borrill, J., Bouchet, F. R., Burigana, C., Butler, R. C., Calabrese, E., Chaballu, A., Chiang, H. C., Christensen, P. R., Clements, D. L., Colombo, L. P. L., Couchot, F., Curto, A., Cuttaia, F., Danese, L., Davies, R. D., Davis, R. J., de Bernardis, P., de Rosa, A., de Zotti, G., Delabrouille, J., Diego, J. M., Dole, H., Doré, O., Dupac, X., Enßlin, T. A., Eriksen, H. K., Fabre, O., Finelli, F., Forni, O., Frailis, M., Franceschi, E., Galeotta, S., Galli, S., Ganga, K., Giard, M., González-Nuevo, J., Górski, K. M., Gregorio, A., Gruppuso, A., Hansen, F. K.,

- Hanson, D., Harrison, D. L., Henrot-Versillé, S., Hernández-Monteagudo, C., Herranz, D., Hildebrandt, S. R., Hivon, E., Hobson, M., Holmes, W. A., Hornstrup, A., Hovest, W., Huppenberger, K. M., Jaffe, A. H., Jones, W. C., Keihänen, E., Keskitalo, R., Kneissl, R., Knoche, J., Kunz, M., Kurki-Suonio, H., Lamarre, J.-M., Lasenby, A., Lawrence, C. R., Leonardi, R., Lesgourgues, J., Liguori, M., Lilje, P. B., Linden-Vørnle, M., López-Caniego, M., Lubin, P. M., Macías-Pérez, J. F., Mandolesi, N., Maris, M., Martin, P. G., Martínez-González, E., Masi, S., Matarrese, S., Mazzotta, P., Meinhold, P. R., Melchiorri, A., Mendes, L., Mene-goni, E., Mennella, A., Migliaccio, M., Miville-Deschênes, M.-A., Moneti, A., Montier, L., Morgante, G., Moss, A., Munshi, D., Murphy, J. A., Naselsky, P., Nati, F., Natoli, P., Nørgaard-Nielsen, H. U., Noviello, F., Novikov, D., Novikov, I., Oxborrow, C. A., Pagano, L., Pajot, F., Paoletti, D., Pasian, F., Patanchon, G., Perdureau, O., Perotto, L., Perrotta, F., Piacentini, F., Piat, M., Pierpaoli, E., Pietrobon, D., Plaszczynski, S., Pointecouteau, E., Polenta, G., Ponthieu, N., Popa, L., Pratt, G. W., Prunet, S., Rachen, J. P., Rebolo, R., Reinecke, M., Remazeilles, M., Renault, C., Ricciardi, S., Ristorcelli, I., Rocha, G., Roudier, G., Rusholme, B., Sandri, M., Savini, G., Scott, D., Spencer, L. D., Stolyarov, V., Sudiwala, R., Sutton, D., Suur-Uski, A.-S., Sygnet, J.-F., Tauber, J. A., Tavagnacco, D., Terenzi, L., Toffolatti, L., Tomasi, M., Tristram, M., Tucci, M., Uzan, J.-P., Valenziano, L., Valiviita, J., Van Tent, B., Vielva, P., Villa, F., Wade, L. A., Yvon, D., Zacchei, A., and Zonca, A.: 2015, *A&A* **580**, A22
- Prochaska, J. X., Herbert-Fort, S., and Wolfe, A. M.: 2005, *ApJ* **635**, 123
- Prochaska, J. X. and Wolfe, A. M.: 2009, *ApJ* **696**, 1543
- Quast, R., Reimers, D., and Levshakov, S. A.: 2004, *A&A* **415**, L7
- Rahmani, H., Srianand, R., Gupta, N., Petitjean, P., Noterdaeme, P., and Vásquez, D. A.: 2012, *MNRAS* **425**, 556
- Rahmani, H., Wendt, M., Srianand, R., Noterdaeme, P., Petitjean, P., Molaro, P., Whitmore, J. B., Murphy, M. T., Centurion, M., Fathivavsari, H., D’Odorico, S., Evans, T. M., Levshakov, S. A., Lopez, S., Martins, C. J. A. P., Reimers, D., and Vladilo, G.: 2013, *MNRAS* **435**, 861

- Reinhold, E., Buning, R., Hollenstein, U., Ivanchik, A., Petitjean, P., and Ubachs, W.: 2006, *Phys. Rev. Lett.* **96**(15), 151101
- Rigden, J. S.: 2002, *Hydrogen: the essential element*, Harvard University Press
- Rosenband, T., Hume, D. B., Schmidt, P. O., Chou, C. W., Brusch, A., Lorini, L., Oskay, W. H., Drullinger, R. E., Fortier, T. M., Stalnaker, J. E., Diddams, S. A., Swann, W. C., Newbury, N. R., Itano, W. M., Wineland, D. J., and Bergquist, J. C.: 2008, *Sci* **319**, 1808
- Roth, K. C. and Blades, J. C.: 1995, *ApJ* **445**, L95
- Salumbides, E. J., Bailly, D., Khramov, A., Wolf, A. L., Eikema, K. S. E., Vervloet, M., and Ubachs, W.: 2008, *Phys. Rev. Lett.* **101**(22), 223001
- Savedoff, M. P.: 1956, *Nat* **178**, 689
- Sommerfeld, A.: 1911, *Z. Phys.* **12**, 1057
- Srianand, R., Gupta, N., Petitjean, P., Noterdaeme, P., Ledoux, C., Salter, C. J., and Saikia, D. J.: 2012, *MNRAS* **421**, 651
- Steinmetz, T., Wilken, T., Araujo-Hauck, C., Holzwarth, R., Hänsch, T. W., Pasquini, L., Manescau, A., D’Odorico, S., Murphy, M. T., Kentischer, T., Schmidt, W., and Udem, T.: 2008, *Sci* **321**, 1335
- Thompson, R. I.: 1975, *Astron. Lett.* **16**, 3
- Thompson, R. I., Bechtold, J., Black, J. H., Eisenstein, D., Fan, X., Kennicutt, R. C., Martins, C., Prochaska, J. X., and Shirley, Y. L.: 2009, *ApJ* **703**, 1648
- Tzanavaris, P., Murphy, M. T., Webb, J. K., Flambaum, V. V., and Curran, S. J.: 2007, *MNRAS* **374**, 634
- Tzanavaris, P., Webb, J. K., Murphy, M. T., Flambaum, V. V., and Curran, S. J.: 2005, *Phys. Rev. Lett.* **95**(4), 041301
- Ubachs, W., Buning, R., Eikema, K. S. E., and Reinhold, E.: 2007, *J. Molecular Spectrosc.* **241**, 155

-
- Ubachs, W., Eikema, K. S. E., Hogervorst, W., and Cacciani, P. C.: 1997, *J. Opt. Soc. Am. B* **14**, 2469
- Ubachs, W. and Reinhold, E.: 2004, *Phys. Rev. Lett.* **92**, 101302
- Uzan, J.: 2003, *Rev. Mod. Phys.* **75**, 403
- Valenti, J. A., Butler, R. P., and Marcy, G. W.: 1995, *PASP* **107**, 966
- van Veldhoven, J., Küpper, J., Bethlem, H. L., Sartakov, B., van Roij, A. J. A., and Meijer, G.: 2004, *European Physical Journal D* **31**, 337
- van Weerdenburg, F., Murphy, M. T., Malec, A. L., Kaper, L., and Ubachs, W.: 2011, *Physical Review Letters* **106**(18), 180802
- Varshalovich, D. A., Ivanchik, A. V., Petitjean, P., Srianand, R., and Ledoux, C.: 2001, *Astron. Lett.* **27**, 683
- Varshalovich, D. A. and Levshakov, S. A.: 1993, *Sov. Phys. JETP Lett.* **58**, 237
- Varshalovich, D. A., Panchuk, V. E., and Ivanchik, A. V.: 1996, *Astron. Lett.* **22**, 6
- Varshalovich, D. A. and Potekhin, A. Y.: 1995, *Space Sci. Rev.* **74**, 259
- Varshalovich, D. A., Potekhin, A. Y., and Ivanchik, A. V.: 2000, in R. W. Dunford, D. S. Gemmel, E. P. Kanter, B. Kraessig, S. H. Southworth, and L. Young (eds.), *X-Ray and Inner-Shell Processes*, Vol. 506 of *AIP Conf. Proc.*, p. 503, Argonne National Laboratory, Argonne, IL, USA
- Vogt, S. S. and et al.: 1994, in D. L. Crawford and E. R. Craine (eds.), *Instrumentation in Astronomy VIII*, Vol. 2198 of *Proc. SPIE*, p. 362
- Webb, J. K., Flambaum, V. V., Churchill, C. W., Drinkwater, M. J., and Barrow, J. D.: 1999, *Phys. Rev. Lett.* **82**, 884
- Webb, J. K., King, J. A., Murphy, M. T., Flambaum, V. V., Carswell, R. F., and Bainbridge, M. B.: 2011, *Physical Review Letters* **107**(19), 191101
- Wendt, M. and Molaro, P.: 2012, *A&A* **541**, A69

Wendt, M. and Reimers, D.: 2008, *Eur. Phys. J. Special Topics* **163**, 197

Whitmore, J. B. and Murphy, M. T.: 2015, *MNRAS* **447**, 446

Whitmore, J. B., Murphy, M. T., and Griest, K.: 2010, *ApJ* **723**, 89

Wolfe, A. M., Brown, R. L., and Roberts, M. S.: 1976, *Phys. Rev. Lett.* **37**, 179

A

Fiducial models of blending Mg I absorption

Section 3.2.2 presented the fiducial absorption models of the Zn II and Cr II transitions that were constructed to constrain $\Delta\alpha/\alpha$, but omitted models of the blending Mg I absorption. As described in Section 3.2.1, the Zn II 2026 transition used for constraining $\Delta\alpha/\alpha$ is overlapped by the Mg I 2026 transition, where this blending is resolved by the unblended Mg I 2852 transition. This Appendix tables the Mg I model parameters and errors for each individual absorption system separately. The Mg I transition spectra are also each plotted with overlaid fiducial model fits and their residuals (i.e. [data] – [fit], normalised by the $1\text{-}\sigma$ errors). Note that no Mg I transitions were fit for the HIRES and UVES spectra of PHL957 as described in Section 3.2.2.6.

A.1 J0058+0051

Table A.1: Fiducial fit Mg I absorption line parameters and $1\text{-}\sigma$ statistical uncertainties for the J0058+0051 HIRES spectrum. The errors are given in units of the least significant digit of the measurement itself; for example, $b = 3.68(109)$ implies a $1\text{-}\sigma$ error of 1.09 km s^{-1} . This is the same for all subsequent tables.

z_{abs}	b [km s^{-1}]	$\log N(\text{Mg I})$ [cm^{-2}]
1.0712793(118)	2.72(371)	10.05(22)
1.0714302(30)	4.84(72)	10.86(4)
1.0716024(239)	0.50(1507)	10.26(51)
1.0716515(743)	3.61(1102)	11.19(437)
1.0716955(2083)	5.55(3854)	11.30(381)
1.0717427(72)	0.50(96)	11.28(66)
1.0717779(87)	1.35(316)	11.43(31)
1.0718203(427)	3.56(865)	11.67(237)
1.0718679(1045)	5.26(5509)	11.47(569)
1.0719433(272)	5.44(2466)	11.80(219)
1.0719856(187)	2.30(357)	12.05(85)
1.0720088(27)	0.92(132)	12.62(10)
1.0720388(157)	3.11(403)	11.83(43)
1.0720892(74)	1.91(301)	11.36(29)
1.0721232(79)	0.50(32)	11.53(19)
1.0721635(65)	3.75(593)	11.24(43)
1.0722064(84)	0.54(807)	11.02(275)
1.0722594(50)	6.43(197)	11.50(10)
1.0723291(89)	0.50(1550)	10.36(95)
1.0723790(733)	0.50(3401)	10.71(461)
1.0724050(621)	0.52(3897)	10.75(564)
1.0724436(358)	2.78(558)	10.52(70)

Table A.2: Fiducial fit Mg I absorption line parameters and 1- σ statistical uncertainties for the J0058+0051 UVES spectrum.

z_{abs}	b [km s ⁻¹]	$\log N(\text{Mg I})$ [cm ⁻²]
1.0712899(676)	14.62(2613)	10.46(58)
1.0714267(104)	3.87(193)	10.86(14)
1.0715901(305)	2.78(706)	10.27(56)
1.0716600(108)	3.88(228)	11.39(17)
1.0717234(132)	3.17(557)	11.25(49)
1.0717648(104)	1.20(597)	11.19(39)
1.0718165(123)	6.08(552)	11.88(44)
1.0719516(2869)	10.52(3686)	12.03(267)
1.0720018(80)	1.86(106)	12.62(6)
1.0720156(309)	6.71(770)	12.10(203)
1.0720942(70)	0.80(113)	11.28(31)
1.0721426(148)	7.03(469)	11.53(25)
1.0722084(112)	0.54(37)	11.42(31)
1.0722421(103)	0.50(40)	11.53(33)
1.0722715(143)	1.18(414)	11.17(16)
1.0723135(440)	3.09(727)	10.90(51)
1.0723760(241)	0.50(649)	10.70(116)
1.0724064(198)	0.50(579)	10.73(113)
1.0724441(123)	0.62(582)	10.74(72)

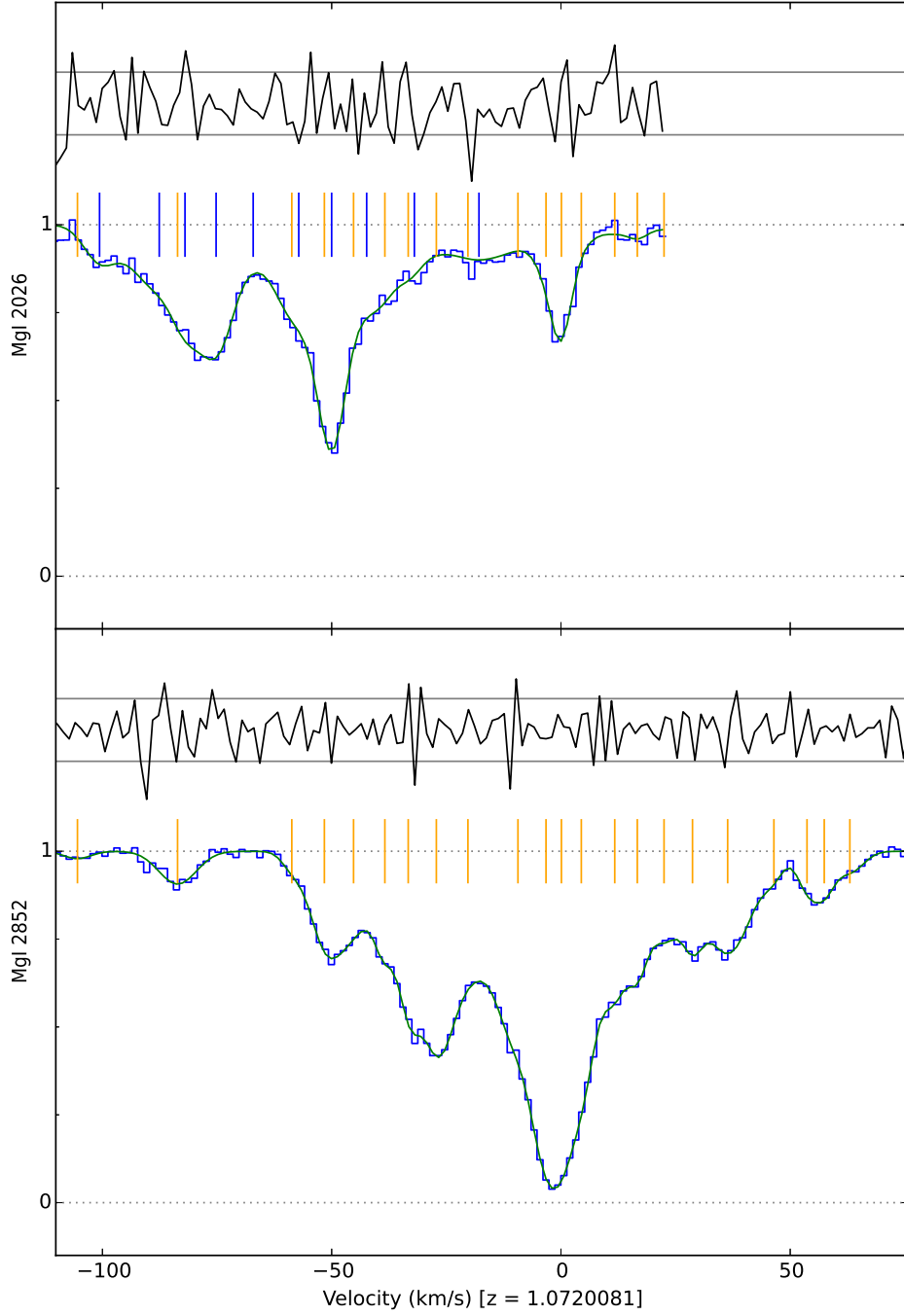


Figure A.1: Data and model fit for the J0058+0051 HIRES spectrum Mg I transitions, centred at $z_{\text{abs}} = 1.072$. The fit (continuous green line) is overlaid on the normalised spectrum (blue histogram). Each transition is labelled on the vertical axis for that panel. The vertical tick marks indicate the positions of the fit Zn II (blue) and MgI (orange) velocity components. Above each fit the residuals (i.e. [data] – [fit], normalised by the 1- σ errors denoted by grey horizontal lines) are plotted. This is the same for all subsequent figures.

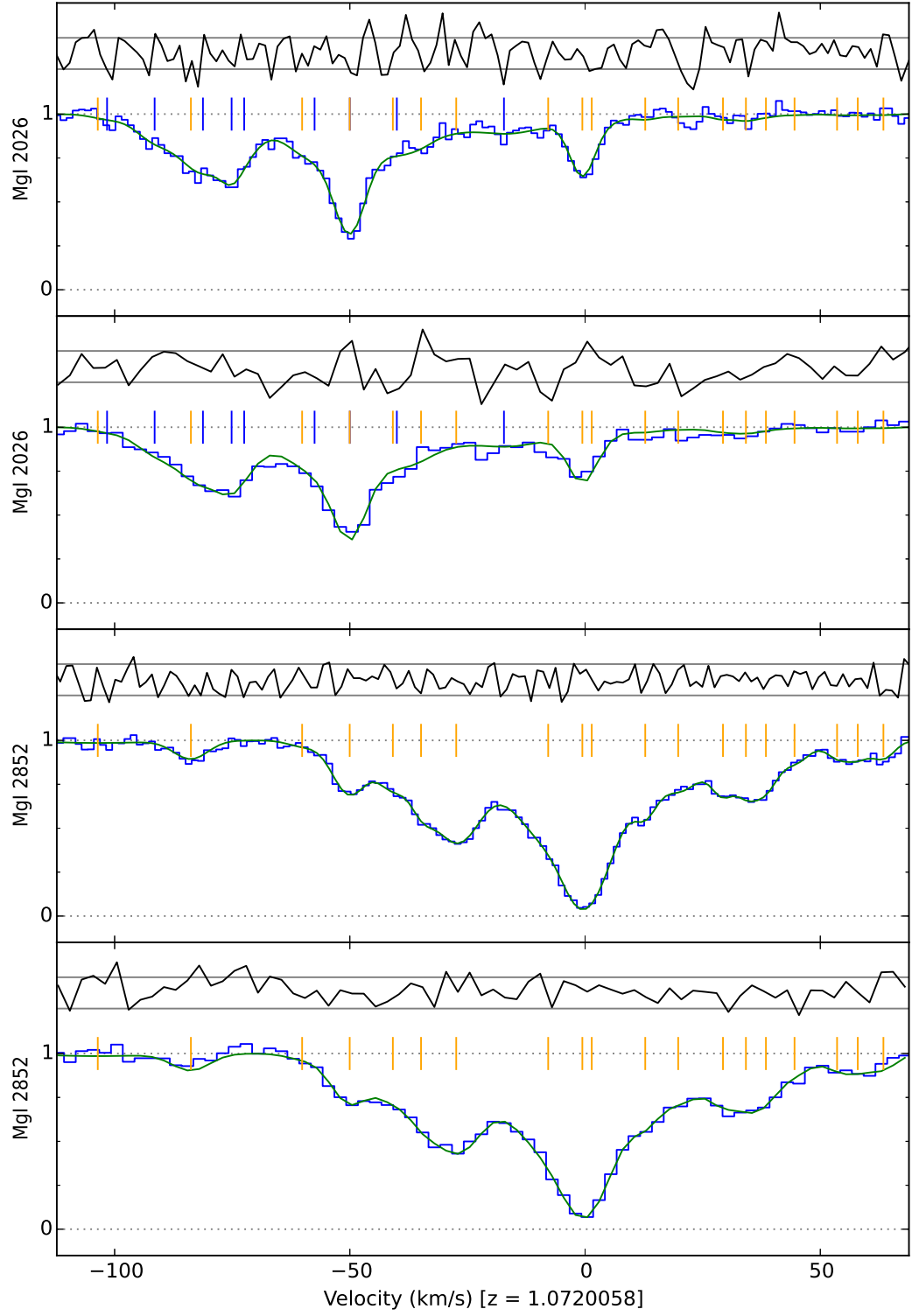


Figure A.2: Data and model fit for the J0058+0051 UVES spectrum Mg I transitions, centred at $z_{\text{abs}} = 1.072$. The alternating panels are 1×1 and 2×2 binned spectra.

A.2 J0108–0037

Table A.3: Fiducial fit Mg I absorption line parameters and 1- σ statistical uncertainties for the J0108–0037 spectrum.

z_{abs}	b [km s ⁻¹]	$\log N(\text{Mg I})$ [cm ⁻²]
1.3707376(175)	0.50(2322)	10.22(147)
1.3708941(96)	0.50(27)	11.72(25)
1.3709366(82)	1.40(58)	11.77(18)
1.3710029(52)	12.01(48)	12.34(4)
1.3710648(37)	3.22(73)	12.08(7)
1.3712684(89)	1.50(446)	10.56(12)

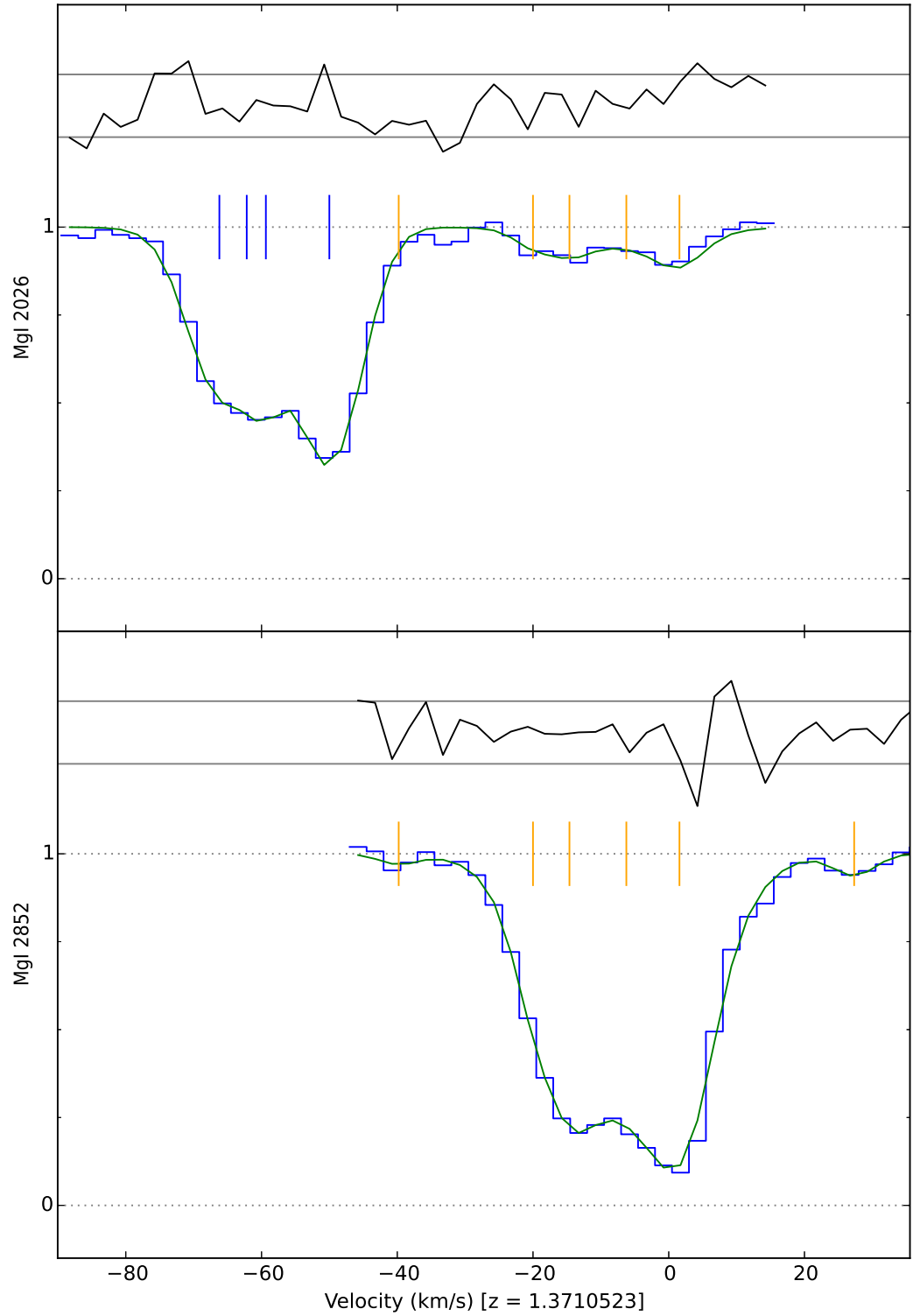


Figure A.3: Data and model fit for the J0108–0037 UVES spectrum Mg I transitions, centred at $z_{\text{abs}} = 1.371$.

A.3 J0226–2857

Table A.4: Fiducial fit Mg I absorption line parameters and 1- σ statistical uncertainties for the J0226–2857 spectrum.

z_{abs}	b [km s ⁻¹]	$\log N(\text{Mg I})$ [cm ⁻²]
1.0217116(119)	3.05(364)	10.40(22)
1.0219025(158)	14.02(291)	11.54(9)
1.0220362(18)	7.59(49)	12.10(3)
1.0221576(16)	6.46(43)	11.97(2)
1.0222793(43)	4.91(82)	11.88(17)
1.0223455(109)	2.63(420)	11.46(97)
1.0223988(569)	0.50(6024)	10.43(265)
1.0224634(67)	7.53(358)	12.46(53)
1.0225697(1319)	20.87(2223)	12.64(47)
1.0226264(13)	3.42(25)	13.21(3)
1.0227664(42)	5.23(225)	11.70(35)
1.0228414(36)	4.15(123)	11.97(21)
1.0229211(105)	9.06(997)	11.94(44)
1.0229943(50)	3.54(180)	11.86(33)
1.0230508(61)	5.50(86)	12.11(8)
1.0231826(32)	0.51(248)	11.54(482)
1.0232393(84)	17.57(366)	11.82(6)
1.0232406(43)	5.21(181)	11.41(20)
1.0234336(50)	0.50(729)	10.69(149)
1.0235311(127)	2.49(442)	10.33(25)
1.0237293(226)	13.04(297)	11.68(13)
1.0238185(258)	6.44(754)	10.75(110)
1.0239660(65)	0.50(836)	10.53(117)
1.0240997(189)	8.82(433)	10.70(16)

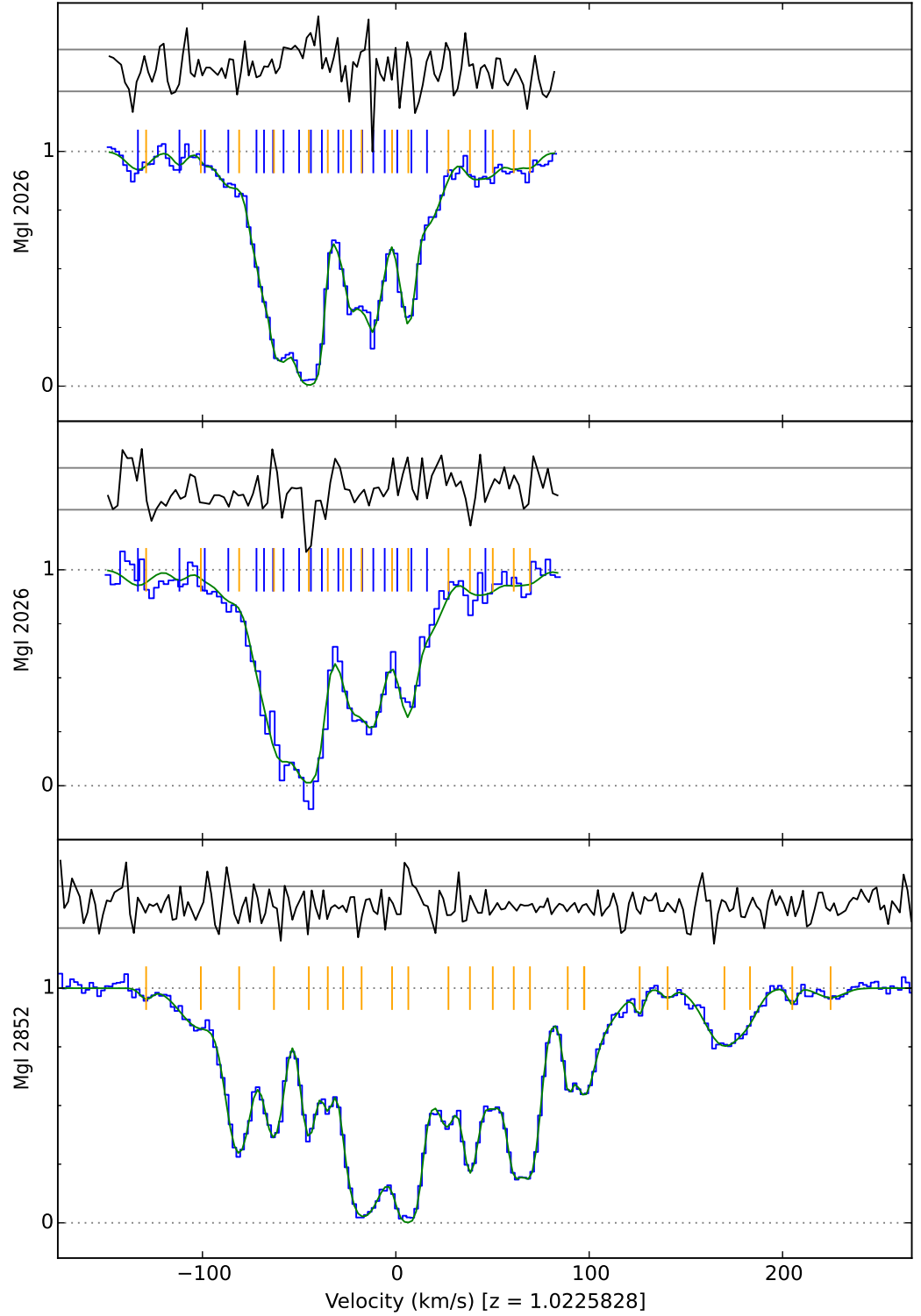


Figure A.4: Data and model fit for the J0226–2857 UVES spectrum Mg I transitions, centred at $z_{\text{abs}} = 1.023$. The panels show 0.8'', 1.2'' and 0.8'' slit data, from top to bottom.

A.4 J0841+0312

Table A.5: Fiducial fit Mg I absorption line parameters and 1- σ statistical uncertainties for the J0841+0312 HIRES spectrum.

z_{abs}	b [km s ⁻¹]	$\log N(\text{Mg I})$ [cm ⁻²]
1.3421698(107)	7.10(218)	11.08(37)
1.3423072(79)	14.05(659)	11.66(19)
1.3424056(257)	3.45(708)	10.42(125)
1.3424706(47)	4.11(121)	11.20(12)
1.3426046(83)	8.72(133)	11.91(8)
1.3426397(42)	0.50(82)	11.06(39)
1.3426979(22)	4.14(63)	12.04(7)
1.3427650(42)	4.21(88)	11.72(11)
1.3428438(193)	7.20(252)	11.13(18)

Table A.6: Fiducial fit Mg I absorption line parameters and 1- σ statistical uncertainties for the J0841+0312 UVES spectrum.

z_{abs}	b [km s ⁻¹]	$\log N(\text{Mg I})$ [cm ⁻²]
1.3421920(286)	9.22(443)	11.37(25)
1.3423021(108)	6.92(443)	11.35(36)
1.3423686(73)	2.46(273)	10.79(51)
1.3424677(82)	8.75(253)	11.53(11)
1.3425924(243)	5.95(315)	11.72(35)
1.3426594(195)	4.21(505)	11.75(69)
1.3427038(64)	2.34(133)	11.96(26)
1.3427631(54)	4.80(83)	11.83(7)
1.3428606(41)	3.19(108)	10.92(7)

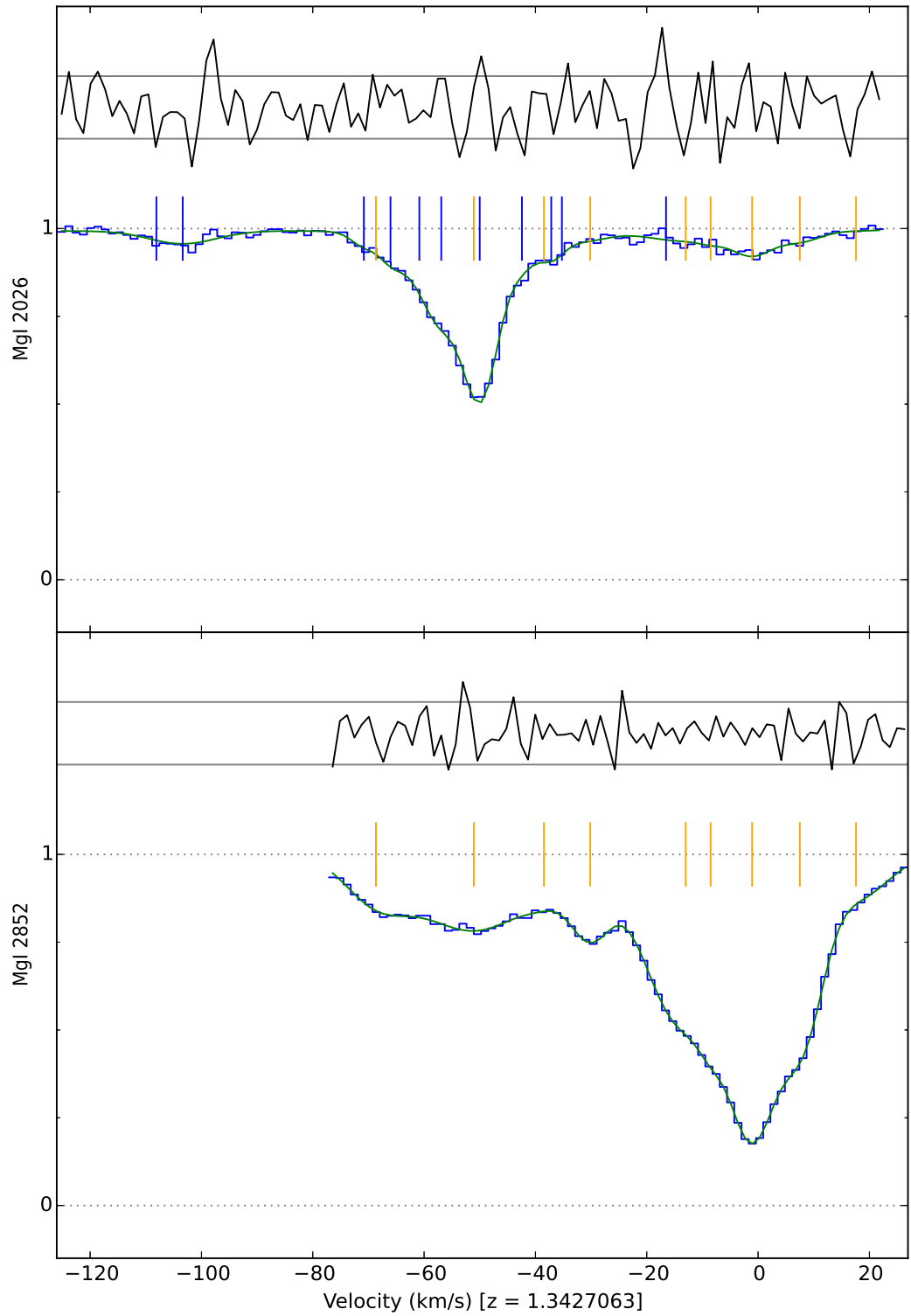


Figure A.5: Data and model fit for the J0841+0312 HIRES spectrum Mg I transitions, centred at $z_{\text{abs}} = 1.023$.

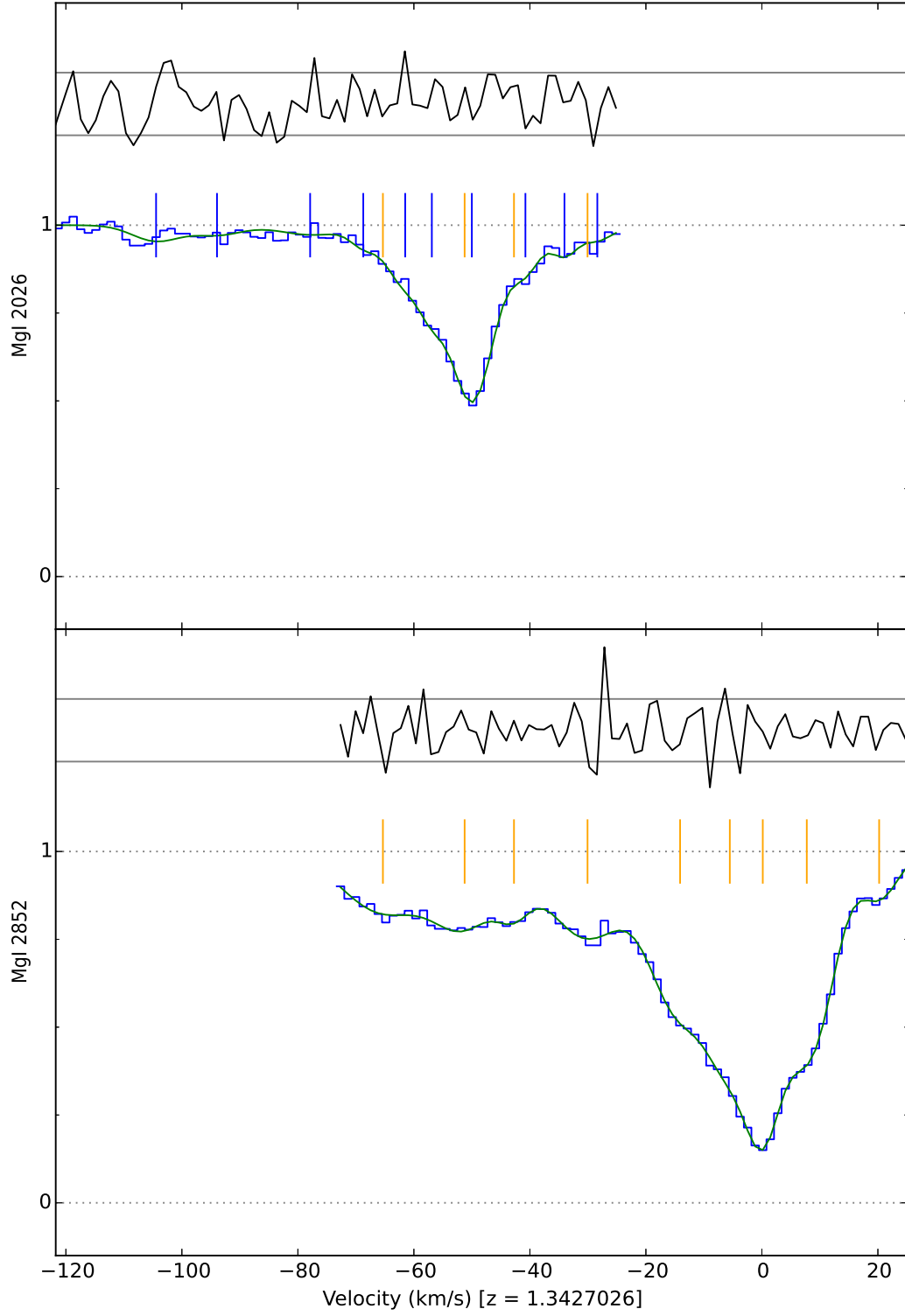


Figure A.6: Data and model fit for the J0841+0312 UVES spectrum Mg I transitions, centred at $z_{\text{abs}} = 1.343$.

A.5 J1029+1039

Table A.7: Fiducial fit Mg I absorption line parameters and 1- σ statistical uncertainties for the J1029+1039 spectrum.

z_{abs}	b [km s ⁻¹]	$\log N(\text{Mg I})$ [cm ⁻²]
1.6212573(192)	3.63(374)	10.75(26)
1.6213462(184)	3.34(435)	11.12(38)
1.6213970(268)	0.50(1574)	10.71(250)
1.6214841(64)	8.30(251)	12.12(10)
1.6215611(80)	1.40(57)	12.15(23)
1.6215981(265)	0.57(362)	12.22(72)
1.6216382(135)	3.19(215)	13.03(21)
1.6217064(284)	1.52(189)	11.94(59)
1.6217329(65)	0.53(318)	12.77(377)
1.6217677(263)	2.58(358)	12.12(37)
1.6218262(199)	2.75(893)	11.80(79)
1.6218745(513)	0.86(2649)	11.37(274)
1.6219196(1185)	3.56(4941)	11.62(592)
1.6219859(701)	3.75(4877)	11.73(610)
1.6220475(2196)	3.37(4311)	11.49(654)
1.6220934(353)	0.94(552)	11.29(171)
1.6221338(83)	0.50(31)	11.86(16)
1.6221977(124)	5.28(316)	11.88(24)
1.6222894(134)	5.10(373)	11.80(51)
1.6223877(443)	8.49(1024)	11.72(63)
1.6224523(37)	0.76(25)	11.79(14)
1.6225669(1015)	13.11(811)	11.56(27)
1.6226430(83)	2.99(282)	11.01(37)
1.6228690(94)	3.70(206)	11.01(23)
1.6230094(122)	10.82(412)	11.64(13)
1.6231244(80)	3.02(184)	11.33(24)
1.6232031(58)	5.51(72)	11.84(5)

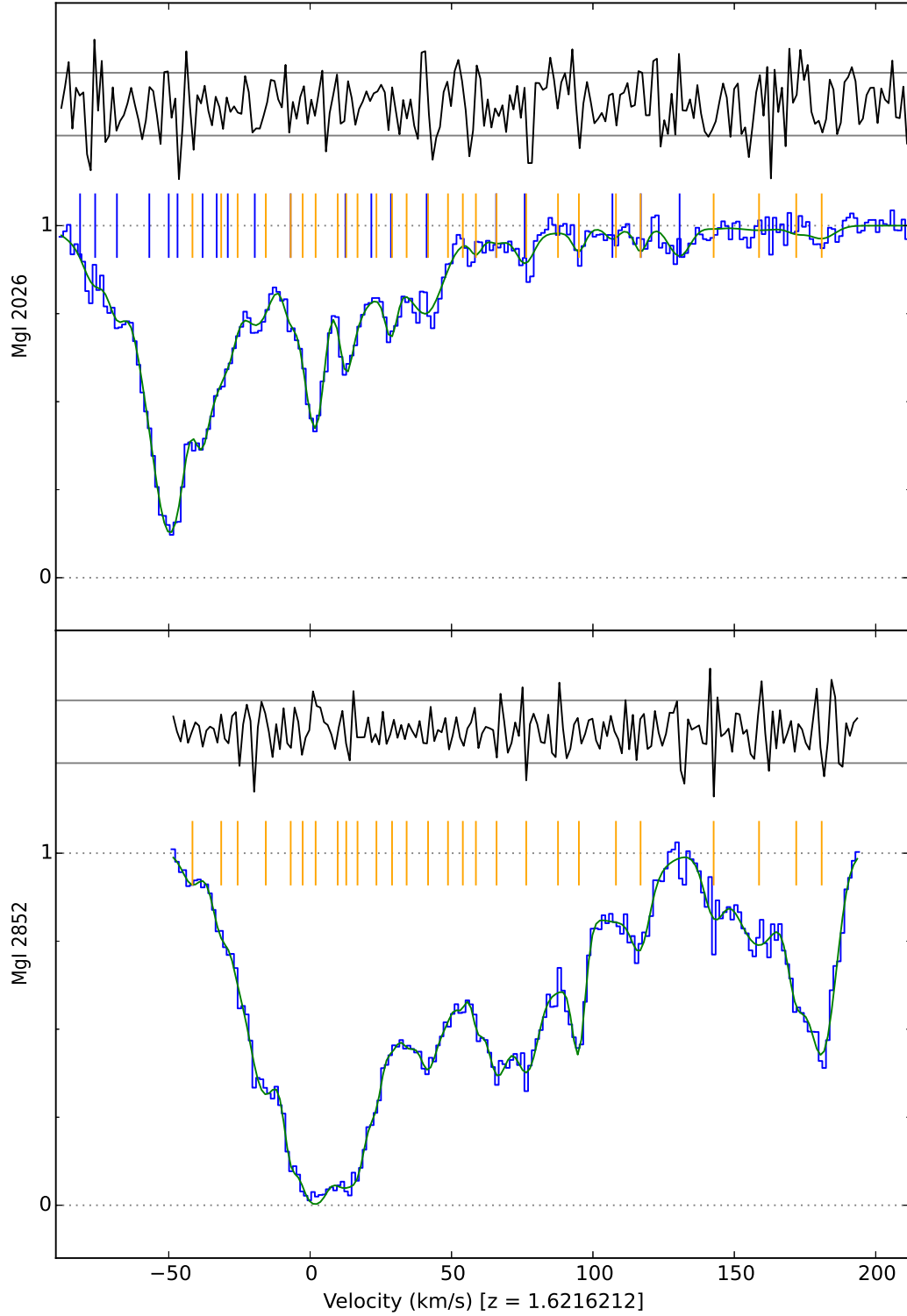


Figure A.7: Data and model fit for the J1029+1039 HIRES spectrum Mg I transitions, centred at $z_{\text{abs}} = 1.622$.

A.6 Q1755+57

Table A.8: Fiducial fit Mg I absorption line parameters and 1- σ statistical uncertainties for the Q1755+57 spectrum.

z_{abs}	b [km s ⁻¹]	$\log N(\text{Mg I})$ [cm ⁻²]
1.9685222(155)	0.50(1282)	10.39(115)
1.9686429(1997)	4.16(1105)	11.16(304)
1.9687007(904)	3.84(1031)	11.42(194)
1.9687696(356)	0.50(1803)	10.76(300)
1.9688400(361)	0.50(3857)	10.55(355)
1.9688963(473)	0.50(5892)	10.32(206)
1.9690714(703210)	12.78(469529)	11.62(194454)
1.9690906(2791584)	16.27(309952)	11.61(311894)
1.9691963(108)	1.00(198)	13.72(366)
1.9692360(166)	0.55(366)	13.16(919)
1.9692439(243990)	13.49(110981)	12.26(29808)
1.9692873(640)	2.51(980)	11.41(254)
1.9693731(274047)	17.79(106802)	11.83(12002)
1.9694422(121)	2.18(515)	11.01(97)
1.9695748(213)	0.50(555)	10.77(114)
1.9696324(161)	0.50(958)	10.69(158)
1.9697034(331)	2.33(1351)	10.69(290)
1.9698032(882)	3.83(1333)	10.34(261)
1.9699295(88)	0.50(713)	10.55(100)
1.9702704(473)	14.09(530)	11.32(19)
1.9703592(121)	0.62(801)	10.76(98)
1.9704417(169)	3.50(398)	11.13(34)
1.9705107(189)	0.52(1579)	10.83(369)
1.9705746(128)	1.64(891)	10.96(148)
1.9706692(441)	10.08(1975)	11.85(80)
1.9707890(1201)	4.36(1588)	11.46(268)
1.9708587(2396)	3.34(4307)	11.28(803)
1.9709179(1097)	3.20(2090)	11.63(312)
1.9709678(253)	0.85(106)	12.04(70)
1.9710183(40)	0.78(89)	14.02(424)
1.9710428(1107)	4.81(730)	12.21(179)
1.9711301(59)	1.27(46)	12.60(15)

Continued on next page

Table A.8: *Continued from previous page*

z_{abs}	b [km s ⁻¹]	$\log N(\text{Mg I})$ [cm ⁻²]
1.9711988(119)	6.22(189)	12.31(12)
1.9712939(59)	0.52(35)	11.70(49)
1.9713483(44)	0.50(12)	12.05(26)
1.9714062(51)	1.35(32)	12.48(11)
1.9714657(145)	3.49(488)	11.75(50)
1.9715672(45)	2.70(133)	12.78(32)
1.9715939(1950)	5.61(780)	11.92(235)
1.9716979(106)	2.61(283)	11.75(44)
1.9717758(1528)	4.45(2775)	11.32(376)
1.9718648(717)	5.25(2468)	11.65(211)
1.9719178(79)	0.94(76)	12.17(21)
1.9719712(82)	3.03(183)	12.17(12)
1.9720321(75)	0.97(41)	11.93(26)
1.9720826(59)	0.75(32)	12.12(11)
1.9721531(255)	4.01(265)	12.35(38)
1.9722494(137)	2.92(284)	12.38(89)
1.9722598(1113)	6.04(407)	12.27(152)
1.9724397(180)	5.25(211)	12.12(19)
1.9725004(156)	1.80(265)	11.83(31)
1.9725486(854)	1.33(1804)	11.37(712)
1.9725815(3627)	3.04(3850)	11.42(784)
1.9726816(7788)	7.34(3907)	11.36(368)
1.9727272(656)	3.24(2012)	11.08(712)
1.9728501(445)	6.48(1884)	11.38(139)
1.9729917(140)	3.33(383)	11.79(99)
1.9730526(502)	0.50(1785)	10.55(235)
1.9730878(4823)	9.78(6414)	11.69(294)
1.9731752(478)	4.30(1524)	11.46(534)
1.9732369(8113)	6.98(6097)	11.20(702)
1.9733534(199)	0.85(1463)	10.51(88)
1.9734258(175)	0.50(1610)	10.32(116)
1.9735107(137)	0.50(1174)	10.32(90)
1.9736392(81)	3.39(156)	10.76(9)

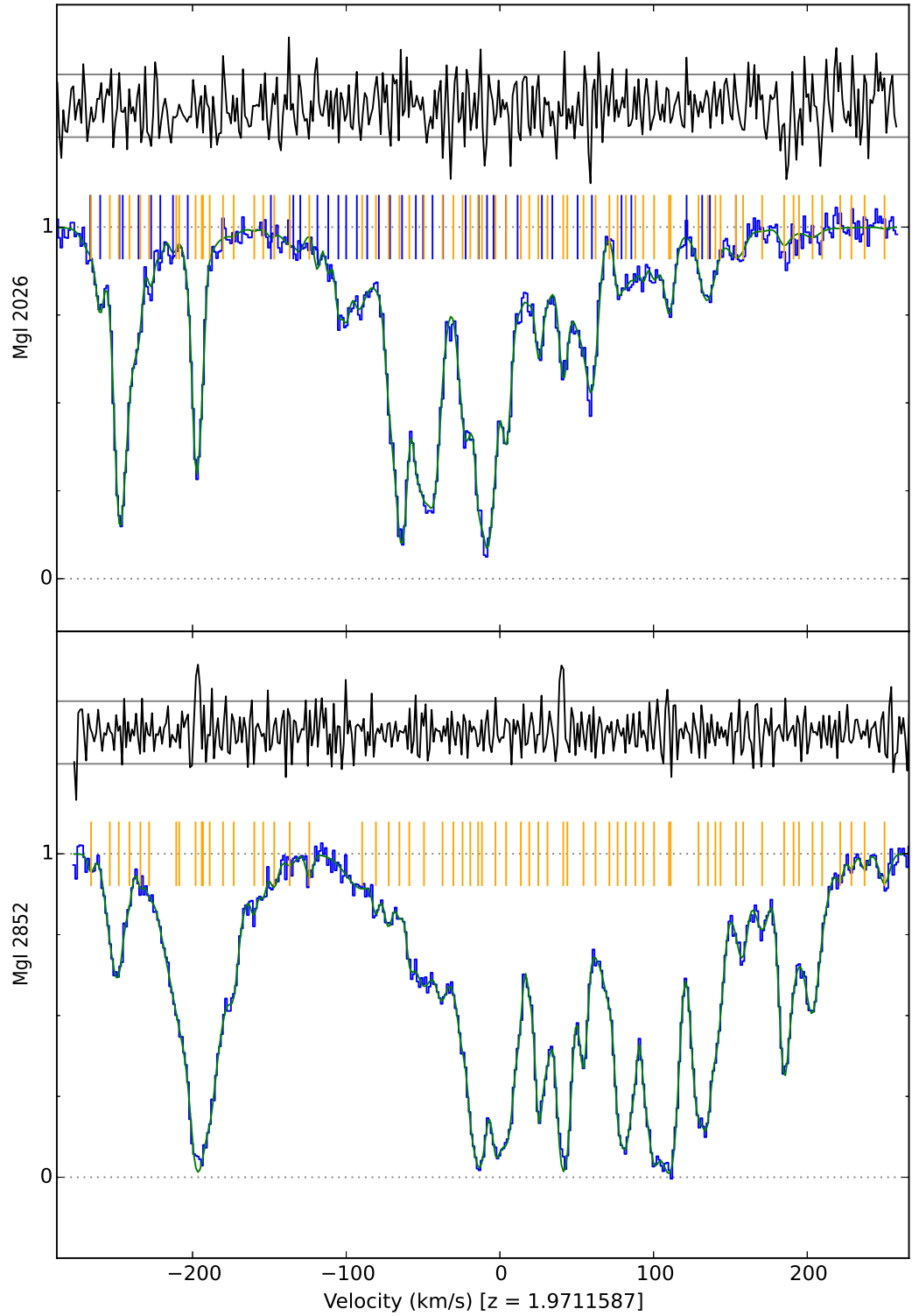


Figure A.8: Data and model fit for the Q1755+57 HIRES spectrum Mg I transitions, centred at $z_{\text{abs}} = 1.971$.

A.7 Q2206–1958

Table A.9: Fiducial fit Mg I absorption line parameters and 1- σ statistical uncertainties for the Q2206–1958 spectrum.

z_{abs}	b [km s ⁻¹]	$\log N(\text{Mg I})$ [cm ⁻²]
1.9197407(105)	1.04(949)	10.57(45)
1.9197898(622)	10.33(623)	11.32(11)
1.9199067(80)	2.91(213)	11.27(33)
1.9199997(33)	6.19(56)	12.17(3)
1.9201161(82)	0.50(568)	10.79(137)
1.9202149(61)	8.64(132)	11.84(7)
1.9203496(83)	3.19(271)	10.97(49)
1.9204736(306)	7.74(329)	11.59(54)
1.9206221(2795)	14.32(9208)	11.63(1542)
1.9206917(62)	0.50(170)	10.97(72)
1.9207741(33683)	21.06(22498)	11.79(1102)
1.9209331(106)	0.50(1041)	10.48(103)
1.9210986(432)	11.23(478)	11.57(71)
1.9214079(242)	18.42(789)	11.33(16)
1.9216006(134)	5.09(461)	10.56(49)

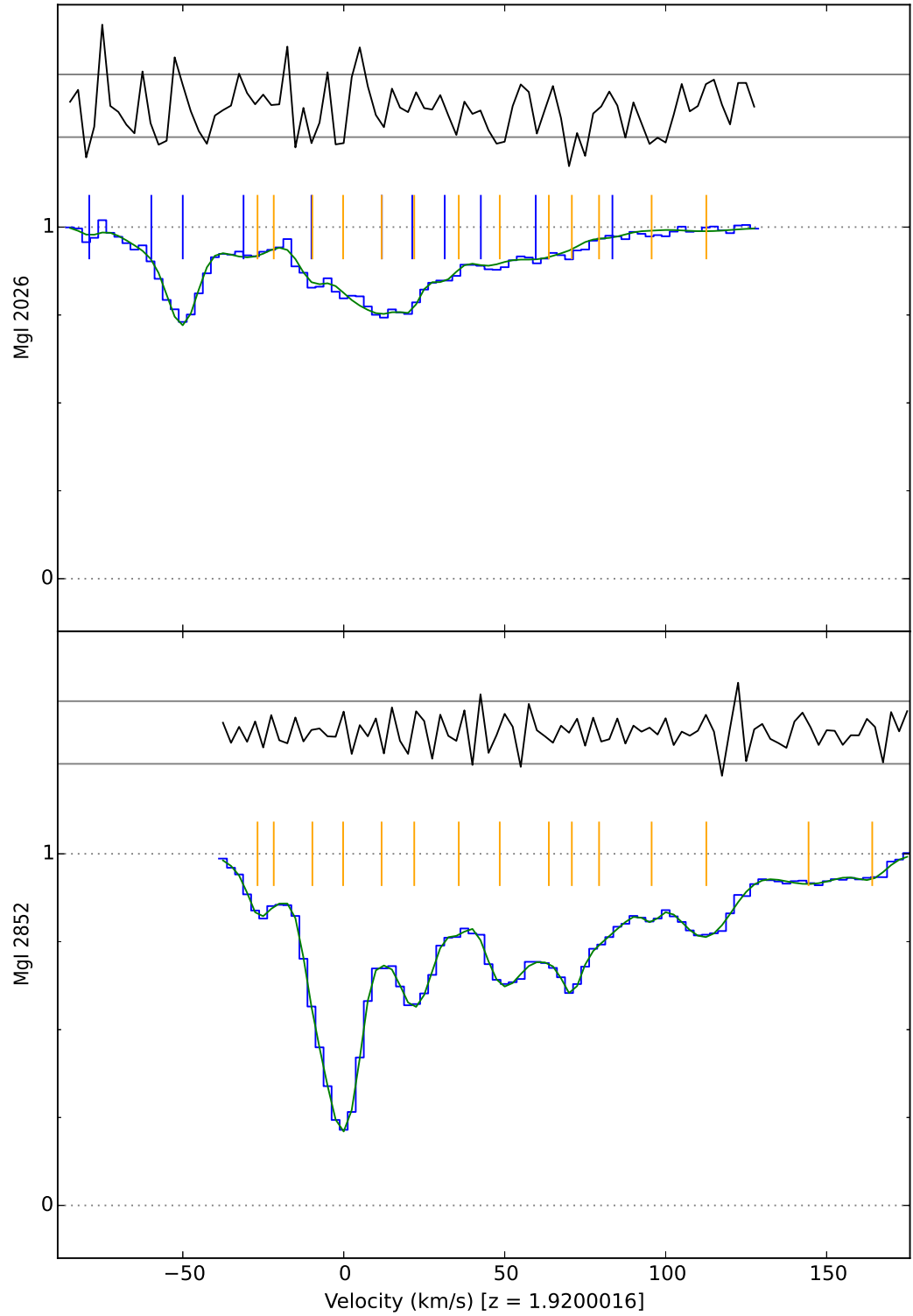


Figure A.9: Data and model fit for the Q2206–1958 UVES spectrum Mg I transitions, centred at $z_{\text{abs}} = 1.920$.

A.8 J1237+0106

Table A.10: Fiducial fit Mg I absorption line parameters and 1- σ statistical uncertainties for the J1237+0106 spectrum.

z_{abs}	b [km s ⁻¹]	$\log N(\text{Mg I})$ [cm ⁻²]
1.3042918(202)	14.09(407)	11.00(10)
1.3044772(127)	3.04(319)	10.70(22)
1.3045422(61)	2.02(245)	11.03(17)
1.3046127(84)	4.04(350)	11.21(23)
1.3046746(109)	1.63(238)	11.65(20)
1.3047181(108)	2.60(253)	11.79(19)
1.3047665(92)	0.50(28)	12.04(21)
1.3047931(82)	0.72(31)	11.66(40)
1.3048293(37)	0.81(13)	12.30(17)
1.3048666(42)	1.02(29)	12.02(19)
1.3049230(35)	4.88(210)	11.98(12)
1.3049871(39)	1.94(170)	11.70(10)
1.3050302(62)	1.25(50)	12.02(17)
1.3050822(287)	4.25(663)	11.92(70)
1.3051410(381)	3.84(1202)	11.59(180)
1.3052098(261)	4.53(877)	11.82(127)
1.3052840(477)	6.10(2172)	11.78(157)
1.3053474(113)	2.48(570)	11.58(105)
1.3053821(160)	0.68(81)	11.75(37)
1.3054178(178)	3.76(1321)	11.53(339)
1.3054821(669)	7.76(4369)	11.92(325)
1.3055777(1379)	7.55(1623)	11.97(184)
1.3056650(76)	3.00(252)	11.75(37)
1.3057016(66)	0.85(51)	11.96(15)
1.3057508(49)	5.43(251)	12.08(14)
1.3058163(60)	1.58(252)	11.45(28)
1.3058785(114)	5.11(371)	11.87(29)
1.3059565(195)	4.73(513)	11.78(83)
1.3060230(1104)	6.20(2005)	11.39(191)
1.3060783(130)	0.50(1319)	10.56(114)
1.3061446(1917)	9.99(3403)	10.73(166)
1.3062392(112)	0.50(1819)	10.32(100)

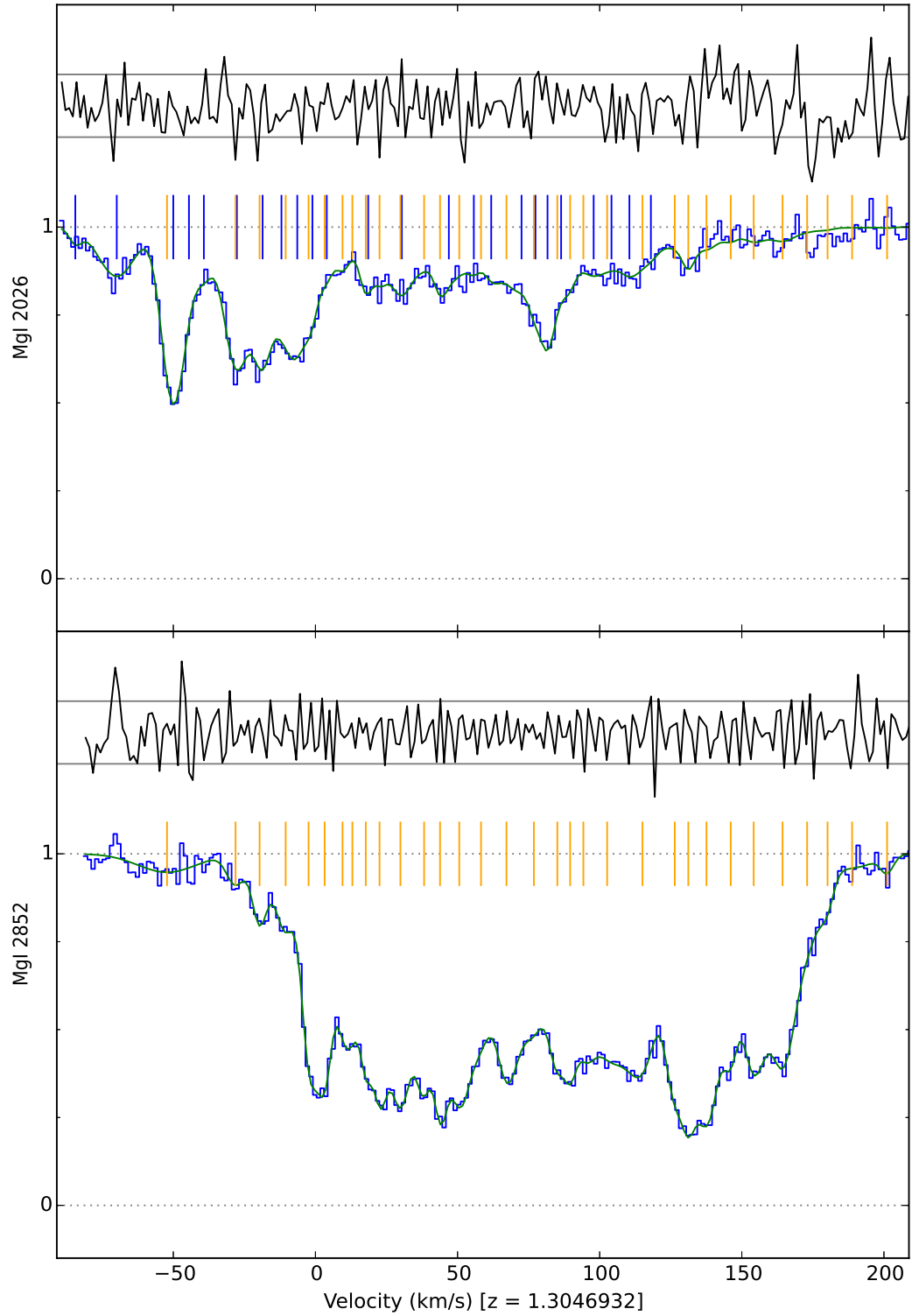


Figure A.10: Data and model fit for the J1237+0106 HIRES spectrum Mg I transitions, centred at $z_{\text{abs}} = 1.305$.

Catalogue of H₂ laboratory parameters

Table B.1: Catalogue of the most accurate and precise laboratory parameters for fitting H₂ absorptions lines. Represented are all allowed Lyman and Werner H₂ transitions between the lowest 8 rotational levels in the ground and excited states with excited state vibrational quantum numbers up to 20 and 6 for Lyman and Werner transitions, respectively. The first column provides a short-hand notation for the transition: letters denote a Lyman (L) or Werner (W) line and the branch, where P, Q and R represent $J' - J = -1, 0$ and 1 , respectively, for J and J' the ground state and excited state J -levels, respectively; the first integer is the excited state vibrational quantum number and the second is J . The second column gives the most precise reported laboratory wavelength and its $1\text{-}\sigma$ uncertainty and the note mark indicates the reference: 1 = Bailly et al. (2010), 2 = Ubachs et al. (2007) (a suffix “a” refers to directly measured wavelengths while “b” refers to wavelengths calculated from directly measured lines via combination differences) and 3 = Abgrall et al. (1993) for the excited state energy levels with ground states derived directly from Jennings et al. (1984). Note that wavelengths with reference 3 are much less precise than those from references 1 and 2. The third column gives the oscillator strengths which were calculated from the Einstein A coefficients given by Abgrall et al. (1994). The fourth column gives the (natural) damping coefficients which were calculated from the total transition probabilities (A_t) in Abgrall et al. (2000). The final column gives the sensitivity coefficients calculated in Ubachs et al. (2007) which have estimated uncertainties of typically $< 5 \times 10^{-4}$ (see Section 4.3.3).

Trans.	λ_{lab} [Å]	f [10^{-2}]	Γ [10^9 s^{-1}]	K
L0P1	1110.062558(3) ¹	0.0573914	1.87	−0.00973852
L0P2	1112.495989(3) ¹	0.0691459	1.86	−0.01190946
L0P3	1115.895530(3) ¹	0.0738064	1.86	−0.01491660
L0P4	1120.248839(3) ¹	0.0755955	1.85	−0.01872438

Continued on next page

Table B.1: *Continued from previous page*

Trans.	λ_{lab} [Å]	f [10^{-2}]	Γ [10^9 s^{-1}]	K
L0P5	1125.540690(5) ¹	0.0757692	1.84	−0.02329085
L0P6	1131.753504(6) ¹	0.0748072	1.83	−0.02857077
L0P7	1151.6384(14) ³	0.0729867	1.82	−0.03451983
L0R0	1108.127317(2) ¹	0.166457	1.86	−0.00800319
L0R1	1108.633244(3) ¹	0.1077	1.86	−0.00846231
L0R2	1110.120562(3) ¹	0.0932201	1.85	−0.00980419
L0R3	1112.583944(5) ¹	0.0846784	1.84	−0.01201537
L0R4	1116.014618(7) ¹	0.0777988	1.83	−0.01507444
L0R5	1120.400623(5) ¹	0.0715714	1.82	−0.01895450
L0R6	1125.727077(5) ¹	0.0656326	1.80	−0.02362649
L1P1	1094.051949(3) ¹	0.196852	1.74	−0.00259287
L1P2	1096.438914(5) ¹	0.236713	1.74	−0.00474693
L1P3	1099.787177(5) ¹	0.252569	1.73	−0.00774742
L1P4	1104.083933(7) ¹	0.259547	1.73	−0.01155644
L1P5	1109.313238(4) ¹	0.261585	1.72	−0.01612812
L1P6	1115.456467(5) ¹	0.260431	1.71	−0.02141170
L1P7	1134.8965(13) ³	0.256861	1.70	−0.02735538
L1R0	1092.195201(4) ¹	0.578358	1.74	−0.00092454
L1R1	1092.732382(4) ¹	0.378015	1.73	−0.00143170
L1R2	1094.244560(7) ¹	0.33148	1.73	−0.00282772
L1R3	1096.725316(4) ¹	0.305571	1.72	−0.00509470
L1R4	1100.164528(7) ¹	0.28543	1.71	−0.00820532
L1R5	1104.548705(5) ¹	0.267606	1.70	−0.01212508
L1R6	1109.861422(8) ¹	0.25058	1.68	−0.01681549
L2P1	1078.925400(3) ¹	0.392257	1.63	0.00397218
L2P2	1081.265950(4) ¹	0.469983	1.63	0.00183764
L2P3	1084.560256(3) ¹	0.500946	1.63	−0.00114925
L2P4	1088.795369(4) ¹	0.515046	1.62	−0.00494895
L2P5	1093.954976(3) ¹	0.520673	1.61	−0.00951288
L2P6	1100.019972(5) ¹	0.520974	1.60	−0.01478632
L2P7	1119.0297(13) ³	0.517602	1.59	−0.02071215
L2R0	1077.138656(3) ¹	1.16679	1.63	0.00558220
L2R1	1077.698852(3) ¹	0.769324	1.63	0.00503784
L2R2	1079.225425(4) ¹	0.681799	1.62	0.00360188
L2R3	1081.711274(3) ¹	0.636247	1.61	0.00129543
L2R4	1085.145527(5) ¹	0.603064	1.60	−0.00184988
L2R5	1089.513848(5) ¹	0.573951	1.59	−0.00579408
L2R6	1094.798877(5) ¹	0.546325	1.58	−0.01049178

Continued on next page

Table B.1: *Continued from previous page*

Trans.	λ_{lab} [Å]	f [10^{-2}]	Γ [10^9 s^{-1}]	K
L3P1	1064.605318(4) ¹	0.594138	1.54	0.01000951
L3P2	1066.900633(4) ¹	0.709045	1.53	0.00789541
L3P3	1070.140818(3) ¹	0.753828	1.53	0.00492550
L3P4	1074.312899(5) ¹	0.774358	1.53	0.00114033
L3P5	1079.400450(4) ¹	0.783446	1.52	−0.00340979
L3P6	1085.384151(6) ¹	0.78606	1.51	−0.00866755
L3P7	1103.9823(13) ³	0.784325	1.50	−0.01457227
L3R0	1062.882074(4) ¹	1.78952	1.53	0.01156759
L3R1	1063.460086(3) ¹	1.19024	1.53	0.01099293
L3R2	1064.994759(4) ¹	1.06482	1.53	0.00952560
L3R3	1067.478598(4) ¹	1.00421	1.52	0.00718891
L3R4	1070.900286(6) ¹	0.962639	1.51	0.00401739
L3R5	1075.244947(6) ¹	0.928142	1.50	0.00005478
L3R6	1080.494745(24) ¹	0.895452	1.49	−0.00464885
L4P1	1051.032451(5) ¹	0.760153	1.45	0.01555697
L4P2	1053.284210(4) ¹	0.902223	1.45	0.01346322
L4P3	1056.471373(3) ¹	0.955567	1.45	0.01051153
L4P4	1060.580970(4) ¹	0.979364	1.44	0.00674295
L4P5	1065.596570(4) ¹	0.990006	1.43	0.00220871
L4P6	1071.498770(5) ¹	0.99386	1.43	−0.00303240
L4P7	1089.7065(12) ³	0.994149	1.42	−0.00891760
L4R0	1049.367383(4) ¹	2.31929	1.45	0.01706801
L4R1	1049.959704(3) ¹	1.55494	1.45	0.01646751
L4R2	1051.498512(4) ¹	1.40303	1.44	0.01497399
L4R3	1053.976051(4) ¹	1.33569	1.43	0.01261209
L4R4	1057.380706(7) ¹	1.29372	1.43	0.00941815
L4R5	1061.697413(5) ¹	1.26059	1.42	0.00543822
L4R6	1066.907971(34) ¹	1.23026	1.41	0.00072530
L5P1	1038.157044(4) ¹	0.866057	1.37	0.02064400
L5P2	1040.367202(3) ¹	1.02228	1.37	0.01856997
L5P3	1043.503090(4) ¹	1.07672	1.37	0.01563663
L5P4	1047.551786(4) ¹	1.09902	1.36	0.01188511
L5P5	1052.496918(4) ¹	1.10794	1.36	0.00736695
L5P6	1058.319102(9) ¹	1.11122	1.35	0.00214153
L5P7	1076.1556(12) ³	1.11219	1.34	−0.00372739
L5R0	1036.545680(2) ¹	2.68337	1.37	0.02211196
L5R1	1037.149822(3) ¹	1.81342	1.37	0.02148875
L5R2	1038.690179(3) ¹	1.6503	1.36	0.01997239

Continued on next page

Table B.1: *Continued from previous page*

Trans.	λ_{lab} [Å]	f [10^{-2}]	Γ [10^9 s^{-1}]	K
L5R3	1041.158832(4) ¹	1.58464	1.36	0.01758824
L5R4	1044.543977(5) ¹	1.54839	1.35	0.01437358
L5R5	1048.830369(5) ¹	1.52277	1.34	0.01037564
L5R6	1053.9987(12) ³	1.50045	1.33	0.00564897
L6P1	1025.935181(6) ¹	0.90943	1.30	0.02529614
L6P2	1028.105875(7) ¹	1.06298	1.30	0.02324105
L6P3	1031.192672(4) ¹	1.11102	1.30	0.02032577
L6P4	1035.182762(5) ¹	1.12657	1.29	0.01659124
L6P5	1040.059726(4) ¹	1.13034	1.29	0.01208886
L6P6	1045.804318(5) ¹	1.13046	1.28	0.00687799
L6P7	1063.2888(12) ³	1.13078	1.27	0.00102254
L6R0	1024.373738(6) ¹	2.87085	1.30	0.02672449
L6R1	1024.987976(3) ¹	1.95752	1.30	0.02608105
L6R2	1026.528323(5) ¹	1.79656	1.29	0.02454448
L6R3	1028.986607(4) ¹	1.73884	1.29	0.02214038
L6R4	1032.350972(8) ¹	1.71203	1.28	0.01890632
L6R5	1036.60473(2) ¹	1.69652	1.27	0.01488993
L6R6	1041.734691(54) ¹	1.68443	1.26	0.01014630
L7P1	1014.327128(6) ¹	0.898222	1.24	0.02953792
L7P2	1016.461136(5) ¹	1.02323	1.24	0.02750099
L7P3	1019.502139(3) ¹	1.04758	1.23	0.02460346
L7P4	1023.436799(5) ¹	1.04924	1.23	0.02088590
L7P5	1028.248570(4) ¹	1.04684	1.22	0.01639930
L7P6	1033.918239(21) ¹	1.04606	1.22	0.01120261
L7P7	1051.0715(12) ³	1.04866	1.21	0.00535938
L7R0	1012.812914(4) ¹	2.9702	1.24	0.03092982
L7R1	1013.436916(2) ¹	2.05043	1.23	0.03026841
L7R2	1014.976843(5) ¹	1.89365	1.23	0.02871411
L7R3	1017.424212(4) ¹	1.83845	1.22	0.02629246
L7R4	1020.767035(11) ¹	1.81358	1.22	0.02304091
L7R5	1024.990170(11) ¹	1.80093	1.21	0.01900700
L7R6	1030.0736(11) ³	1.7934	1.20	0.01424573
L8P1	1003.296508(5) ¹	0.846599	1.18	0.03339412
L8P2	1005.393086(5) ¹	0.991071	1.18	0.03137464
L8P3	1008.386075(3) ¹	1.04293	1.17	0.02849467
L8P4	1012.262348(5) ¹	1.07544	1.17	0.02479431
L8P5	1017.004186(5) ¹	1.12202	1.17	0.02029474
L8P6	1022.585960(21) ¹	1.25592	1.16	0.01498634

Continued on next page

Table B.1: *Continued from previous page*

Trans.	λ_{lab} [Å]	f [10^{-2}]	Γ [10^9 s^{-1}]	K
L8P7	1039.2104(11) ³	2.3255	1.17	−0.00116452
L8R0	1001.823741(4) ¹	2.67679	1.18	0.03475253
L8R1	1002.452009(3) ¹	1.82317	1.17	0.03407534
L8R2	1003.985377(5) ¹	1.66161	1.17	0.03250586
L8R3	1006.414053(5) ¹	1.57143	1.17	0.03004038
L8R4	1009.71969(2) ¹	1.41081	1.16	0.02664915
L8R5	1013.7065(11) ³	0.116013	1.17	0.01243063
L8R6	1019.0189(11) ³	2.04951	1.14	0.01766495
L9P1	992.809625(4) ¹	0.769885	1.12	0.03688977
L9P2	994.874026(6) ¹	0.865918	1.12	0.03488711
L9P3	997.827121(3) ¹	0.876095	1.12	0.03202454
L9P4	1001.655682(5) ¹	0.869116	1.12	0.02834180
L9P5	1006.343184(3) ¹	0.863341	1.11	0.02388888
L9P6	1011.870513(50) ¹	0.864503	1.11	0.01872364
L9P7	1028.4114(11) ³	0.875861	1.10	0.01290853
L9R0	991.378851(5) ¹	2.61242	1.12	0.03821743
L9R1	992.016320(2) ¹	1.82598	1.12	0.03752654
L9R2	993.550563(5) ¹	1.70432	1.12	0.03594442
L9R3	995.972783(3) ¹	1.66863	1.11	0.03349627
L9R4	999.270807(5) ¹	1.65603	1.11	0.03021901
L9R5	1003.4284(11) ³	1.64978	1.10	0.02615952
L9R6	1008.4289(11) ³	1.64072	1.09	0.02137208
L10P1	982.835296(5) ¹	0.68112	1.07	0.04004930
L10P2	984.864026(7) ¹	0.817085	1.07	0.03806275
L10P3	987.768823(4) ¹	0.892793	1.07	0.03515959
L10P4	991.533853(6) ¹	0.991957	1.07	0.03138155
L10P5	996.124697(6) ¹	1.27433	1.07	0.02610094
L10P6	1001.9117(11) ³	0.0262827	1.09	0.00917942
L10P7	1017.9765(11) ³	0.373993	1.05	0.01492525
L10R0	981.438709(7) ¹	2.06903	1.07	0.04134865
L10R1	982.074245(4) ¹	1.36447	1.07	0.04058840
L10R2	983.591063(5) ¹	1.15741	1.07	0.03888367
L10R3	985.962767(6) ¹	0.827655	1.07	0.03558931
L10R4	989.55727(98) ³	3.10766	1.09	0.02068108
L10R5	993.49192(99) ³	2.01634	1.05	0.02801621
L10R6	998.42833(100) ³	1.78819	1.04	0.02399851
L11P1	973.344571(6) ¹	0.589912	1.03	0.04289516
L11P2	975.345771(8) ¹	0.66437	1.02	0.04092386

Continued on next page

Table B.1: *Continued from previous page*

Trans.	λ_{lab} [Å]	f [10^{-2}]	Γ [10^9 s^{-1}]	K
L11P3	978.218030(3) ¹	0.673539	1.02	0.03809495
L11P4	981.948441(3) ¹	0.670767	1.02	0.03444786
L11P5	986.520717(4) ¹	0.671492	1.02	0.03003235
L11P6	991.915746(17) ¹	0.683092	1.01	0.02490619
L11P7	998.111832(73) ^{2b}	0.712953	1.01	0.01913197
L11R0	971.986230(8) ¹	2.0043	1.02	0.04416825
L11R1	972.632731(3) ¹	1.40478	1.02	0.04345479
L11R2	974.157875(2) ¹	1.31537	1.02	0.04185365
L11R3	976.552811(4) ¹	1.28986	1.02	0.03939034
L11R4	979.80509(2) ¹	1.27815	1.01	0.03610218
L11R5	983.898956(68) ^{2a}	1.26202	1.01	0.03203650
L11R6	988.81351(98) ³	1.22149	1.00	0.02724831
L12P1	964.310524(6) ¹	0.502802	0.982	0.04544644
L12P2	966.275434(9) ¹	0.649635	0.982	0.04340505
L12P3	969.089768(4) ¹	0.816003	0.983	0.04022253
L12P4	972.69064(3) ¹	1.35586	1.00	0.03305977
L12P5	977.463601(5) ¹	0.0364005	0.994	0.02751866
L12P6	982.726751(11) ¹	0.257392	0.972	0.02634450
L12P7	988.838329(91) ^{2b}	0.358014	0.964	0.02121293
L12R0	962.977981(8) ¹	1.31586	0.982	0.04661091
L12R1	963.607928(3) ¹	0.707397	0.983	0.04552063
L12R2	965.04571(3) ¹	0.158292	1.00	0.04040726
L12R3	967.676976(5) ¹	2.27601	0.994	0.03681687
L12R4	970.838045(10) ¹	1.60389	0.972	0.03742072
L12R5	974.886485(86) ^{2a}	1.42339	0.964	0.03396998
L12R6	979.76132(96) ³	1.352	0.958	0.02940565
L13P1	955.708153(9) ¹	0.422758	0.941	0.04771815
L13P2	957.652228(9) ¹	0.480776	0.940	0.04577359
L13P3	960.450567(5) ¹	0.493219	0.939	0.04297335
L13P4	964.09079(2) ¹	0.498546	0.937	0.03935778
L13P5	968.556580(7) ¹	0.509638	0.933	0.03497826
L13P6	973.828541(20) ¹	0.536302	0.930	0.02989496
L13P7	989.31987(98) ³	0.595954	0.926	0.02417375
L13R0	954.413268(9) ¹	1.41587	0.940	0.04894292
L13R1	955.065759(5) ¹	0.988009	0.939	0.04820903
L13R2	956.579917(18) ¹	0.921098	0.937	0.04659168
L13R3	958.946624(7) ¹	0.896715	0.933	0.04411846
L13R4	962.15273(6) ¹	0.875105	0.930	0.04082942

Continued on next page

Table B.1: *Continued from previous page*

Trans.	λ_{lab} [Å]	f [10^{-2}]	Γ [10^9 s^{-1}]	K
L13R5	966.17871(94) ³	0.832436	0.926	0.03677543
L13R6	970.99762(95) ³	0.711421	0.925	0.03201589
L14P1	947.514033(99) ^{2a}	0.352235	0.903	0.04972156
L14P2	949.352458(100) ^{2b}	0.928258	0.971	0.03930819
L14P3	952.274166(100) ^{2b}	0.0657805	0.927	0.04104973
L14P4	955.854830(61) ^{2b}	0.169072	0.907	0.03998528
L14P5	960.26564(93) ³	0.224404	0.899	0.03624932
L14P6	965.48139(94) ³	0.261446	0.893	0.03144234
L14P7	980.75837(97) ³	0.292951	0.888	0.02588968
L14R0	946.169306(99) ^{2a}	0.133958	0.971	0.04247182
L14R1	946.980395(99) ^{2a}	1.96578	0.927	0.04625180
L14R2	948.47125(6) ^{2a}	1.29431	0.907	0.04715304
L14R3	950.81869(91) ³	1.09208	0.899	0.04529959
L14R4	954.00391(92) ³	1.00543	0.893	0.04226582
L14R5	958.01140(92) ³	0.961679	0.888	0.03836088
L14R6	962.82129(93) ³	0.935859	0.883	0.03368526
L15P1	939.706716(98) ^{2a}	0.291382	0.868	0.05146650
L15P2	941.599214(98) ^{2b}	0.336792	0.867	0.04954168
L15P3	944.33046(6) ^{2a}	0.352469	0.866	0.04676022
L15P4	947.887847(61) ^{2b}	0.365429	0.864	0.04316527
L15P5	952.254963(62) ^{2b}	0.387851	0.862	0.03881266
L15P6	957.410209(63) ^{2b}	0.435348	0.861	0.03376881
L15P7	972.44061(95) ³	0.558134	0.862	0.02810778
L15R0	938.467757(97) ^{2a}	0.951063	0.867	0.05264552
L15R1	939.124212(98) ^{2a}	0.65582	0.866	0.05188763
L15R2	940.62637(6) ^{2a}	0.602792	0.864	0.05024936
L15R3	942.96422(6) ^{2a}	0.573822	0.862	0.04776314
L15R4	946.12271(6) ^{2a}	0.533399	0.861	0.04447549
L15R5	950.07344(91) ³	0.436762	0.862	0.04044555
L15R6	954.70212(92) ³	0.114293	0.901	0.03574293
L16P1	932.266208(96) ^{2a}	0.239836	0.835	0.05296626
L16P2	934.144795(97) ^{2b}	0.223943	0.836	0.05084687
L16P3	936.857092(97) ^{2b}	0.204989	0.835	0.04791941
L16P4	940.387542(98) ^{2b}	0.199323	0.833	0.04428935
L16P5	944.72052(90) ³	0.203185	0.830	0.03996189
L16P6	949.83996(91) ³	0.213559	0.827	0.03495694
L16P7	964.70461(94) ³	0.230595	0.823	0.02937510
L16R0	931.062642(96) ^{2a}	1.06711	0.836	0.05392193

Continued on next page

Table B.1: *Continued from previous page*

Trans.	λ_{lab} [Å]	f [10^{-2}]	Γ [10^9 s^{-1}]	K
L16R1	931.732882(96) ^{2a}	0.753127	0.835	0.05300015
L16R2	933.240091(96) ^{2a}	0.6886	0.833	0.05130933
L16R3	935.57550(88) ³	0.657153	0.830	0.04883117
L16R4	938.72921(89) ³	0.6378	0.827	0.04556605
L16R5	942.68787(89) ³	0.623818	0.823	0.04159919
L16R6	947.43378(90) ³	0.609298	0.818	0.03696031
L17P1	925.174530(95) ^{2a}	0.19672	0.804	0.05424593
L17P2	927.020019(95) ^{2b}	0.232754	0.804	0.05233481
L17P3	929.689572(96) ^{2b}	0.250827	0.803	0.04956415
L17P4	933.17050(88) ³	0.27111	0.802	0.04598242
L17P5	937.44275(88) ³	0.308293	0.802	0.04165374
L17P6	942.47736(89) ³	0.400691	0.807	0.03665595
L17P7	956.99373(92) ³	0.769999	0.857	0.03107800
L17R0	923.984626(94) ^{2a}	0.616671	0.804	0.05538162
L17R1	924.643257(95) ^{2a}	0.416144	0.803	0.05459732
L17R2	926.13193(86) ³	0.37013	0.802	0.05293621
L17R3	928.43742(87) ³	0.330312	0.802	0.05043924
L17R4	931.53720(87) ³	0.252976	0.807	0.04716450
L17R5	935.32358(88) ³	0.0455546	0.857	0.04318584
L17R6	940.49158(89) ³	0.99348	0.829	0.03859103
L18P1	918.413305(93) ^{2a}	0.160977	0.776	0.05535517
L18P2	920.243231(94) ^{2b}	0.168347	0.776	0.05345167
L18P3	922.894904(94) ^{2b}	0.161894	0.775	0.05068943
L18P4	926.354670(95) ^{2b}	0.157497	0.774	0.04712078
L18P5	930.60522(87) ³	0.158386	0.771	0.04281575
L18P6	935.63098(88) ³	0.165464	0.769	0.03786035
L18P7	950.12370(91) ³	0.180098	0.766	0.03235406
L18R0	917.251984(93) ^{2a}	0.617555	0.776	0.05647264
L18R1	917.921885(93) ^{2a}	0.442958	0.775	0.05567990
L18R2	919.418156(93) ^{2a}	0.416768	0.774	0.05401546
L18R3	921.73016(85) ³	0.406946	0.771	0.05152632
L18R4	924.84828(86) ³	0.40013	0.769	0.04827866
L18R5	928.76010(87) ³	0.391557	0.766	0.04435672
L18R6	933.44461(88) ³	0.375904	0.764	0.03986101
L19P1	911.96720(17) ^{2a}	0.131627	0.749	0.05638629
L19P2	913.77014(17) ^{2a}	0.161406	0.749	0.05447034
L19P3	916.38293(34) ^{2a}	0.182459	0.749	0.05167878
L19P4	919.78999(17) ^{2b}	0.213475	0.751	0.04802474

Continued on next page

Table B.1: *Continued from previous page*

Trans.	λ_{lab} [Å]	f [10^{-2}]	Γ [10^9 s^{-1}]	K
L19P5	923.96165(18) ^{2b}	0.286714	0.760	0.04325677
L19P6	928.77793(87) ³	0.56257	0.837	0.03450348
L19P7	943.54717(90) ³	0.0004714	0.785	0.03004227
L19R0	910.82073(17) ^{2a}	0.386549	0.749	0.05746684
L19R1	911.47950(17) ^{2a}	0.248482	0.749	0.05662896
L19R2	912.95107(17) ^{2a}	0.201527	0.751	0.05486433
L19R3	915.21226(17) ^{2a}	0.134894	0.760	0.05190177
L19R4	918.15171(85) ³	0.0045274	0.837	0.04488527
L19R5	922.47501(86) ³	0.666706	0.785	0.04199436
L19R6	927.05157(86) ³	0.498923	0.746	0.04030239
W0P2	1012.16946(2) ¹	0.878387	1.18	−0.00830958
W0P3	1014.504259(5) ¹	1.1105	1.18	−0.01056398
W0P4	1017.385588(5) ¹	1.22766	1.18	−0.01330997
W0P5	1020.799172(6) ¹	1.27454	1.18	−0.01647897
W0P6	1024.73454(9) ¹	1.19609	1.17	−0.01995118
W0P7	1039.7737(11) ³	0.0633991	1.16	−0.01356055
W0Q1	1009.770899(6) ¹	2.38007	1.18	−0.00595909
W0Q2	1010.938509(8) ¹	2.38098	1.18	−0.00709859
W0Q3	1012.679615(6) ¹	2.38304	1.18	−0.00878174
W0Q4	1014.98244(3) ¹	2.38617	1.17	−0.01097807
W0Q5	1017.83147(3) ¹	2.38871	1.17	−0.01364833
W0Q6	1021.2095(11) ³	2.39051	1.17	−0.01674587
W0Q7	1035.4267(11) ³	2.39457	1.16	−0.02021825
W0R0	1008.55192(2) ¹	1.53493	1.18	−0.00476718
W0R1	1008.498181(5) ¹	1.28722	1.18	−0.00471844
W0R2	1009.024969(5) ¹	1.16636	1.18	−0.00524664
W0R3	1010.130272(6) ¹	1.11813	1.18	−0.00631306
W0R4	1011.81449(3) ¹	1.18774	1.17	−0.00782388
W0R5	1014.2425(11) ³	2.29175	1.16	0.00022003
W0R6	1016.7433(11) ³	0.570076	1.17	−0.01232471
W1P2	989.088421(9) ¹	1.29261	1.16	0.00259876
W1P3	991.380493(5) ¹	1.59986	1.16	0.00039069
W1P4	994.229935(6) ¹	1.70007	1.16	−0.00228095
W1P5	997.64142(7) ¹	1.51938	1.15	−0.00470129
W1P6	1001.208696(30) ¹	3.05349	1.12	0.00337501
W1P7	1015.7497(11) ³	2.70703	1.15	−0.01223158
W1Q1	986.798049(8) ¹	3.64673	1.16	0.00486880
W1Q2	987.974478(9) ¹	3.64958	1.16	0.00367586

Continued on next page

Table B.1: *Continued from previous page*

Trans.	λ_{lab} [Å]	f [10^{-2}]	Γ [10^9 s^{-1}]	K
W1Q3	989.729361(3) ¹	3.65227	1.16	0.00191129
W1Q4	992.05124(3) ¹	3.65615	1.15	−0.00039590
W1Q5	994.92543(2) ¹	3.66104	1.15	−0.00320842
W1Q6	998.335667(13) ¹	3.66674	1.15	−0.00648190
W1Q7	1012.1346(11) ³	3.67154	1.14	−0.01016654
W1R0	985.633709(9) ¹	2.40614	1.16	0.00602255
W1R1	985.644316(4) ¹	2.0708	1.16	0.00604040
W1R2	986.244066(6) ¹	1.95224	1.16	0.00551177
W1R3	987.44868(7) ¹	2.07847	1.15	0.00511604
W1R4	988.87151(4) ¹	0.0740979	1.12	0.01493980
W1R5	991.37172(5) ¹	0.944833	1.15	0.00122097
W1R6	994.26049(99) ³	1.15345	1.15	−0.00231093
W2P2	968.29519(6) ¹	1.15224	1.14	0.01184321
W2P3	970.563360(7) ¹	1.30736	1.13	0.00992403
W2P4	973.45239(2) ¹	0.855244	1.11	0.01061912
W2P5	976.54879(3) ¹	2.57208	1.11	0.00841259
W2P6	980.502255(25) ¹	2.3747	1.13	0.00066493
W2P7	994.45410(99) ³	2.27604	1.13	−0.00417212
W2Q1	966.096120(7) ¹	3.49812	1.14	0.01396322
W2Q2	967.28107(3) ¹	3.50109	1.14	0.01271847
W2Q3	969.049316(10) ¹	3.50406	1.14	0.01087504
W2Q4	971.38968(2) ¹	3.50968	1.13	0.00846055
W2Q5	974.28818(2) ¹	3.51643	1.13	0.00551054
W2Q6	977.72731(9) ¹	3.5241	1.13	0.00206724
W2Q7	991.16345(99) ³	3.53107	1.12	−0.00182201
W2R0	964.98397(6) ¹	2.39558	1.14	0.01516367
W2R1	965.064884(7) ¹	2.19251	1.13	0.01540176
W2R2	965.79552(2) ¹	2.40472	1.11	0.01814876
W2R3	966.78038(3) ¹	0.614792	1.11	0.01789318
W2R4	968.66686(8) ¹	1.07236	1.13	0.01202620
W2R5	971.07625(6) ¹	1.21176	1.13	0.00889150
W2R6	974.05209(95) ³	1.36709	1.12	0.00568077
W3P2	949.61045(3) ¹	0.142114	1.05	0.02782290
W3P3	951.67184(1) ¹	1.69938	1.09	0.02096940
W3P4	954.47400(5) ¹	1.67173	1.11	0.01552446
W3P5	957.81887(3) ¹	1.67029	1.11	0.01144081
W3P6	961.70355(6) ¹	1.65031	1.11	0.00722576
W3P7	975.30210(96) ³	1.54503	1.10	0.00268414

Continued on next page

Table B.1: *Continued from previous page*

Trans.	λ_{lab} [Å]	f [10^{-2}]	Γ [10^9 s^{-1}]	K
W3Q1	947.421917(3) ¹	2.74384	1.12	0.02149264
W3Q2	948.61582(18) ¹	2.74671	1.12	0.02019735
W3Q3	950.397767(18) ¹	2.75027	1.12	0.01827700
W3Q4	952.75740(6) ¹	2.75578	1.12	0.01575800
W3Q5	955.68059(92) ³	2.76314	1.11	0.01267422
W3Q6	959.15121(16) ¹	2.77083	1.11	0.00906590
W3Q7	972.27175(95) ³	2.78011	1.11	0.00497811
W3R0	946.42556(3) ¹	2.16224	1.05	0.03102591
W3R1	946.384745(9) ¹	0.807449	1.09	0.02627974
W3R2	947.11165(5) ¹	0.993795	1.11	0.02287064
W3R3	948.41978(3) ¹	1.03723	1.11	0.02071173
W3R4	950.31519(7) ¹	1.07393	1.11	0.01829419
W3R5	952.80462(91) ³	1.16602	1.10	0.01540740
W3R6	955.97749(92) ³	1.47625	1.05	0.01208778
W4P2	932.604679(96) ^{2a}	0.760932	1.10	0.02569217
W4P3	934.79006(11) ^{2a}	0.951256	1.10	0.02349760
W4P4	937.551755(97) ^{2b}	1.03268	1.10	0.02058324
W4P5	940.88292(11) ^{2b}	1.05472	1.09	0.01703590
W4P6	944.78324(90) ³	0.994692	1.08	0.01295017
W4P7	958.19002(92) ³	0.61521	1.03	0.00836457
W4Q1	930.577079(96) ^{2a}	1.94219	1.10	0.02758111
W4Q2	931.780857(96) ^{2a}	1.94461	1.10	0.02623615
W4Q3	933.57794(11) ^{2a}	1.9482	1.10	0.02424031
W4Q4	935.95938(88) ³	1.95421	1.10	0.02161881
W4Q5	938.90912(89) ³	1.95995	1.10	0.01840400
W4Q6	942.41510(89) ³	1.96795	1.10	0.01463426
W4Q7	955.26209(92) ³	1.97683	1.09	0.01035250
W4R0	929.532719(96) ^{2a}	1.19405	1.10	0.02884502
W4R1	929.688358(96) ^{2a}	0.984172	1.10	0.02870046
W4R2	930.447184(96) ^{2a}	0.898322	1.10	0.02776182
W4R3	931.81170(11) ^{2a}	0.874581	1.09	0.02609047
W4R4	933.78979(88) ³	0.91659	1.08	0.02375924
W4R5	936.46628(88) ³	1.09825	1.03	0.02079095
W4R6	939.11418(89) ³	0.269982	1.05	0.01730411
W5P2	917.36978(85) ³	0.470052	1.09	0.03033591
W5P3	919.54444(85) ³	0.581784	1.09	0.02806908
W5P4	922.30602(86) ³	0.619111	1.08	0.02526343
W5P5	925.65859(86) ³	0.581884	1.07	0.02227953

Continued on next page

Table B.1: *Continued from previous page*

Trans.	λ_{lab} [Å]	f [10^{-2}]	Γ [10^9 s^{-1}]	K
W5P6	929.69736(87) ³	0.301969	0.987	0.02212683
W5P7	942.23361(89) ³	0.952228	1.03	0.01669738
W5Q1	915.40107(84) ³	1.30148	1.09	0.03231442
W5Q2	916.61694(85) ³	1.30368	1.09	0.03092034
W5Q3	918.43092(85) ³	1.30632	1.09	0.02884989
W5Q4	920.83403(85) ³	1.31189	1.09	0.02612717
W5Q5	923.81654(86) ³	1.31785	1.08	0.02278312
W5Q6	927.36262(87) ³	1.32411	1.08	0.01885435
W5Q7	939.97920(89) ³	1.33193	1.08	0.01438179
W5R0	914.39716(84) ³	0.846484	1.09	0.03342239
W5R1	914.60737(84) ³	0.722537	1.09	0.03316301
W5R2	915.42979(84) ³	0.677763	1.08	0.03229127
W5R3	916.87718(85) ³	0.693433	1.07	0.03113926
W5R4	919.05021(85) ³	0.791087	0.987	0.03266013
W5R5	921.21942(85) ³	0.216944	1.03	0.02881256
W5R6	924.49763(86) ³	0.383095	1.06	0.02270836

